



HAL
open science

Frequency shift due to blackbody radiation in a cesium atomic fountain and improvement of the clock performances

Shougang Zhang

► **To cite this version:**

Shougang Zhang. Frequency shift due to blackbody radiation in a cesium atomic fountain and improvement of the clock performances. Atomic Physics [physics.atom-ph]. Université Pierre et Marie Curie - Paris VI, 2004. English. NNT: . tel-00007074

HAL Id: tel-00007074

<https://theses.hal.science/tel-00007074>

Submitted on 10 Oct 2004

HAL is a multi-disciplinary open access archive for the deposit and dissemination of scientific research documents, whether they are published or not. The documents may come from teaching and research institutions in France or abroad, or from public or private research centers.

L'archive ouverte pluridisciplinaire **HAL**, est destinée au dépôt et à la diffusion de documents scientifiques de niveau recherche, publiés ou non, émanant des établissements d'enseignement et de recherche français ou étrangers, des laboratoires publics ou privés.

LABORATOIRE DES SYSTÈMES DE RÉFÉRENCE TEMPS-ESPACE



THÈSE DE DOCTORAT DE L'UNIVERSITÉ PARIS VI
spécialité : Physique Quantique

présentée par
Shougang ZHANG

pour obtenir le grade de
Docteur de l'Université de Paris VI

sujet de thèse :

*Déplacement de Fréquence dû au Rayonnement du
Corps Noir dans une Fontaine Atomique à Césium
et Amélioration des Performances de l'Horloge*

soutenue le 9 juillet 2004 devant le jury composé de :

M.	André CLAIRON	Directeur de thèse
M.	Claude FABRE	Président du jury
M.	Michel GRANVEAUD	Directeur de thèse
M.	Mark David PLIMMER	Rapporteur
M.	Christophe SALOMON	Examineur
Mme	Fernande VEDEL	Rapporteur

巴黎天文台时间空间参考实验室



巴黎 *Pierre et Marie CURIE* 大学
量子物理 专业

张 首 刚

博士论文题目:

利用铯原子喷泉钟研究黑体辐射频移及
原子钟性能的改进

答辩日期: 2004年7月9日

答辩委员会:

André Clairon	导师
Claude Fabre	主席
Michel Granveaud	导师
Mark David Plimmer	评审专家
Christophe Salomon	邀请专家
Fernande Vedel	评审专家

Remerciements

Grace au soins de Jean Dalibard j'ai pu m'inscrire comme étudiant en thèse à l'université Paris 6 et je tiens à le remercier chaleureusement. Ce travail de thèse a été effectué au sein du Laboratoire Primaire du Temps et des fréquences du Bureau National de Métrologie (BNM-LPTF), qui a fusionné avec le Laboratoire de l'Horloge Atomique (LHA) pour former le Laboratoire des Systèmes de Références Temps-Espace (BNM-SYRTE). Je remercie Michel Granveaud de m'avoir accueilli dans son laboratoire, le LPTF et d'avoir accepté de diriger ma thèse, ainsi que Philip Tuckey, qui a pris sa succession à la direction du SYRTE. Leur compréhension et leur gentillesse m'ont beaucoup soutenues.

Mon travail de thèse a été effectué sous la direction scientifique d'André Clairon et je tiens à lui exprimer toute ma reconnaissance pour son enthousiasme, pour les innombrables connaissances et conseils qu'il m'a apportées. J'ai beaucoup apprécié la confiance qu'il a toujours placée en moi, en me laissant prendre des initiatives. Je ne saurai jamais le remercier suffisamment pour sa compétence, son dynamisme et sa patience.

Je remercie tout particulièrement Claude Fabre d'avoir accepté la présidence du jury, ainsi que madame Fernande Vedel et Mark David Plimmer pour avoir bien voulu faire partie du jury en qualité de rapporteur. Je tiens également à remercier Christophe Salomon pour l'intérêt qu'il a porté dans le développement de mon travail de thèse et d'avoir accepté de faire partie du jury de thèse.

Je remercie très chaleureusement Peter Rosenbusch et Céline Vian qui ont poursuivi et beaucoup amélioré l'expérimentation lors de la rédaction de mon manuscrit. Mes remerciements vont à Cipriana Mandache, Daniel Varela Magalhaes et Thibault Andrieux qui ont apporté leur contribution en tant que chercheur invité, visiteur ou stagiaire.

Je suis également très reconnaissant à Giorgio Santarelli, qui dirige le service d'électronique du SYRTE ainsi que Damien Chambon, qui ont mis au point les chaînes de synthèse micro-onde et l'interrupteur interférométrique. Je remercie également Michel Dequin, Michel Lours et Laurent Volodimer pour leur efficacité et pour leur disponibilité. Leurs interventions et leurs

conseils se sont toujours été très cordiaux et très chaleureux.

La réalisation des systèmes à vide a bénéficié des compétences d'Annie Gérard dans le domaine de l'ultra-vide. Je la remercie pour ses précieuses contributions au montage de l'expérience et pour sa gentillesse.

Une grande partie des expériences a été dessinée et réalisée grâce au service mécanique de Armel Legrand, Jean-Pierre Aoustin, Jacques Hammès et Samuel Sirmon. Je leur adresse tous mes remerciements.

Je remercie très chaleureusement les autres membres de l'équipe "atomes froids" du SYRTE, Philippe Laurent, Pierre Lemonde et Sébastien Bize, qui, avec Giorgio Santarelli et André Clairon constituent une équipe extrêmement compétente et dynamique.

Je remercie également tous les membres du SYRTE qui m'ont renseigné ou aidé de nombreuses fois. Je remercie notamment mes collègues thésards: Anders Brusch, Patrick Cheinet, Irène Courtillot, Albane Douillet, Franck Ducos, Jérôme Fils, To Kaing, Ala'a Makdissi, Ivan Maksimovix, Paul-Eric Pottie, Audrey Quessada, Yvan Sortais, Stéphane Trémine, Florence Leduc, Thomas Zanon, ainsi que les autres chercheurs permanents du laboratoire: Ouali Acef, Emeric de Clerq, Stéphane Guérandel, Arnaud Landragin, Franck Peirera Dos Santos, Daniele Rovera, David Valat, Pierre Uhrich, Peter Wolf, et Jean Jacques Zondy. Je remercie Noël Dimarcq pour ses discussions et son soutien.

J'ai notamment beaucoup apprécié de travailler avec Michel Abgrall, qui m'a épaulé dans la joie et la bonne humeur, lors du travail de caractérisation de la cavité d'interrogation de l'horloge spatiale. Il m'a encouragé à être soigneux et méticuleux dans mon travail. Mille merci à mon ami Michel pour son aide pendant à préparation de ma soutenance orale. Luigi Cacciapuoti, Jan Grünert, Harold Marion et Jean-Yves Richard m'ont aussi beaucoup aidé pour rédiger ce manuscrit et leur en suis très reconnaissant.

Je n'oublierai pas de remercier Frédéric Allard et Michel Abgrall avec lesquels j'ai partagé avec joie le même bureau pendant les trois premières années.

J'exprime toute ma gratitude à l'ensemble du personnel du secrétariat pour tout les soins qu'ils ont manifesté au travers des nombreuses taches administratives, en particulier Yertha Baïdomti, Annick Bounoure, Liliane Garin, Catherine Laurent et Katia Vadet. Je remercie Pascal Blondé pour ses compétences et son efficacité dans la gestion de l'informatique.

Je remercie le BNM et l'Observatoire de Paris, qui ont co-financé cette thèse. Je veux adresser également mes remerciements à Maguelonne Chambon et Sebastien Merlet.

J'ai eu la chance de travailler ici grâce à la coopération étroite entre le SYRTE et le NIM (National Institute of Metrology, China), je remercie

REMERCIEMENTS

très sincèrement monsieur le directeur Biqing Pan et mes collègues chinois Changhua Wu, Bingying Huang, Mingshou Li, Tianchu Li, Jin Qian, Pingwei Li et Guangqiu Tong pour leurs encouragements. Je souhaite enfin remercier les professeurs chinois Yiqiu Wang, Yuzhu Wang et Haifeng Liu pour leurs renseignements utiles.

Merci à mes amis et à ma famille qui m'ont apporté leurs soutiens et leurs compréhensions pendant toutes ces années de recherche et je leur en suis très reconnaissant.

Table of Contents

Remerciements	3
Introduction	17
0.1 Introduction en français	17
0.2 Introduction in English	20
1 Principle and characteristics of an atomic clock	25
1.1 Résumé en français	25
1.2 Principle of the Cs atomic clock	26
1.3 The clock performance	29
1.3.1 Frequency accuracy	29
1.3.2 Frequency stability	30
1.4 The primary frequency standards	32
1.4.1 The thermal caesium atomic beam	32
1.4.2 The cold atom fountain	34
1.4.3 Advantage and drawbacks of a pulsed fountain	38
2 FO1 description and performances	43
2.1 Résumé en français	43
2.2 Introduction	45
2.3 The time sequence of the fountain operation	47
2.4 The optical system	50
2.4.1 The optical bench	50
2.4.2 Control of the optical parameters	50
2.5 The fountain physical package	52
2.5.1 The vacuum chamber	52
2.5.2 Microwave cavity	54
2.5.3 The magnetic field	57
2.5.4 The temperature control	59
2.6 The capture and selection zone	59
2.7 The detection zone	60
2.8 Microwave frequency synthesis chain	62

2.9	Fountain performance	64
2.9.1	Frequency stability	68
2.9.2	Frequency accuracy	79
2.10	Frequency comparison among three fountains at BNM-SYRTE	87
2.10.1	The link among fountains	87
2.10.2	Interrogation oscillator noise rejection	89
2.10.3	Frequency comparison between three fountains and measurement of Rb hyperfine splitting	91
3	Search for a variation of the fine structure constant α	95
3.1	Résumé en français	95
3.2	Introduction	96
3.3	A change of α would violate the Equivalence Principle	97
3.4	Non-laboratory searches	97
3.5	Laboratory search using atomic clocks	99
3.5.1	α and g_I dependence of the atomic spectra	99
3.5.2	Experiments with Rb and Cs fountains	102
3.6	Conclusion	106
4	Test of the PHARAO Ramsey cavity	109
4.1	Résumé en français	109
4.2	ACES scientific objectives	111
4.3	Brief description of PHARAO	112
4.4	Test of the PHARAO Ramsey cavity	114
4.4.1	Cavity phase shift	114
4.4.2	Test of the Ramsey cavity phase shift using FO1	116
5	Cs clock frequency shift due to blackbody radiation	123
5.1	Résumé en français	123
5.2	Introduction	126
5.3	The BBR shift theory	127
5.3.1	AC Zeeman frequency shift of Cs clock	127
5.3.2	Stark frequency shift of Cs clock	129
5.4	The experimental setup	137
5.4.1	Experimental setup	138
5.4.2	Characteristics	138
5.5	Measurement sequence	144
5.6	Effective temperature calculation	144
5.7	Experimental results	148
5.8	Conclusion	152

6	The improved FO1	155
6.1	Résumé en français	155
6.2	Introduction	156
6.3	The optical system	157
6.3.1	Cold atom manipulation	159
6.3.2	The optical bench	159
6.3.3	Control of the light beam parameters	163
6.3.4	Extended cavity semiconductor laser using a Fabry-Perot etalon	164
6.4	The capture zone	168
6.5	Deceleration of the caesium beam	170
6.5.1	Characteristics of the thermal beam	170
6.5.2	Deceleration of the atomic beam	172
6.5.3	The chirp laser system	173
6.5.4	Atom capture results	176
6.6	State selection system	176
6.6.1	Selection cavity	177
6.6.2	Adiabatic passage	177
6.7	The detection system	186
6.8	Interrogation microwave synthesis chain	189
6.9	Recent results of the improved FO1	192
6.9.1	Frequency stability	192
6.9.2	Frequency accuracy	194
7	Conclusion	197
7.1	Conclusions en français	197
7.2	Conclusions and outlook in English	199
A		203
A.1	Abbreviations	203
A.2	Physical constants	204
A.3	The atom ^{133}Cs	205
A.4	Parameters of the improved FO1	207
B		209
B.1	Ramsey microwave interrogation	209
B.2	Servo on the atomic resonance in Ramsey interrogation mode	213
B.3	The atomic sensitivity function in fountain	214
B.4	Conversion of the frequency stability analysis between frequency and time domains	217
	Bibliography	219

List of Figures

1.1	Scheme of a Cs atomic clock.	27
1.2	Ramsey transition probability against the microwave field frequency detuning to the atomic resonance.	28
1.3	Relative frequency fluctuations.	31
1.4	Diagram of a caesium beam frequency standard using magnetic state selection and detection.	33
1.5	Polarization-gradient cooling for an atom with an $F = 1/2$ ground state and $F = 3/2$ excited state.	36
1.6	Calculation of the force as a function of the atomic velocity for an atom in the case of polarization gradient cooling in lin \perp lin configuration.	37
1.7	Schematic diagram of a cold caesium atom fountain clock. . .	39
2.1	Schematic of the caesium fountain FO1.	46
2.2	The atom manipulation timing sequence in FO1.	48
2.3	The schematic of the optical bench of FO1.	51
2.4	RF system driving the AOMs.	52
2.5	The interrogation cavity section and the magnetic field TE ₀₁₁ mode.	54
2.6	Mode TE ₀₁₁ of the microwave cavity.	57
2.7	The capture zone and the caesium source.	60
2.8	Principle of the atomic hyperfine state detection.	61
2.9	Time of flight signals.	62
2.10	Block diagram of the interrogation frequency synthesis chain of FO1.	63
2.11	Block diagram of the frequency synthesis chain for the state selection in FO1.	63
2.12	Microwave spectrum of Cs without selection.	65
2.13	Population distribution after the selection was carried out. . .	66
2.14	Ramsey fringes from the fountain clock FO1.	67
2.15	Time of flight signals.	70

2.16	The equivalent filter function of the detection system for electronic noise.	72
2.17	Results of a Gaussian or Lorentzian shape filter used to fit the TOF signals.	72
2.18	The equivalent filter function of the detection system for the detection laser noise.	74
2.19	Down-conversion coefficients $(g_n/g_0)^2$ versus the rank n for the function $g(t)$ in three Ramsey interrogation cases.	76
2.20	Estimated frequency stability at $\tau = T_c$ versus the number of the detection atoms.	78
2.21	Frequency stability of the fountain clock FO1.	79
2.22	The measured magnetic field map.	82
2.23	Modified Ramsey fringe ($m_F = 1 \leftrightarrow m_F = 1$ transition).	82
2.24	The measured frequency difference when feeding the cavity symmetrically <i>vs</i> asymmetrically.	84
2.25	Schematic of the symmetric cavity supply.	85
2.26	The linked cold atom fountain clocks at BNM-SYRTE.	88
2.27	A microwave link connecting an interrogation oscillator to two fountains.	89
2.28	Interrogation oscillator noise rejection results.	90
2.29	The measured frequencies of the H-maser by 3 fountains at SYRTE in 2000.	91
2.30	The relative frequency differences among 3 fountains.	92
2.31	Allan variance of the residues in function the order of polynomial fit.	93
3.1	The correction function $d \ln F_{rel}(Z\alpha)/d \ln \alpha$ against the atomic number Z	100
3.2	The frequency comparison data of 2002	103
3.3	Measured ^{87}Rb frequencies referenced to the ^{133}Cs fountains over 57 months.	105
4.1	Principle of ACES.	113
4.2	The caesium tube of the PHARAO clock.	114
4.3	Photograph of the Ramsey cavity of the PHARAO clock and drawing of its internal magnetic field distribution.	115
4.4	The experimental set-up used to test the PHARAO Ramsey cavity inside the FO1 fountain.	117
4.5	Map of the static magnetic field.	119
4.6	The Ramsey fringes obtained with interaction process C and D for two different launching velocities.	120

LIST OF FIGURES

4.7	The measured frequency shift due to the phase difference of the microwave field in the two Ramsey interaction zones compared the H-maser.	121
5.1	Spectral density of blackbody radiation for four temperatures.	128
5.2	An electric field \mathbf{E} which induces the Stark effect in an atomic clock.	131
5.3	Sketch of the BBR frequency shift measurement setup in FO1.	139
5.4	BBR shift measurement setup.	140
5.5	Non-uniform temperature along the atomic trajectory.	147
5.6	The time-averaged frequency shift above the interrogation cavity as a function of the effective temperature T_{BBR}	151
5.7	Experimental and theoretical values for K_{Stark}	152
6.1	Schematic of the improved F01.	158
6.2	The atom manipulation time sequence.	160
6.3	Schematic of the capture laser beams.	161
6.4	Optical bench of the improved F01.	162
6.5	AOMs control system.	164
6.6	Photograph of the ECL using an intra cavity etalon.	165
6.7	Frequency and power servo loops system of the detection laser using an etalon as selective element.	166
6.8	Error signal of the detection laser.	167
6.9	Photograph of the capture chamber, the selection zone and the detection zone.	169
6.10	Optical collimator for the capture zone.	170
6.11	Schematic diagram of the decelerated caesium beam source.	171
6.12	Measurements of the atomic beam flux as a function of Cs oven temperature.	172
6.13	Schematic of the chirp servo system.	174
6.14	Schematic of the chirp lasers sources.	174
6.15	Saturated absorption spectroscopy signal of the chirp lasers.	175
6.16	The optical molasses loading curve.	176
6.17	Energies of the dressed levels as a function of the detuning from resonance.	179
6.18	Blackman pulse and the associated detuning which satisfies the adiabaticity condition.	181
6.19	Sensitivity of the transition probability for HBP as a function of the final detuning between the TE_{011} mode and the atomic resonance.	183
6.20	The microwave chain used to drive the adiabatic passage in the selection cavity.	184

6.21	Allan standard deviation of the ratio of the number of the atoms detected between for the half-Blackman and Blackman pulses, as a function of the number of fountain cycles.	185
6.22	Intensity profiles of the detection beams.	187
6.23	Fluorescence collection system.	188
6.24	Noise spectral density of the detection electronic system.	188
6.25	Block diagram of the microwave synthesis chain used for the improved FO1.	189
6.26	Phase noise of the frequency synthesis chain of the improved FO1 at 9.192 GHz.	191
6.27	Ramsey fringes obtained in the improved FO1.	192
6.28	The frequency stability of the improved FO1.	193
6.29	Allan standard deviation of frequency difference between the high and the low atom density configurations.	195
A.1	Level scheme of the ground and first two excited states of the ^{133}Cs atom.	206
A.2	Parameters of improved FO1.	208
B.1	Atomic sensitivity function $g(t)$ at half maximum of the Ramsey resonance when atomic trajectory is along the cavity axis.	216

List of Tables

2.1	Degradation of Allan variance for five types of noise with different Ramsey interrogation power.	77
2.2	Relative frequency corrections and uncertainty budget of FO1 in 2002.	80
2.3	Test of the frequency shift as a function of the fountain tilt.	86
3.1	Different atomic clock comparison experiments for testing the stability of fundamental constants.	106
5.1	Thermal conductivity and emissivity values for the materials in our experimental temperature range 300-500 K.	141
5.2	Several tests to verify the thermal calculations.	143
5.3	Uncertainties of the measurement of the time averaged frequency shift above the cavity as a function of the effective BBR temperature T_{BBR}	150
6.1	The optimized parameters for BP and HBP in the improved FO1.	182
B.1	The noise expression correspondence in frequency and time domains.	217

Introduction

0.1 Introduction en français

La seconde, l'unité de temps, est une unité de base du Système International (SI). Jusqu'à 1960, la seconde était déterminée à partir de la rotation de la terre autour de son axe (temps universel) et plus tard (1960-1967) de la rotation autour du soleil (temps d'éphéméris) avec une exactitude de $\sim 10^{-9}$. En 1950, on a constaté que les résonances atomiques sont beaucoup plus stables que la rotation de la Terre. En 1967, une nouvelle définition de l'unité de temps SI a été donnée par la fréquence d'une transition hyperfine de l'isotope stable du césium (temps atomique) [1]:

La seconde est égale à la durée de 9 192 631 770 périodes du rayonnement correspondant à la transition entre les deux niveaux hyperfins de l'état fondamental de l'atome du césium 133¹.

La durée de la seconde est alors réalisée par une horloge atomique de Cs. Un oscillateur à quartz à l'intérieur de l'horloge est contrôlé en fréquence par le signal de résonance des atomes de césium (voir le chapitre 1) et son signal est électroniquement divisé pour atteindre 1 Hz (une oscillation par seconde), délivrant ainsi le signal d'horloge à la seconde.

Le temps atomique international (TAI) est une échelle de temps calculée par le BIPM avec un algorithme de moyenne pondérée. L'unité de temps du TAI est approchée aussi étroitement que possible de la définition de la seconde SI. L'échelle de temps EAL (Echelle Atomique Libre qui comprend environ 200 horloges) est étalonnée à l'aide des horloges primaires de différents laboratoires. On estime que l'incertitude est de quelques 10^{-15} .

Le temps et la fréquence mesurés avec des horloges atomiques sont toujours les unités physiques les mieux mesurées [2]. Actuellement, la seconde est réalisée par des étalons primaires de fréquence à atome de césium avec une incertitude de 4 à 5 ordres de grandeur meilleure que les réalisations des

¹En 1997, le Comité International des Poids et Mesures (CIPM) a complété cette définition: le Comité international a confirmé que cette définition se réfère à un atome de césium au repos, à une température de 0 K.

autres unités de base. Certaines définitions d'unités bénéficient de l'avantage de cette exactitude. Par exemple, l'unité de la longueur, le mètre, est dérivée de la définition du temps en prenant la vitesse de la lumière comme constante. L'effet Josephson a conduit à la possibilité de créer un étalon de tension se rapportant à une mesure de fréquence.

Des étalons primaires de fréquence sont employées pour effectuer l'étalonnage en fréquence des étalons secondaires de temps utilisées dans les laboratoires nationaux de métrologie temps-fréquence. Ceux-ci sont généralement les horloges commerciales à césium ou des masers à hydrogène. Les horloges atomiques jouent également un rôle essentiel dans les nouveaux systèmes de navigation, comme par exemple le système LORAN-C, le système de positionnement GPS, le système satellite de navigation globale (GLONASS) et le futur système GALILEO. La précision du positionnement est directement rattachée à l'exactitude et la stabilité des horloges atomiques utilisées.

Les horloges atomiques sont également extrêmement utiles dans la recherche fondamentale: par exemple, la recherche d'éventuelles de la variation des constantes fondamentales de la physique dans le but de vérifier la relativité générale [3, 4, 5], les collisions atomiques [6], l'effet Stark [7], le déplacement de la fréquence dû à la gravitation et la relativité restreinte [8, 9], l'interférométrie à très longue base (VLBI) [10], la recherche des ondes gravitationnelles, etc.. Les atomes froids eux-mêmes ont été également utilisés pour d'autres applications où une longue durée d'interaction est importante, par exemple, les interféromètres à ondes de matière, et la mesure du rapport h/m d'un atome [11, 12, 13]. Les étalons atomiques de fréquence sont également employés pour la synchronisation des réseaux de communication.

La méthode de résonance magnétique de jets moléculaires développée par Rabi et ses collègues dans les années 1930 a permis de mesurer exactement les résonances atomiques et moléculaires et d'ouvrir le développement d'un étalon de fréquence atomique. Ramsey a introduit la méthode à deux champs oscillants séparés [14]. Cette découverte a permis à Essen et Parry de construire la première horloge atomique à jet de césium en 1955 [15]. Ils ont effectué une mesure de la fréquence hyperfine du ^{133}Cs . La valeur mesurée par ce dispositif, en prenant la définition de la seconde des éphémérides, est 9 192 631 770 Hz, ce qui est devenu la base de la nouvelle définition de la seconde. En fait, en 1953 Zacharias [16, 17] avait essayé d'obtenir des franges de Ramsey plus étroites en disposant son jet atomique verticalement. Dans cette géométrie de "fontaine", les atomes lents projetés vers le haut de la cavité interagissent une première fois avec le champ oscillant puis retombent sous l'effet de la pesanteur et subissent une deuxième interaction avec le même champ oscillant, ce qui permet d'obtenir un signal de résonance très étroit. Malheureusement, l'expérience a échoué en raison de l'éjection des

atomes lents du faisceau par collision avec les atomes rapides, majoritaires. Le premier succès d'une expérience de fontaine atomique a dû attendre le développement des techniques de capture et de refroidissement d'atome par laser [18].

En 1975 Hänsch et Schawlow [19], et Wineland et Dehmelt [20] ont proposé de refroidir des atomes neutres par le transfert de l'impulsion des photons de faisceaux laser. En 1982 Phillips et Metalf ont réalisé un ralentissement d'un jet atomique par laser [21]. En 1985 Chu et ses associés [22] ont été les premiers à réaliser le refroidissement d'atomes neutres par laser dans un fluide visqueux de photons, qu'ils ont appelés "mélasse optique". En 1988 Phillips et ses collègues ont obtenu des atomes à une température au-dessous de la limite Doppler [23], puis Cohen-Tannoudji, Dalibard [24] et Chu [25] en ont proposé une interprétation par la théorie du refroidissement par gradient de polarisation (refroidissement Sisyphe). L'idée de Zacharias a pour la première fois été mise en application par le groupe de Chu [26] avec une fontaine à atomes de sodium, à l'université de Stanford en 1989. Un an après, Clairon, Salomon et ses collègues ont construit la première fontaine atomique à césium à l'Ecole Normale Supérieure [27]. La largeur des raies observées de la résonance de Ramsey était de 2 Hz, environ deux ordres de grandeur inférieure à celle obtenue dans une horloge à jet thermique [28].

En 1994, le groupe du BNM-LPTF (Laboratoire Primaire du Temps et des Fréquences), mené par Clairon, a mis en oeuvre le premier étalon de fréquence en fontaine de césium (appelé FO1), ayant une largeur de raie aussi étroite que 0,7 Hz et un rapport signal à bruit excédant 10^3 . En 1995, la première évaluation d'exactitude a mené à une valeur relative de 3×10^{-15} , environ un ordre de grandeur mieux que la meilleure horloge conventionnelle à jet. La stabilité de fréquence à court terme était $3 \times 10^{-13} \tau^{-1/2}$, où τ est le temps d'intégration en seconde [29]. Cette même année, FO1 a contribué pour la première fois à TAI [30].

Cette thèse décrit une première version de la fontaine FO1 et quelques résultats obtenus avec cet étalon, ainsi qu'un second montage développé dans le but d'améliorer ses performances. La thèse est composée de six chapitres:

Le chapitre 1 rappelle le principe de fonctionnement d'une horloge atomique. L'étalon primaire est basé sur la mesure de la fréquence de la transition d'atomes quasi-isolés. Les caractéristiques d'exactitude et de stabilité d'un étalon de fréquence sont des moyens de qualifier une horloge. Ce chapitre décrit également comment fonctionne une fontaine à atomes froids et discute des limites de performances obtenues.

Le chapitre 2 donne une description de FO1 en détaillant chaque partie du

fonctionnement de la fontaine atomique. En conclusion, les performances de FO1 sont évaluées. Nous présentons également la méthode pour la comparaison de fréquence des trois fontaines du BNM-SYRTE, ainsi que des résultats de comparaison de fréquence entre celles ci.

Le chapitre 3 présente une nouvelle limite sur la variation possible de la constante de structure fine α . Une variation de α violerait le Principe d'équivalence d'Einstein (Einstein Equivalence Principle). Tirant profit de la stabilité remarquable des fontaines Cs et Rb du BNM-SYRTE, des comparaisons de fréquence effectuées sur un intervalle de 5 ans permettent de réduire la limite supérieure de cette variation possible de α . Une limite pour l'éventuelle variation possible du facteur gyromagnétique g_p de proton est également déterminée.

Le chapitre 4 présente une mesure sur la différence de phase entre les deux zones d'interaction dans une cavité de Ramsey développée pour l'horloge spatiale PHARAO. Les résultats indiquent que la géométrie de la cavité répond aux exigences demandées.

Le chapitre 5 fournit une étude théorique et expérimentale du déplacement de fréquence dû au rayonnement du corps noir. Le champ isotrope du rayonnement du corps noir émis par l'enceinte à vide de l'horloge induit un déplacement de fréquence, de l'horloge dû à un effet Stark de l'ordre de 1.7×10^{-14} à température ambiante, ce qui constitue une limite importante à l'exactitude de l'horloge.

Le chapitre 6 donne une description détaillée des améliorations apportées à la fontaine FO1, portant sur la source d'atomes, la zone de capture, la zone de sélection, la zone de détection, le système optique, les chaînes micro-onde et le système de contrôle. Le déplacement de fréquence dû aux collisions constitue la limite principale de l'exactitude des fontaines à atome de césium, la difficulté réside dans l'évaluation de la densité atomique. Nous présenterons une nouvelle méthode appelée passage adiabatique destinée à préparer des échantillons d'atomes dont les rapports en densité atomique et en nombre sont bien définis. Cette méthode a été mise en oeuvre dans la nouvelle version de la fontaine FO1. Les résultats récents sont aussi présentés.

0.2 Introduction in English

The second, the unit of time, is one of the base units of the International System of Units SI (Système International). Until 1960 the second was derived from the earth's rotation around its axis (Universal Time) and later (1960-1967) from the rotation around the sun (Ephemeris Time) with an accuracy of $\sim 10^{-9}$. In 1950, it was found that some atomic electromagnetic resonances are much more stable than the earth's rotation. In 1967, a new

definition of the SI unit of time was chosen based on the frequency of a hyperfine transition of the non-radioactive isotope of caesium (Atomic Time) [1]:

The second is the duration of 9 192 631 770 periods of the radiation corresponding to the transition between the two hyperfine levels of the ground state of the caesium 133 atom².

The duration of the second is then realized by a Cs atomic clock. A quartz oscillator inside the clock is frequency controlled by the caesium atom resonance signal (see chapter 1) and its signal is electronically divided down to 1 Hz (one oscillation per second), so the second is realized.

The International Atomic Time (TAI) is a time scale calculated with a weighted average algorithm (Algos) by BIPM. The scale unit of TAI is kept as close as possible to the SI second definition by using data from national laboratories (about two hundred atomic clocks) which maintain the best primary caesium standards. The uncertainty is estimated to be a few parts in 10^{-15} .

Measured with atomic clocks, time and frequency are always the most accurate among all physical quantities [2]. At present, the second is realized by primary caesium frequency standards with an uncertainty more than 4 to 5 orders of magnitude better than the realizations of definitions of the other basic units. The definitions of other units take the advantage of this accuracy. For example, the unit of length, the metre, is derived from the definition of the unit of time since the speed of light is considered constant. The Josephson effect has led to the possibility of creating a voltage standard referring to a frequency measurement.

Primary frequency standards are usually used for frequency calibration of secondary time and frequency standards. Atomic clocks also play a vital role in the navigation systems, for example, the LORAN-C system, the Global Positioning Systems (GPS) and Global Navigation Satellite System (GLONASS), relying on the accuracy and the stability of atomic clocks. Atomic frequency standards are also used for network synchronization in the telecommunication field. They are also extremely useful in fundamental research, such as:

- ◆ In relativity: Search for variation of fundamental constants of physics [3, 4, 5], gravitational red-shift measurement tests of general relativity [8, 9]
- ◆ In atomic physics: Atomic collisions [6], Stark effect [7]
- ◆ In astronomy: Very Long Baseline Interferometers (VLBI) [10]...

Cold atoms have been used for other applications where the long inter-

²In 1997, the CIPM (Comité International des Poids et Mesures) completed this definition: the definition refers to a caesium atom at a thermodynamic temperature of 0 K.

action time is important, for example, the matter wave interferometers and the measurement of the h/m ratio [11, 12, 13].

The molecular beam magnetic resonance method developed by Rabi and his colleagues in 1937 allowed to accurately measure atomic and molecular resonances and opened up the possibility of developing a frequency standard based on an atomic system. Ramsey introduced the method of separated and successive oscillatory fields [14], which led Essen and Parry to construct and operate the first caesium atomic beam clock in 1955 [15]. They performed a measurement of the hyperfine splitting frequency in ^{133}Cs . The result of this measurement referenced to ephemeris second, 9 192 631 770 Hz, became the basis of the new definition of the second. In fact, in 1953 Zacharias [16, 17] had attempted to obtain an even narrower separated oscillatory field resonance in a “fountain” experiment to measure the gravitational red shift as a function of the average height of the atom above the microwave cavity. The very slow atoms were allowed to travel upward through a first oscillatory field and then to fall under gravity to pass again the same field to achieve very narrow resonance signal. Unfortunately the experiment failed because the slow atoms were scattered out of the beam by fast atoms. The first successful atomic fountain had to wait for the development of laser cooling and trapping techniques [18].

The idea that neutral atoms may be cooled by the momentum transfer of laser photons was proposed by Hänsch and Schawlow [19], and by Wineland and Dehmelt [20] in 1975. In 1982 Phillips and Metcalf realized the laser deceleration of an atomic beam [21]. In 1985 Chu and his co-workers [22] obtained the first laser cooled and trapped atoms in a viscous fluid of photons, which they called “optical molasses”. In 1988 Phillips [23] and his colleagues reduced the temperature of their trapped atom ensemble well below the Doppler limit, which was later explained by Cohen-Tannoudji, Dalibard [24] and Chu [25] presenting the theory of polarization-gradient cooling. The feasibility of Zacharias’ idea was demonstrated by Chu group [26] with a sodium fountain at Stanford in 1989. One year later, Clairon, Salomon and their co-workers constructed the first caesium atomic fountain at the Ecole Normale Supérieure [27] in Paris. The observed linewidth of the Ramsey resonance, about 2 Hz, was nearly two orders of magnitude below that of the thermal caesium clock [28].

In 1994, the group of BNM-LPTF (Laboratoire Primaire du Temps et des Fréquences), led by Clairon, operated the first Caesium fountain frequency standard (named FO1), having a linewidth as narrow as 0.7 Hz and a signal-to-noise ratio exceeding 10^3 . In 1995, a first evaluation yielded a relative accuracy of 3×10^{-15} , about one order of magnitude better than the best conventional beam clock. The short-term frequency stability was

$3 \times 10^{-13} \tau^{-1/2}$, where τ is the averaging time in seconds [29]. In the same year, FO1 first contributed to TAI [30].

This thesis work firstly presents several relevant results obtained with a first version of the FO1 fountain and secondly the new set-up developed to improve the performance and to overcome the limitations of the previous version. This thesis is divided into six chapters as follows:

Chapter 1 recalls the principle of an atomic clock. This chapter also describes how a cold atom fountain works and presents its performance limits.

Chapter 2 gives a description of FO1, including the physical package, the optical system, the microwave synthesis and the control system. We also present the most recent performance evaluation and introduce the method for frequency comparison of the three fountains at SYRTE and discuss the results of these comparisons.

Chapter 3 presents a new limit for the possible variation of the fine structure constant α . A variation of α would violate the Einstein Equivalence Principle (EEP), and give support to recent many-dimensional cosmological (Kaluza-Klein model, super-string) theories. Taking advantage of the remarkable stability of the Cs and Rb fountains at SYRTE, frequency comparison measurements spreading over an interval of five years reduce the upper limit for a possible variation of α . A limit for a possible variation of the proton gyromagnetic factor g_p is also determined.

Chapter 4 introduces a measurement of the phase difference between the two interaction zones in the Ramsey type cavity which was developed for the PHARAO space clock.

Chapter 5 provides a theoretical and experimental study of the blackbody radiation shift. The isotropic blackbody radiation field emitted from the surroundings of the cold caesium atoms leads to a clock frequency shift due to the AC Stark effects at the level of 10^{-14} at room temperature, an important limit for the fountain clock accuracy.

Chapter 6 gives first a detailed description of the improvements in FO1, including the source of atoms, the capture zone, the selection zone, the detection zone, the optical system, the microwave synthesis and the control system. For the atomic state selection, a new method of adiabatic passage is used to prepare two atomic samples with a well-defined ratio both in atom number and density. This allows one to measure and control the cold collisional shift and cavity pulling with a resolution of 10^{-3} . Second, we present the recent results in the improved FO1.

Chapter 1

Principle and characteristics of an atomic clock

1.1 Résumé en français

Dans ce chapitre, nous présentons les raisons pour les quelles la définition de la seconde est basée sur la fréquence de transition hyperfine de l'état du césium 133. Une horloge atomique, ou étalon atomique de fréquence, fournit un signal périodique d'excellente exactitude et de grande stabilité obtenue par la résonance atomique. Pour réaliser une résonance atomique très fine dans une horloge atomique, on utilise habituellement la méthode d'interrogation micro-onde de Ramsey. Une partie du signal de l'oscillateur à quartz asservi sur la résonance atomique est à la disposition des utilisateurs.

Les principales performances d'une horloge atomique sont exprimées en termes d'exactitude de fréquence et de stabilité de fréquence. Après avoir défini ces deux termes, nous présentons la liste des principales sources qui décalent la fréquence de l'horloge.

Pour mieux comprendre le fonctionnement d'une horloge atomique disposée en fontaine à atomes froids, nous présentons brièvement la théorie de refroidissement d'atomes par laser et le mode de fonctionnement de cette horloge. Après examen des différents types d'étalons primaires de fréquence, nous présentons les avantages majeurs ainsi que les limites principales des fontaines à atomes froids. A priori une fontaine atomique peut atteindre une exactitude de fréquence de l'ordre de 10^{-16} . Néanmoins, pour atteindre une telle exactitude, l'effet du rayonnement du corps noir et l'effet des collisions entre atomes froids tous deux de l'ordre de 10^{-14} doivent être étudiés avec précision. Et toutes les difficultés techniques, par exemple, les fuites micro-onde, les perturbations synchrones doivent être résolues.

1.2 Principle of the Cs atomic clock

An atomic clock, or atomic frequency standard, generates a very stable and very accurate periodic signal, which is stabilized by the atomic resonance signal. Atomic clocks can be divided into two main classes: active clocks and passive clocks. The active devices, such as the hydrogen and the rubidium maser, emit radiation in the microwave range. In passive devices, such as caesium frequency standards and passive hydrogen maser, the atomic transition is probed by an external microwave source, which is frequency locked to the atomic transition by means of an appropriate electronic system.

In this thesis we study a passive clock based on cold caesium atoms, the FO1 fountain.

The alkali atom caesium 133 (^{133}Cs) is a non-radioactive and very electropositive element. It has a nuclear spin $I = 7/2$. In the ground state $6^2S_{1/2}$, the hyperfine manifold is composed of 16 sub-levels (see figure A.1) and the atomic transition involved in the caesium atomic clock is $F = 4, m_F = 0 \longleftrightarrow F = 3, m_F = 0$. Its frequency is 9 192 631 770 Hz in the definition of SI time.

Caesium 133 has been chosen for definition of the second for the following reasons:

- (1) It is the only stable caesium isotope (natural abundance 100%).
- (2) The clock transition ($F = 3, m_F = 0$ to $F = 4, m_F = 0$) is a magnetic dipole transition with a low sensitivity to external magnetic fields (caesium is the least sensitive element in the alkali group).
- (3) Its hyperfine frequency can be easily probed and detected by available microwave systems, which was important at the time of the definition of the SI second.
- (4) The observed value of the hyperfine splitting in the ground state is the largest among all the stable alkalis.

Figure 1.1 illustrates the operation principle of a passive Cs atomic clock. It is composed of three parts: the quantum system, the microwave system and the frequency servo system. The microwave system includes a frequency generator which usually is a quartz crystal oscillator at 5 or 10 MHz. This frequency is synthesized up to $\nu(t) = 9\,192\,631\,770$ Hz, and is phase or frequency modulated to interrogate the atomic resonance. The quantum system plays the role of a frequency discriminator. The transition probability $P(\nu)$ between the two hyperfine levels gives the information about the difference between the synthesized frequency $\nu(t)$ and the atomic resonance frequency ν_{at} (for details and references see section B.1). The microwave interrogation is usually performed using the Ramsey method [31]. The transition proba-

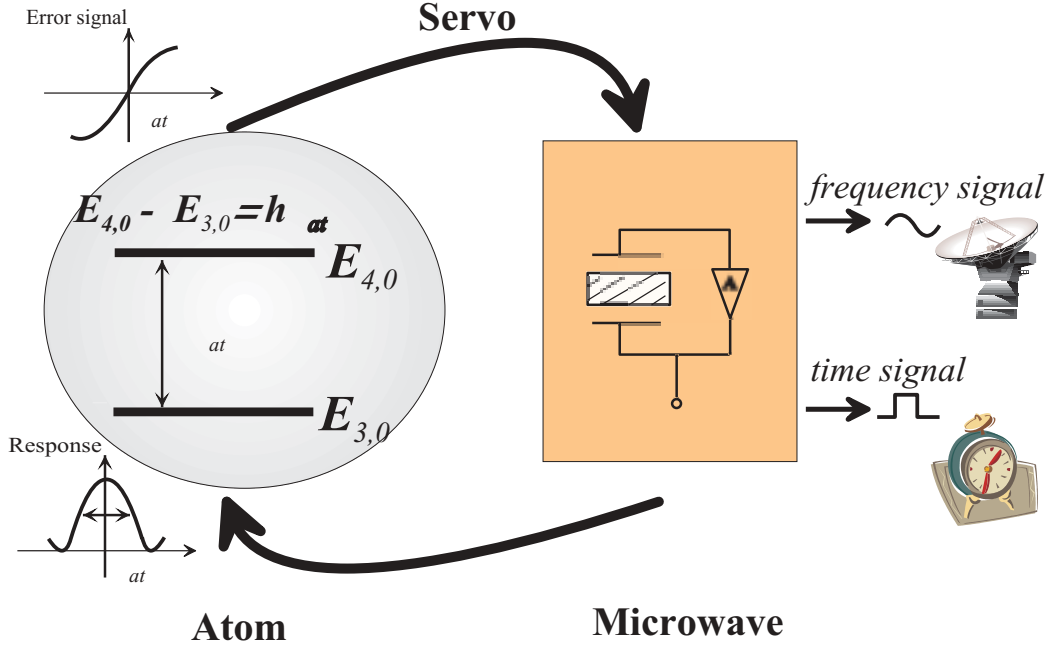


Figure 1.1: Scheme of a Cs atomic clock.

bility is well described by the following equation:

$$P_{Ramsey}(\nu) = \frac{1}{2} \sin^2(b\tau) \{1 + \cos[2\pi(\nu - \nu_{at})T]\} \quad (1.1)$$

where τ is the time taken by an atom to pass through one oscillator field and T is the time of flight between these fields. As defined in section B.1, the quantity b is the Rabi frequency $\mu_B B / \hbar$. It characterizes the rate at which the quantum state of the atom evolves. The transition probability as a function of the microwave frequency is represented in fig. 1.2. The full width at half maximum of the central fringe $\Delta\nu_{Ramsey}$ is given by

$$\Delta\nu_{Ramsey} \simeq \frac{1}{2T} \quad (1.2)$$

This fringe is centered at the atomic resonance frequency ν_{at} defined by

$$\nu_{at} = \frac{E_{4,0} - E_{3,0}}{h}, \quad (1.3)$$

where h is Planck's constant, $E_{4,0}$ and $E_{3,0}$ are the energies of the ground states $F = 4, m_F = 0$ and $F = 3, m_F = 0$, respectively.

To lock the microwave frequency on the atomic resonance, its frequency is modulated with an amplitude equal to $\Delta\nu_{Ramsey}/2$. A servo system demodulates the response signal by a synchronous detector, and an error signal

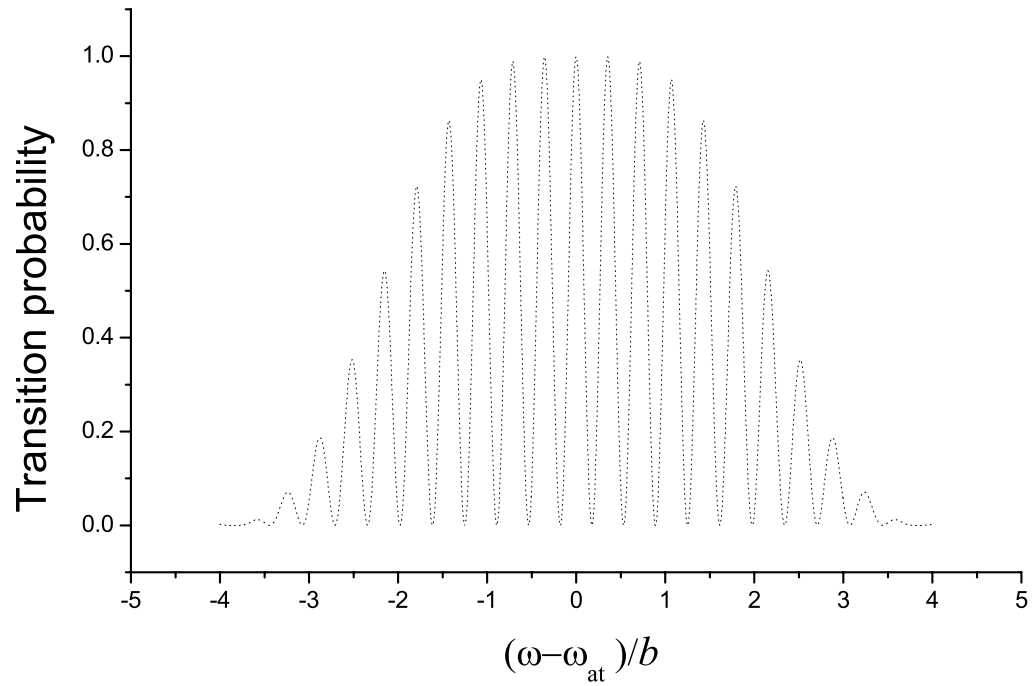


Figure 1.2: *Ramsey transition probability against the microwave field frequency detuning to the atomic resonance, where $b\tau = \pi/2$. As defined in section B.1, the quantity b is the Rabi frequency referring to the amplitude of the microwave field, and τ is the time taken by an atom to pass through one oscillator field.*

proportional to the frequency difference is generated. This error signal is integrated and applied to control the quartz frequency in order to match its frequency with the atomic resonance.

A part of the output from the quartz crystal is available to the users as an accurate and stable frequency reference, and the periodic pulses obtained by frequency division provide time marks.

1.3 The clock performance

The instantaneous frequency $\nu(t)$ of the controlled signal delivered by the oscillator can be expressed by

$$\nu(t) = \nu_0[1 + \epsilon + y(t)], \quad (1.4)$$

where the value ν_0 corresponds to the unperturbed atomic frequency, and ϵ is a relative frequency offset due to several physical effects and instrumental imperfections that produce a slight change in the clock transition frequency. The uncertainty of ϵ determines accuracy of the clock. The variance $y(t)$ represents relative frequency fluctuations with $\langle y(t) \rangle = 0$, which determine frequency stability of the clock .

The performance of an atomic clock is then expressed in terms of frequency accuracy and frequency stability.

1.3.1 Frequency accuracy

The relative frequency shift ϵ has several components ϵ_i arising from the black-body radiation, collisional effect, etc.. We have to carefully evaluate each of them with an uncertainty as low as possible. With an evaluation for each perturbation i , we can write the correction ϵ_i as

$$\epsilon_i \pm \sigma_i \quad (1.5)$$

where σ_i is the corresponding one sigma uncertainty. It is usually assumed that the various perturbations are mutually independent. The accuracy of the corrected frequency is given by

$$\sigma = \left(\sum_i \sigma_i^2 \right)^{1/2} \quad (1.6)$$

Let us list the major sources of frequency shift:

Second order Zeeman shift. A constant and homogeneous magnetic field is applied to separate the clock transition from other atomic transitions, and it shifts the clock transition frequency.

Blackbody shift. The atoms experience a thermal radiation field in equilibrium with a blackbody. This produces different shifts in the atomic energy levels due to the ac Stark effect.

Collisional shift. Collisions between the caesium atoms, or with background atoms, shift the clock frequency.

Rabi pulling. The wings of the Rabi pedestal for transitions $F = 3, m_F = 1 \longleftrightarrow F = 4, m_F = 1$ and $F = 3, m_F = -1 \longleftrightarrow F = 3, m_F = -1$ may perturb the symmetry of the clock transition spectrum.

First order Doppler shift. This arises mainly from the phase gradient due to losses in the walls of the microwave cavity.

Cavity pulling. The apparent frequency of the atomic transition depends on the frequency offset between that of the cavity and the atomic resonance frequency.

Ramsey pulling. If the static magnetic field is not parallel to the microwave field, transitions of $\Delta F = \pm 1, \Delta m_F = \pm 1$ can be induced, which may perturb the sub-levels $F = 4, m_F = 0$ and $F = 3, m_F = 0$.

Majorana transition. If the atoms are subjected to a varying magnetic field, which has spectral components corresponding to the transition $\Delta F = 0, \Delta m_F = \pm 1$ of the states $F = 3$ or $F = 4$, the clock transition is shifted.

Microwave spectral purity. When the spectrum of the interrogation signal includes unwanted components or phase perturbations synchronized with the interrogation cycle, the clock frequency is shifted.

Microwave leakage. Any stray resonant microwave field seen by atoms outside the microwave cavity produces a frequency shift.

Light shift. Stray light from laser beams modifies the hyperfine energy levels.

Relativistic effects. There are the gravitational red shift (correction due to the variation of the gravitational potential with the altitude of the clock) and the second order Doppler shift.

1.3.2 Frequency stability

The frequency stability can be characterized either in the time domain or in the frequency domain. In the time domain, we study the behavior of the frequency samples averaged over a varying duration. In the spectral domain, we exploit the properties of the Fourier transform of the frequency fluctuations (see appendix B.4).

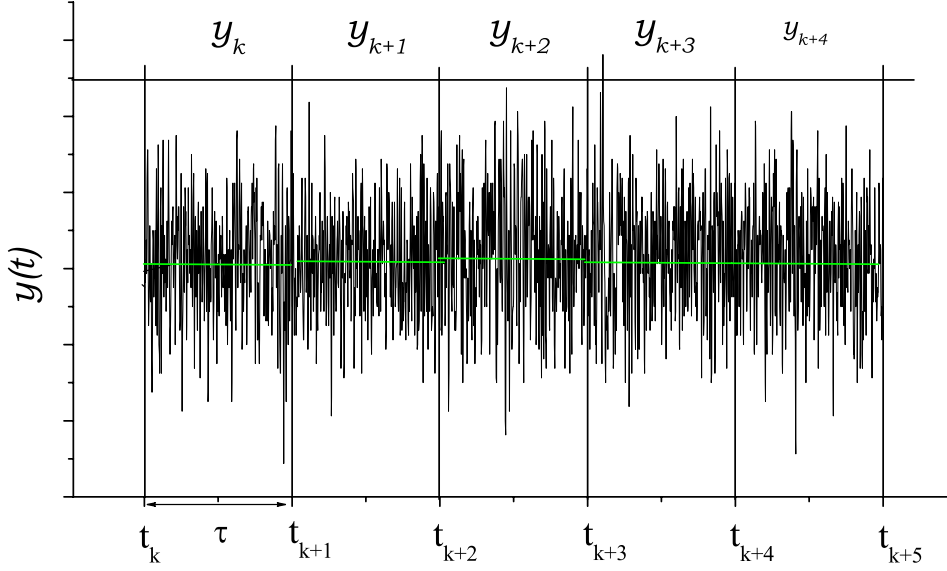


Figure 1.3: *Relative frequency fluctuations. The interval time is defined as τ .*

According to the conference of the CCIR (Comité Consultatif International des Radiocommunications) in 1978, we use the Allan variance [32], also known as the two-sample variance, to express the relative frequency stability in the time domain. The Allan variance is defined as:

$$\sigma_y^2(\tau) = \lim_{N \rightarrow \infty} \frac{1}{2(N-1)} \sum_1^{N-1} (y_{k+1} - y_k)^2, \quad (1.7)$$

where N is the number of samples, and y_k is the mean value during the interval time τ in the k^{th} successive measurement phase (see figure 1.3), given by

$$y_k = \frac{1}{\tau} \int_{t_k}^{t_{k+1}} y(t) dt, \quad (1.8)$$

where $\tau = t_{k+1} - t_k$ is the averaging time, also called integration time.

In practice, since N is a finite number, we estimate $\sigma_y^2(\tau, N)$ instead of $\sigma_y^2(\tau)$. The relative uncertainty of $\sigma_y^2(\tau, N)$ is characterized by its own standard deviation as follows

$$\sigma(\sigma_y) = \frac{K(\alpha)}{\sqrt{N}} \simeq \frac{1}{\sqrt{N}} \quad (1.9)$$

where the factor $K(\alpha)$ is on the order of unity and depends on the type of noise and α is an integer varying from -2 to $+2$ (see appendix B.4).

The common expression for the stability of a passive atomic clock is given by

$$\sigma_y(\tau) = \eta/[Q_{at}(S/N)\sqrt{\tau}], \quad (1.10)$$

where $Q_{at} \equiv \nu_0/\Delta\nu_{Ramsey}$ is the quality factor of the atomic resonance, $S/N \equiv P/\sigma_P$ is the signal-to-noise ratio of the transition probability measurement, and η is a numerical factor of order unity, depending on the shape of the resonance line and the method of frequency modulation used to determine the center of the clock fringe. According to formula (1.10), to obtain a high frequency stability, we should increase the quality factor and the signal-to-noise ratio.

1.4 The primary frequency standards

After a review of the more recent types of the primary frequency standards, we can show the major advantages and the main limits of the cold atom fountain clock.

1.4.1 The thermal caesium atomic beam

After Ramsey developed the method of successive oscillatory field, the first operational caesium beam atomic frequency standard was built in 1955 by Essen and Parry at the National Physical Laboratory in the United Kingdom [15]. Until 1990, all caesium clocks were built in much the same way as Essen and Parry's original instrument, using in particular magnetic deflection of the atoms.

Figure 1.4 shows the schematic diagram of a conventional caesium beam clock. The atoms are heated inside an oven at about 100°C (the most probable speed is about 260 m/s) to create an atomic beam which is collimated. The atomic beam passes successively through the state selection region (magnet A and getter), the Ramsey cavity and the detection region (magnet B, getter and hot-wire ionizing detector). The atoms emerging from the oven are equally distributed over the $16 m_F$ sub-levels of the ground state $6^2S_{1/2}$. When the atoms pass through the inhomogeneous magnet A which produces a strong, inhomogeneous magnetic field they are spatially separated due to the atoms' different effective magnetic moment. The deflected beam may contain the atoms either in level $|4, 0\rangle$ or $|3, 0\rangle$ depending on the chosen geometry. In the Ramsey cavity made up of a U-shaped waveguide the excited

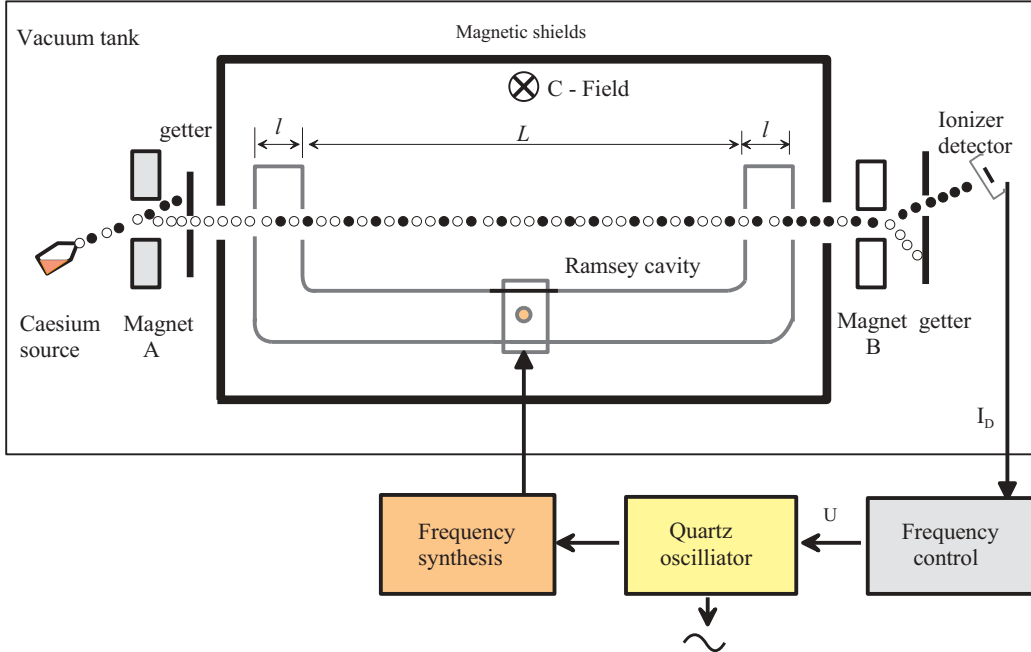


Figure 1.4: The U-shaped microwave cavity is called a Ramsey cavity, where the microwave fields are spatially separated.

transition between $|4, 0\rangle$ and $|3, 0\rangle$ is induced by the two probing standing microwave fields. Then the second inhomogeneous magnet B is used to direct atoms, which have been stimulated to the other $m_F = 0$ level, to the hot-wire ionizing detector. A continuous electronic current proportional to the transition probability is generated by the detector. This signal is used to control the quartz oscillator frequency. A homogeneous and stable magnetic field of the order of 10 mG (about one tenth of the strength of the terrestrial magnetic field) is applied along the whole cavity zone to separate resonance frequencies of $\Delta F = 1$ transitions (this field is sometimes called the C field to distinguish it from magnet A and magnet B). The whole interaction zone is magnetically shielded in order to protect atoms against stray magnetic fields. Typically, the microwave cavity is 1 meter long. The longest one, NBS-5 (the 5th atomic frequency standard at NIST) measures 3.74 m. A longer cavity is not useful because the detected signal decreases rapidly due to the atomic beam divergence and gravity. Furthermore, the uncertainty of the residual first order Doppler effect can increase due to the difference of the atomic velocity (modulus and direction) between the two interaction zones of the microwave cavity.

To improve the detection signal, the use of light beams to replace magnets was suggested by Kastler in 1950 [33]. After the development of the

tunable semiconductor laser, the first demonstration was carried out at the Institut d'Electronique Fondamentale in France [34]. The general layout of an optically pumped caesium beam frequency standard is similar to that of the conventional one, only the state-selector and the state-detector magnets (A and B) are replaced by laser beams, and the hot-wire detector is replaced by a fluorescence detector. This type of atomic clock has a slight drawback concerning the light shift. It is estimated to have a relative value of around 10^{-14} in long laboratory tube [35].

1.4.2 The cold atom fountain

Obviously, if the atomic beam velocity and divergence are both decreased, the interaction time between the atoms and the microwave field becomes longer without a loss of signal-to-noise ratio. The clock frequency will then be more stable, and all frequency shifts associated with the atomic velocity are reduced. The development of laser cooling has opened a way to use cold caesium atoms in a fountain clock.

Principle of laser cooling of atoms Atom manipulation using laser light has been investigated for over 20 years. In 1997, the Nobel prize in physics was awarded to researchers in this field [18]. We recall the principles of two cooling methods and some notations which are associated with the cold atom fountain.

A. Doppler cooling An atom is exposed to two monochromatic travelling light beams, with the same intensity and frequency ν_R , propagating in opposite directions. The laser frequency ν_R is red detuned with respect to the atomic resonance frequency. For the caesium atom the cooling transition is the D_2 line, $F = 4 \rightarrow F' = 5$, $\nu_{4,5'}$ (see fig. A.1). The absorption of photons propagating against the atoms' motion occurs preferentially because of the Doppler effect. As the spontaneous emission is isotropic, the associated recoil momentum averages to zero. The overall effect is that the atoms slow down in the direction of the light. At the intersection of 6 laser beams along the 3 spatial directions the atoms are cooled in an "optical molasses".

Due to the Doppler effect, theory [36] predicted a minimum temperature T_D , known as Doppler limit, to occur at low intensities and at a detuning $\Delta\nu_R = \Gamma/2$ where the Doppler shift asymmetry is maximal. This temperature is given by

$$T_D = \frac{\hbar\Gamma}{2k_B} \tag{1.11}$$

where k_B is Boltzmann's constant. For Cs, T_D is about 124 μK , corresponding to a velocity of 8.8 cm/s.

B. Sub-Doppler cooling by Sisyphus effect There are several more subtle and more effective cooling mechanisms based on the multiplicity of atomic sublevels [37]. These processes are called sub-Doppler cooling.

They are based on two effects: optical pumping (selection rule) and light shift (AC Stark effect). The important feature of the models explaining these mechanisms is the non-adiabatic response of moving atoms to the light field. Atoms at rest in a steady state have ground-state orientations caused by different optical pumping among the ground-state sublevels. For atoms moving in a light field that varies in space, optical pumping acts to adjust their internal states to the changing light field. This adjustment cannot be instantaneous because the pumping process takes a finite time (the pumping rate is proportional to the light intensity in the weak field limit). The internal state orientation of moving atoms always lags behind the orientation that would exist in steady state.

There are several ways to produce this kind of spatially dependent optical pumping process [38]. One way was introduced by Dalibard and Cohen-Tannoudji, using the orthogonal linear polarization of two counter-propagating laser beams (they also introduced the $\sigma^+ - \sigma^-$ configuration). As shown in figure 1.5, the polarization of the light field varies over half a wavelength from linear at 45° with respect to the polarization of the two incoming beams, to σ^+ , to linear at 45° , to σ^- . This pattern repeats itself every half wavelength. The light field has a strong polarization gradient, and a spatially varying light shift arises. Dalibard considered the simplest transition $F = 1/2$ to $F = 3/2$. As shown in figure 1.5, a moving atom in this light field climbs the potential hills, and its kinetic energy is being converted to potential energy. By optically pumping the potential energy is radiated away because the spontaneous emission happens at a higher frequency than that of the absorbed light. Thus the effect extracts the kinetic energy from the atoms. The process continues until the atomic kinetic energy is too small to climb the next hill. This process brings to mind a Greek myths and is thus called "Sisyphus laser cooling."

A theoretical temperature relation, $T \propto I/\Delta\omega$, was first verified by Salomon *et al.* [39] in 3D Cs molasses, where I and $\Delta\omega$ are the light intensity and the detuning respectively.

This polarization gradient laser cooling is effective over a limited velocity range. The damping force as a function of the atomic velocity using the calculation by Metcalf *et al.* [40] is shown in figure 1.6. From this follows that cooling by the Sisyphus effect must be preceded by Doppler cooling.

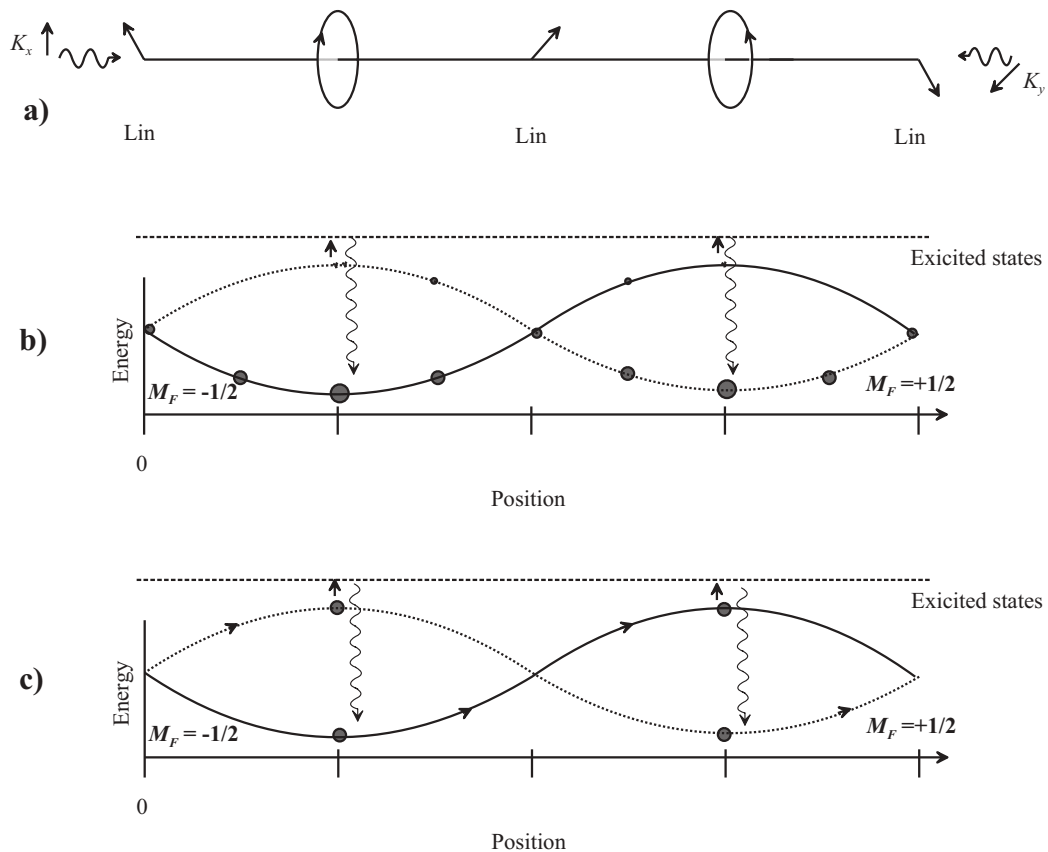


Figure 1.5: Polarization-gradient cooling for an atom with an $F = 1/2$ ground state and $F = 3/2$ excited state. (a) The polarization gradient light field of the interference of two linearly polarized beams light in the case of $\text{lin} \perp \text{lin}$ configuration. The polarization varies in space with a periodic length of $\lambda/2$. (b) The spatial distribution of the atoms at rest in a steady state is shown. (c) Through its motion, the atom climbs towards a potential hill. Optical pumping causes it to fall back to the bottom of the hill.

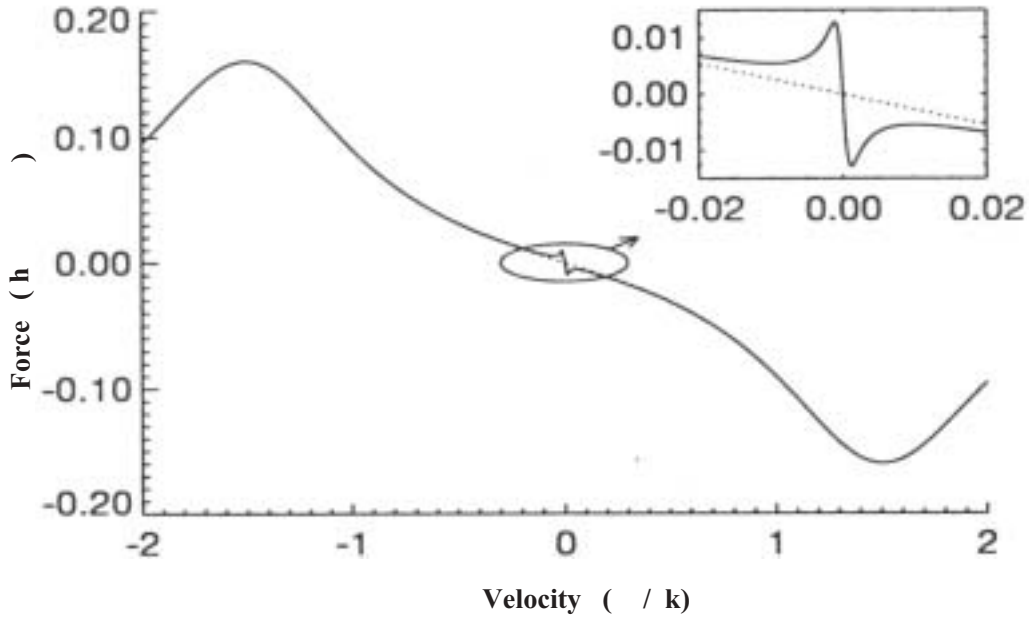


Figure 1.6: Calculation of the force as a function of the atomic velocity for an atom in the case of polarization gradient cooling in $lin\perp lin$ configuration with saturation $s = 0.5$ and a detuning $\Delta\omega = -1.5\Gamma$ [40]. The solid line is the combined force of Doppler and sub-Doppler cooling, whereas the dashed line represents the force for Doppler cooling only. The inset shows an enlargement of the curve around $v = 0$. A strong increase in the damping rate over a very narrow velocity range arises from the sub-Doppler process.

Using the Doppler cooling and sub-Doppler cooling in sequence, we can create a cold caesium atomic sample with a velocity distribution of about 1 cm/s.

Principle of the fountain clock To optimize the interaction time between the microwave field and the cold atoms, we use a fountain geometry.

Figure 1.7 illustrates the schematic diagram of a cold caesium fountain clock. It is operated in a pulsed mode using the following guideline:

1. Capture a cloud of cold atoms inside the intersection of six red detuned and orthogonal laser beams.

2. Launch the atomic cloud by an additional detuning of the two vertical beams ($\pm \Delta \nu_L$). The atoms are exposed to a “travelling wave” and thus are accelerated to a speed v_L in several milliseconds, where $v_L = \Delta \nu_L \lambda$.

3. Cool the atomic cloud by changing the intensity and the detuning of the 6 laser beams. The duration of this phase is about 2 ms. Then, all the laser beams are switched off. The launched atoms continue to evolve along free ballistic trajectories.

4. After the launch, one microwave pulse is used to excite the transition $F = 4, m_F = 0 \leftrightarrow F = 3, m_F = 0$. Then the atoms in $F = 4, m_F \neq 0$ are pushed away by radiation pressure using a very short laser pulse before the atoms enter the microwave cavity. This process is used to keep only the atoms with $m_F = 0$ in order to reduce parasitic atomic interactions and to improve the signal-to-noise ratio of the detection.

5. Interrogate the atomic resonance with the Ramsey method by using only one cavity, since the atoms pass through the cavity both on their way up and down.

6. Detect the transition probability using the fluorescence signal induced by two laser beams to monitor populations in $F = 3$ and $F = 4$.

7. Frequency correction: the transition probability difference of two successive measurements acts as an error signal used to control the local oscillator frequency.

1.4.3 Advantage and drawbacks of a pulsed fountain

In this subsection, we will briefly analyze the advantages (\blacktriangle) and drawbacks (\blacktriangledown) of a fountain clock.

Frequency stability

\blacktriangle The linewidth $\Delta \nu_{\text{Ramsey}}$ of the atomic resonance depends on the time T that the atoms spend in the interrogation region: $\Delta \nu_{\text{Ramsey}} \propto \frac{1}{T}$. In a

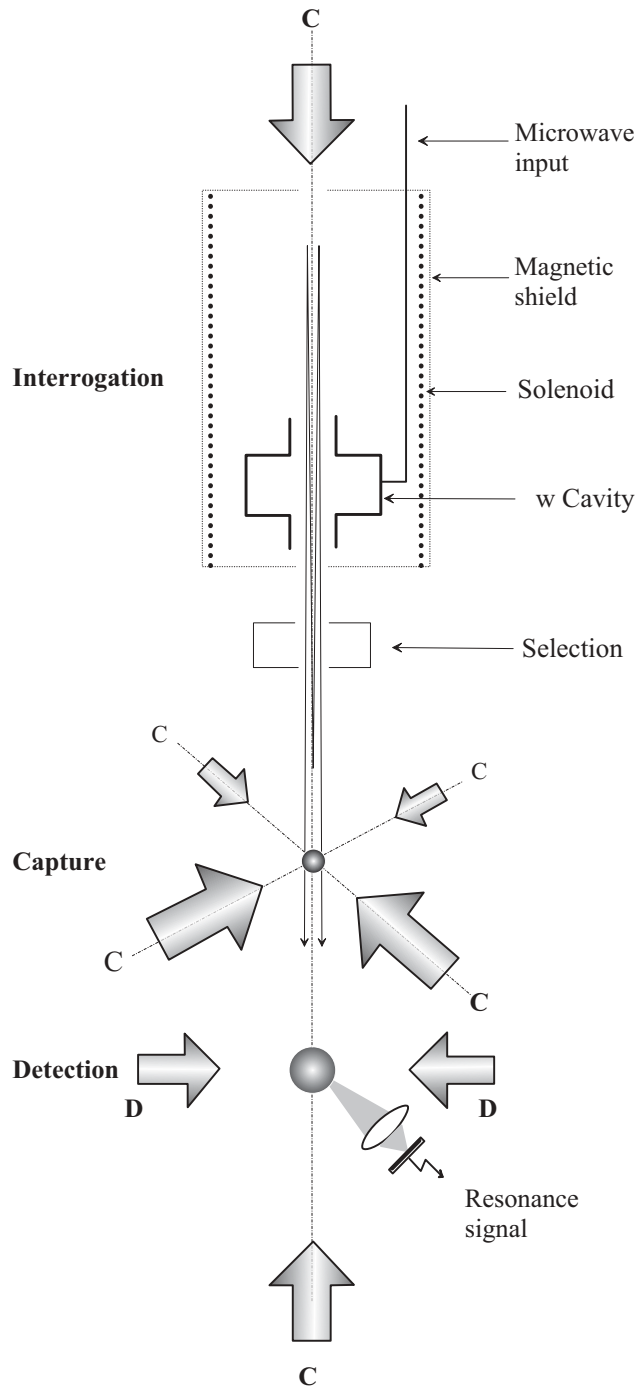


Figure 1.7: Schematic diagram of a cold caesium atom fountain clock. *C* is a laser beam forming the optical molasses and *D* a laser beam detecting the hyperfine resonance.

fountain, T can reach 500 ms, and the resulting quality factor Q_{at} is about 100 times larger than that of the atomic beam clock.

▲ As the cooling mechanisms are efficient, the number of detected atoms can reach as much as 10^7 .

These lead to a potential short term frequency stability of $10^{-14}\tau^{-1/2}$, an improvement by a factor about 35 with respect to the best thermal atomic beam clock [35].

▽ Due to the pulsed operation of the fountain clock, the frequency stability becomes sensitive to the phase noise at high frequency of the microwave signal (Dick effect [41]).

Frequency accuracy

▲ As the Q factor is large, the frequency shift effects depending on Q_{at} are much reduced. The cavity pulling shift due to the frequency offset between the cavity resonance and the atom resonance is $\Delta\nu_c \propto 1/Q_{at}^2$. The static magnetic field needed to remove the degeneracy of the Zeeman substates can be reduced to a level of 1 mG. An atomic fountain makes it possible to map the magnetic field $B(h)$ by launching atoms to different heights h . The second-order Zeeman frequency shift is thus 10^{-13} with an uncertainty of 10^{-16} .

▲ The frequency shift due to the second order Doppler shift effect is reduced to roughly 10^{-17} . The uncertainty on its value is extremely small (10^{-18}) since the width of the atomic velocity distribution is about 1 cm/s.

▲ Thanks to the pulsed operation, there is no light during the interrogation phase, thus the light shift can be completely eliminated.

▲ As the atoms pass twice the same microwave cavity with opposite velocity, the “end-to-end phase shift” no longer exists in a fountain clock. The only remaining effect is the spatial variation of the phase of the oscillatory field in the cavity.

▲ The possibility to vary the cycle time and the interaction time allows for various tests to improve the frequency accuracy.

▽ As the atom temperature is about 1 μK in a fountain, the spin-exchange frequency shift (commonly known as collisional shift) becomes important. Calculation by Tiesinga and his coworkers estimate this shift at $10^{-22}/(\text{atoms}/\text{cm}^3)$ for Cs [42]. For the transportable fountain clock at SYRTE, the shift is $< 3.4 \times 10^{-15}$, and its uncertainty is $< 5.8 \times 10^{-16}$ [43, 44].

However, we can estimate this effect at a level of 10^{-16} by a new selection method based on adiabatic passage, whatever the number of the detected atoms.

In order to reduce this drawback (also for the Dick effect), one laboratories has successfully operated a continuous fountain clock of laser-cooled caesium atoms [45], but it requires careful isolation of the cooling light in the microwave interaction zone in order to avoid the lightshifts and induces some other drawbacks compared to a pulsed fountain, for example, the operation with only a fixed launch velocity is not convenient to evaluate the second order Zeeman shift by using the atoms as a probe.

In summary, a fountain clock can lead to a potential frequency accuracy close to 10^{-16} . Nevertheless, to reach such a performance in a Cs fountain, the blackbody effect which shifts the clock frequency by 1.7×10^{-14} at room temperature should be precisely studied in detail. And all technical difficulties, such as microwave leakage, synchronous perturbation..., must be solved.

Chapter 2

FO1 description and performances

2.1 Résumé en français

En ce chapitre, une description détaillée de la fontaine FO1 est présentée ainsi qu'un complément sur ses performances métrologiques.

La fontaine FO1 est décrite en quatre parties: (1) le coeur de l'horloge, système principal où ont lieu les manipulations et l'interrogation des atomes de césium. (2) le système optique, générateur de tous les faisceaux optiques destinés aux diverses manipulations des atomes de césium. (3) deux chaînes de synthèse de micro-onde, création de signaux pour la sélection et l'interrogation des états atomiques. (4) le système de commande électronique par ordinateur, cet ensemble permet de fixer les paramètres de l'horloge, d'effectuer l'acquisition de signaux et de fournir la correction de fréquence appliquée au signal micro-onde. L'horloge FO1 opère en 6 phases lors d'un cycle complet d'horloge T_c (en général 1 s) qui successivement sont: capture, lancement, re-refroidissement, sélection (ou préparation), interrogation et détection.

Après le lancement, nous pouvons respectivement obtenir 10^8 atomes quand un MOT (magnet-optical trap) est utilisé ou 10^7 atomes en employant directement une mélasse optique. Dans les deux cas la vitesse rms est de 0.8 cm/s déduite de la largeur du signal de TOF (time of flight). Les atomes lancés sont distribués parmi les 9 sous-niveaux de l'état $F=4$ ($\sim 10\%$ des atomes sont dans l'état $F = 4, m_F = 0$). Après une sélection très efficace de l'état (la population de $m_F \neq 0$ est moins de 2%), la probabilité de transition est calculée par une méthode de normalisation en utilisant les signaux

détectés par temps de vol

$$P = \frac{S_3}{S_3 + S_4}, \quad (2.1)$$

où S_3 et S_4 , les intégrales des signaux de fluorescence induits par les faisceaux de détection. Elles sont proportionnelles au nombre d'atomes détectés dans les niveaux $|3, 0\rangle$ et $|4, 0\rangle$, respectivement. La largeur de la frange centrale à mi-hauteur est de 1 Hz lorsque le lancement des atomes est effectué à une vitesse de 3.4 m/s. Afin de verrouiller la fréquence du signal micro-onde d'interrogation sur cette frange centrale, nous modulons fréquence du signal micro-onde par un signal carré de période $2T_c$ et nous mesurons la probabilité de transition à chaque cycle. La différence de probabilité de transition entre deux mesures successives produit un signal d'erreur permettant de contrôler la fréquence du signal d'interrogation. Ce signal est généré à partir d'un oscillateur local à quartz 10 MHz BVA (Oscilloquartz) faiblement verrouillé en phase sur le signal d'un maser à hydrogène. Le calcul de la variance d'Allan des corrections de fréquence permet de caractériser la stabilité de l'horloge FO1 par rapport au maser à hydrogène et la correction moyenne de fréquence représente le décalage en fréquence entre l'horloge FO1 et le Maser à hydrogène.

Nous avons analysé l'influence de chaque bruit sur la stabilité de fréquence de la fontaine FO1. Nous avons constaté que lorsque le nombre d'atomes détectés est inférieur à 10^4 le bruit technique est dominant (principalement, le bruit électronique de la détection, le bruit dû à la lumière parasite et le bruit du jet atomique résiduel dans la zone de détection). Quand le nombre d'atomes détectés est supérieur à 2×10^5 , la stabilité de la fontaine FO1 est limitée par l'échantillonnage du bruit de l'oscillateur d'interrogation par les atomes (effet Dick [41, 46, 47]). Typiquement, quand le nombre d'atomes détectés est 3×10^5 , la stabilité de fréquence obtenue est $1.3 \cdot 10^{-13} \tau^{-1/2}$ en utilisant un oscillateur à quartz de type BVA. Ce résultat est conforme à la valeur prévue de $1.1 \times 10^{-13} \tau^{-1/2}$ (voir section 2.9.1).

En synchronisant le cycle d'opération de deux horloges atomiques et en interrogeant les atomes en même temps et avec le même oscillateur, les fluctuations de fréquence de chaque horloge dues à l'oscillateur d'interrogation sont corrélées, ainsi l'effet Dick est supprimé lors de la comparaison de fréquence. Cette méthode peut être employée pour comparer deux ou plusieurs fontaines atomiques au niveau du bruit de projection quantique [48]. Une expérience de démonstration a été faite avec les fontaines FO1 et FO2(Rb) qui fonctionne avec du Rb. Un oscillateur à quartz bruyant a été utilisé afin de tester la réjection de son bruit de phase [49]. L'effet Dick a comme conséquence de limiter la stabilité de chaque fontaine à $2.4 \times 10^{-12} \tau^{-1/2}$. Ce bruit est beaucoup plus élevée que tous les autres bruits des fontaines. Une impulsion au

début de chaque cycle de FO1 est utilisée pour synchroniser le cycle de la fontaine FO2(Rb). Quand les fontaines sont synchronisées à 1 ms près l'écart type d'Allan sur la différence de fréquence relative entre les deux fontaines (environ $2 \times 10^{-13} \tau^{-1/2}$ correspond à un facteur de réjection de 16) est proche de la valeur obtenue en utilisant un meilleur oscillateur à quartz BVA ($1.1 \times 10^{-13} \tau^{-1/2}$).

Nous avons évalué l'exactitude de la fontaine FO1. La plus récente obtenue est de 1×10^{-15} quand FO1 fonctionne en mélasse optique. Afin de comparer les fréquences des trois fontaines atomiques du laboratoire, nous avons distribué le même oscillateur à quartz faiblement asservi en phase sur un maser à hydrogène comme référence de fréquence pour chaque chaîne de synthèse micro-onde. Malheureusement, les trois horloges ne sont pas en parfait synchronisme et le bruit à moyen-terme n'est pas parfaitement rejeté dans la comparaison. Il est difficile d'en extraire directement une différence de fréquence. Pour faciliter la comparaison, nous avons ajusté aux données de H-maser/FO1 un polynôme d'ordre trois. Ce polynôme est utilisé comme référence pour calculer les différences de fréquence entre les trois fontaines. Les mesures sont en accord avec les bilans d'évaluation. Par ce moyen, nous avons également mesuré la valeur de la transition hyperfine du Rubidium à une valeur de 6 834 682 610.904 314(21) Hz en mai 2000 (voir section 2.10.3). Cette valeur a été utilisée pour tester une variation éventuelle de la constante de structure fine.

2.2 Introduction

In this chapter, a detailed description of the FO1 fountain is presented with an extensive discussion of the metrological performance. Figure 2.1 shows the schematic of F01. In the cold caesium atom fountain setup, we identify four parts: (1) The fountain physical package, where we manipulate and interrogate the caesium atoms. (2) The optical system, that provides all the optical beams for the atom manipulation. (3) Two microwave synthesis chains, that provide the signals for the atomic state selection and interrogation. (4) The electronic control system with a computer, that sets the clock parameters, performs the signal acquisition and provides the frequency correction to the applied microwave signal.

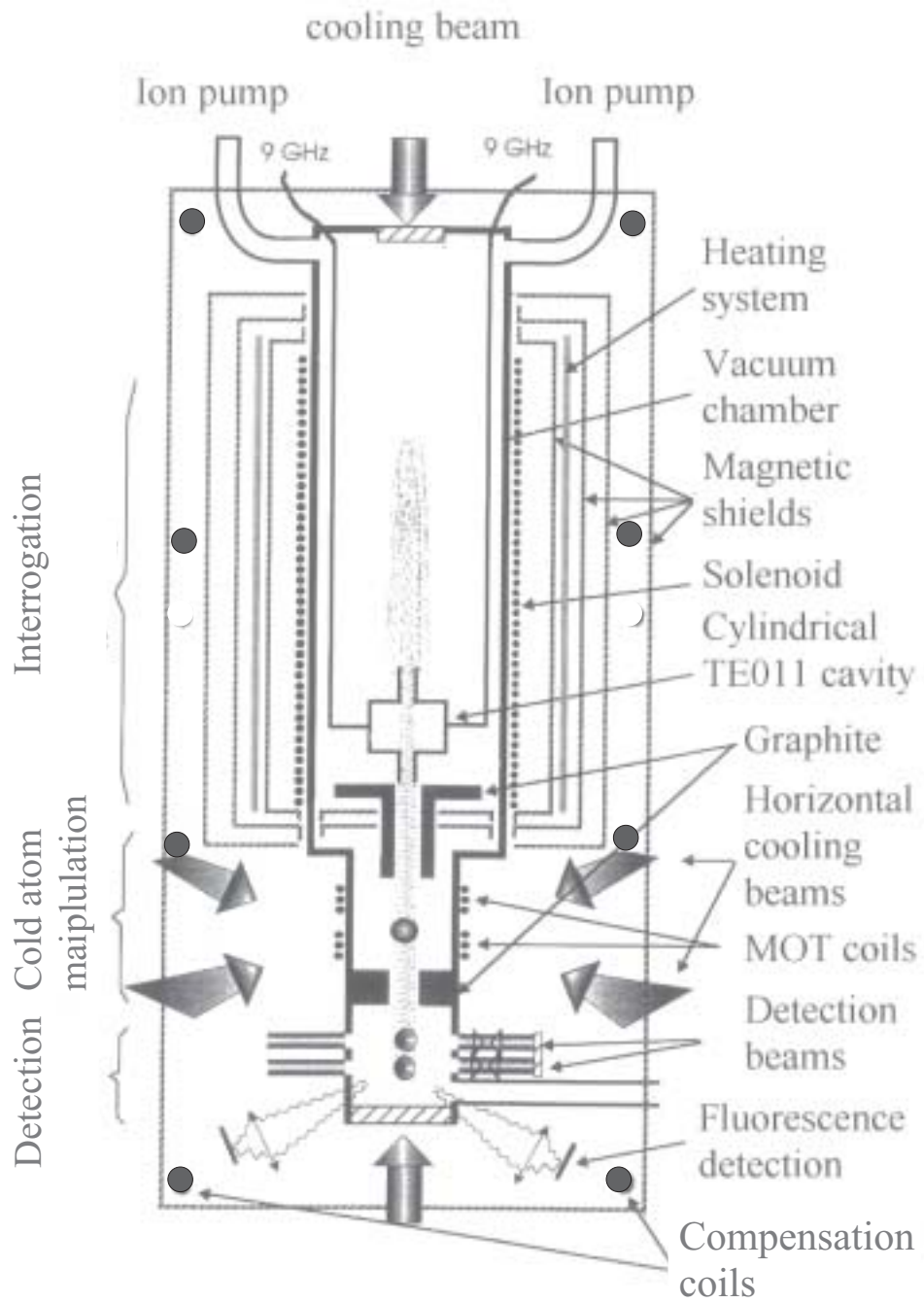


Figure 2.1: Schematic of the caesium fountain FO1. The C-field region extends over 70 cm. The setup has a total height of 1.5 m.

2.3 The time sequence of the fountain operation

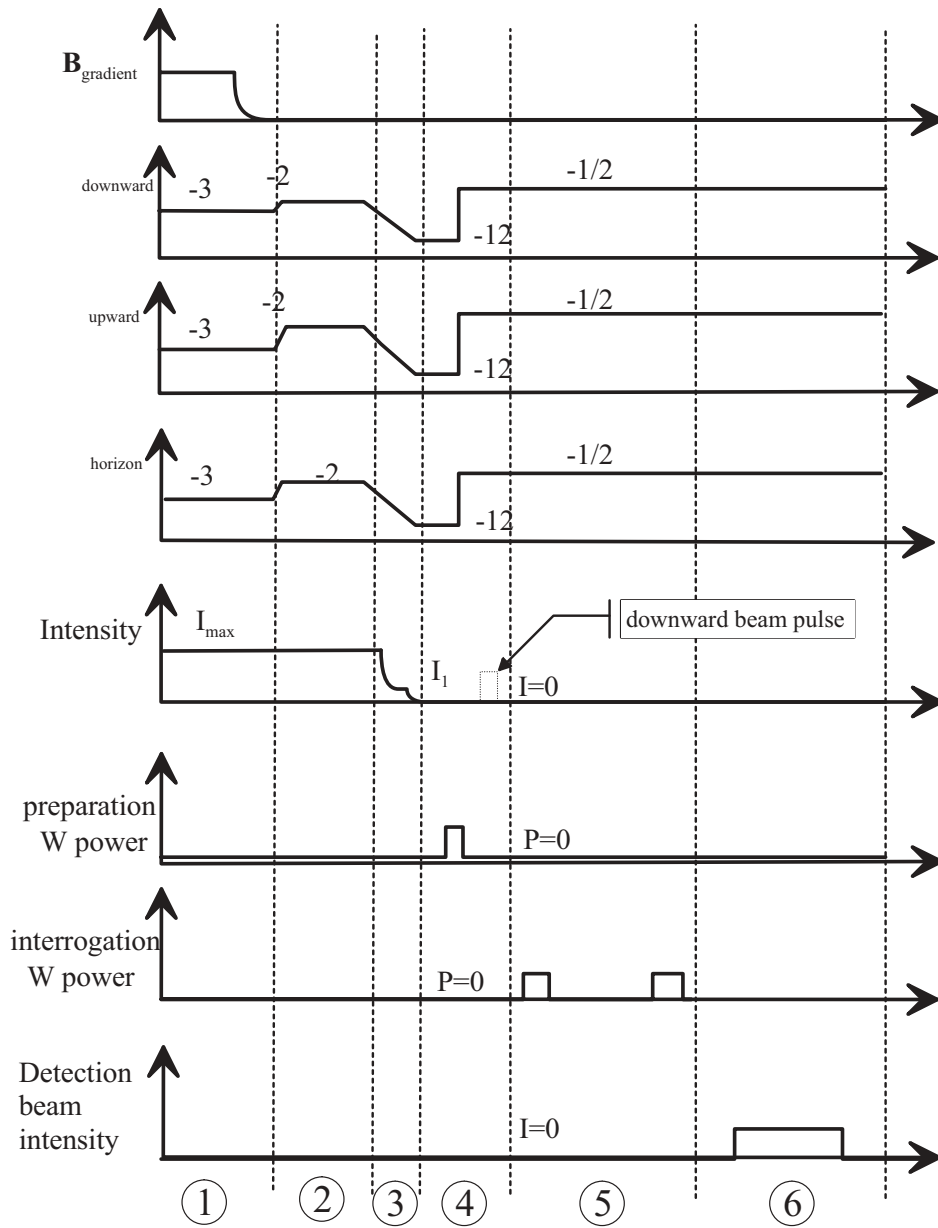
We have presented the principle of the atom cooling in section §1.4.2. Here, we introduce the atom manipulation in the fountain. The fountain clock operates in a sequential mode. There are 6 phases in sequence to realize one clock cycle T_c : capture, launching, re-cooling, selection (or preparation), interrogation and detection. Fig. 2.2 presents the atoms manipulation timing sequence in the fountain clock. The duration of one fountain cycle T_c is typically 1 s.

1. Capture phase : The intersection of 3 pairs of polarized laser beams defines the capture volume. For MOT operation [50], the polarization configuration is $\sigma^- - \sigma^+$ with a magnetic gradient of about 12 G/cm. The MOT operation produces both a large number of captured atoms and a high atomic density to study the cold atoms collisional frequency shift and to have a better short-term frequency stability. FO1 can also operate in a pure optical molasses configuration by moving quarter wave plates. The laser frequency is red shifted by 3Γ from the $F = 4 \rightarrow F' = 5$ transition. The 6 independent beams have an average intensity of about 5 mW/cm², which is higher than the saturation intensity of the D_2 line (1.1 mW/cm²). The four horizontal beams are superimposed with four repumping beams ($\sim 60 \mu\text{W}/\text{cm}^2$) tuned to the $F = 3 \rightarrow F' = 4$ transition. The caesium atoms are captured from a low pressure vapor ($\sim 10^{-8}$ Torr) and cooled to 2.5 μK . We can vary the duration of this phase adjust the number of captured atoms. Varying between 200 ms and 600 ms, we obtain 10^6 to 10^8 atoms in a MOT and 10^5 to 10^7 atoms in a lin \perp lin optical molasses. In normal operation, we pass from MOT configuration to optical molasses by switching off the current supply of the magnetic field (magnetic field fall-time ~ 100 ms) to avoid the the effect of Majorana transition after the selection phase.

2. Launch : We launch the cold atoms with the moving molasses technique by using different detunings for the upward and the downward beam. They are respectively red shifted to $-2\Gamma + \Delta\nu_L$ and $-2\Gamma - \Delta\nu_L$ of the transition $F = 4 \rightarrow F' = 5'$. Because of the radiation pressure, the atoms' acceleration is very large ($\sim 30\,000$ m/s²), and the atoms are re-captured in an optical molasses defined by the moving frame where the relative phase of the two laser beams is constant. The upward velocity v_L is given by:

$$v_L = \lambda_l \times \Delta\nu_L \quad (2.2)$$

where λ_l is the wavelength of the laser. The launching velocity for Cs is 0.85 m/s \cdot MHz⁻¹. The duration of this phase is less than 1.5 ms. The launching velocity only depends on the detuning, and it can be adjusted



- ① Capture ② Launch ③ Post cooling
 ④ Preparation ⑤ Interrogation ⑥ Detection

Figure 2.2: *The atom manipulation timing sequence in FO1.*

2.3. THE TIME SEQUENCE OF THE FOUNTAIN OPERATION

with a resolution much smaller than the atomic velocity distribution (~ 1 cm/s). This is only true if the phase fluctuations of both laser beams are well correlated. During this phase, all the capture beams are kept at the maximum intensity. The global detuning of around -2Γ is chosen experimentally to optimize the number of launched atoms .

3. Recooling The horizontal and vertical beams during the launching phase warm up the atoms by ~ 30 μK . As we presented in section 1.4.2, the cold atom temperature T is proportional to $I_{laser}/\Delta\nu$ with the Sisyphus effect. To cool the atoms in their moving frame, we linearly increase the laser detuning frequencies up to -12Γ and slowly ramp down the intensity to $I_1 \sim 1.0$ mW/cm² during about 700 μs . Finally, the beams are blocked by mechanical shutters with a fall-time of about about 1 ms. This process produces an adiabatic condition for the cooling mechanism to reach a lower temperature. The final temperature of the moving atoms is about 1 μK , corresponding to an rms velocity on the order of 1 cm/s. The re-pumping beams are turned off about 1 ms after the capture beams.

4. Selection The launched atoms are nearly equally distributed among the nine Zeeman sub-levels of the $F = 4$ state. We feed a microwave antenna with a 9.192 631 770 GHz signal to excite the $F = 4, m_F = 0$ to $F = 3, m_F = 0$ transition by a microwave π pulse (~ 1.5 ms) immediately after the launching phase. The atoms remaining in the state $F = 4$ are pushed away by the downwards laser beam which is $\Gamma/2$ red tuned from the $F = 4 \rightarrow F' = 5$ transition. At the end of this phase, only atoms in the state $F = 3, m_F = 0$ continue their upwards parabolic flight.

5. Interrogation The selected atoms pass twice the interrogation cavity, once on their way up, once again on their way down, undergoing two microwave pulses of a Ramsey interaction. During this phase, all the laser beams entering the fountain package are completely blocked by mechanical shutters in order to avoid any light shift.

6. Detection The interrogated atoms are in a coherent superposition of the states $F = 3, m_F = 0$ and $F = 4, m_F = 0$. The detection performs a measurement of the population of each state. We need 3 laser beams to realize this detection. The two detection beams have the same detuning between 0 and $-\Gamma/2$ with respect to the transition $F = 4 \leftrightarrow F' = 5$ and an equal intensity of ~ 0.6 mW/cm². The third is a repumping beam tuned to the transition $F = 3 \leftrightarrow F' = 4$ with an intensity of about 5 $\mu\text{W}/\text{cm}^2$. These detection beams are turned on about 50 ms before atoms arrive.

2.4 The optical system

In this paragraph we describe the optical system which provides the laser beams to manipulate the caesium atoms.

2.4.1 The optical bench

All the optical elements are arranged on a 2 m² granite bench. Figure 2.3 describes the scheme of the optical bench. There are four commercial AlGaAs semiconductor lasers (model SDL-5422-H1) with a maximum output power of 150 mW and a nominal wavelength of 852 ± 4 nm. Two laser diodes are mounted in an extended cavity lasers (ECL) configuration: master1 and master2. The linewidth of the ECL is about 100 KHz.

The master1 and master2 are respectively frequency stabilized to the $F=4$ ($6^2S_{1/2}$) to $F'=5$ ($6^2P_{3/2}$), and $F=3$ ($6^2S_{1/2}$) to $F'=3$ ($6^2P_{3/2}$) transitions using the saturated absorption technique. The master1 is red detuned about 2 MHz from the transition line. One part of the master1 beam, after passing through a mechanical shutter and a spatial filter, is expanded to 2.5 cm in diameter and used as a detection beam. The other part of the master1 beam passes twice through AOM1¹ operating at 78-100 MHz. The red detuned beam is then used to inject and lock two laser diodes (slave1 and slave2). These diodes provide about 120 mW optical power. This laser power is needed for atom capture and cooling. Slave1 provides the two vertical beams. The upward beam and the downward beam are blue detuned by passing twice through AOM (2 and 3) operating at 70 or $70 \pm \Delta\nu_L$ MHz, respectively. These AOM frequencies ($70 \pm \Delta\nu_L$ MHz) define the launching velocity. The four horizontal beams, supplied by diode slave2, are blue detuned by passing twice AOM4, operating at 70 MHz. All six capture and cooling beams are spatially filtered and expanded to 2.5 cm in diameter. The frequency of the six beams is controlled by AOM1. The repumping beams for the detection and the capture are generated by master2. It is tuned to the $F=3$ ($6^2S_{1/2}$) to $F'=4$ ($6^2P_{3/2}$) transition by AOM5 operating at 100 MHz. One repumping beam is superposed on the four horizontal capture beams. The RF levels of the AOMs (2, 3 and 4) allow us to control the powers of all laser beams.

2.4.2 Control of the optical parameters

The cycle time T_c is defined by a programable counter. About twenty pulses generated by a retriggerable monostable multivibrator (SN74123, Semiconductor) and synchronized on T_c provide all characteristic times. The delay

¹AOM: acousto-optic modulator.

2.4. THE OPTICAL SYSTEM

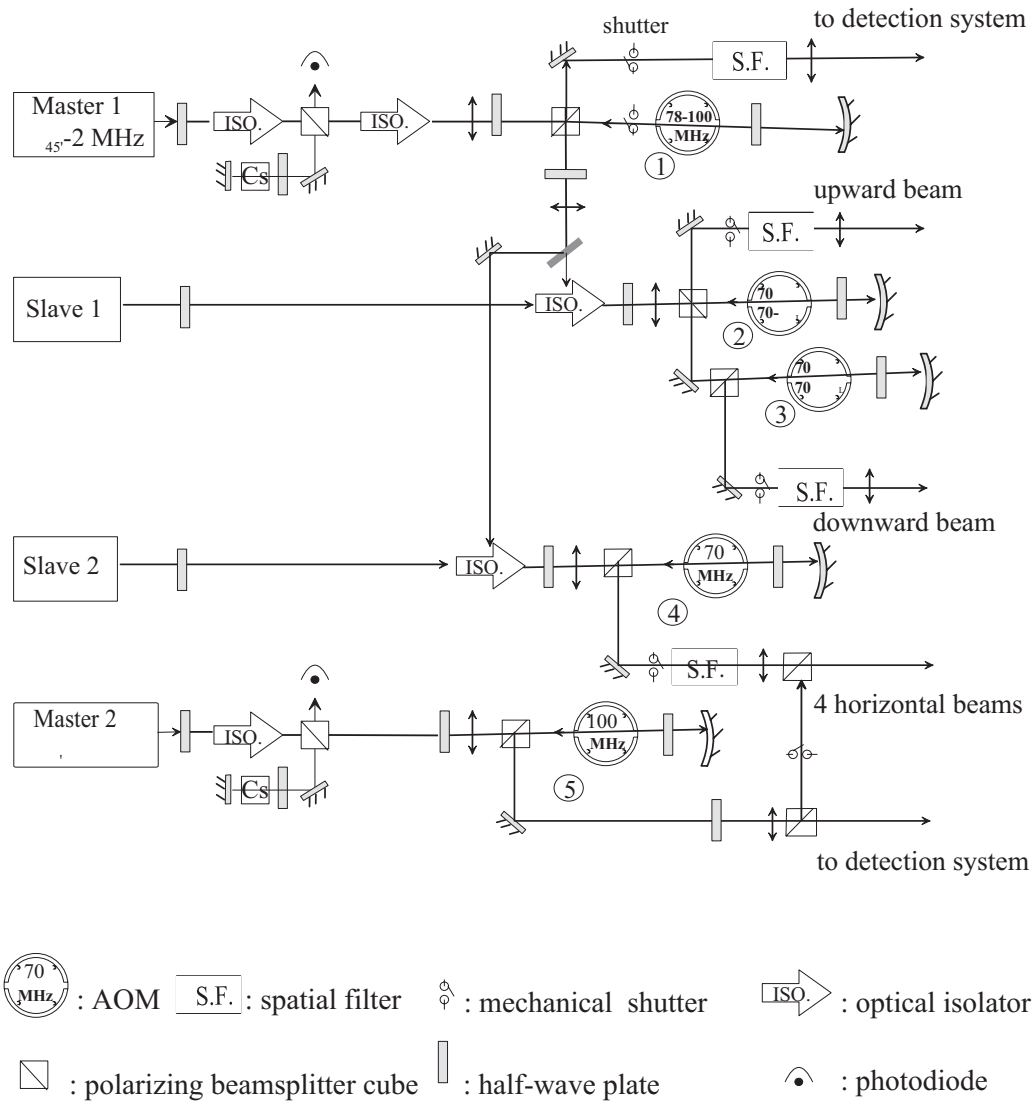


Figure 2.3: *The schematic of the optical bench of FO1.*

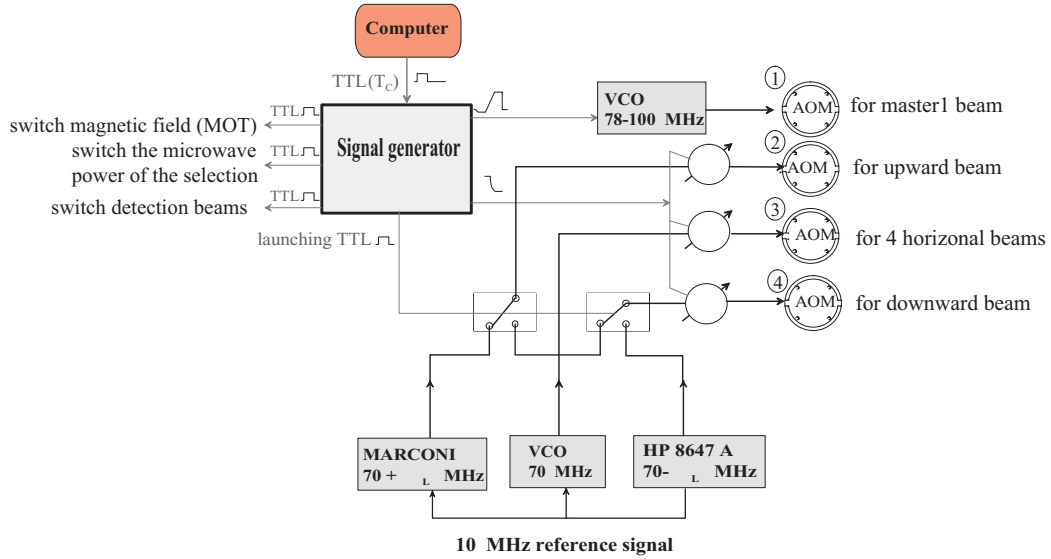


Figure 2.4: *RF system driving the AOMs.*

and duration of the pulses are driven by about 30 potentiometers. Some pulse signals trigger analog switches to change the frequency and the power of the laser beams.

The different frequency detunings of the two vertical beams during the launching phase are performed by two selection switches (PSW-1211, Mini-Circuits) which change the frequency drivers for AOM2 and AOM3 from a 70 MHz VCO to the two radiofrequency generators. The two frequency generators and the 70 MHz VCO are phase locked to each other.

During the launching phase and the post-cooling phase, the frequency detuning (-2Γ , -3Γ to -12Γ) is performed by a voltage applied to a 78 - 100 MHz VCO. The power control of the six capture beams (I_{max} to I_1) is carried out through three RF attenuators (PAS 3, Mini-Circuits) in the AOM (2, 3 and 4) drivers.

2.5 The fountain physical package

In this paragraph we describe the fountain vacuum system where the caesium atoms are cooled, interrogated and detected.

2.5.1 The vacuum chamber

The vacuum chamber is composed of two parts: the interrogation zone and cold atom manipulation zone. These two parts are connected via an alu-

minium table placed on the marble optical bench. It has three legs used to adjust the interrogation zone verticality. Three rods screwed on the aluminium table support the cold atoms source. The vacuum connection is made of a flexible stainless steel tube. This configuration allows to adjust its axis to be vertical.

The interrogation zone is made of copper OFHC tube, to provide a high temperature homogeneity. The diameter is 150 mm and the length is 700 mm. The top of this cylindrical tube is closed by a glass window with a diameter of 40 mm. The interrogation cavity is centered and blocked inside the tube. Three screws allow vertical alignment of the microwave cavity with a resolution of 1 mrad. The cavity is electrically isolated from the mounting plate to avoid stray circulating currents which disturb the C-field. Several ceramic feed-throughs are placed at the tube top for the coaxial microwave cables and for some wires used for the blackbody setup (see chapter 5)

The atom manipulation zone is made of stainless steel (316LN). We can distinguish two parts: capture and detection, separated by 15 cm. The first part contains five glass windows for passing the cooling laser beams and observing the cold atom cloud. The second one contains four glass windows, three for the detection system and one at the bottom.

All glass windows have an AR coating and are soldered on the vacuum flanges. The ultra-vacuum connections are realized with copper gaskets using non-magnetic screws made of “ARCAP”.

A vacuum tube connects the capture zone with the caesium source.

The caesium source is a vacuum tube ($\phi 5 \text{ cm} \times l 8 \text{ cm}$) which contains three small caesium glass cells (1 or 2 grammes) together with stainless steel balls. After out-gassing (residual pressure $\sim 10^{-10}$ Torr), we shake this chamber to break the glass cells using the steel balls, and connect the caesium source chamber to the capture zone via a vacuum valve.

In order to control the caesium vapor pressure in the capture zone, we change the chamber temperature by using a Peltier element. The chamber and the Peltier element are enclosed in an aluminum box (the air inside the box is kept dry by a small pump to avoid water condensation). Cooling water, circulating inside the Peltier mounting plate, avoids excessive heating. Typically, the chamber temperature is kept at about 6 °C.

In order to reduce the caesium vapor pressure² to $\sim 10^{-10}$ Torr inside both the interrogation and detection zones, we have placed graphite tubes with a helicoidal inner profile at the junctions between the capture chamber, the detection zone, and the interrogation zone. The graphite tubes reduce the Cs vapor background pressure in these latter two regions. This reduces the level of stray fluorescence in the detection region.

²It can be measured by the absorption of a laser beam.

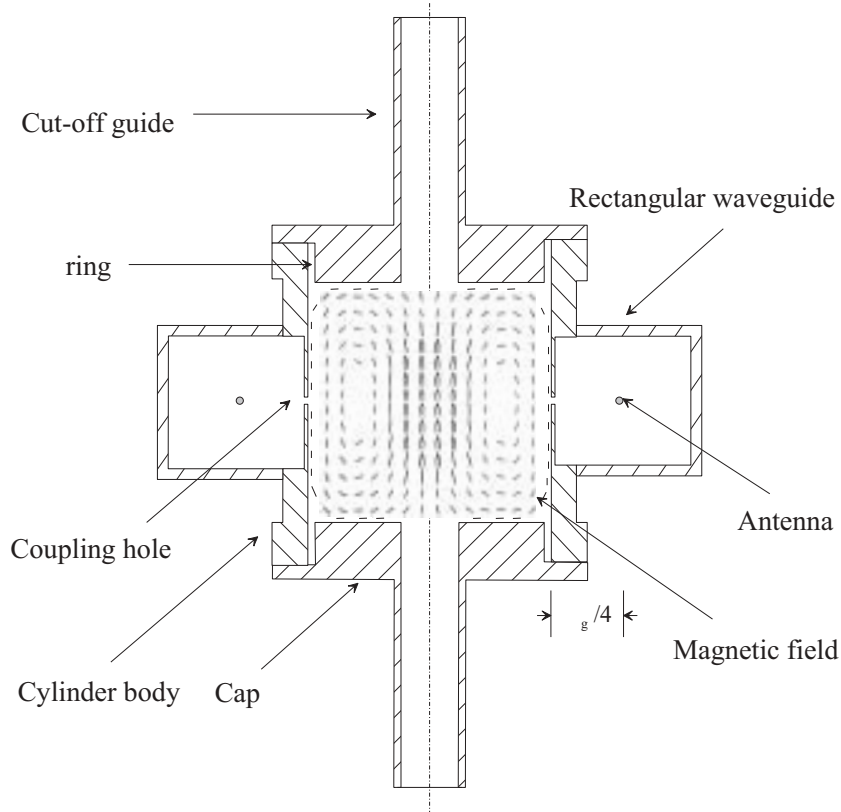


Figure 2.5: *The interrogation cavity section and the magnetic field TE_{011} mode. There is only a H_r component in the inner surface of the caps, and only a H_z component in the inner surface of the cylindrical body. The double arrows indicate fields from 0 dB to -3 dB.*

All the metal vacuum pieces and the graphite tubes inside the vacuum tank were heated to about 250 °C to be outgassed at the level of 10^{-8} Torr before assembly.

During the establishment of the vacuum and the outgassing of the apparatus (at about 100 °C), a primary turbo pump and a mass spectrometer can be connected to the low vacuum part through a CF35 cross. In normal operation, 4 ion pumps are used to maintain the ultra high vacuum. Two of them (PID 25 MECA 2000, 25 l/s) are placed near the capture zone while the two others (RIBER, 25 l/s) sit at the top of the fountain tube. The vacuum level is a few times 10^{-10} Torr inside the tube.

2.5.2 Microwave cavity

To probe the clock transition, we need a microwave cavity where the magnetic field is parallel to the static magnetic field. In addition, the cavity must let a large number of cold atoms pass through.

The cylindrical cavity is a good candidate for the atom interrogation (see fig. 2.5). This cavity has a very high Q value and an axial symmetry. The fundamental TE_{011} mode allows one to open “large” holes on the end-caps of the cavity, with only a slight perturbation of the electro-magnetic field structure. The mode TE_{011} structure has also a small transverse phase gradient and negligible transverse components of the magnetic field which could excite the transitions $\Delta m = \pm 1$.

The cavity is a cylinder whose the diameter of the cylinder is equal to its length so as to maximize the cavity factor Q_{cav} for a given TE_{011} mode. Our cavity is made of 3 OFHC CUC2 copper parts: the cavity body is closed at each end by a cap (see figure 2.5). Its electric conductivity is 5.8×10^7 S/m and its thermal expansion coefficient $\alpha \simeq 1.7 \times 10^{-5}/^\circ\text{C}$ [51].

The resonance wavelength in vacuum³ is given by

$$\lambda = \frac{2R}{1.318} \quad (2.3)$$

where R is the radius of the cylinder. To be resonant with the clock transition $\lambda = 3.261$ cm, the cavity diameter is found to be $L = 4.297$ cm. This corresponds to a cut-off wavelength of $\lambda_c = 3.526$ cm and a guided wavelength of $\lambda_g \simeq 8.58$ cm. The microwave field inside the cavity is expressed in the following way:

$$\begin{cases} \vec{E}(\vec{r}, \omega) = E(\omega) \vec{E}(\vec{r}) \\ \vec{B}(\vec{r}, \omega) = B(\omega) \vec{B}(\vec{r}) \\ E(\omega) = icB(\omega). \end{cases} \quad (2.4)$$

The mode TE_{011} is given by [52] in cylindrical coordinates

$$\vec{E}(\vec{r}) = \begin{cases} E_r & = 0 \\ E_\theta & = j\mu\omega \frac{R}{x'_{01}} \sin\left(\frac{\pi z}{L}\right) J_1\left(\frac{x'_{01}r}{R}\right) \\ E_z & = 0 \end{cases} \quad (2.5)$$

and

$$\vec{H}(\vec{r}) = \begin{cases} H_r & = \frac{\pi R}{x'_{01}L} \cos\left(\frac{\pi z}{L}\right) J_1\left(\frac{x'_{01}r}{R}\right) \\ H_\theta & = 0 \\ H_z & = \sin\left(\frac{\pi z}{L}\right) J_0\left(\frac{x'_{01}r}{R}\right), \end{cases} \quad (2.6)$$

³In air, the resonance frequency is reduced by 2.68 MHz.

where $\mu \simeq \mu_0$ is the magnetic permeability, and $x'_{01} = 3.832$ is the first root of $J'_0(x) = 0$, where $J'_0(x)$ is the derivative of the 0th order Bessel function. The most obvious feature is the axial symmetry. E_θ exhibits the same radial variation as H_r , which is maximal at $r = R/2.08$. The average stored electromagnetic energy is given by

$$\begin{aligned} W_e &= \frac{\mu}{2} \iiint \mathbf{H} \cdot \mathbf{H} dr^3 \\ &\equiv \frac{\mu H_0^2}{2} \cdot V_{mode} \\ &= \frac{\mu H_0^2}{2} \cdot \frac{\pi L R^2}{2} \left[1 + \left(\frac{\pi R}{L x'_{01}} \right)^2 \right] J_0^2(x'_{01}), \end{aligned} \quad (2.7)$$

where $J_0^2(x'_{01}) \simeq 0.4082$, and H_0 is the amplitude of the magnetic field inside the cavity. $V_{mode} = 6.07 \text{ cm}^3$ is the mode volume.

When we excite the cavity of this geometry, modes other than TE_{011} , such as TM_{111} , TM_{012} , TE_{212} , TE_{311} may resonate at frequencies 9.19 GHz, 8.85 GHz, 9.72 Hz, 9.96 GHz, respectively. The frequency of the degenerate mode TM_{111} is the same as for the TE_{011} mode (the Q value is 2 ~ 3 times lower than that of the mode TE_{011}). The TM_{111} mode electromagnetic field is orthogonal to that of TE_{011} . The TM_{111} can induce $\Delta m_F = \pm 1$ microwave transitions. We avoid this mode by slightly reducing ($\sim 1 \text{ mm}$) the diameter of the two caps over a length of $\lambda/4$ (see figure 2.5). This detunes the TM_{111} mode resonance frequency by about 100 MHz. Moreover, these $\lambda/4$ rings cut off the longitudinal current lines in the inner surface of the cylinder body. The cavity Q factor of TM mode is then much reduced. As shown in figure 2.6, the current lines of the TE_{011} mode are co-axis circular on the inner surfaces of the cavity. Hence, this modification does not disturb this mode.

As shown in figure 2.5, there is only a H_r component on the inner surface of the caps. It is then possible to open two holes in order to let the cold atoms cross the cavity without perturbing the TE_{011} mode. We open two holes with radius $R_h = 0.5 \text{ cm}$. In order to avoid the microwave leakage, a circular cut-off waveguide of diameter $\phi = 1.0 \text{ cm}$ and length $l = 6.0 \text{ cm}$ is installed at each end of the caps. The cut-off wavelength is $\lambda_c^c = 0.82 \text{ cm}$, much shorter than the resonant wavelength $\lambda = 3.26 \text{ cm}$. This leads to a 60 dB/cm attenuation [53]. The total attenuation is larger than 120 dB.

At half-height of the cylinder body, we symmetrically open two $\phi = 5 \text{ mm}$ diameter coupling holes to excite the cavity. Two T-shaped rectangular waveguides with a section of $10.16 \times 22.86 \text{ mm}^2$ are screwed in front of the holes to guide its fundamental TE_{10} mode. The guided wavelength is $\lambda_g^g = 4.65 \text{ cm}$, and the cut-off wavelength $\lambda_c^g = 4.57 \text{ cm}$. This symmetric geometry minimizes the phase gradient [54]. The cavity is electrically coupled: the

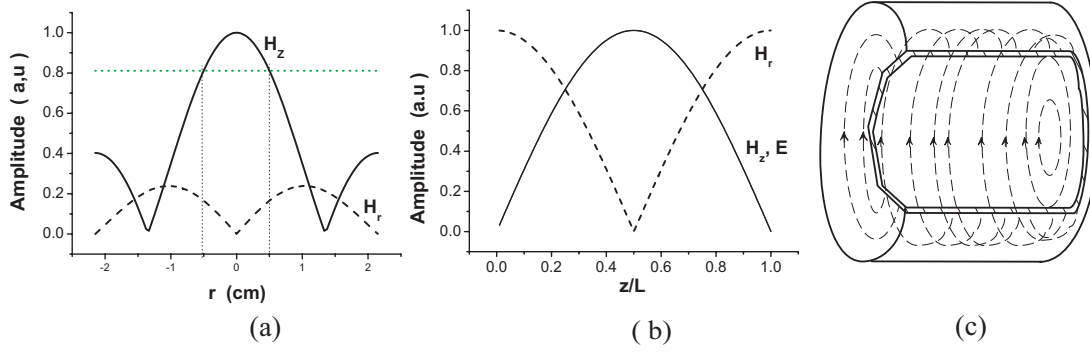


Figure 2.6: Mode TE_{011} of the microwave cavity. (a) The radial variation, at $r=0.5$ cm, $H_z \simeq 0.81$. (b) The longitudinal variation at $r = 0$. (c) The circular current on the inner surface of the cavity, there is no current passing through the side-surface of the caps.

TE_{011} mode of the cavity and the TE_{01} mode of waveguide provide parallel electric fields inside the cylindrical cavity, perpendicular to the vertical axis of the cavity. The waveguide is enclosed by a soldered copper part, whose position is adjusted to a distance about $\lambda_g^g/2$ from the coupling hole on cavity wall in order to maximize the coupling and to realize a short circuit. The waveguides are fed respectively by two dipole antennas, formed by the core of a 3.6 mm diameter semi-rigid copper coaxial cable and placed on the orthogonal direction to the vertical axis of the cavity. They are passed and soldered in 3.6 mm diameter holes in the waveguides. The coupling efficiency depends on the antenna length and position.

Indium rings are put between the connecting parts of the cavity to ensure a good electric conductivity and avoid microwave leakage. The level of the leakage is better than -120 dB.

The cavity is overcoupled to reach a loaded quality factor Q_{cav} about 10 000 (the calculated unloaded factor is about 30 000) to reduce the effect of cavity pulling ($\propto Q_{cav}^2 \Delta\nu_{cav}$, where $\Delta\nu_{cav}$ is the detuning of the cavity resonance frequency to the atomic resonance) and its temperature sensitivity.

2.5.3 The magnetic field

A weak, uniform, static magnetic field is applied in the interrogation zone to provide the quantization axis and to separate the clock transition ν_{00} ($F = 4, m_F = 0 \longleftrightarrow F = 3, m_F = 0$) from other transitions. The frequency

ν_{00} is shifted by $\Delta\nu_Z$, the second order Zeeman shift⁴. For F01, this field B_0 is about 1.6 mG. The frequency shift of the clock transition $\Delta\nu_Z \simeq 1.1$ mHz and the neighboring transition lies 560 Hz further away.

To produce this static magnetic field, a solenoid made of copper wire is spirally wound around a carved aluminium tube (ϕ 24 cm \times l 70 cm), which is coaxial with the copper tube (~ 1 mrad).

Three cylindrical magnetic shields made of μ -metal (high magnetic permeability $m_r \simeq 3 \times 10^5$, thickness 2 mm) are placed around the solenoid (see fig. 2.1). Each of them is closed by two end caps. These three shields provide an attenuation of the external magnetic field of more than 10^4 . Six compensation coils are placed on the end-caps of the magnetic shield to ensure the continuity and the smoothness of the magnetic field, to avoid rapid field variations that might induce Majorana transitions [55]. The coils are also used to improve the C-field homogeneity. The current supply (a few hundred μ A) of the coils has a relative stability better than 5×10^{-5} over one day (this gives a Zeeman frequency shift stability better than 10^{-17}). In order to compensate the fluctuations of the residual magnetic field, we put a magnetic sensor MAG-03MC (70 μ G/mV) near the capture zone in order to generate a correction current (a few tens of milliamps) supplied to four big identical, parallelepiped copper coils which are uniformly distributed along the fountain tube axis. A fourth magnetic shield surrounds the fountain tube. The total attenuation in the capture zone is about 100 and it is better than 10^5 in the interrogation zone.

In addition, the copper tube is electrically isolated from the shields to avoid any thermoelectric effect which could produce magnetic fluctuations in the interrogation zone.

Two copper wires enclosing respectively the first and the second magnetic shield are used for degaussing. We alternatively supply these two circuits with a 50 Hz sinusoidal current with a slow decreasing amplitude (from a maximum 15A, corresponding to a field which passes beyond the shield coercive magnetic field $H_c \sim 0.5$ A/m). When necessary, we perform the degaussing of the third shield using the four big compensation coils (see figure 2.1).

The initial adjustment of the compensation coil current at the beginning of the vacuum assembly was performed by moving magnetic sensors (resolution 30 μ G) inside the copper tube, and by measuring the vertical and transverse field component. This method is used to ensure that the magnetic field gradient is below 50 μ G/cm .

The fine adjustment of the magnetic field is done using the 1st order

⁴ $\Delta\nu_Z = 427.45 \times \langle B_0^2 \rangle$ where, B_0 is the magnetic field value in gauss, and $\langle \rangle$ is the average over time during the flight of the atoms above the cavity

Zeeman effect on the cold atoms (see section 2.9.2).

2.5.4 The temperature control

The caesium atoms are moving in a thermal radiation environment which produces a frequency shift, the so-called blackbody shift. The shift $\Delta\nu_{BBR}$ is approximately given by

$$\Delta\nu_{BBR} \simeq 1.5 \times 10^{-4} \times \left(\frac{T}{300}\right)^4 \quad (2.8)$$

From this expression we deduce a temperature accuracy and a stability below 0.5°C to obtain clock performance better than 10^{-16} .

In order to regulate the temperature, the working temperature is $T = 29$ °C (above the room temperature). A heating wire made of “ARCAP” (non-magnetic and high resistivity) is wound in double spiral coils on an aluminium tube placed between the first and second magnetic shields. The applied current is continuous.

Double layers of polystyrene and mylar film surround the heater. A thermistor (4.7 kΩ) is used to control automatically the copper tube temperature. The temperature is regulated and maintained within ± 0.5 °C. As the cavity resonance has a temperature dependence of 150 kHz/°C, a measurement of its resonance frequency allows one to control the temperature with a resolution of 10^{-3} °C in the interrogation region. In nominal operation, the induced magnetic field by the heating system is not measurable.

2.6 The capture and selection zone

Four windows of the cold atom manipulation zone are used to pass the horizontal capture beams (see figure 2.7). The beam diameter is 1.5 cm. The two vertical capture beams pass through a glass window at the bottom of the detection zone and a glass window at the top of the fountain tube, respectively. The upward beam has a diameter of 1.5 cm. The downward beam, as it passes through the microwave cavity, has only a diameter of 1 cm.

The three capture beam pairs are orthogonal within 1 mrad and the two beams in each pair are well superposed. The verticality of the beams is obtained by using a liquid mirror. This mirror consists of a cup filled with sugared water (the sugar increases the refractive index). To center the axis of the two vertical beams with the cavity axis better than better than 0.5 mm, we use the diffraction patterns of the cavity apertures.



Figure 2.7: *The capture zone and the caesium source.*

To form a MOT, a quadrupole magnetic gradient field (~ 10 G/cm) is provided by a pair of anti-Helmholtz coils which are symmetrically placed around the capture center.

The selection system is composed of a microwave antenna (~ 10 mm) fed by a 9.192 631 770 GHz signal to induce an $F = 4, m_F = 0 \rightarrow F = 3, m_F = 0$ transition, and a push laser beam. The antenna is placed horizontally nearby the observation window. The push beam is the vertical, downward capture laser beam.

2.7 The detection zone

The detection zone is situated 15 cm below the capture center (see figure 2.7). Three laser beams and two low-noise photodiodes are used in the detection process (see figure 2.8). Two laser beams are red de-tuned by about $\Gamma/2$ from the $\nu_{45'}$ resonance in order to induce the fluorescence of atoms which rest in the state $|F = 4\rangle$. The detuning avoids heating of the detected atoms along the lasers direction. The intensity of each beam is about 0.6 W/cm². The rectangular cross-section of the laser beams sheets has a height of 8 mm and a width of 14 mm. The separation between the sheets is 15 mm and the

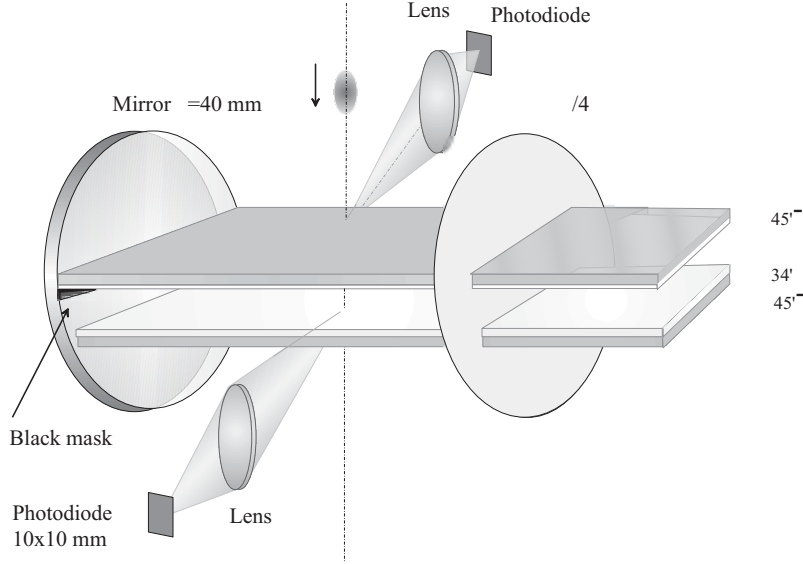


Figure 2.8: *Principle of the atomic hyperfine state detection.*

beams are σ^+ polarized. The third beam tuned to $\nu_{34'}$ is placed 2 mm above the lower beam. This sheet has a height of 2 mm and a width of 14 mm. Its intensity is about $5 \mu\text{W}/\text{cm}^2$. All three beams are retroreflected by a mirror to create standing waves.

The lower part of the upper beam (height about 2 mm) is a travelling wave realized by putting a black mask onto the mirror. This travelling wave pushes away the atoms in state $|F = 4\rangle$ that have been detected. The remaining atoms which are in state $|F = 3, m_F = 0\rangle$ are then optically pumped to the state $|F = 4\rangle$ by the beam $\nu_{34'}$. Finally, the number of atoms originally in the state $|F = 3, m_F = 0\rangle$ is measured as before.

Two condenser lenses gather the photon fluorescence (the solid angle of the collection optics is 0.09 rad) with an efficiency of 0.7%. $n_{\text{photon}} \approx 150$ photons per atom are detected. The photodiode (with a sensitivity of 0.55 A/W at 852 nm) signals are amplified and digitized by the computer. The computer calculates the time-integrated fluorescence pulse signals S_4 and S_3 (see fig. 2.9) and derives the transition probability

$$P = \frac{S_4}{S_4 + S_3}. \quad (2.9)$$

This normalization procedure rejects the transition probability noise due to shot-to-shot fluctuations in the captured atom number. These fluctuations amount typically to about 3%. The transition probability measured in each fountain cycle is used for the frequency stabilization of the interrogation oscillator.

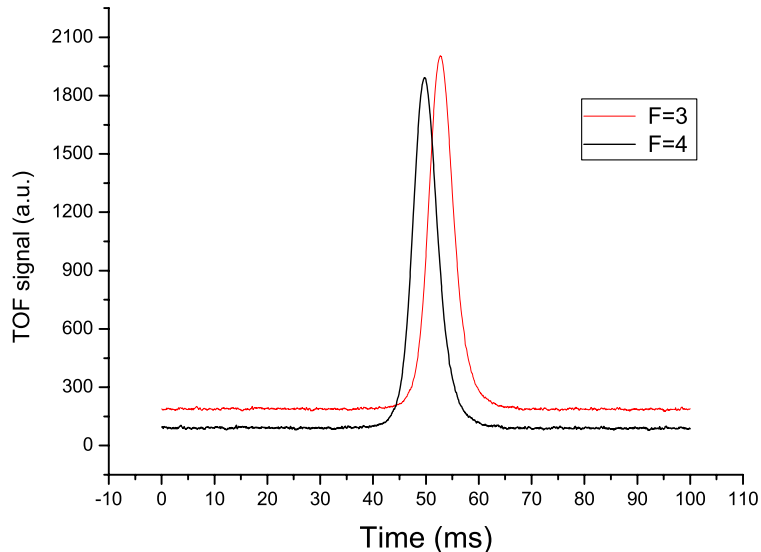


Figure 2.9: *Time of flight signals: the integration of each curve represents the number of detected atoms.*

2.8 Microwave frequency synthesis chain

The phase noise of the interrogation signal in the range $1 \sim 10$ Hz degrades the frequency stability of the fountain clock via the “Dick effect” [41]. In order to minimize this effect, we chose a state-of-the-art room-temperature oscillator: the 10 MHz quartz oscillator (BVA, Oscilloquartz). The principle of the frequency synthesis chain is presented in fig. 2.10. We multiply the 10 MHz signal up to 100 MHz using a low noise phase lock loop circuit and a voltage controlled 100 MHz quartz oscillator (VCXO 100 MHz). This phase lock filters out the white phase noise floor of the BVA oscillator. The 100 MHz signal is then doubled and used to drive the LO port of a sampling mixer. This device acts as an harmonic mixer, producing a beat-note signal between the 23^{rd} harmonic of the 200 MHz signal and the output of a dielectric resonator oscillator (DRO) at 4.59 GHz. This beat-note is then low-pass filtered and mixed with the frequency divided (factor 16) output of a low phase noise synthesizer. The mix output is used to phase lock the DRO with a bandwidth of about 200 kHz. In this way, we produce a low phase noise tunable microwave source at half of the clock frequency. This signal is frequency doubled to obtain about -20 dBm of 9.192 631 770 GHz signal.

If we phase lock an oscillator operating at 9.192 6 GHz to provide the

2.8. MICROWAVE FREQUENCY SYNTHESIS CHAIN

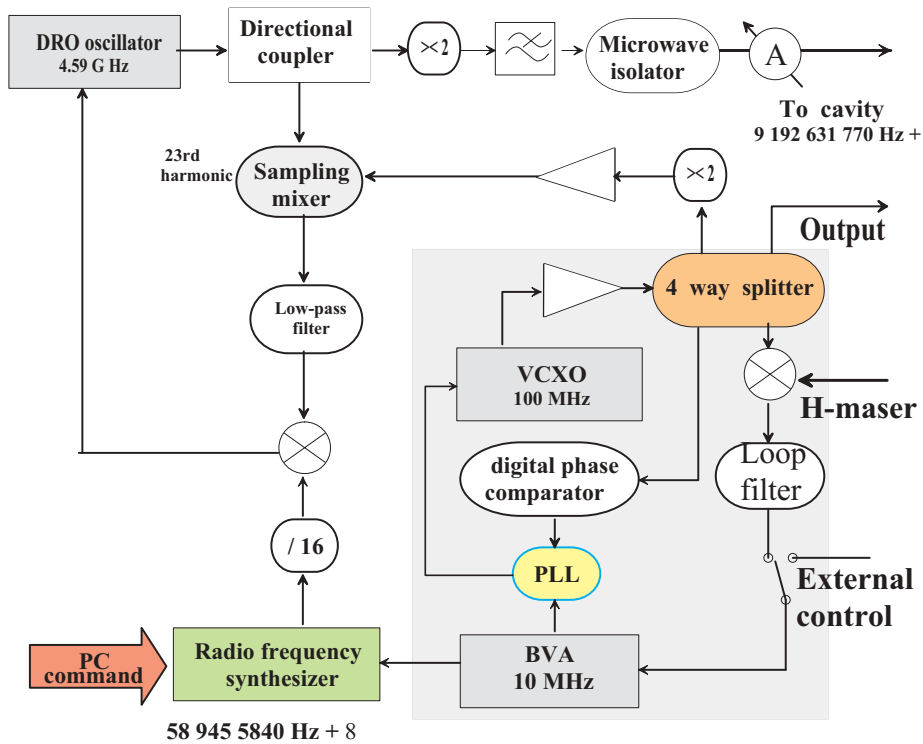


Figure 2.10: Block diagram of the interrogation frequency synthesis chain of FO1.

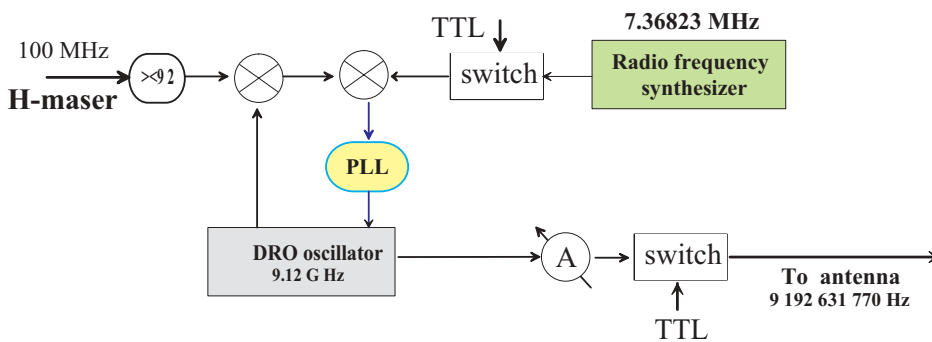


Figure 2.11: Block diagram of the frequency synthesis chain for the state selection in FO1.

microwave interrogation signal, we would increase the microwave leakage by about 30 dB. A variable microwave attenuator is used to prepare the -60 dBm signal typically necessary to probe the atoms. The synthesizer (with a resolution of 1 mHz) is synchronized on the 10 MHz signal from the BVA oscillator. Its frequency is controlled by the computer. The frequency resolution ($1 \div 16 \times 2$ mHz) of the interrogation signal is about 1.4×10^{-14} . This resolution⁵ is good enough comparing to the current fountain stability at 1 cycle ($\sim 1 \times 10^{-13}$).

The state selection needs a microwave signal at 9.192 GHz to induce a π -pulse on the atomic sample.

In principle we could use the same signal generated for the interrogation. As the preparation microwave pulse is radiated with an antennae, we need about 20 dBm of signal power. To avoid microwave leakage, we need to switch off the signal with more than 200 dB of attenuation, which is extremely difficult to realize. Using a second microwave generator described in fig. 2.11, we are able to switch off and frequency de-tune (a few MHz) the microwave signal in order to reach the required extinction ratio for the preparation signal.

The requirements for this synthesizer are less stringent than for the interrogation signal. The signal used to supply the antenna comes from a DRO operating at 9.192631 GHz. The frequency of the DRO is phase locked to the 92nd harmonic of a 100 MHz signal of the H-Maser via an external frequency synthesizer (6061A, Fluke). A TTL signal drives a microwave switch to reduce the output power by about 90dB and a RF switch to turn off the 6061A external synthesizer signal. This signal also drives the detuning of the DRO central frequency.

Finally, to study the performance of the fountain, the BVA quartz oscillator is phase locked to an H-maser with a bandwidth of 0.1 Hz.

2.9 Fountain performance

In the previous paragraphs, we have described all the sub-systems necessary for operation of the fountain. We now present the experimental results of the fountain and discuss the influence of the different parameters which contribute to the clock performance.

After launching, we can obtain 10^8 atoms in MOT operation or 10^7 atoms by directly using an optical molasses. In both cases, the rms velocity is 0.8

⁵Referencing to [56], the rms value of this quantization error $\sigma_\nu \simeq 0.29 \times 1/8$ mHz. This induces a standard deviation of the transition probability at half maximum $\sigma_P < 6 \times 10^{-5}$. According to the study in section 2.9.1, this value corresponds to a frequency stability of the fountain $\sigma_y(\tau = T_c) < 4 \times 10^{-15}$ at 1 cycle.

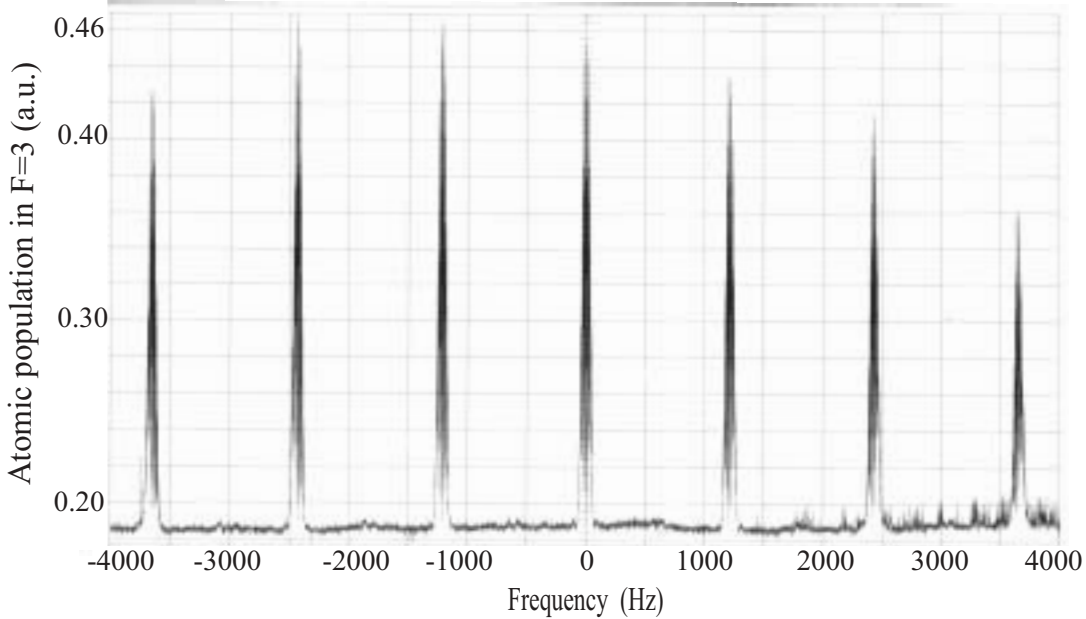


Figure 2.12: *Microwave spectrum of Cs without selection: 7 σ transitions and 9 π transitions.*

cm/s as deduced from the width of the TOF signal.

After launching, the atoms are distributed among the 9 sub-levels of the $F=4$ state. To determine the population distribution, we scan the frequency of the microwave interrogation signal and record the $F=3$ population. As shown in figure 2.12 we obtain the seven $\Delta m_F = 0$ resonances. From this figure we deduce that 10% of the atoms are in the state $F = 4, m_F = 0$. As the atoms in $m_F \neq 0$ levels do not contribute to the clock signal but instead they degrade frequency stability and accuracy, we perform a state selection process. Figure 2.13 shows the transition probabilities when the selection is active. We note that the selection is very efficient, since the population of $m_F \neq 0$ is less than 2%. We can also see that there is a tiny signal (signal (1) inside the inset of figure 2.13) close to the transition $\Delta m_F = 1$. The transition probability is null in the center of the line. This is due to a π phase change of the transverse component of the magnetic field between the two cavity ends. This also shows that there is no real $\Delta m_F = 1$ resonance and allows us to conclude that the C-field is well aligned with the cavity axis.

With this selection function, we can easily calculate the transition probability from the TOF detected signals. It is given by

$$P = \frac{N_4}{N_3 + N_4} = \frac{S_4}{S_3 + S_4} \quad (2.10)$$

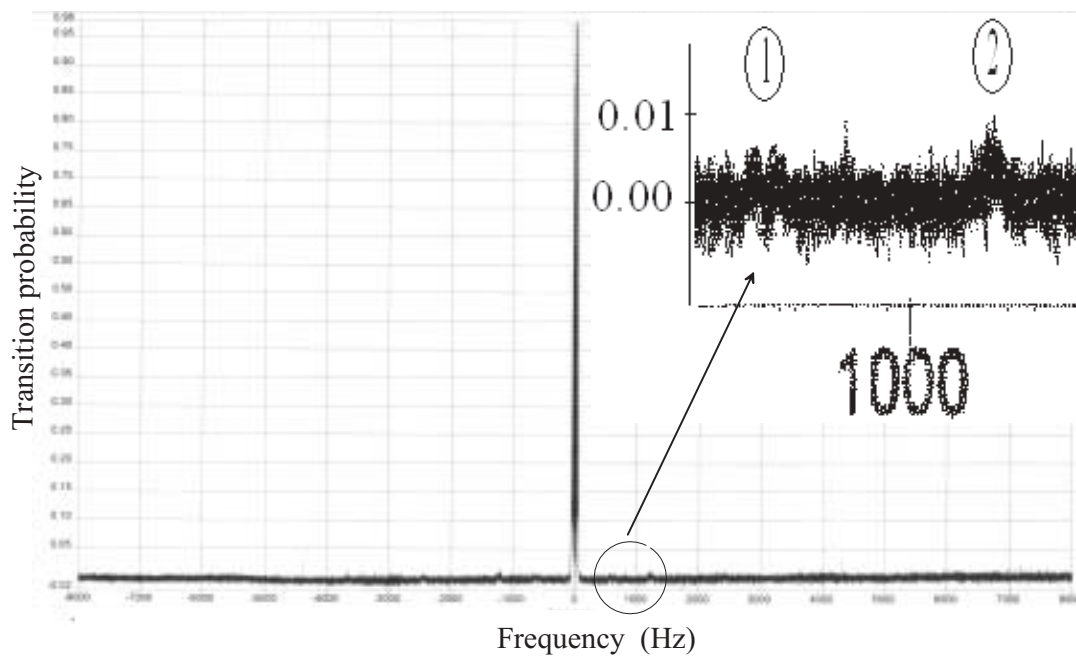


Figure 2.13: *Population distribution after the selection was carried out. The central peak represents the transition $F = 3, m_F = 0 \rightarrow F = 4, m_F = 0$. The enlarged inset shows (1) π transition of $F = 3, m_F = 0 \rightarrow F = 4, m_F = 1$ and (2) σ transition of $F = 3, m_F = 1 \rightarrow F = 4, m_F = 1$.*

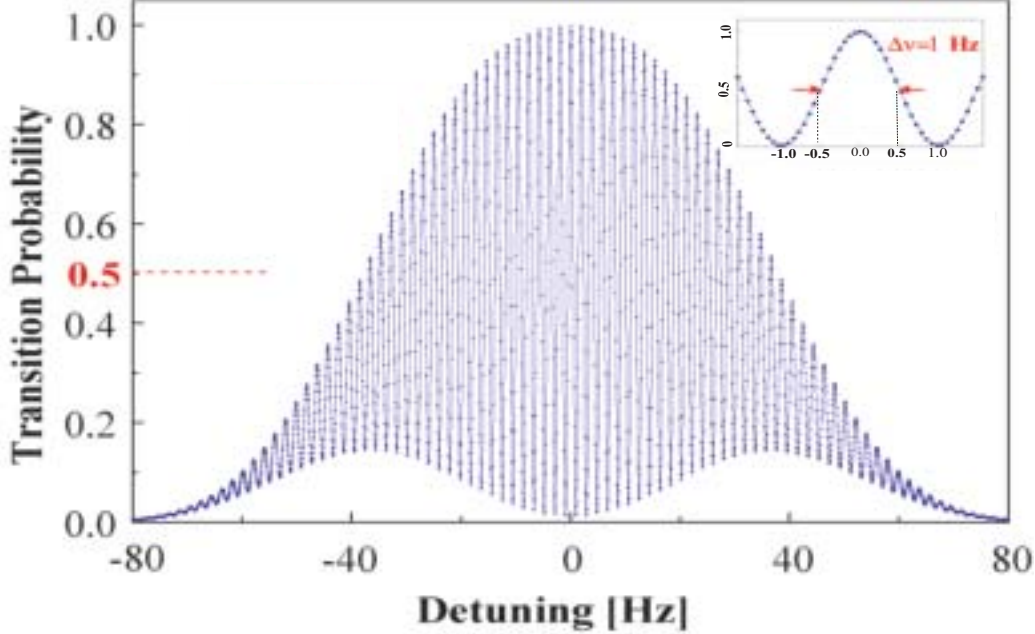


Figure 2.14: *Ramsey fringes from the fountain clock FO1: the central fringe is 1 Hz wide. The points were obtained from a single scan. The inset is the central Ramsey fringe, the transition probability is measured alternately at $\nu_{at} \pm \Delta\nu/2$, where $\Delta\nu$ is the linewidth. The difference between two successive measurement cycles of the transition probability constitutes the error signal of the atomic clock.*

where S_3 and S_4 , the time integrals of the TOF fluorescence pulse signal induced by the detection beams, are proportional to the number of the detected atoms in levels $|3, 0\rangle$ and $|4, 0\rangle$, respectively. The behavior of the transition probability as a function of the microwave frequency is shown in fig. 2.14. We obviously obtain a Ramsey pattern which contains about 60 fringes corresponding to the ratio T/τ , where $T = 0.5$ s is the atomic ballistic flight time above the cavity and τ is the time the atoms spend inside the cavity. The microwave signal amplitude is set to the optimum value $b\tau = \pi/2$. When the detuning between the atomic resonance and the microwave field is not zero, the transition probability depends on the atomic velocity. As the rms atomic velocity is about 1 cm/s, the contrast of the fringes varies with the detuning. The central fringe has a full width of 1 Hz at half maximum.

2.9.1 Frequency stability

In order to lock the frequency of the interrogation microwave signal to the central fringe, the frequency of the microwave signal is square-wave modulated with a period of $2T_C$ (T_C is the cycle time) and the transition probability is synchronously measured. The frequency corrections are calculated in the following way:

$$\delta\nu_{k+1} = \delta\nu_{k-1} + (-1)^k G(P_k - P_{k-1}) \quad (2.11)$$

where G is the loop gain and k is the cycle number. The signal-to-noise ratio is optimized when the modulation amplitude is equal to the resonance half width ($1/4T$). In standard operation, the 10 MHz BVA oscillator is phase locked on a H-maser signal. The modulation and frequency corrections are then applied to the radio frequency synthesizer (see fig. 2.10). In this configuration the frequency correction represents the frequency offset between the H-maser and the fountain clock.

The Allan variance calculated from the frequency corrections characterizes the stability of the fountain clock versus the H-Maser. According to the study in [47], the frequency stability of the fountain clock can be expressed as:

$$\sigma_y(\tau) = \frac{1}{\pi Q_{at}} \frac{\sigma_P}{P} \sqrt{\frac{T_c}{\tau}} \quad (2.12)$$

where the integration time τ is longer than the servo time constant (a few cycle times T_c), and σ_P is the standard deviation of the transition probabilities⁶. We present in the following the different sources of noise which contribute to the value of σ_P .

Detection noise

According to equation (2.10) the fluctuation of the transition probability P can be written as

$$\delta P = \frac{(1 - P)\delta N_4 - P\delta N_3}{N_{det}} \quad (2.13)$$

where N_{det} is the total number of the detected atoms. Here $P = 1/2$, thus

$$\frac{\delta P}{P} = \frac{1}{2} \frac{\delta N_4}{N_4} - \frac{1}{2} \frac{\delta N_3}{N_3} \quad (2.14)$$

⁶Strictly speaking, the expression (2.12) is true if transition probability noise is white.

where δN_3 (or δN_4) is the fluctuations of the atom number detected in the state $|F = 3, m_F = 0\rangle$ (or $|F = 4, m_F = 0\rangle$). For shot-to-shot fluctuations on the initial number of cold atoms, $\delta N_3 = \delta N_4$ when the state selection is performed. Consequently, σ_P is independent of these fluctuations.

The quantum projection noise

After interrogation, the atoms are in the superposition of the two states $F = 4, m_F = 0$ and $F = 3, m_F = 0$: $|\psi\rangle = c_4|4, 0\rangle + c_3|3, 0\rangle$, where $|c_3|^2 + |c_4|^2 = 1$. The probability to find an atom in the state $|4, 0\rangle$ is given by

$$P = P_{|4,0\rangle} = \langle \psi | \mathbf{P}_{|4,0\rangle} | \psi \rangle = \langle \psi | 4, 0 \rangle \langle 4, 0 | \psi \rangle = |c_4|^2 \quad (2.15)$$

where $\mathbf{P}_{|4,0\rangle}$ is the probability projection operator onto the state $|4, 0\rangle$. The variance of transition probability is given by

$$\sigma_P^2 = \langle (P_{|4,0\rangle} - \langle P_{|4,0\rangle} \rangle)^2 \rangle = \langle P_{|4,0\rangle}^2 \rangle - \langle P_{|4,0\rangle} \rangle^2 = P(1 - P) \quad (2.16)$$

For N_{det} uncorrelated atoms detected, the standard deviation of the transition probability is induced

$$\frac{\sigma_P}{P} = \frac{\sqrt{P(1 - P)/N_{det}}}{P} \quad (2.17)$$

For the usual operating conditions $P = 1/2$:

$$\frac{\sigma_P}{P} = 1/\sqrt{N_{det}} \quad (2.18)$$

This quantum projection noise (QPN) [48] is the foundational limit of the fountain frequency stability.

Technical noise

There also exists the effect of the uncorrelated (or partial) noise between the population measurements of the two atomic states. The variance of the transition probability P can be written as

$$\sigma_P^2 = \left(\frac{\partial P}{\partial N_4} \right)^2 \sigma_{N_4}^2 + \left(\frac{\partial P}{\partial N_3} \right)^2 \sigma_{N_3}^2 \quad (2.19)$$

for our case, $P = 1/2$,

$$\frac{\sigma_P}{P} = \sqrt{\left(\frac{\sigma_{N_4}}{2N_4} \right)^2 + \left(\frac{\sigma_{N_3}}{2N_3} \right)^2} \quad (2.20)$$

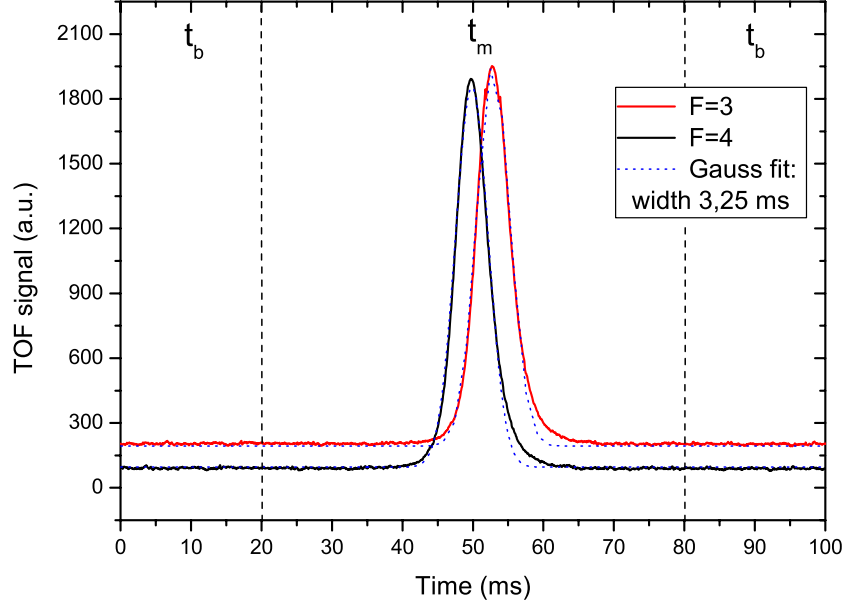


Figure 2.15: *Time of flight signals. The integration of each curve represents the number of detected atoms.*

One uncorrelated noise source is the photon shot noise. The population of both atomic states is deduced from the fluorescence signals. When we detect N_{photon} photons, the noise is given by

$$\sigma_{N_{\text{photon}}} = \sqrt{N_{\text{photon}}} = \sqrt{n_{\text{photon}} \cdot N_{\text{det}}} \quad (2.21)$$

and thus

$$\frac{\sigma_{P_{\text{shot}}}}{P} = 1/\sqrt{N_{\text{photon}}} = 1/\sqrt{n_{\text{photon}} \cdot N_{\text{det}}} \quad (2.22)$$

where n_{photon} is the number of detected photons per atom during the detection process. In FO1, as we detect about 150 photons per atom, the photon shot noise contribution is negligible compared with the QPN. Some noise results from fluctuations of each TOF signal. The TOF acquisition signals are divided into three parts as shown in fig. 2.15. The maximum of the cold atom fluorescence is adjusted in the center of the acquisition window. The signal offset is calculated by using the extreme parts (duration $2t_b$) of the TOF. Its fluctuations result from the electronic noise of the detection system, the stray light, and the thermal caesium beam. The TOF integration signal

after eliminating the contribution of the baseline at each fountain cycle is obtained by

$$\begin{aligned}
 S_{TOF} &= \int_{t_b}^{t_b+t_m} v(t)dt - \frac{t_m}{2t_b} \left(\int_0^{t_b} v(t)dt + \int_{t_b+t_m}^{2t_b+t_m} v(t)dt \right) \\
 &= \int_{-\infty}^{+\infty} v(t)h(t)dt
 \end{aligned} \tag{2.23}$$

where $v(t)$ is the detected signal, and the function $h(t)$ is defined as

$$h(t) = \begin{cases} 0, & t < 0 \\ -\frac{t_m}{2t_b}, & 0 \leq t < t_b \\ 1, & t_b \leq t < t_b + t_m \\ -\frac{t_m}{2t_b}, & t_b + t_m \leq t \leq 2t_b + t_m \\ 0, & t > 2t_b + t_m \end{cases} \tag{2.24}$$

In the frequency domain, its Fourier transform is given by

$$\begin{aligned}
 H(f) &= \int_{-\infty}^{+\infty} h(t)e^{-i2\pi ft} dt \\
 &= \frac{1}{\pi f} \left\{ \left(1 + \frac{t_m}{2t_b}\right) \sin(\pi f t_m) - \frac{t_m}{2t_b} \sin[\pi f(t_m + 2t_b)] \right\}
 \end{aligned} \tag{2.25}$$

Fig. 2.16 represents the function $|H(f)|^2$. Experimentally, we chose $t_m = 60$ ms and $t_b = 20$ ms. The atomic state population measurement is then mainly sensitive to noise in a bandwidth of 30 Hz centered around 15 Hz. In this way, the 50 Hz component and the harmonics are completely rejected.

A better filter is to take the matched function: we use a Gaussian or Lorentzian shape to fit the TOF signal in each fountain cycle and calculate the transition probability. The experimental results shown in fig. 2.17 indicate that the noise level is always lower. For a number of the detected atoms larger than 2×10^5 they coincide.

1. Detection electronics noise To measure the fluorescence signal, we use two photo diodes (Hamamatsu S1337-1010BR. They have a sensitivity of 0.5 A/W and a noise level (NEP) of 8.2×10^{-15} A/ $\sqrt{\text{Hz}}$. The signal is amplified by an OPA637 (Burr-Brown) with a gain of 10^8 V/A and a bandwidth of 1.5 kHz before to be digitized with 12bit resolution and a sampling rate of 2 kHz. The noise of this system has been measured (with neither laser beam nor caesium atoms) at a level of 2×10^{-6} V/ $\sqrt{\text{Hz}}$ which corresponds to 180 detected atoms. For the usual fountain operation this noise is negligible when several 10^5 atoms are detected.

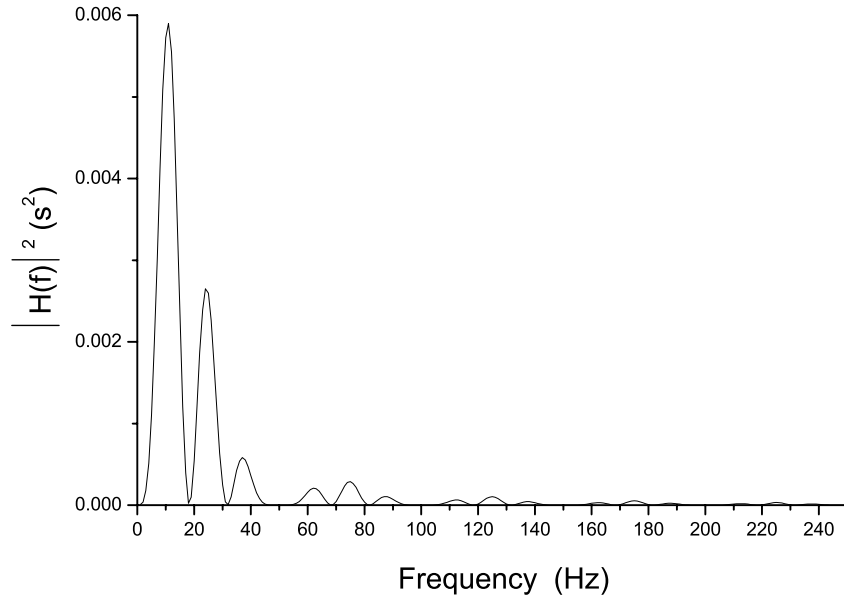


Figure 2.16: *The equivalent filter function of the detection system for electronic noise.*

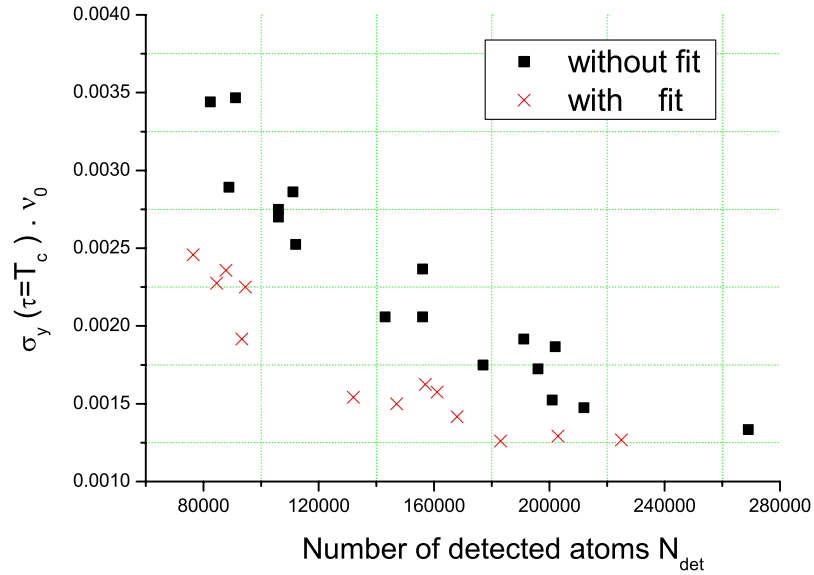


Figure 2.17: *Results of a Gaussian or Lorentzian shape filter used to fit the TOF signals. The fitted points always are below the unfitted ones when the number of detected atoms N_{det} is small.*

2. Noise due to stray light and thermal beam Some possible scattered light and its instability cause a fluctuation of the baseline. We measure this noise by tuning the detection laser beams far away from the caesium resonance. The difference in caesium vapor pressure between the zones of capture and detection produces a weak caesium atomic beam. The uncorrelated rms fluctuation of the number of atoms per detection channel corresponds to about 85 atoms per fountain cycle.

3. Laser noise The transition probability is measured by the fluorescence emitted by the atoms when they pass through the detection beams. The spontaneous emission rate is expressed by [40]

$$\gamma = \frac{\Gamma}{2} \frac{I/I_s}{1 + I/I_s + (2\Delta\omega/\Gamma)^2}. \quad (2.26)$$

The detection laser noise in intensity I and frequency detuning $\Delta\omega$ cause a fluctuation of the photon emission rate $\delta\gamma$, and thus fluctuations of the number of detected atoms. A filter connected with the amplifier is used to reject the high-frequency fluctuations above 1.5 kHz. We experimentally optimize the re-pumping laser beam⁷ power to saturate the transition in order to minimize the laser noise (but the laser power has to be low enough to minimize the stray light). When neglecting the influence of the repumping laser beam, we have

$$\delta N_4 = N_4 \int_{t_{det}} \delta\gamma(t) f(t) dt \quad (2.27)$$

$$\delta N_3 = N_3 \int_{t_{det}} \delta\gamma(t) f(t - \Delta t) dt \quad (2.28)$$

where t_{det} is the detection time and Δt is the time interval between the two TOF signals, and $f(t)$ is the profile of the TOF signal (see figure 2.15) which depends on the detection laser beam shape, on the spatial distribution and on temperature of the detected atoms. Its profile is very close to a Gaussian function

$$f(t) = \frac{1}{\sqrt{\pi}t_w} e^{-\frac{t^2}{t_w^2}} \quad (2.29)$$

where t_w is the $1/e$ half-width. The detection laser $F = 4 \leftrightarrow F' = 5$ beams are identical in our detection set-up. According to equation (2.14),

⁷which repumps the atoms from $F = 3$ into $F = 4$ after they have crossed the first detection laser beam.

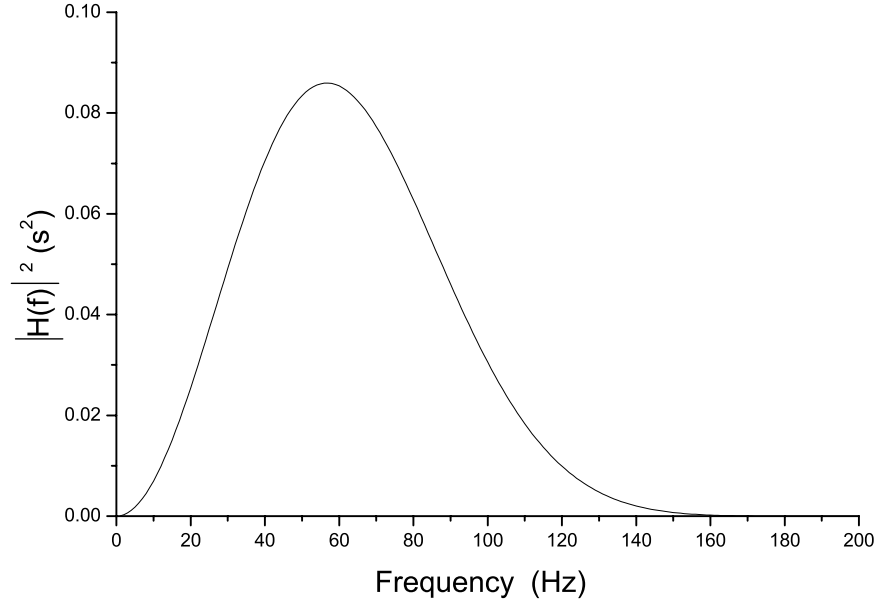


Figure 2.18: *The equivalent filter function of the detection system for the detection laser noise.*

the transition probability fluctuation around $P = 1/2$ can be written as

$$\begin{aligned}\delta P &= \frac{1}{4} \int_{t_{det}} \delta\gamma(t) \left[f(t) - f(t - \Delta t) \right] dt \\ &= \int_{t_{det}} \delta\gamma(t) h(t) dt.\end{aligned}\tag{2.30}$$

The Fourier transfer function $H(f)$ of $h(t)$ is expressed by

$$H(f) = \frac{1}{4} e^{-\pi^2 f^2 t_w^2} (1 - e^{-i2\pi f \Delta t}).\tag{2.31}$$

Figure 2.18 represents the transform function $|H(f)|$ with the typical parameters $\Delta t = 4$ ms and $t_w = 3.2$ ms.

We suppose that the fluctuations of the relative frequency noise $S_y(f)$ and the relative intensity noise $S_{\delta I/I}(f)$ are uncorrelated. The spectral density of the fluctuation of the photon emission rate $S_{\delta\gamma}(f)$ in the fountain is given by

$$S_{\delta\gamma}(f) = \left(\frac{2\omega_{laser}}{\Gamma} \right)^2 S_y(f) + S_{\delta I/I}(f).\tag{2.32}$$

The detection laser is an extended cavity semiconductor laser (ECL) using a grating. The white frequency noise is $S_y(f) = 3.2 \times 10^{-25} \text{ Hz}^{-1}$ for $f < 1$

Hz [57], its contribution to the fountain stability is $\sigma_y(\tau = T_c) < 10^{-14}$. In FO1, $S_{\delta I/I}(f) \leq 10^{-7}/f \text{ Hz}^{-1}$, thus the fountain stability limitation is $\sigma_y(\tau) \leq 1 \times 10^{-14} \sqrt{\frac{T_c}{\tau}}$ due to only this noise. Finally, we can conclude that the limitation on fountain frequency stability due to the detection laser noise can be neglected at the level of $10^{-13} \tau^{-1/2}$.

Interrogation oscillator noise

The periodic operation of the fountain induces frequency down-conversion of LO frequency noise for multiple frequencies of $1/T_c$. This phenomenon is called the *Dick effect* [41, 46, 47]. The Allan variance contribution of the interrogation oscillator noise is related to the frequency noise spectral density of the free running oscillator and to the harmonic content of the sensitivity function $g(t)$ (see formula (B.29) in appendix B)

$$\sigma_y^2(\tau) = \left(\sum_1^{\infty} \frac{g_n^2}{g_0^2} S_y^{LO}(nf_c) \right) \frac{1}{\tau} \quad (2.33)$$

where

$$g_n = \frac{1}{T_c} \int_0^{T_c} g(t) e^{i2\pi n f_c t} dt \quad (2.34)$$

is the Fourier coefficient associated with $g(t)$ at the frequency $n f_c \equiv n (1/T_c)$, and $S_y^{LO}(nf_c)$ is the single-side power spectral density of the relative frequency noise of the free running oscillator at the frequency $n f_c$ (central frequency is ν_0).

Fig. 2.19 shows the first 1000 coefficients $(g_n/g_0)^2$ versus the rank n for the function $g(t)$ in the Ramsey interrogation scheme for three cases: $b\tau = \pi/2$, which provides the optimal interrogation condition, $b\tau = 3\pi/2$, and $b\tau = 5\pi/2$. The calculation is done for the case of a typical operation cycle of our fountain ($\tau = 0.017 \text{ s}$, $T = 0.5 \text{ s}$, $T_c = 1.2 \text{ s}$, and $\Omega_0 = -\pi \Delta\nu_{\text{Ramsey}}$). Approximately, for $b\tau = \pi/2$, $(g_n/g_0)^2$ decreases as n^{-2} until $n = T/\tau \sim 30$, whereafter it decreases as n^{-4} .

The noise spectral density of an oscillator can be represented by a sum of five terms [55]:

$$S_y^{LO}(f) = \sum_{\alpha=-2}^2 h_\alpha f^\alpha \quad (2.35)$$

where the integer α characterizes the noise type: $\alpha = -2, -1, 0, 1, 2$ corresponds to random walk of frequency, flicker frequency noise, white frequency noise, flicker phase noise, and white phase noise, respectively.

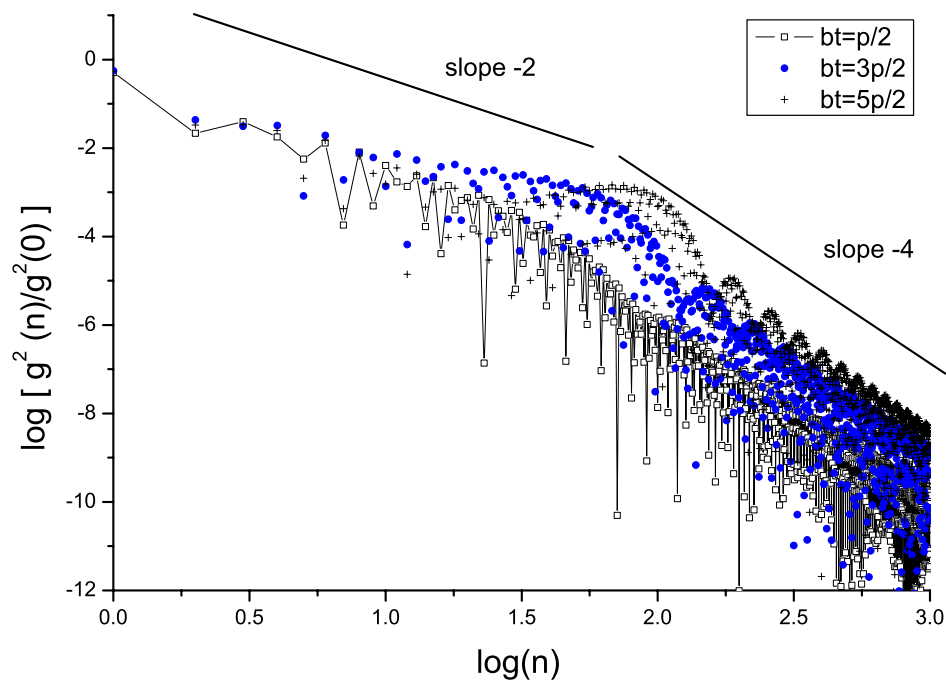


Figure 2.19: Down-conversion coefficients $(g_n/g_0)^2$ versus the rank n for the function $g(t)$ in three Ramsey interrogation cases: $b\tau = \pi/2$, $b\tau = 3\pi/2$, and $b\tau = 5\pi/2$, with $T_c = 1.2$ s, $T=0.5$ s, and $\tau = 17$ ms.

Table 2.1: Degradation of Allan variance for five types of noise with different Ramsey interrogation power. We have normalized the contributions of each noise type to the case $b\tau = \pi/2$.

$b\tau$	$\alpha = +2$	$\alpha = +1$	$\alpha = 0$	$\alpha = -1$	$\alpha = -2$
$\pi/2$	1	1	1	1	1
$3\pi/2$	10	3	1	1	1
$5\pi/2$	26	4	1	1	1

For the clock evaluation, it is very useful to change the microwave power in order to amplify some systematic effects (Doppler, microwave spectrum, ...). Table 2.1 lists the power dependence of the Allan variance degradation for each type of noise. We find a strong dependence when the noise character α is larger than 0.

The measurement of the spectrum of the state-of-the-art quartz oscillator shows that:

$$S_y^{Lo}(f) = 1.94 \times 10^{-29} f^2 + 2.13 \times 10^{-27} f + 1.06 \times 10^{-26} f^{-1}. \quad (2.36)$$

The phase noise below a few hertz is determined mainly by the flicker frequency noise. With this condition, the standard deviation can be expressed using the first coefficient $g(1)$:

$$\sigma_y(\tau) \simeq \sqrt{h_{-1}} \left| \frac{g_1}{g_0} \right| \sqrt{\frac{T_c}{\tau}}, \quad (2.37)$$

where g_1/g_0 can be expressed as a function of the duty cycle $d = T/T_c$: $g_1/g_0 \simeq \sin(\pi d)/\pi d$. Typically the FO1 duty cycle is $d = 0.42$ (for $T_c = 1.2$ s).

The calculated contribution of the quartz noise to the fountain stability is 8.4×10^{-14} at 1 s, which corresponds to a quantum projection noise of 1.74×10^5 detected atoms.

By taking into account the main sources of noise, we can express the Allan standard deviation of the relative frequency fluctuations of a fountain :

$$\sigma_y(\tau) = \left[\frac{T_c}{\pi^2 Q_{at}^2} \left(\frac{1}{N_{det}} + \frac{\sigma_{\delta N_4}^2}{N_{det}^2} + \frac{\sigma_{\delta N_3}^2}{N_{det}^2} + \sigma_{laser} \right) + \sum_1^{\infty} \frac{g_n^2}{g_0^2} S_y^{LO} \left(\frac{n}{T_c} \right) \right]^{1/2} \tau^{-1/2} \quad (2.38)$$

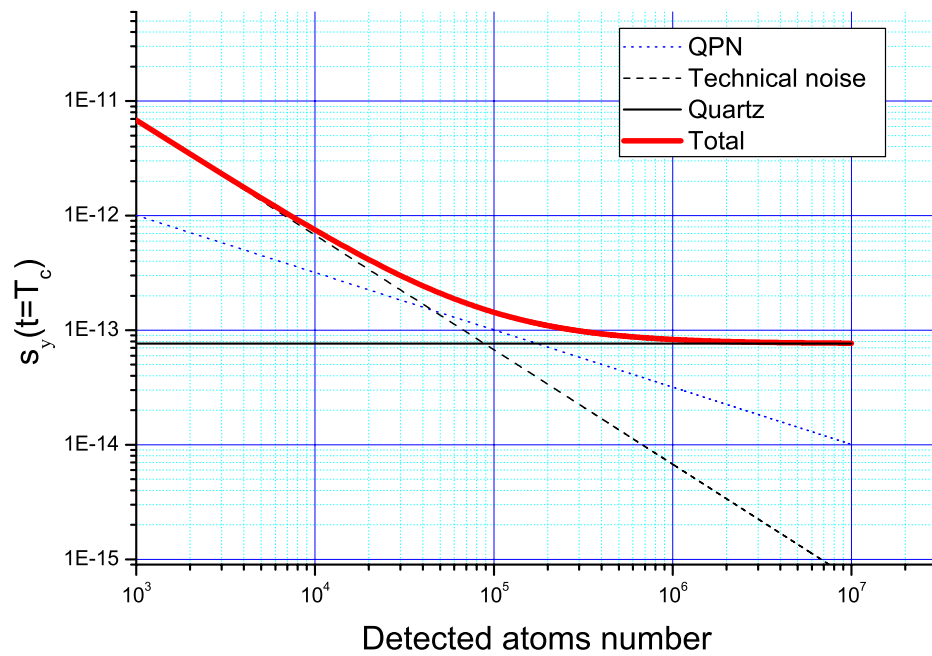


Figure 2.20: *Estimated frequency stability at $\tau = T_c$ versus the number of the detection atoms.*

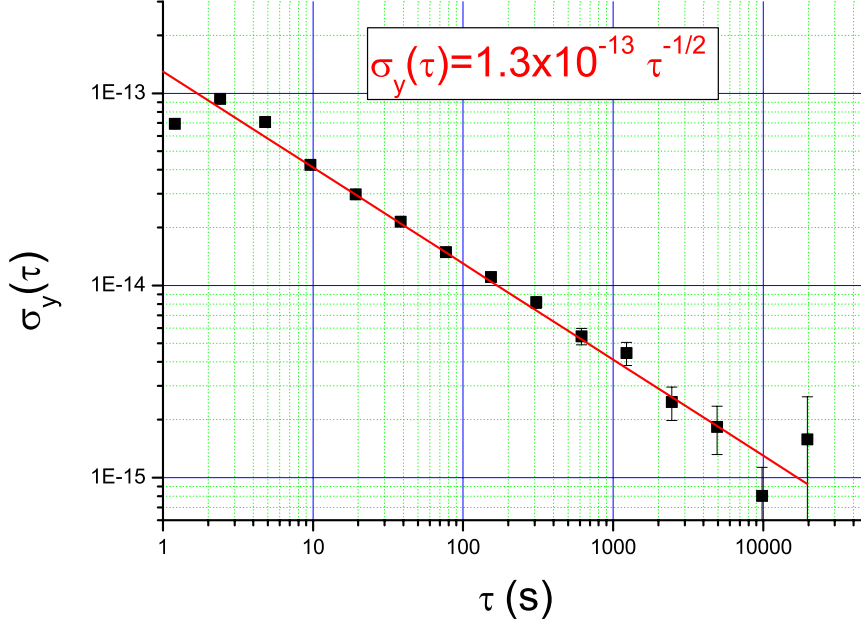


Figure 2.21: Frequency stability of the fountain clock FO1 with 3×10^5 detected atoms when a BVA quartz is used as local oscillator.

where $\sigma_{\delta N_4}$ and $\sigma_{\delta N_3}$ represent the expected effect of the technical noise of the detection system. Figure 2.20 shows the influence of each noise on the fountain frequency stability. We can find that when the number of the detected atoms is less than 10^4 the technical noise is dominant, and when the number of the detected atoms is larger than 2×10^5 , the fountain stability is limited by interrogation oscillator noise. Typically, when $N_{det} = 3 \times 10^5$, the measured frequency stability is $1.3^{-13} \tau^{-1/2}$ when we use the BVA quartz oscillator (see figure 2.21). This agrees with the predicted value of $1.1 \times 10^{-13} \tau^{-1/2}$.

2.9.2 Frequency accuracy

In this section we analyze the main systematic effects except the blackbody shift which will be studied in detail in chapter 5.

Table 2.2 shows the most recent (2002) accuracy budget of FO1. The fourth column describes the method used for determination of the error bars. In the following we describe these methods and discuss the results obtained.

Table 2.2: Relative frequency corrections and uncertainty budget of FO1 in 2002.

Effect	Correction [10 ⁻¹⁵]	Uncertainty [10 ⁻¹⁵]	Method
Quadratic Zeeman	adjustable	≤ 0.3	C-field map
Black-body radiation	17.6	≤ 0.3	DC Stark shift and direct measurement
Collisions + “cavity pulling” (molasses)	5	≤ 0.5	Changing the number of the captured atoms
Microwave recoil	0	< 0.3	Theory [58]
Microwave leakage	0	0.2	Microwave power
First-order Doppler	0	≤ 0.3	Microwave symmetry, fountain tilt, detection choice...
Microwave spectrum, synchronous perturbations	0	0.2	Microwave power and timing
Pulling by other lines	0	0.2	Microwave power and C-field
Background gas collisions	0	≤ 0.1	Theory [55]
<i>total</i>		0.9	
Second-order Doppler, and gravitational red shift	6.64	< 0.1	Launching height

Quadratic Zeeman effect

A C-field of 1.65 mG is applied to separate the seven $\Delta m_F = 0$ transitions. The frequency separation between the neighbouring transitions is then ~ 1.1 kHz (see figure 2.12). In figure 2.12 we can also see that the contrast of the fringes of the magnetic field sensitive transitions is better than 80%. This demonstrates that the average magnetic field for different atom trajectories differs by $\leq 1\mu\text{G}$. The C-field shifts the clock frequency via the quadratic Zeeman effect by

$$\delta\nu_{\text{Zeeman}} = \frac{427.45 \int_0^{T+2\tau} B^2(t) g(t) dt}{\int_0^{T+2\tau} g(t) dt} \quad (2.39)$$

where $B(t)$ is the static magnetic strength in Gauss at an instant t .

The evaluation for this shift requires a knowledge of the magnetic field

evolution seen by the atoms. This can be obtained by measuring the frequency of the first order field sensitive transition, such as $F = 4, m_F = 1 \leftrightarrow F = 3, m_F = 1$, as a function of the launching height ($\propto v_L^2$, where v_L is the launch velocity). A microwave radiation pulse of about 10 ms duration is applied (with an antenna placed at top of the fountain tube) and realizes a Rabi transition when the atoms are at their apogee (within ± 1 mm, see figure 2.22). This method can obviously not be performed when the atoms' apogee lies inside the microwave cut-off guide (6 cm length). An extra measurement is then performed by a Ramsey interrogation for different launching heights. The frequency of the central fringe contains the information of the time average magnetic field experienced by the atoms. However, it is difficult to identify confidently the central fringe when increasing the launching height (the Ramsey fringe number exceeds several tens). In order to overcome this problem, we modify the Ramsey fringe contrast by launching the cold atomic cloud at 3 different velocities (see figure 2.23). This launch is obtained by changing the frequency of the 4 horizontal capture beams by a small quantity Δf (a few tens of kilohertz). The velocity difference (can be clearly observed with the TOF signal) is $\Delta v = 2\pi\Delta f/k \sim 3$ cm/s, where, k is the wave vector. Figure 2.23 illustrates this method which allows the determination of the central fringe position (the highest contrast) with an uncertainty of a half fringe width.

Figure 2.22 shows the results of the magnetic field map measurement. A polynomial fit of this map is used to evaluate the Zeeman shift. For the launching velocities of 3.40 m/s and 2.89 m/s the calculated values are respectively 1160.32 Hz and 1161.40 Hz, and the corresponding measured values are 1160.88 Hz and 1162.18 Hz. They agree within 0.80 Hz. This small difference is mainly due to the atomic velocity distribution which was not taken into account in our calculation. The corresponding correction uncertainty is 1.6×10^{-16} for the clock transition frequency.

By locking the clock signal on the field sensitive transition, we never find a frequency stability worse than 4×10^{-12} over one day. In order to detect any magnetic field fluctuations due to a variation of room temperature (± 2 °C), we heated the fountain tube from 22 °C to 35°C and never found a frequency shift at a level of 1 Hz for the field sensitive transition.

By taking into account a slow (in several weeks) fluctuation⁸ of the uncontrolled magnetic field, a conservative Zeeman shift uncertainty has been set to 3×10^{-16} .

Atom number dependent frequency shifts

Two effects contribute to these shifts: cold atom collisions frequency shift

⁸In the improved FO1 described in chapter 6, we automatically measure the static magnetic field in every 15 minutes.

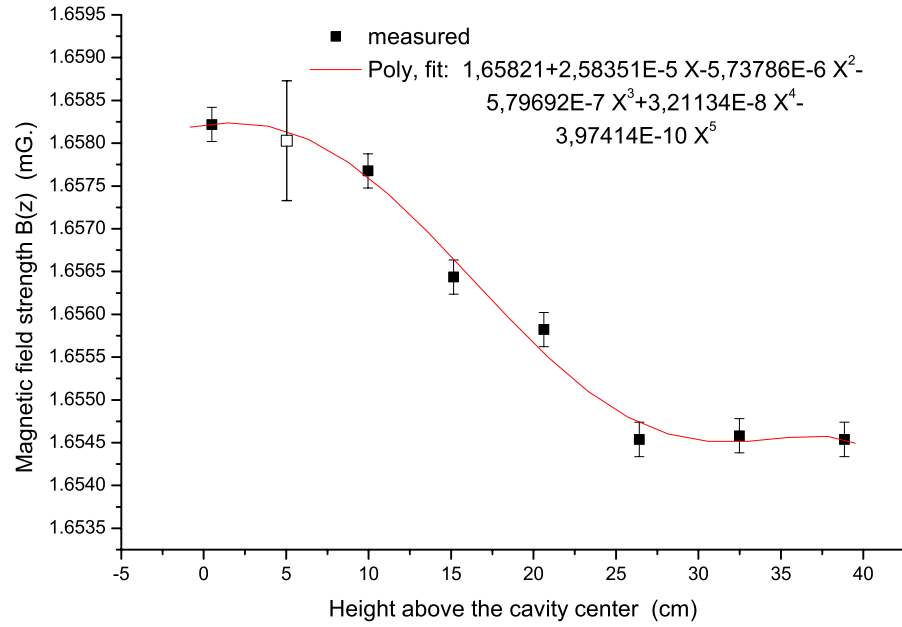


Figure 2.22: The magnetic field map measured by $F = 4, m_F = 1 \leftrightarrow F = 3, m_F = 1$ Rabi transition (■) and a Ramsey transition (□).

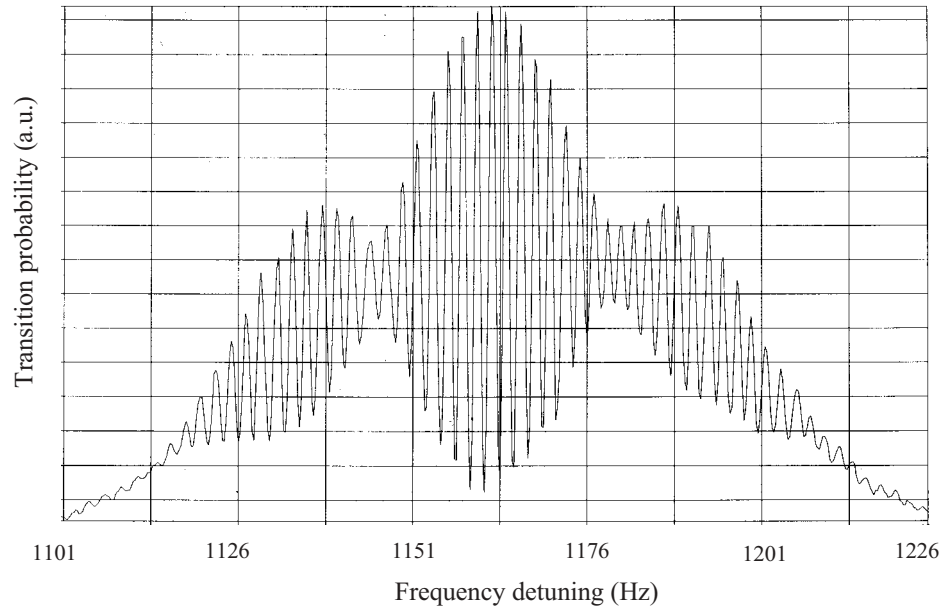


Figure 2.23: Modified Ramsey fringe ($m_F = 1 \leftrightarrow m_F = 1$ transition). The symmetry shows that the temporal average of the magnetic field strengths inside the cavity and inside the drift zone are almost equal.

and cavity pulling (due to the microwave interference inside the interrogation cavity [59]). As the maximum number of atoms crossing the cavity is less than 10^6 , the latter frequency shift⁹ is less than 3×10^{-16} . For the collisional effect, it is considered that only the *s*-wave scattering contributes to the collisional frequency shift and that the shift depends linearly on the average density of the atom cloud [42]. The atomic density can be varied by loading time and caesium source pressure. During each fountain operation we change the atomic densities every 512 fountain cycles. This method provides efficient rejection of slow frequency fluctuations which are not related to atom number or density, in particular the H-maser drift. Although we have a 50% uncertainty of the absolute determination of the atomic density, an extrapolation to zero density with only about 10% uncertainty can be carried out.

Microwave photon recoil

Absorption of a photon by an atom leads to a momentum change and an additional energy difference (kinetic, potential). The change of resonance due to the photon recoil is $\delta\omega/\omega_0 \simeq \hbar\omega_0/2mc^2 = 1.5 \times 10^{-16}$.

In a fountain, the atoms interacting with an electromagnetic standing wave inside the interrogation cavity are subjected to multiple photon processes: absorbing photons from one travelling wave component of the field and emitting them into another. A numerical simulation for Cs fountains using a MOT has been carried out Wolf, where the atomic velocity distribution is treated as Gaussian [58]. The result shows that the recoil shift is less than 3×10^{-16} .

Microwave leakage

The stray microwave radiation outside the cavity inside the fountain tube can be due to cavity leakage and microwave source (synthesizers) via feeding circuitry and optical feedthroughs. The spurious fields produce a clock frequency shift associated with Doppler effect. An estimation of the frequency shift would need knowledge of the field (direction, polarization, phase amplitude) everywhere along the atomic trajectories between the selection and the detection zones, which is not realistic. In a fountain, the almost symmetric atomic trajectory reduces much the induced shift. The shift is linearly dependent on the microwave amplitude [60]. When the cavity is feeded with high power (90 dB more than the normal operation) when the atoms are outside the cavity, no frequency shift is observed with a resolution of 1.5×10^{-15} . We conservatively estimate the relative uncertainty to be 2×10^{-16} .

First-order Doppler effect

⁹When the microwave power is $b\tau = \pi/2$, such that the shift $\Delta\nu_{cp} \cong 2.56 \cdot 10^{-12} \times N_{at} \delta\omega_c \Gamma_c / [\delta\omega_c^2 + (\Gamma_c/2)^2]$, where Γ_c is the cavity resonance width, $\delta\omega_c$ cavity detuning, and N_{at} the number of atoms crossing the cavity.

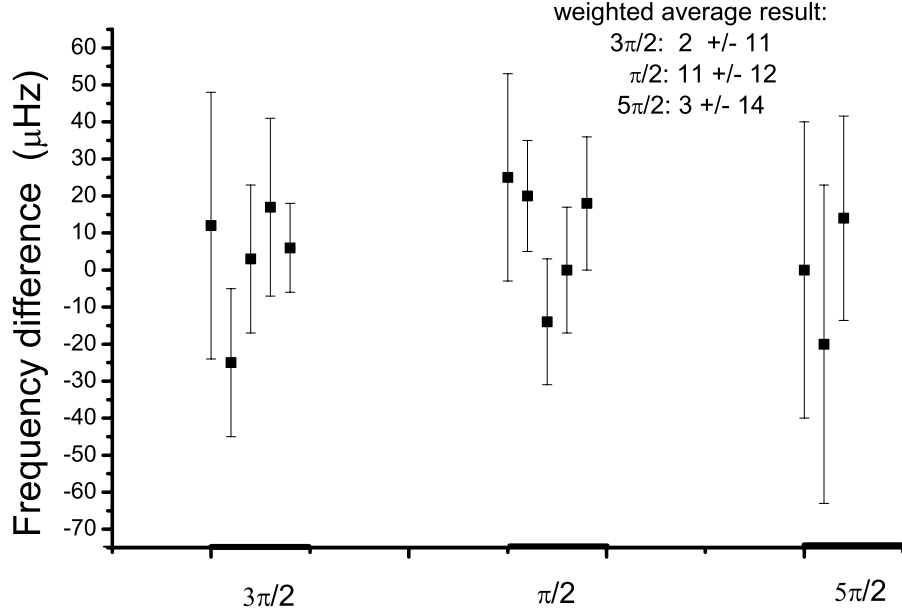


Figure 2.24: *The measured frequency difference when feeding the cavity symmetrically vs asymmetrically, using different microwave powers ($\pi/2$, $3\pi/2$, and $5\pi/2$).*

The Ramsey interrogation is performed by the double passage of the atoms in the same cavity with the opposite velocity. The residual first-order Doppler effect is due to the spatial phase distribution of the microwave field resulting from the coupling, the losses in the copper walls and the expansion of the atomic cloud. It is worth noting that the most relevant direction of spatial phase variation is indeed the transverse one, since vertical phase variations cancel their effect between the two passes in opposite directions. Restrictions must then be imposed mostly on the transverse phase variations. If $\langle \varphi_1 \rangle$ and $\langle \varphi_2 \rangle$ are respectively the average phase seen by the atoms during the two microwave interactions, the frequency shift is given by

$$\frac{\Delta\nu}{\nu_0} = \frac{\langle \varphi_1 \rangle - \langle \varphi_2 \rangle}{\pi Q_{at}} \quad (2.40)$$

Using a 2D model, A. De Marchi and coworkers have calculated the phase distribution of the field in a TE_{011} copper cavity [61]. Using these results and our FO1 parameters in molasses operation, the residual first-order Doppler shift is calculated to be less than 10^{-16} when we allow a possible 1 mrad misalignment of the launching direction with respect to the cavity axis.

As the phase distribution also depends on the cavity coupling, different

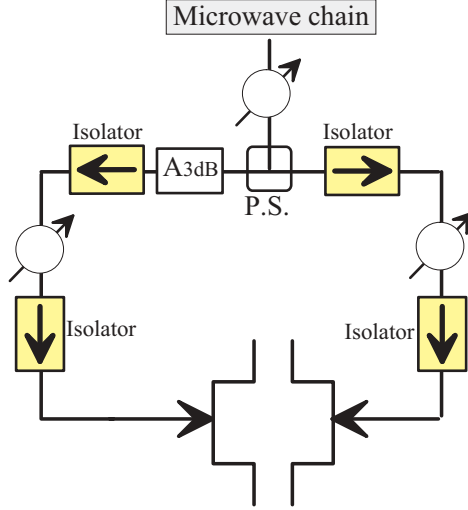


Figure 2.25: Schematic of the symmetric cavity supply. P.S.: power splitter. The 3 dB attenuator A_{3dB} is used to simplify a dynamic adjustment. Each isolator has an isolation of 40 dB.

frequency shifts could then be obtained according to symmetric or asymmetric coupling.

In order to increase the phase distribution sensitivity, we used a MOT (Gaussian distribution with an initial standard deviation σ_i of 2 mm) as a cold atom source. The measurement result (see figure 2.24) shows that the difference is $(1.2 \pm 1.3) \times 10^{-15}$ when we feed the cavity symmetrically¹⁰ and asymmetrically (see figure 2.25). As differential measurements¹¹ cannot be performed over short durations, the frequency resolution is limited by the H-maser long-term stability. Another verification is done by tilting the fountain tube with respect to the vertical direction, with a maximum tilt angle of 1.7 mrad. This tilt changes the phase distribution along the atomic trajectories. We did not find a frequency difference of more than $2(2) \times 10^{-15}$ (see table 2.3) between the different tilts. Furthermore, a variation of the launching velocity from 3.4 m/s to 3.8 m/s did not produce any observable difference in the measured frequency. An important test performed by Clairon [30] was to block the central detection beams (only 50% of atoms are detected compared to normal operation), The maximum frequency shift observed is $3 - 4 \times 10^{-15}$. A worse case based on [62] gives fractional frequency shift of 3×10^{-16} . Finally we take it as the uncertainty for the residual first-order Doppler shift correction.

¹⁰It seems to be possible to improve the field flatness and reduce the phase gradient.

¹¹We alternate series of measurements of a few hundred fountain cycles in different configurations (parameters).

Table 2.3: *Test of the frequency shift as a function of the fountain tilt.*

Tilt (mrad), direction	Measured frequency (μHz)	Resolution($1 \sigma \mu\text{Hz}$)
1.6, west	-4333	13.5
1.4, east	-4314	14.5
1.7, north	-4321	10.0
1.7, south	-4316	8.0
0	-4322	11.5

Microwave spectrum, synchronous perturbations

Using the formula in [55] and the measured spectrum of the microwave generator (the unwanted and asymmetric stray microwave components are at least 60 dB below the carrier components [57]), the shift due to the spectral impurities is estimated to be smaller than 2×10^{-16} when the carrier is at optimum power ($b\tau = \pi/2$). To test the undesirable synchronous effect, we change the duty cycle and the launching height. No frequency difference can be found at the present resolution.

Other lines effect

This includes the Rabi pulling, the Ramsey pulling and Majorana transitions. They depend on the atom quality factor, RF power and the Rabi frequency to Zeeman frequency ratio. After the selection phase, the atoms are prepared in the $m_F = 0$ state, the distributions of the populations of the $m_F = \pm 1$ levels are symmetric and the $\Delta m_F = 1$ transition probabilities are $< 0.5\%$ (see figure 2.13). The Rabi pulling is then estimated to be of the order of 10^{-18} . To evaluate the order of magnitude of the other shifts, the microwave power is changed. The maximum power dependent frequency shift is $4 \times 10^{-16} P/P_0$, where P_0 is the microwave power for a $\pi/2$ pulse [30]. In fact, there are other effects which also depend on the microwave power such as microwave leakage and spectral impurities. A preliminary estimation for all these effects results in a maximum total shift of less than 2×10^{-16} .

Background gas collisions

The background pressure of the vacuum system is below 10^{-9} Torr. According to [55] the shift due to the soft collisions with the residual, thermal atoms (helium, hydrogen...) is less than 10^{-16} .

Cavity pulling

With a low atom number (10^6) and a microwave cavity with a loaded quality factor $Q_{cav} = 10^4$, the shift can be calculated as in a passive caesium

2.10. FREQUENCY COMPARISON AMONG THREE FOUNTAINS AT BNM-SYRTE

beam standard:

$$\frac{\Delta\nu}{\nu_0} = \frac{\Delta\nu_{cav}}{\nu_0} \frac{Q_{cav}^2}{Q_{at}^2} \quad (2.41)$$

where $\Delta\nu_{cav}$ is the cavity detuning and Q_{at} is the atomic quality factor. The controlled cavity temperature can easily keep the cavity resonance to within 100 kHz. The large value $Q_{at} = 10^{10}$ ensures that the shift is less than 10^{-17} .

Second-order Doppler effect and the gravitational red shift

The maximum speed of atoms during the interaction is about 3.5 m/s and the rms velocity is 1 cm/s, the resulting second-order Doppler shift is $\sim 10^{-17}$. The microwave cavity of FO1 is located at (61 ± 1) m above mean sea level. The uncertainty ($g \delta h / c^2$, where c is the speed of light, and g is the acceleration of gravity, and δh is the resolution of the determination of the altitude above the geoid surface.) of the gravitational red shift¹² is 1.1×10^{-16} .

The anticipated improvement of the frequency stability to 10^{-16} per day is a prerequisite to a 10^{-16} accuracy. This is one reason why we want to synchronize the operations of the three fountains at SYRTE.

2.10 Frequency comparison among three fountains at BNM-SYRTE

2.10.1 The link among fountains

In order to frequency compare the three cold atom fountains at the BNM-SYRTE laboratory, we distribute the same local oscillator (LO) signal as a frequency reference for each microwave synthesis chain by a link as shown in fig. 2.26. FOM (FOntaine Mobile) is a transportable fountain operating since 1998 [9, 43, 63, 64]. FO2 is a double fountain which can operate alternately with rubidium and caesium [4, 51]. The performances of the three fountains are similar.

The common frequency reference signal for the three fountains is produced by a 100 MHz quartz oscillator which is properly phase locked to a BVA quartz oscillator and a H-maser.

The H-maser has a stability of $2 \times 10^{-13} \tau^{-1} + 2 \times 10^{-14} \tau^{-1/2}$ and reaches a flicker floor of $\sim 10^{-15}$ over about 1000 s.

¹²The gravitational frequency shift is not intrinsic to a clock.

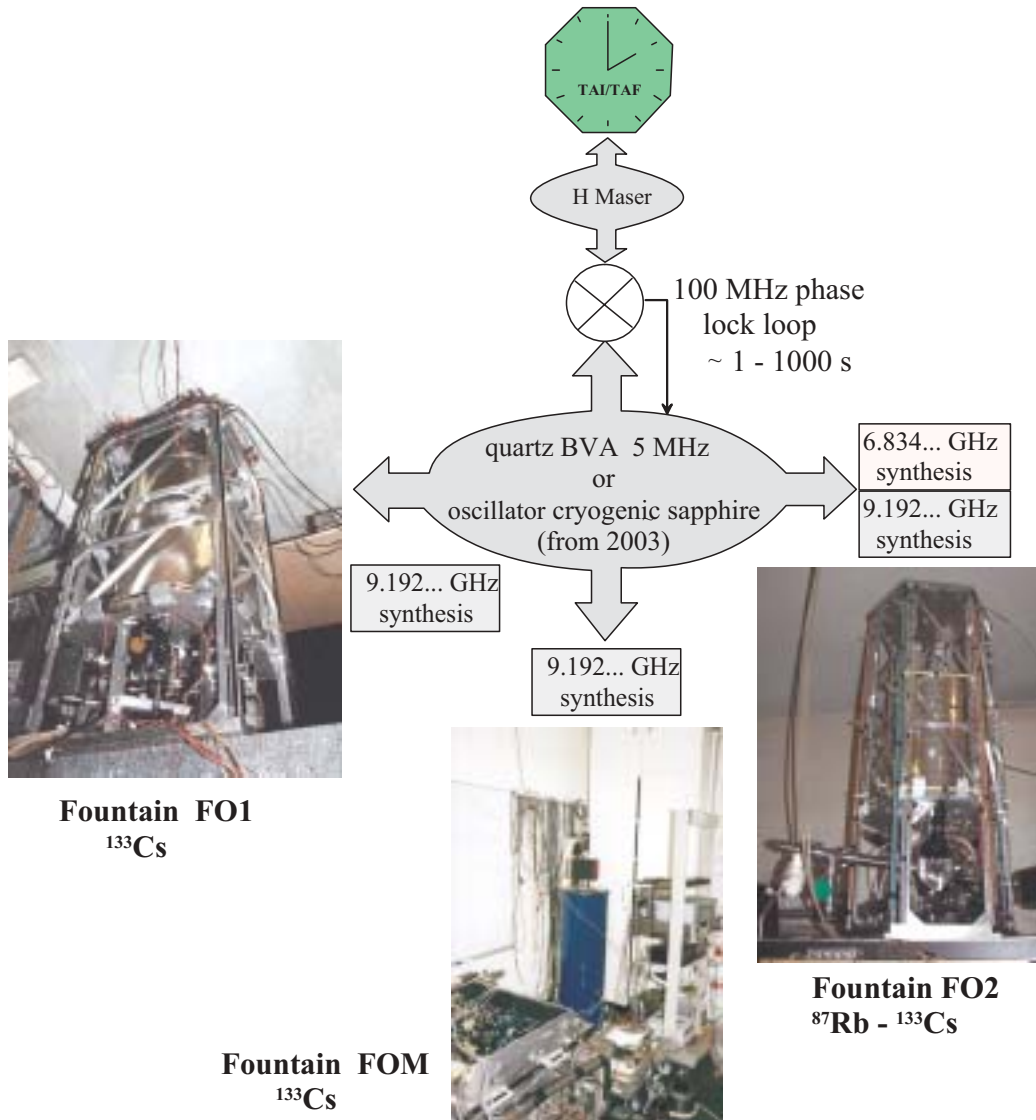


Figure 2.26: The linked cold atom fountain clocks at BNM-SYRTE. The common frequency reference signal is 100 MHz.

2.10. FREQUENCY COMPARISON AMONG THREE FOUNTAINS AT BNM-SYRTE

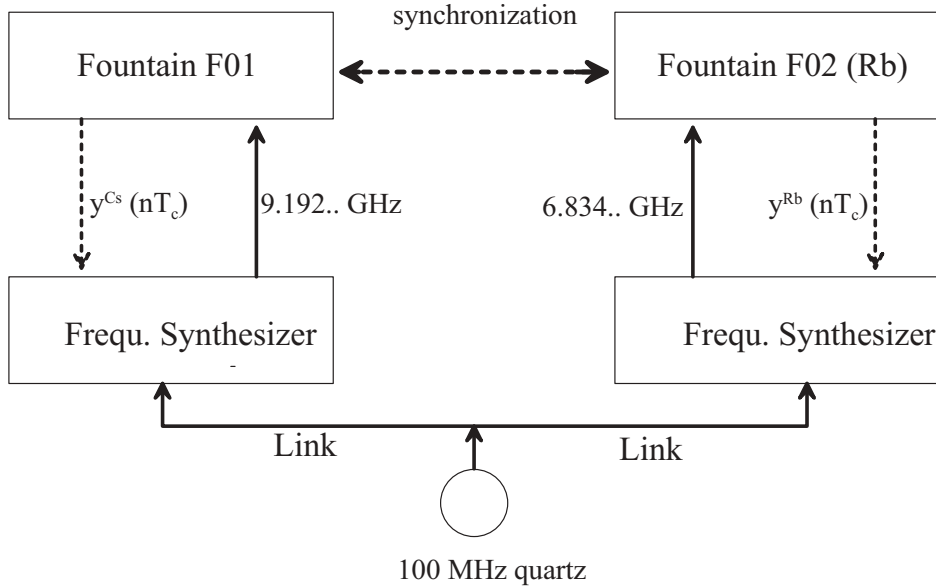


Figure 2.27: *Link connecting an interrogation oscillator to two fountains. The low noise link is about 200 m long, the synchronization stability is better than 1 ms.*

2.10.2 Interrogation oscillator noise rejection

By synchronizing the operation cycle of a pair of identical frequency standards and interrogating the atoms at the same time and with the same oscillator, the frequency fluctuations due to the interrogation oscillator are correlated, and thus the Dick effect is cancelled in the comparison.

Fig. 2.27 shows an experimental link between the two fountains and the interrogation oscillator [49]. A trigger pulse at the beginning of each FO1 cycle is used to synchronize the fountain FO2(Rb) cycle¹³. A noisy quartz oscillator was chosen in order to demonstrate the noise rejection. Its Allan standard deviation of about 5×10^{-12} at 1 s and the Dick effect result in an Allan deviation limit for each fountain of $2.4 \times 10^{-12} \tau^{-1/2}$, much higher than all other limitations.

Fig. 2.28 shows the quadratic sum of the Allan deviation of FO2(Rb) and FO1 compared against a H-maser that would result from an unsynchronized comparison. The Allan deviation of the relative frequency difference between the two fountains (about $2 \times 10^{-13} \tau^{-1/2}$ at a rejection factor of 16) is close to the value obtained with the best quartz oscillator ($1.1 \times 10^{-13} \tau^{-1/2}$). The experimental result and numerical simulation also show that a few milliseconds

¹³The sensitivity function $g(t)$ of each fountain is slightly different due to the different geometries and the size of the microwave cavities.

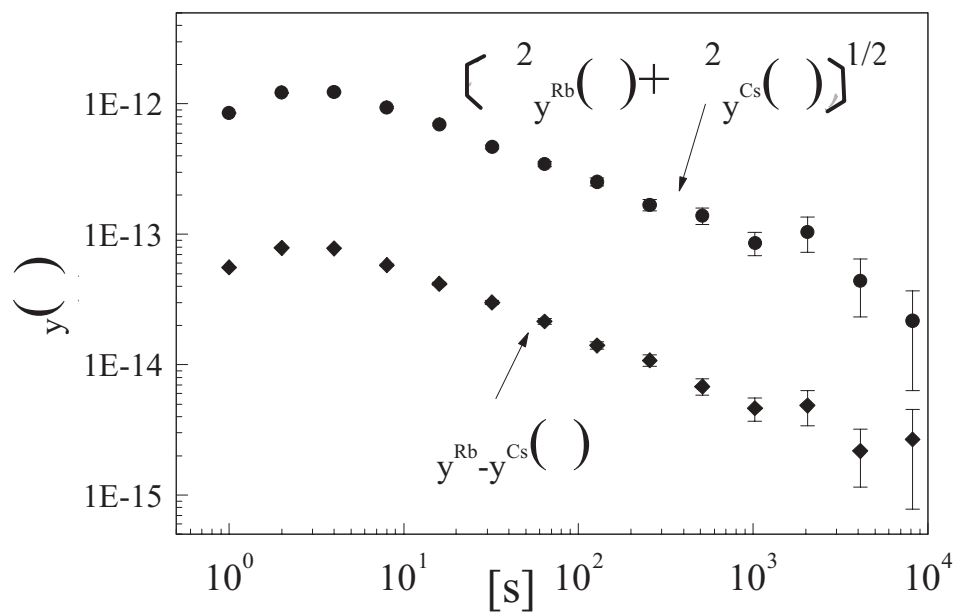


Figure 2.28: *Dots: Quadratic sum of the Allan deviation of the two linked fountains (Rb and Cs), Diamonds: Allan deviation of the frequency difference of the two fountains.*

2.10. FREQUENCY COMPARISON AMONG THREE FOUNTAINS AT BNM-SYRTE

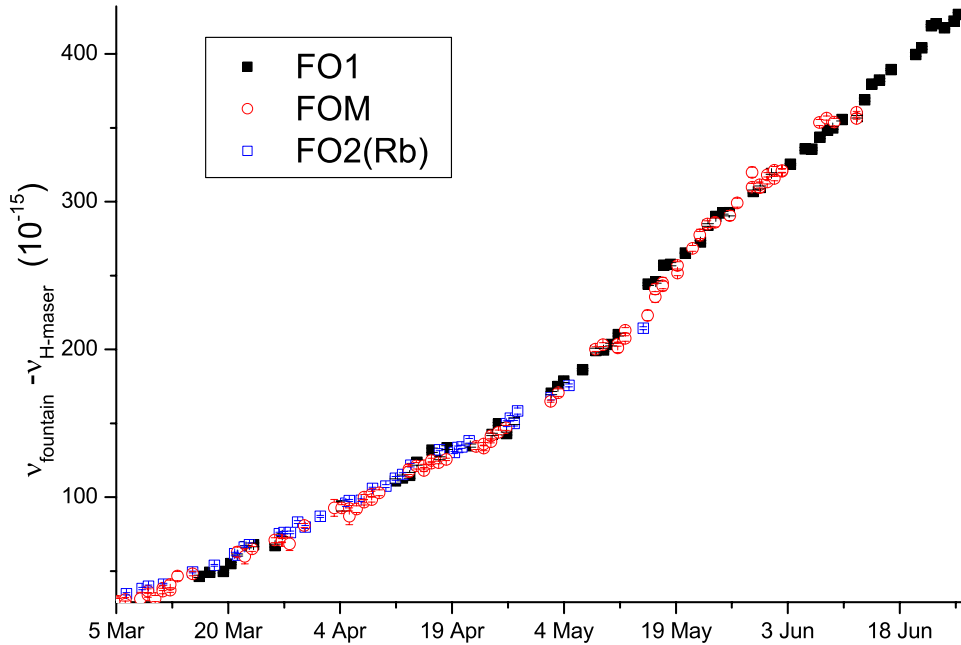


Figure 2.29: *The measured frequencies of the H-maser by 3 fountains at SYRTE in 2000.*

of synchronization are needed for a significant rejection of the interrogation oscillator noise. This method could be used to compare two or more fountain standards at the QPN limit.

2.10.3 Frequency comparison between three fountains and measurement of Rb hyperfine splitting

Figure 2.29 presents the frequency comparisons between the H-maser and the three fountains in 2000 (During this year, FO2 worked only with Rb). The frequencies are corrected for all systematic effects¹⁴. The error bars give the statistic uncertainties of each measurement. Unfortunately, the three measurement sets are not well synchronized and it is difficult to infer directly a frequency difference. To facilitate the comparison, we have fitted the H-maser/FO1 measurements by a third order polynomial. It acts as reference to calculate the frequency differences among the three fountains as shown in the figure 2.30, where the results are weighted averages. The resulting frequency differences for FO1, FOM and FO2(Rb) with respect to the reference fit are

¹⁴The Rb conventional frequency is set to 6 834 682 610.904 333 Hz.

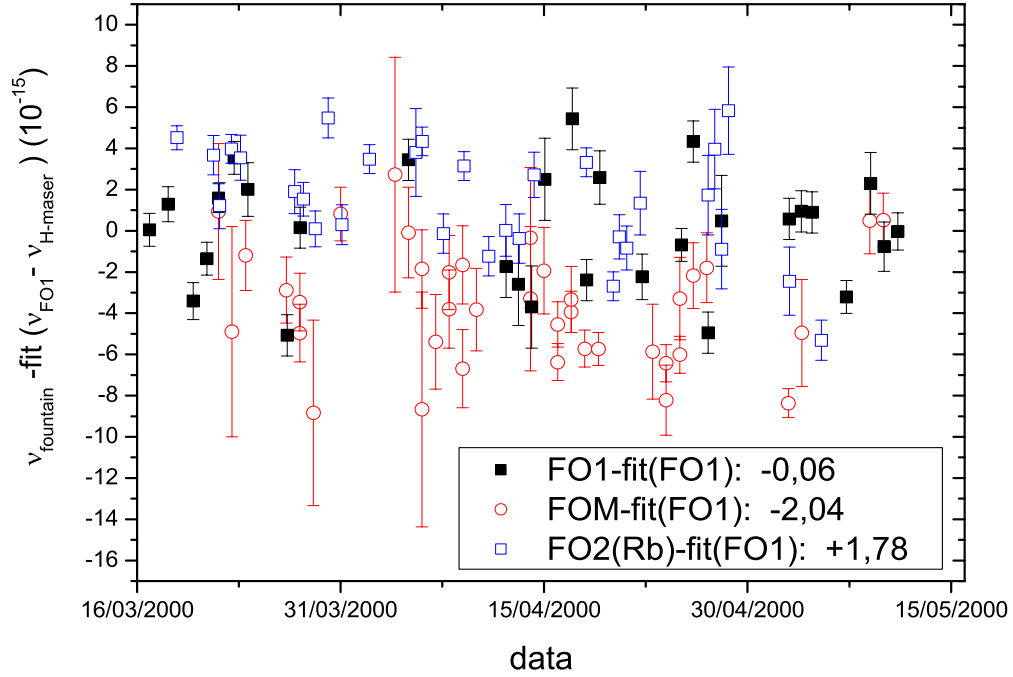


Figure 2.30: *The relative frequency differences among 3 fountains. The reference is a third-order polynomial fit of the frequencies of the H-maser measured by FO1.*

-0.06×10^{-15} , -2.04×10^{-15} , and 1.78×10^{-15} respectively. The evaluated accuracy of fountain FO2(Rb) is 2×10^{-15} , and the accuracy of the two Cs fountains is 1.1×10^{-15} in 2000. We can conclude that the measurements are in agreement with the evaluation budgets.

In order to evaluate the statistical uncertainty for the Rb frequency determination due to the contributions of the two Cs fountains', we have studied the residual influence due to the noise of the H-maser, especially the frequency drift and the $1/f$ noise, which affects the measurement resolution. We have tried several order polynomial simulations to weighted fit the FO1 points. The variances of the residual data¹⁵ in each fountain with respect to this fit always move around the value of 2×10^{-15} as shown in figure 2.31. When we take this number as the statistical uncertainty for each residual date, the measured relative frequency compared with its conventional value is $+2.8 \times 10^{-15}$, with a type A uncertainty of 2×10^{-15} . Taking the above two accuracies as the type B uncertainty of the measurement, we found the measured value of Rb hyperfine splitting to be 6 834 682 610.904 314 (21) Hz

¹⁵The difference between each measurement and the polynomial fit.

2.10. FREQUENCY COMPARISON AMONG THREE FOUNTAINS AT BNM-SYRTE

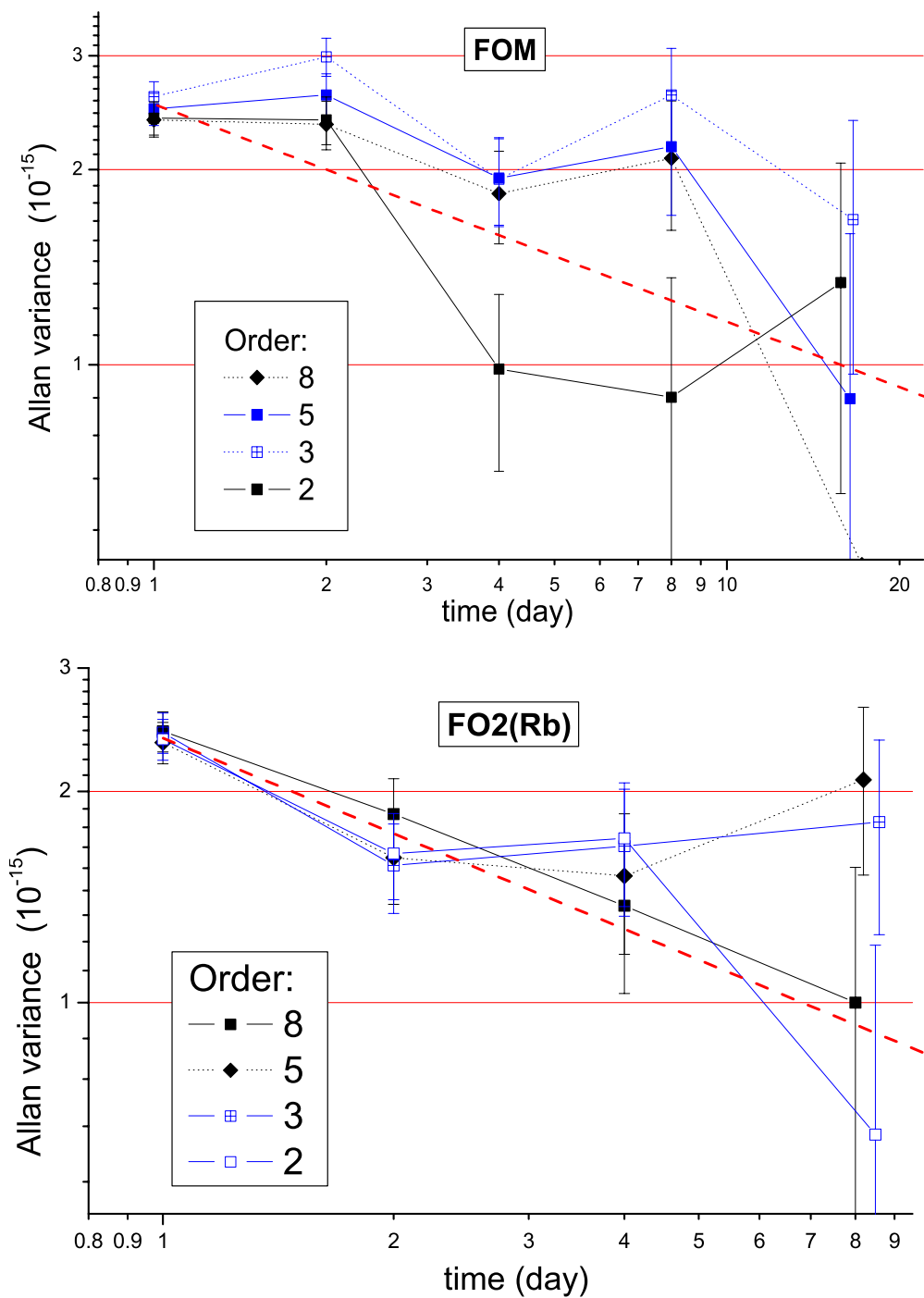


Figure 2.31: Allan variance of the residues in function the order of polynomial fit. The dash lines represent the variance of the white frequency noise.

during May 2000. This value will be used in next chapter to study a possible variation of the fine structure constant α .

Chapter 3

Search for a variation of the fine structure constant α

3.1 Résumé en français

La constante de structure fine est définie comme $\alpha = e^2/4\pi\epsilon_0\hbar c$, avec e est la charge d'un électron, ϵ_0 la permittivité du vide, \hbar la constante de Planck réduite, et c la vitesse de la lumière dans le vide. α est un nombre sans dimension et donc ne dépend pas de la réalisation des unités du système international (SI). Si nous voulons étudier les éventuels changements des lois de la nature, nous devons mesurer des quantités sans dimensions, comme c'est le cas pour α .

En 1937, quand Dirac a essayé de lier la force de la pesanteur aux divers constantes de la physique et les nombres qui caractérisent les propriétés de petite taille de l'univers, il déclara qu'une (ou plusieurs) constantes fondamentales pouvait changer au court du temps [65]. Il y a plusieurs raisons théoriques pour lesquelles α et d'autres constantes sans dimensions pourraient changer avec le temps. Une des recherches des physiciens théoriciens consiste à trouver une théorie unifiant les 4 forces fondamentales : force gravitationnelle, force électromagnétique, et les forces nucléaires forte et faible (voir [66, 67]). Toute variation de α violerait le Principe d'équivalence d'Einstein (EEP) et changerait notre compréhension fondamentale de l'univers.

Jusqu'à présent toutes les études réalisées sur la variation des constantes physiques effectuées en dehors du laboratoire sont sur l'échelle de temps de l'âge de l'univers (déplacement vers le rouge $z \sim 0.1 - 100$). Une analyse récente des données d'Oklo a fourni le test contraignant sur la stabilité de α : $|\dot{\alpha}/\alpha| = 0.4 \pm 0.5 \cdot 10^{-17} \text{ yr}^{-1}$ [68]. Webb *et al.* ont mesuré depuis 1998, l'absorption par des nuages interstellaires de la lumière de 78 quasars dans trois constellations distinctes à l'aide de télescopes [69]. Chacune de ces

constellations rapporte une valeur de α plus petite que dans le passé, le résultat de la moyenne est $\Delta\alpha/\alpha = -0.57 \pm 0.10 \cdot 10^{-5}$ sur la gamme $z \sim 0.2 - 3.7$ (20% à 90% de l'âge de l'univers). Aujourd'hui, ce résultat est le seul à déclarer que les constantes fondamentales pourraient changer. Mais cette conclusion a été contredite par une autre étude ($z \sim 0.4 - 2.3$) plus récente [70].

Les comparaisons d'horloges atomiques sont complémentaires des mesures cosmologiques parce qu'elles mettent une limite sur $\dot{\alpha}/\alpha$ pour le temps présent. Grâce à la très bonne stabilité des fontaines à Cs et à Rb du SYRTE, les comparaisons de fréquences de transitions hyperfines effectuées sur une période de 5 ans (1998-2003) ont fourni une limite très contraignante sur la variation relative possible de la grandeur $(g_{\text{Rb}}/g_{\text{Cs}})\alpha^{-0.44}$ à $(-0.2 \pm 7.0) \times 10^{-16}\text{yr}^{-1}$. Dans l'hypothèse où alpha est constante, la variation de $\nu_{\text{Rb}}/\nu_{\text{Cs}}$ est ramenée à la variation du rapport g-facteur de proton¹ g_p , et l'on obtient $\dot{g}_p/g_p = (0.1 \pm 3.5) \times 10^{-16}\text{yr}^{-1}$.

3.2 Introduction

The fine structure constant is defined as $\alpha = e^2/4\pi\epsilon_0\hbar c$, where e is the electron charge, ϵ_0 the electric permeability of the vacuum, \hbar the reduced Planck constant, and c the speed of light in vacuum. α is a dimensionless number which does not depend on a man-made system of units and can be measured without reference to such a system. If we want to investigate whether the laws of nature are changing, we must measure dimensionless quantities, such as α .

In 1937, when Dirac attempted to link the strength of gravity with the various constants and numbers that characterize the small-scale properties of the universe, he claimed that the value of various dimensionless physical constants of nature could change with time [65]. There are some theoretical reasons why α and other dimensionless constants might vary with time. The holy grail of theoretical physics is to find a single unified theory that describes the 4 fundamental forces all together: gravity, electromagnetism, and the strong and weak nuclear forces (see [66, 67]).

Any variation of α would violate the Einstein Equivalence Principe (EEP) and change our fundamental understanding of the universe. Taking advantage of the high stability of Cs and Rb fountains at SYRTE, hyperfine transition frequency comparisons spreading over an interval of 5 years have reduced the upper limit for the possible variation of α . A new bound on a possible

¹Dans le modèle de Schmidit, pour les atomes ^{87}Rb et ^{133}Cs , le g-facteur nucléaire se dépend seulement du g-facteur de proton g_p .

3.3. A CHANGE OF α WOULD VIOLATE THE EQUIVALENCE PRINCIPLE

variation of the proton g-factor g_p has also been determined.

3.3 A change of α would violate the Equivalence Principle

Einstein's equivalence principle (EEP), one of the cornerstones of modern physics, is closely related to the development of the theory of gravity from Newton's theory to general relativity. The gravitational field is described as a geometrical property of space-time in general relativity and other metric theories of gravity, where any variation of the non-gravitational constants is forbidden. EEP states that in local freely falling frames, the outcome of any non-gravitational experiment is independent of the velocity of the frame (Local Lorentz Invariance), and of when and where it is performed (Local Position Invariance) (For detailed discussion and definitions see [71]). Some tests to verify EEP aim at determining the relative rate of change of non-gravitational fundamental constants, such as α .

On the other hand, there are a lot of physicists who firmly believe in unified theories, such as string theory and multi-dimensional theory, which lead us to expect that an additional compact dimension of space may exist, where the constants seen in the three-dimensional subspace of the theory will vary at the same rate as any change occurring in the scale length of these extra compact dimensions. Naturally, the temporal variation of α is predicted [66, 72], but it would violate LPI.

3.4 Non-laboratory searches

All the studies on the variation of the constant outside the laboratory are on time scale of the age of the universe (redshift² $z \sim 0.1 - 100$).

The Oklo natural fission reactor The best terrestrial limit on the time variation of α outside the laboratory is based on examination of the decay products of the Oklo phenomenon - a natural uranium fission reactor. This test analyzes the isotope ratio $^{149}\text{Sm}/^{147}\text{Sm}$ in a self-sustained nuclear fission reaction which took place around 1.8×10^9 years ago ($z \sim 0.15$) in an underground uranium depot in Oklo, Gabon (West Africa). The fission reaction continued off-and-on for hundreds of thousands of years. The constraint on time variation of α is inferred from the constraint on the variation of the

²The redshift z is defined from Hubble's law for the universe expansion: $1 + z = \nu_e/\nu$, where ν_e and ν are respectively the frequencies at emission and today.

resonance energy (related to the capture cross section of ^{149}Sm) under the assumption that the nuclear energy is independent of α [73]. A recent analysis of the Oklo data has provided *the most stringent* test of the stability of α : $|\dot{\alpha}/\alpha| = 0.4 \pm 0.5 \cdot 10^{-17} \text{ yr}^{-1}$ [68].

Absorption lines in quasar spectra The universe itself is about 13.5 billion years old. We can test the possible α variation at earlier evolutionary phase of the universe by analysis of the spectral lines from distant quasars³.

What one examines is the dark, narrow line in quasar absorption spectra which is produced when the radiation passes through the gas around the galaxy that lies between the earth and the quasars. After comparing this absorption line with what one measures for the same atoms and ions in the laboratory, we can determine if the physics that is responsible for the absorption has changed over the history of the universe (as long ago as one billion years after the Big Bang). Alternatively, one can find out if α has changed. Webb and *et al.* have measured 78 quasars in three samples with telescopes since 1998 [69]. Each sample yields a small α in the past, the entire result is $\Delta\alpha/\alpha = -0.57 \pm 0.10 \cdot 10^{-5}$ at level 4σ over the redshift range 0.2 – 3.7 (20% to 90% of the age of universe). Today this result is the *only claim* that fundamental constants might change. But, this conclusion has been recently contradicted by another study [70].

Conclusion The geological result does not conflict with the astrophysical result obtained by Webb *et al.*, because they probe very different epochs in the history of the universe. However, it excludes a linear variation. It is possible that the value of α was changing relatively rapidly in the first few billion years after Big Bang, and it has changed 100 times less since the time of the Oklo event. It suggests that the time-dependence as a function of cosmic time was non-monotonic, or even oscillating. Unfortunately, we can not repeat the Oklo “experiment”. Moreover, the difficult task remaining is understanding and modelling carefully the correlation of the variation of weak strength, the strong interaction force, as well as the effect of m_e/m_p [74]. This means that the interpretation of the data with an assumption, that only α varies, is not serious. When one performs astrophysical observations, a lot of systematic effects have to be taken into account, such as the uncertainty of the wavelength calibration in laboratory, the effect of the unresolved velocity substructure in the absorption lines, the different sensitivity of the very strong line and the very weak lines of Fe^+ to small perturbations⁴, light

³The name “quasar” is derived from an early description “QUAsi-StellAR-objects”.

⁴Any small perturbation would affect the weak lines much more than the strong ones, thus could skew the results.

blending, and so on. This is why Songaila proposed not to directly use this stringent upper limit [75].

Both the cosmological methods of CMB (cosmic microwave background) and of BBN (Big Bang nucleosynthesis) are not yet very accurate because their interpretation is very model-dependent [76]. They may be important if the variations of α at the beginning of the evolution of the universe were faster.

3.5 Laboratory search using atomic clocks

Unlike the results inferred from the phenomena taking place over cosmological time scales, atomic clock comparisons are complementary to the cosmological tests because they put a limit on $\dot{\alpha}/\alpha$ for the present. Thanks to the ultrahigh stability of atomic clocks, we can get a very good measurement resolution. Besides, we can repeat the measurement and continue it for a long duration. Thus we have a better control of the systematic effects.

This method involves the comparison of ultra-stable oscillators of different composition and of atomic clocks with different atomic species. Solid resonators, electronic, fine structure and hyperfine structure transitions respectively give access to R_∞/α , R_∞ , $\alpha^2 R_\infty$ and $\alpha^2 g_I (m_e/m_p) R_\infty$ (in the non-relativistic approximation). R_∞ stands for the Rydberg constant, m_e and m_p are the electron and proton mass, and g_I is the nuclear g-factor.

Compared to other tests on cosmological timescales, these laboratory tests have a short time base (a few years). This drawback is compensated by an extremely high sensitivity.

3.5.1 α and g_I dependence of the atomic spectra

All the microwave atomic clocks are operated on the transition between the ground hyperfine levels determined by the interaction of a nuclear magnetic moment with the magnetic moment of an $S_{1/2}$ state valence electron. The method of the atomic clock rate comparison for different atomic number Z is based on the Z dependence of the relativistic contribution to the hyperfine energy splitting. In other words, any variation in α will induce a variation in the relative clock rates.

The value of the hyperfine splitting in an atomic state can be expressed

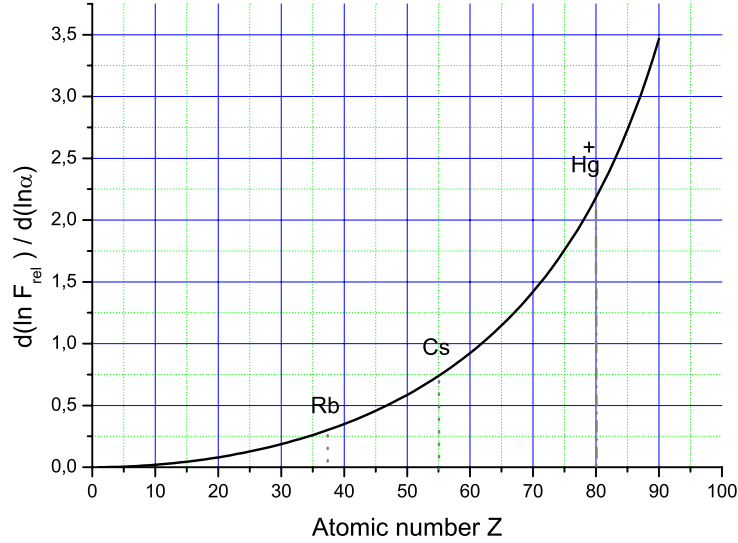


Figure 3.1: *The correction function $d \ln F_{rel}(Z\alpha)/d \ln \alpha$ against the atomic number Z .*

in the form

$$\nu_{hfs} = a_0 \alpha^2 g_I F_{rel}(Z\alpha) \frac{m_e}{m_p} R_\infty c, \quad (3.1)$$

where a_0 is a constant specific for the atomic state and all the dependence of α is contained in a function $F_{rel}(Z\alpha)$, the Casimir correction [3]. $F_{rel}(Z\alpha)$ is obtained when the relativistic wave equation is solved to evaluate the electron wave function in the vicinity of the nucleus. For an $S_{1/2}$ state electron $F_{rel}(Z\alpha) = 3[\lambda(4\lambda^4 - 1)]^{-1}$, where $\lambda = [1 - (Z\alpha)^2]^{1/2}$ showing that $F_{rel}(Z\alpha)$ is a strong function of α for high Z and $F_{rel}(0) = 1$ (see figure 3.1). For Hg, this relativistic Casimir contribution amounts to 56% of the hyperfine splitting ($F_{rel}(Hg) = 2.26$).

Following [3] and neglecting possible changes of the strong and weak interactions affecting the nuclear magnetons, and assuming everything else is constant, a time variation $\delta\alpha$ of the fine structure constant induces a relative drift rate of two hyperfine frequencies according to the following equation

$$\frac{d}{dt} \ln \frac{\nu_1}{\nu_2} = \left(\left. \frac{d \ln F_{rel}(Z\alpha)}{d \ln \alpha} \right|_1 - \left. \frac{d \ln F_{rel}(Z\alpha)}{d \ln \alpha} \right|_2 \right) \frac{\dot{\alpha}}{\alpha}. \quad (3.2)$$

The sensitivity $\left(\left. \frac{d \ln F_{rel}(Z\alpha)}{d \ln \alpha} \right|_1 - \left. \frac{d \ln F_{rel}(Z\alpha)}{d \ln \alpha} \right|_2 \right)$ will be bigger when a larger atomic number difference is given. It should be noted that this sensitivity

also might be used to detect the spatial variation of α (with replacement of d/dt by d/dU , where U is the solar gravitational potential). For ^{133}Cs , $\frac{d \ln[F_{\text{rel}}(Z\alpha)]}{d \ln \alpha} = 0.74$. For ^{87}Rb , this quantity is 0.30 [77]. Finally, the sensitivity of the ratio $\nu_{\text{Rb}}/\nu_{\text{Cs}}$ to a variation of α is simply given by:

$$\frac{\partial}{\partial \ln \alpha} \ln \left(\frac{\nu_{\text{Rb}}}{\nu_{\text{Cs}}} \right) \simeq (0.30 - 0.74) = -0.44. \quad (3.3)$$

If the ratio $\dot{\alpha}/\alpha = 10^{-14}$ /yr, a relative frequency drift of 4.4×10^{-15} /yr between Cs clock and Rb clock should be measured.

In contrast with [3], Ref.[76] argues that a time variation of the nuclear magnetic moments must also be considered in a comparison between hyperfine frequencies. One reason is that the proton g-factor g_p contribution to g_I has a different sign⁵ for Rb. g_I can be calculated using the Schmidt model which assumes the magnetic moment of the nucleus includes a spin part and an orbital part. For atoms with odd A and Z such as ^{87}Rb and ^{133}Cs , the Schmidt g-factor $g_I^{(s)}$ is found to depend only on g_p . With this simple model, Ref.[76] finds:

$$\frac{\partial}{\partial \ln g_p} \ln \left(\frac{\nu_{\text{Rb}}}{\nu_{\text{Cs}}} \right) \simeq \frac{\partial}{\partial \ln g_p} \ln \left(\frac{g_{\text{Rb}}^{(s)}}{g_{\text{Cs}}^{(s)}} \right) \simeq 2.0. \quad (3.4)$$

Moreover, attributing all the time variation of $\nu_{\text{Rb}}/\nu_{\text{Cs}}$ to either g_p or α independently is somewhat artificial. Theoretical models allowing for a variation of α also allow for a variations in the strength of the electromagnetic interactions. For instance, Ref.[78] argues that grand unification of the four interactions implies that a time variation of α necessarily comes with a time variation of the coupling constants of the other interactions. Ref.[78] predicts that a fractional variation of α is accompanied with a ~ 40 times larger fractional change of m_e/m_p . In order to test independently the stability of the four fundamental interactions, several comparisons between different atomic species and/or transitions are required. For instance and as illustrated in [79], absolute frequency measurements of an optical transition, *i.e.*, comparison of a transition frequency with the reference frequency of the ground state hyperfine transition of ^{133}Cs are sensitive to a different combination of fundamental constants: $g_{\text{Cs}}(m_e/m_p)\alpha^x$, where x depends on the particular atom and/or transition.

A more complete theoretical analysis going beyond the Schmidt model would clearly be very useful to interpret frequency comparisons involving

⁵In the Schmidt model, the nuclear g-factor is $g_p/2$ for Rb and $\frac{7}{18}(10 - g_p)$ for Cs respectively.

hyperfine transitions. This is especially important as most precise frequency measurements, both in the microwave and the optical domain [79, 80, 81], are currently referenced to the ^{133}Cs hyperfine splitting. The H hyperfine splitting, which is calculable⁶ at a level of $\sim 10^{-7}$, has already been considered as a possible frequency reference several decades ago. Unfortunately, despite numerous efforts, the H hyperfine splitting is currently measured to only 7 parts in 10^{13} (using H-masers), almost three orders of magnitude worse than our results presented in the next section.

3.5.2 Experiments with Rb and Cs fountains

On much shorter timescales, several tests using frequency standards have already been performed, for example, a comparison using H-masers and superconducting-cavity stabilized oscillator clocks (see [82]), Mg and Cs atomic beam standards [83], H-maser and mercury ion clocks [3].

Our measurements take advantage of the high accuracy ($\sim 10^{-15}$) of several laser cooled Cs and Rb atomic fountains. According to recent atomic structure calculations [3, 84], these measurements are sensitive to a possible variation of the quantity $(g_{\text{Rb}}/g_{\text{Cs}})\alpha^{-0.44}$ as shown in formula (3.1) and (3.3).

In our experiments, three atomic fountains are compared to each other, using a hydrogen maser (H-maser) as a flywheel oscillator (fig.2.26). Two fountains, FO1 and the transportable fountain FOM [43], use caesium atoms, and the accuracy reaches about 1×10^{-15} . The third fountain is a dual fountain [85], named FO2, operating alternately with rubidium (FO2(Rb)) and caesium (FO2(Cs)). This fountain has been continuously upgraded, its accuracy has improved from 2×10^{-15} in 1998 to 8×10^{-16} for caesium and from 1.3×10^{-14} in 2000 to 7×10^{-16} for rubidium [5].

The three fountains have different geometries and operating conditions: the number of detected atoms ranges from 3×10^5 to 2×10^6 at a temperature of $\sim 1 \mu\text{K}$, the fountain cycle duration from 1.1 to 1.6 s. The Ramsey resonance width is between 0.9 and 1.2 Hz. In measurements reported here the fractional frequency instability is $(1 - 2) \times 10^{-13}\tau^{-1/2}$, where τ is the averaging time in seconds. Fountain comparisons have a typical resolution of $\sim 10^{-15}$ for a 12 hour integration, and each of the four data campaigns lasted from 1 to 2 months during which time an accuracy evaluation of each fountain was performed.

The campaign in 2000 was already introduced in section 2.10.3. We would like to present the latest frequency measurement of the Rb hyperfine splitting

⁶The ^1H hydrogen atom consists of a single proton surrounded by a single electron. It is thus the simplest of all atoms.

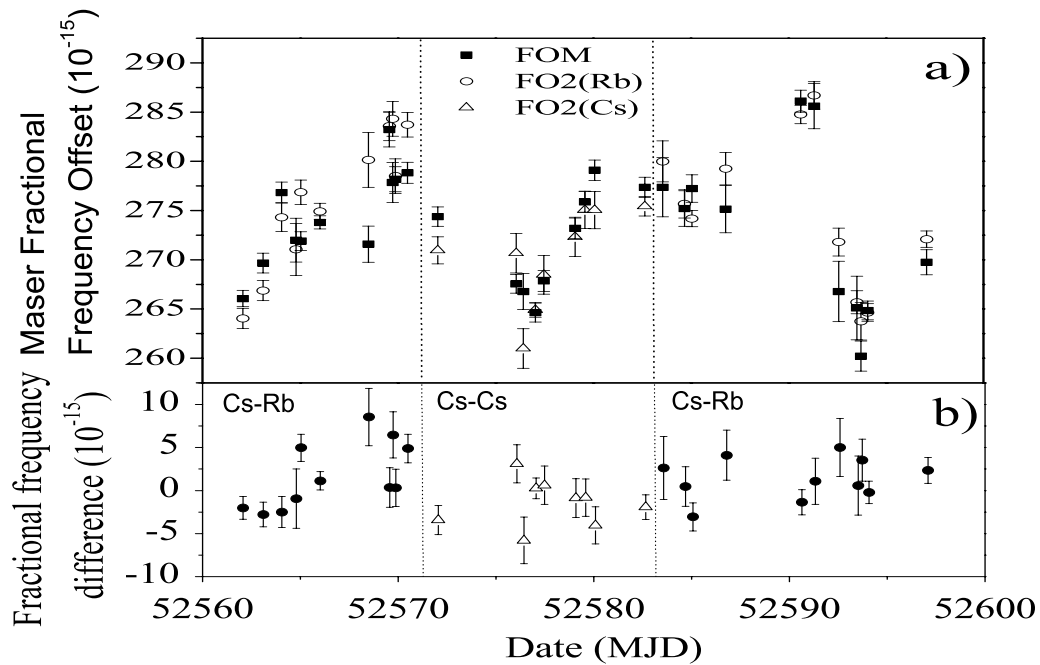


Figure 3.2: *The frequency comparison data of 2002, where MJD is the Modified Julian Day. a) H-maser fractional frequency offset versus FOM (■), and alternately versus FO2(Rb) (○) and FO2(Cs) (△ between dotted lines). b) Fractional frequency differences. Between dotted lines, Cs-Cs comparisons, outside Rb-Cs comparisons. Error bars are purely statistical. They correspond to the Allan standard deviation of the comparisons and do not include contributions from fluctuations of systematic shifts.*

carried out in 2002. The measurements are presented in fig. 3.2, which displays the maser fractional frequency offset, measured by the Cs fountains FOM and FO2(Cs). Also shown is the H-maser frequency offset measured by the Rb fountain FO2(Rb) where the Rb hyperfine frequency is conventionally chosen to be $\nu_{\text{Rb}}(1999) = 6\,834\,682\,610.904\,333$ Hz, the value measured in 1999. The data are corrected for the systematic frequency shifts. The H-maser frequency exhibits fractional frequency fluctuations on the order of 10^{-14} over a few days, ten times larger than the typical statistical uncertainty resulting from the instability of the fountain clocks. In order to reject the H-maser frequency fluctuations, the fountain data are recorded simultaneously (within a few minutes). The fractional frequency differences plotted in fig. 3.2 b illustrate the efficiency of this rejection. FO2 is operated alternately with Rb and Cs, allowing both Rb-Cs comparisons and Cs-Cs comparisons (central part of fig. 3.2) to be performed.

To compare the two Cs clocks running during the 2002 campaign, FOM and FO2(Cs), we calculate the mean fractional frequency difference:

$$\frac{\nu_{\text{Cs}}^{\text{FO2}}(2002) - \nu_{\text{Cs}}^{\text{FOM}}(2002)}{\nu_{\text{Cs}}} = +27(6)(12) \times 10^{-16} \quad (3.5)$$

where the first parenthesis reflects the 1σ statistical uncertainty, and the second the systematic uncertainty, obtained by adding quadratically the inaccuracies of the two Cs clocks. We therefore find that the two Cs fountains are in good agreement despite their significantly different operating conditions, showing that systematic effects are well understood at the 3×10^{-15} level.

To measure the ^{87}Rb frequency, we first calculate the mean fractional frequency difference between FOM and FO2(Rb). We obtain

$$\frac{\nu_{\text{Rb}}^{\text{FO2}}(2002)}{\nu_{\text{Rb}}(1999)} - \frac{\nu_{\text{Cs}}^{\text{FOM}}(2002)}{\nu_{\text{Cs}}} = -7(4) \times 10^{-16} \quad (3.6)$$

where the number in parentheses reflects the 1σ statistical uncertainty, which leads to

$$\frac{\nu_{\text{Rb}}^{\text{FO2}}(2002)}{\nu_{\text{Rb}}(1999)} - 1 = -13(5) \times 10^{-16} \quad (3.7)$$

Finally, the ^{87}Rb frequency measured in 2002 with respect to the average ^{133}Cs frequency is found to be

$$\nu_{\text{Rb}}(2002) = 6\,834\,682\,610.904\,324(4)(7) \text{ Hz} \quad (3.8)$$

where the error bars now include FO2(Rb), FO2(Cs) and FOM uncertainties. This is the most accurate frequency measurement of ν_{Rb} to date.

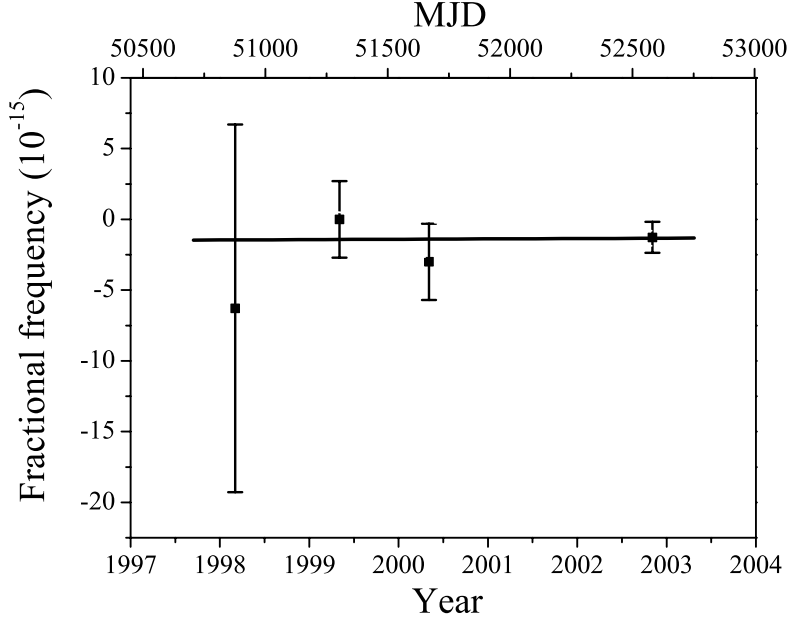


Figure 3.3: Measured ^{87}Rb frequencies referenced to the ^{133}Cs fountains over 57 months. The 1999 measurement value ($\nu_{\text{Rb}}(1999) = 6\,834\,682\,610.904\,333\text{ Hz}$) is conventionally used as reference. Horizontal line: weighted linear fit.

In fig. 3.3 are plotted all our Rb-Cs frequency comparisons. Except for the less precise 1998 data [86], two Cs fountains were used together to perform the Rb measurements. The uncertainties for the 1999 and 2000 measurements were 2.7×10^{-15} , because of lower clock accuracy and lack of rigorous simultaneity in the earlier frequency comparisons [85]. A weighted linear fit to the data in fig. 3.3 determines how our measurements constrain a possible time variation of $\nu_{\text{Rb}}/\nu_{\text{Cs}}$. We find:

$$\frac{d}{dt} \ln \left(\frac{\nu_{\text{Rb}}}{\nu_{\text{Cs}}} \right) = (0.2 \pm 7.0) \times 10^{-16} \text{ yr}^{-1} \quad (3.9)$$

which represents a 5-fold improvement over our previous results [87] and a 100-fold improvement over the $\text{Hg}^+\text{-H}$ hyperfine energy comparison [3]. The same limit applies to the dimensionless quantity $(g_{\text{Rb}}/g_{\text{Cs}})\alpha^{-0.44}$. We thus have:

$$\frac{d}{dt} \ln \left(\frac{g_{\text{Rb}}}{g_{\text{Cs}}} \alpha^{-0.44} \right) = (0.2 \pm 7.0) \times 10^{-16} \text{ yr}^{-1}. \quad (3.10)$$

Assuming g_p is certain, meaning that the contribution to this constraint of the variation of $\nu_{\text{Rb}}/\nu_{\text{Cs}}$ only arises from α , and using formula (3.3), we thus deduce the new limit: $\dot{\alpha}/\alpha = (-0.4 \pm 16) \times 10^{-16} \text{ yr}^{-1}$. Attributing any variation of $\nu_{\text{Rb}}/\nu_{\text{Cs}}$ to a variation of g_p , equation (3.4) and experiment results in formula (3.9) lead to: $\dot{g}_p/g_p = (0.1 \pm 3.5) \times 10^{-16} \text{ yr}^{-1}$. However, it must be noted that the Schmidt model is over-simplified and does not agree very accurately with the actual nuclear magnetic moment. The maximum value of the deviation between the naive value in the Schmidt model μ_s and the measured value $\mu_{\text{mea.}}$. ($\mu_{\text{mea.}}/\mu_s - 1$) is 50% for Cs, and it is 26% for Rb [76].

3.6 Conclusion

Reference	Experiment	Constant X	Duration	Limit $ \dot{X}/X $ (yr^{-1})
Turneure <i>et al.</i> , 1976 see [82]	hfs of Cs vs SCO	$g_p(m_e/m_p)\alpha^3$	12 days	$< 4.0 \times 10^{-12}$
Demidov, 1992[88]	hfs of Cs vs hfs of H	$g_p/g_I\alpha$	1 year	$< 5.5 \times 10^{-14}$
Breakiron, 1993[89]	hfs of Cs vs hfs of H	$g_p/g_I\alpha$		$< 7 \times 10^{-14}$
Godone <i>et al.</i> , 1993, [83]	hfs of Cs vs fs of Mg	$g_p(m_e/m_p)$	1 year	$< 5.4 \times 10^{-13}$
Prestage <i>et al.</i> , 1995[3]	hfs of Hg^+ vs hfs of H	$g_p/g_I\alpha$	140 days	$< 3.7 \times 10^{-14}$
Sortais <i>et al.</i> , 2001[87]	hfs of Cs vs hfs of Rb	$g_{\text{Rb}}/g_{\text{Cs}}\alpha^{0.44}$	2 years	$< 5 \times 10^{-15}$
Bize <i>et al.</i> , 2003[79]	hfs of Cs vs gs of Hg^+	$g_{\text{Cs}}\alpha^{6.0}(m_e/m_p)$	2 years	$< 7 \times 10^{-15}$
This work, 2003[5]	hfs of Cs vs hfs of Rb	$g_{\text{Rb}}/g_{\text{Cs}}\alpha^{0.44}$	5 years	$< 7.2 \times 10^{-16}$

Table 3.1: *Different atomic clock comparison experiments. SCO refers to super conductor cavity oscillator. gs, fs and hfs refer respectively to gross structure, fine structure and hyperfine structure.*

3.6. CONCLUSION

By comparing ^{133}Cs and ^{87}Rb hyperfine energies, we have set a highly stringent bound to a possible fractional variation of the quantity $(g_{\text{Rb}}/g_{\text{Cs}})\alpha^{-0.44}$ at $(-0.2 \pm 7.0) \times 10^{-16}\text{yr}^{-1}$. To demonstrate the improvement of our measurement, we list some important experiments in table 3.1.

In the near future, accuracies near 1 part in 10^{16} should be achievable in microwave atomic fountains, which would improve our present Rb-Cs comparison by one order of magnitude. To reach such an accuracy, we should make use of the new method based on an adiabatic transfer of population to prepare atomic samples in order to control (measure) well the cold collisional shift (see chapter 6).

A further step is the extension of these comparisons for distant clocks in different laboratories in the world. Serving this purpose, a new generation of time/frequency transfer at the 10^{-16} level is currently under development for the ESA (European Space Agency) space mission ACES (Atomic Clock Ensemble in Space) which will fly ultra-stable clocks (PHARAO and SHM) onboard the international space station in 2007 [90]. Furthermore, these comparisons will also allow for a search of a possible change of fundamental constants induced by the annual modulation of the solar gravitational potential due to the elliptical orbit of the Earth [91].

Finally, an unambiguous test of the stability of α should be possible by comparing two optical transitions. The frequency of an electronic transition can be expressed as $\nu_{opt} = R_{\infty} \times f(\alpha)$, where $f(\alpha)$ includes relativistic effects, many-body effects, spin-orbit coupling. We anticipate major advances in these tests using frequency standards, thanks to recent advances in optical frequency metrology using femtosecond lasers [79].

Chapter 4

Test of the PHARAO Ramsey cavity

4.1 Résumé en français

La mission spatiale ACES (Atomic Clock Ensemble in Space) a été retenue par l'ESA (European Space Agency) pour voler pendant une durée d'environ 18 mois à 3 ans à bord de l'ISS (International Space Station), à partir de 2007 [90, 92]. Elle comporte deux horloges : le maser à hydrogène actif SHM (Space active Hydrogen Maser), développé par l'observatoire cantonal de Neuchatel, en Suisse, ainsi que l'horloge spatiale à atomes froids de césium PHARAO (Projet d'Horloge Atomique par Refroidissement d'Atomes en Orbite) développée par le CNES (Centre National d'Etudes Spatiales, France), en collaboration avec les laboratoires scientifiques (BNM-SYRTE et LKB). Le système est équipé d'un lien micro-onde 2 voies (MWL, Micro-Wave Link) permettant des comparaisons de fréquence et des transferts de temps de grande exactitude et stabilité avec des utilisateurs au sol. Le maser SHM sera utilisé lors des comparaisons de fréquence, en temps qu'étalon secondaire de bonne stabilité moyen terme, ainsi que pour l'évaluation en vol des effets systématiques affectant l'exactitude de PHARAO.

L'objectif premier de la mission ACES consiste à étudier le fonctionnement de l'horloge à atomes froids dans l'espace. En tirant parti de l'environnement de gravité réduite, PHARAO devrait atteindre une stabilité à un jour meilleure que 3×10^{-16} et une exactitude de 1×10^{-16} . Le lien MWL permettra la synchronisation à une exactitude de 30 ps, des échelles de temps définis dans des laboratoires de métrologies disséminés à travers la surface du globe. Cette performance constitue une amélioration de plus de deux ordres de grandeur par rapport aux systèmes actuels GPS et GLONASS. Le troisième objectif est de réaliser avec une meilleure résolution différents tests

de physique fondamentale, comme la mesure du déplacement gravitationnel, la recherche d'une éventuelle anisotropie de la vitesse de la lumière ou d'une dérive temporelle de la constante de structure fine...

Au sol, dans une fontaine atomique, la gravité impose inévitablement une limite de l'ordre de 1 s, au temps d'interaction T . En microgravité, de plus longs temps d'interaction sont accessibles, dans une horloge de dimensions raisonnables, simplement en réduisant la vitesse de lancement. Cependant, comme la vitesse atomique est nécessairement constante, l'interrogation doit s'effectuer dans une cavité de Ramsey, comportant deux zones. Le dispositif perd alors sa symétrie et les atomes deviennent sensibles à de possibles dissymétries de la distribution de phase et à la présence d'un déphasage global entre ces deux zones. Ces défauts dépendent directement de la symétrie de construction de la cavité et de la longueur d'inter-zones. Ils se traduisent par un effet Doppler déplaçant la fréquence d'horloge donné par la relation suivante établie à partir de l'équation (B.20):

$$\Delta\nu_{\Delta\varphi} \simeq \left\langle \frac{\overline{\varphi_2} - \overline{\varphi_1}}{2\pi T} \right\rangle. \quad (4.1)$$

Dans cette expression, $\overline{\varphi_1}$ et $\overline{\varphi_2}$ représentent respectivement la phase moyenne du champ observé par les atomes dans les deux zones. T est le temps de vol libre entre les deux impulsions micro-onde qui dépend de la vitesse de lancement. Les crochets représentent la moyenne sur la distribution des trajectoires atomiques.

Nous avons testé dans la fontaine FO1 un prototype de la cavité d'interrogation de l'horloge PHARAO (voir figure 4.4). Au cours de ces mesures, la cavité de Ramsey est placée 2 cm au dessus de la cavité TE_{011} utilisée habituellement pour l'interrogation. Leur deux axes sont superposés. Le mode opératoire consistait initialement à mesurer les déplacements de fréquence pour une même vitesse de lancement, entre le fonctionnement conventionnel de la fontaine (interrogation dans la cavité TE_{011}), et une interrogation dans la cavité de Ramsey. Dans cette configuration, 6 zones d'interrogation sont disponibles et de nombreux schémas de fonctionnement sont possibles (2 ou 3 impulsions micro-onde dans la cavité de Ramsey). Cette expérience nécessite cependant une excellente atténuation du champ micro-onde. Nous avons pour cela utilisé une chaîne d'interrogation pulsée et un interrupteur micro-onde interférométrique, fournissant une atténuation globale de l'ordre de 120 dB. Ajoutons de plus qu'afin d'obtenir une largeur de résonance réduite, il est préférable d'appliquer au moins une impulsion à la montée et une à la descente.

Malheureusement cette méthode n'a pu être mise en pratique. En effet, lors de notre premier test, nous avons découvert une inclusion magnétique à

25 mm de l'entrée du guide sous coupure d'entrée de la cavité de Ramsey. La cavité avait évidemment été testée en magnétisme avant d'être placée sous vide, mais la zone défectueuse n'était malheureusement pas accessible à la sonde. Ce défaut, d'une amplitude d'environ 0.2 mG à une distance de 5 mm, induisait des transitions de Majorana qui produisaient un déplacement de fréquence important et masquaient la mesure des effets de phase. Nous avons donc été amenés à réaliser la préparation et l'interrogation après le passage des atomes devant cette perturbation.

Le mode opératoire finalement adopté consistait à appliquer l'impulsion micro-onde de sélection dans la première zone de Ramsey que les atomes traversent à la montée. L'interrogation s'effectue lors de la descente, en appliquant deux impulsions micro-onde dans les deux zones de Ramsey. L'inclusion magnétique nous empêchant de référencer nos mesures à un fonctionnement avec la cavité TE_{011} , nous avons procédé par comparaison avec le maser à hydrogène, en alternant chaque jour la vitesse de lancement (3.8 m/s et 4.2 m/s).

La moyenne pondérée des points expérimentaux mène à une différence de fréquence de $1.8 \times 10^{-15} \pm 16.6 \times 10^{-15}$ entre les deux vitesses de lancement. L'incertitude relativement importante est due à la limite de stabilité de la fontaine (largeur de frange respectivement de 4 et 6 Hz) et au faible nombre d'atomes détectés ($\sim 5 \times 10^4$) pour de si grandes vitesses de lancement. Elle s'explique également par l'incertitude sur la fréquence du maser. Les autres fontaines du laboratoire n'étant pas opérationnelles au moment des mesures, sa dérive de fréquence n'était pas bien connue. Une simulation a été réalisée [43] en utilisant une modélisation de la distribution de champ dans la cavité de Ramsey, fournie par l'IRCOM (Institut de Recherche en Communications et Micro-onde). Celle-ci suppose la symétrie des distributions phase entre les deux zones, mais que le déplacement de fréquence est dû à la présence d'un déphasage global. Ce calcul mène à un déplacement de fréquence de $6.79 \times 10^{-14} / \text{mrad} + 0.54 \times 10^{-14}$, linéaire avec le déphasage. Ces résultats nous conduisent à estimer un déphasage compris entre -300 et 0 μrad et nous confirme que la géométrie de cavité micro-onde proposée est adéquatée.

4.2 ACES scientific objectives

ACES (Atomic Clock Ensemble in Space) is a space mission which has been selected by European Space Agency (ESA) to fly for about 1.5 years on board the International Space Station (ISS) starting in 2007 [92, 90]. This experiment will be mounted on an external pallet (Express Pallet) of the European module Columbus. The ACES payload consists of two clocks: the cold caesium atom space clock PHARAO (Projet d'Horloge Atomique par

Refroidissement d'Atomes en Orbite, developed by CNES (Centre National d'Etudes Spatiales, France), BNM-SYRTE and LKB (Laboratoire Kastler-Brossel, France)), and a Space active Hydrogen Maser SHM (developed by the Neuchâtel Observatory, Switzerland). A two-way MicroWave Link (MWL) will allow accurate time and frequency transfers to users on earth (see fig. 4.1).

The objectives of ACES are both technical and fundamental.

The first objective is to operate the cold atom clock in space, taking the advantage of the reduced gravity environment, at a frequency stability better than 3×10^{-16} at one day and an accuracy of 1×10^{-16} . The SHM will be used for frequency comparison (stable flywheel oscillator) and for the evaluation of the frequency shifts affecting PHARAO accuracy.

With MWL, ACES will allow the synchronization of the time scales defined at distant ground laboratories with a 30 ps accuracy, more than two orders of magnitude beyond the present GPS and GLONASS system accuracy. Frequency comparisons between these distant clocks will be performed with a relative accuracy of 10^{-16} , about an order of magnitude improvement with respect to the present accuracy.

The third objective is to perform several fundamental physics tests with increased resolution.

-The gravitational red-shift will be measured with an accuracy of 3×10^{-16} , which gives an improvement of a factor 25 compared to previous measurements [93].

-The ACES experiment is expected to improve by about one order of magnitude the previous limit on the isotropy of the speed of light.

-Modern unified theories predict a possible variation of the fine structure constant α with time. This can be tested by measuring the frequencies of clocks using different atomic elements as a function of time (see chapter 4). The ACES experiment flying onboard the ISS (51° orbit inclination) will frequency link the major time and frequency metrology laboratories worldwide. This should improve by a factor of 100 the sensitivity of the α variation tests.

4.3 Brief description of PHARAO

The PHARAO instrument is supported by CNES and backed up by the scientific and technical experience of SYRTE and LKB. The industrial development started in June 2001 and the engineering model will be delivered at the end of 2004. As mentioned above, the relative frequency stability of the PHARAO clock is expected to be better than 3×10^{-16} at one day with a relative accuracy of 1×10^{-16} .

4.3. BRIEF DESCRIPTION OF PHARAO

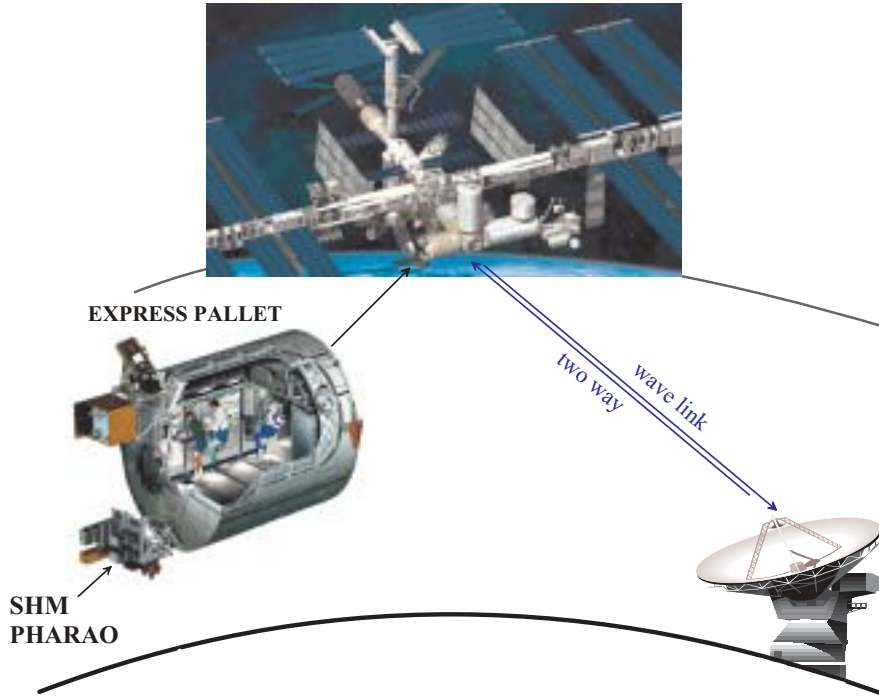


Figure 4.1: *Principle of ACES.*

On earth, in an atomic fountain, gravity obviously imposes a limit on the interaction time T , which is of the order of 1 s. T increases proportionally to the square root of the launching height H . Hence, increasing T by a factor of ten would impose a fountain height enhancement from ~ 1 m to ~ 100 m, a size which is not technically realistic when considering the atom environment control. In microgravity, such a long interaction time can be obtained in a reduced volume, merely by reducing the cold atom velocity.

The operation principle of PHARAO (see figure 4.2) is very similar to atomic fountains (see §1.4.2). During each cycle, caesium atoms are captured in optical molasses, launched and cooled below $1 \mu\text{K}$. They travel inside a 1.2 m long vacuum chamber, with a constant velocity. They first cross a state selection device made of a cylindrical microwave cavity and a pushing laser. They pass then inside a ~ 20 cm long two-zone cavity, where they undergo a Ramsey interrogation. The atomic response is then detected by the same optical system as in atomic fountains by measuring the population of both hyperfine levels. The resonance signal obtained is used to lock the local oscillator frequency.

One fundamental advantage of the set-up is the possibility to vary the atomic velocity over almost two orders of magnitude. This provides a new adjustable parameter to explore the accuracy-stability trade-off. The sta-

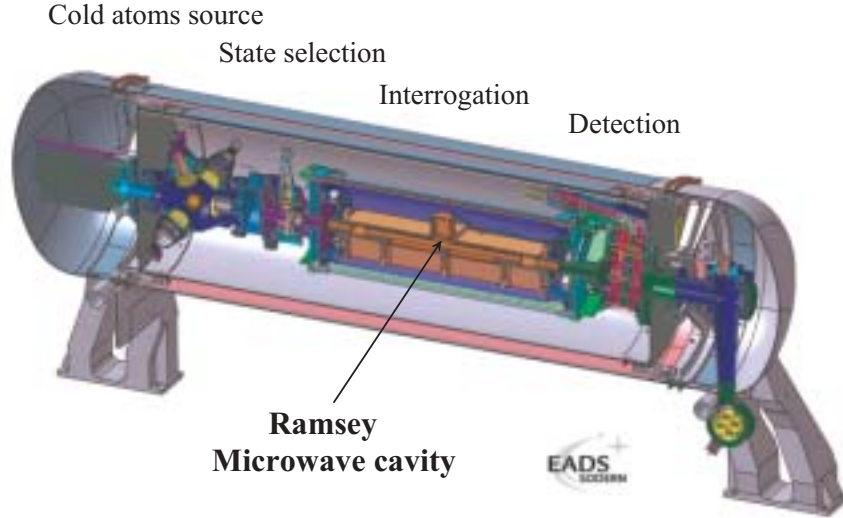


Figure 4.2: *The caesium tube of the PHARAO clock.*

bility will be limited for low velocities (some cm/s) by the loss of detected atoms due to the thermal expansion of the cold atom cloud, and for high velocity (some m/s) by the interaction duration. Nevertheless, since the atomic velocity is constant, the interrogation has to be performed in a two-zone microwave cavity. The system becomes then more sensitive to possible phase asymmetries between the two regions of the resonator, which could produce a frequency shift of the clock, associated with the Doppler effect.

4.4 Test of the PHARAO Ramsey cavity

4.4.1 Cavity phase shift

In order to reduce the Doppler effect in a caesium clock, the interrogation microwave field is confined inside a resonator made of high purity copper, where it is expected to be stationary. Nevertheless, due to the finite conductivity of the cavity walls, the electromagnetic field is not a perfect standing wave, and its phase $\varphi(\vec{r})$ is position dependent. Thus, a moving atom is subjected to a frequency shift

$$\delta\nu_\varphi(t) = \frac{1}{2\pi} \vec{\nabla}\varphi(t) \cdot \vec{v}(t) \quad (4.2)$$

where $\vec{\nabla}\varphi(t)$ and $\vec{v}(t)$ are respectively the phase gradient and the atomic velocity.

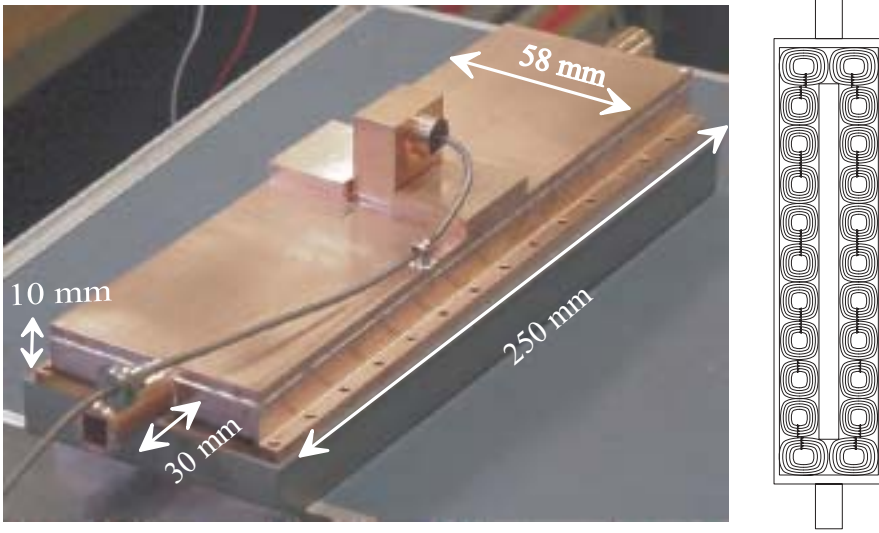


Figure 4.3: *Photograph of the Ramsey cavity of the PHARAO clock and drawing of its internal magnetic field distribution.*

In an atomic fountain, the Ramsey interrogation is performed during the double passage in the same cavity, with an opposite velocity direction during the atoms' ballistic flight. For vertical trajectories, this symmetry provides a perfect cancellation of the first-order Doppler effect, because the phase gradient is identical in the “two” zones. Nevertheless, for other trajectories the atoms are no longer subject to the same phase during their two transits. Hence, in total, a residual effect remains depending on the spatial variations of the field phase and amplitude inside the cavity and depending on the atomic position and velocity distributions. This effect is estimated to be below 10^{-17} [43].

In the PHARAO clock, the interaction is performed in a Ramsey cavity in two separate regions. The interrogation is thus sensitive to possible asymmetries of the phase distribution inside the two zones, and to a possible phase offset between the two regions, which depend directly on the construction symmetry of the cavity and on the distance between the two zones. These defects can be expressed as a phase offset $\Delta\varphi$ that produces a first-order Doppler effect given by the following formula, derived from equation (B.20):

$$\Delta\nu_{\Delta\varphi} \simeq \left\langle \frac{\overline{\varphi_2} - \overline{\varphi_1}}{2\pi T} \right\rangle \quad (4.3)$$

where $\overline{\varphi_1}$ and $\overline{\varphi_2}$ are respectively the average phase of the field seen by the atoms in each zone, T is the free time of flight between the two separated

pulses and the brackets denote the average over distribution of atomic trajectories.

Figure 4.3 gives a description of the Ramsey cavity developed for the PHARAO clock. It is a rectangular ring resonator whose external dimensions are $250 \times 58 \times 10$ mm. Three high purity copper pieces constitute this cavity. The main one includes the two interaction zones, two lateral waveguides and, in the middle, a cut-off waveguide that allows the atoms to pass through. Two cut-off waveguides (3 cm long) protect against microwave leakage. The advantage of this configuration is to have large apertures (8×9 mm) with low disturbances of the internal microwave field. As a precaution, diaphragms reduce the aperture of the entrance holes, to limit possible interactions between the atoms and the cavity walls. This main part is enclosed by a rectangular cover that supports the microwave waveguide coupler. The cavity is fed by a single coupler placed above the middle of the cavity. This is performed by the evanescent coupling between the two lateral waveguides and the supply cap, to limit the phase perturbation inside the interrogation zones.

A simulation of this cavity has been performed by Michel Aubourg at IRCOM (Institut de Recherche en Communications et Micro-onde, France) to determine the amplitude and phase variations inside a single interrogation zone, taking into account the conductivity of copper. It indicates that the maximum phase gradient along the cavity axis is of the order of $50 \mu\text{rad}/\text{mm}$. However, the possible dissymmetries between the two zones are not easy to estimate, because they depend directly on the mechanical realization. To get an order of magnitude, according to equation (4.3), and supposing only a constant phase offset, we obtain a sensitivity of $3.8 \times 10^{-14}/\text{mrad}$, for a launching velocity of 0.5 m/s, which is expected to provide the optimal performance of the clock.

4.4.2 Test of the Ramsey cavity phase shift using FO1

In order to verify the symmetry of the cavity described above, a cavity prototype is mounted inside the fountain FO1 (see fig. 4.4). The Ramsey cavity is placed 20 mm above the TE_{011} cavity. Their two axes are superposed. With this configuration, six interaction zones are available during a clock cycle, and many interrogation schemes can be investigated. For clarity, we name respectively A, B C and D the two interaction zones of the Ramsey resonator, depending on the atomic velocity direction (see fig. 4.4). The principle of the experiment was initially to compare the measured frequency shift between an interrogation inside the Ramsey cavity and the normal operation of FO1 using the TE_{011} cavity, for a constant launching velocity. With this

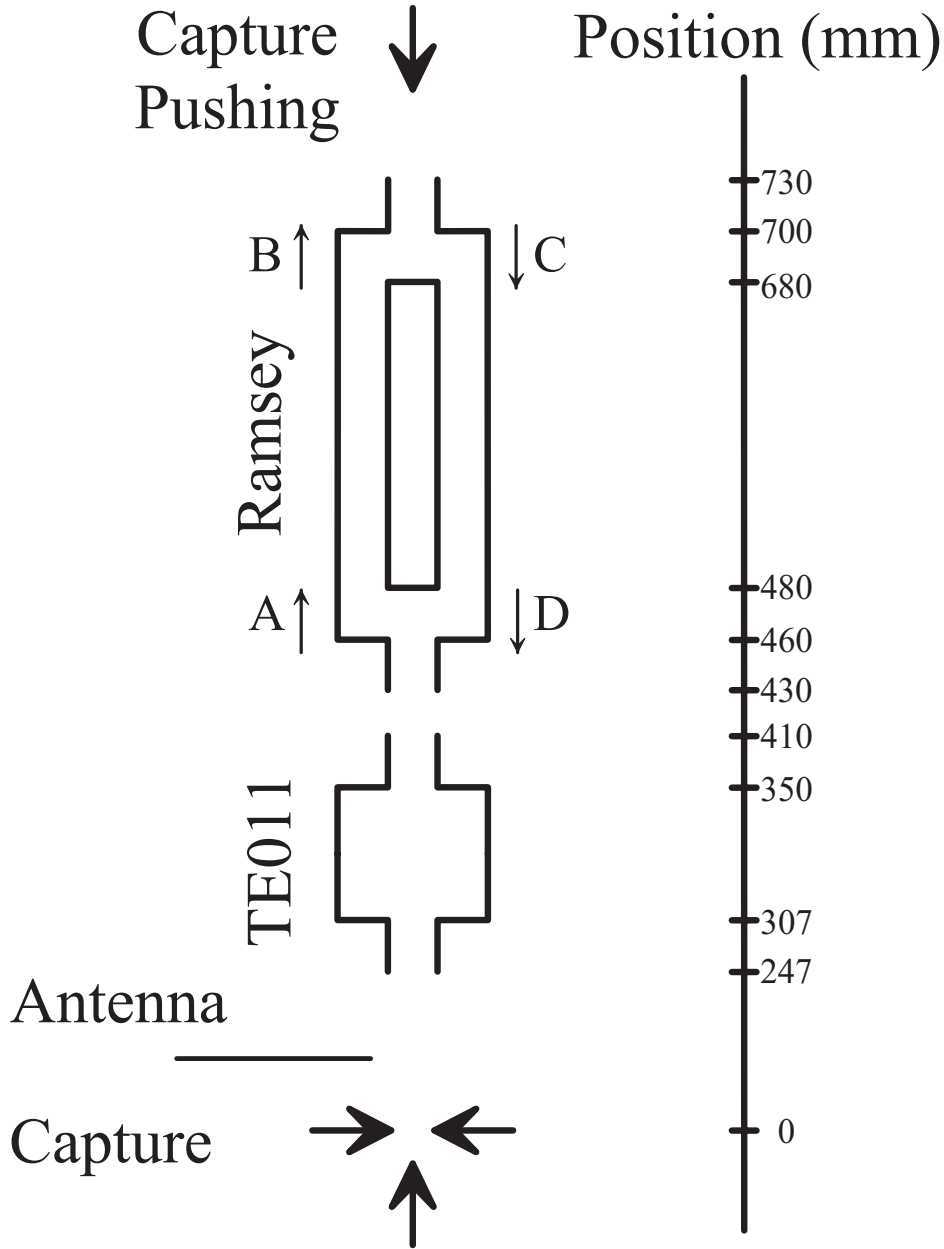


Figure 4.4: *The experimental set-up used to test the PHARAO Ramsey cavity inside the FO1 fountain. We distinguish the 4 different possible interaction process during the atomic ballistic flight as A, B, C and D respectively, where the arrows represent the direction of motion of the atoms.*

differential method, the reference maser frequency drift and the other clock frequency shift fluctuations are rejected.

This test requires the ability to pulse the microwave field at different moments during a clock cycle. This is performed with a pulsed microwave chain in addition to an interferometric switch, both commanded by TTL signals. This provides a total attenuation of \sim -120 dB. Moreover, it is preferable to apply at least one pulse on the way up, and one pulse on the way down. This optimizes the interaction duration to get a reasonable stability. Nevertheless the launching velocity must be larger than 3.7 m/s to ensure an apogee of the atoms above the Ramsey cavity. This induces a reduction of detected atoms and hence a degradation of the stability.

An interrogation with 4 pulses inside the Ramsey cavity is not very sensitive to the phase defects of the resonator. Indeed, as for the usual interaction scheme, in the TE₀₁₁ cavity the first-order effect due to the phase variations inside zone A (resp. B) will be compensated by the effect in zone D (resp. C). Only a residual effect remains due to the cold atom cloud expansion. Thus, a 3-zone interrogation scheme, which breaks this symmetry, is preferable.

Interrogation using three interaction zones

Alternating three interaction zones interrogations give access to the phase defects of the Ramsey cavity. The sequences $A \rightarrow B \rightarrow D$ and $A \rightarrow C \rightarrow D$ give opposite frequency shifts reflecting the phase variation in the upper Ramsey zone. In the same way, the opposite frequency shift measured with $A \rightarrow B \rightarrow C$ and $B \rightarrow C \rightarrow D$ depends on the phase variations inside the lower Ramsey zone. These configurations have been simulated [43] using the amplitude and phase distributions of the microwave field calculated by IRCOM. It assumes that the phase distributions are symmetric in the two Ramsey zones, and that the frequency shift is only due to a phase offset $\Delta\varphi$. For a 4.2 m/s launching velocity, we obtain $\Delta\nu_{ABC} = -2.87 \times 10^{-4}\Delta\varphi + 2 \times 10^{-6}$ Hz and $\Delta\nu_{ABD} = +2.2 \times 10^{-5}\Delta\varphi + 1 \times 10^{-5}$ Hz, where $\Delta\varphi$ is expressed in mrad. With the $\sim 10^{-15}$ resolution of FO1, a clear signature of the phase shift $\Delta\varphi$ should be measurable with a resolution better than 100 μ rad.

Unfortunately we applied this differential method without success. Indeed, the first operation of FO1 after installing the Ramsey cavity, showed a 10% loss of the Ramsey fringes contrast when using the TE₀₁₁ cavity. We found that this was due to a magnetic perturbation inducing Majorana transitions. The frequency of the transition $F = 4, m_F = 1 \leftrightarrow F = 3, m_F = 1$ changed by about 25 Hz when varying the atoms' apogee from 450 mm to 455mm. This was caused by some magnetic inclusion inside the Ramsey cavity, 25 mm above the entrance of the first cut-off guide. Of course, the

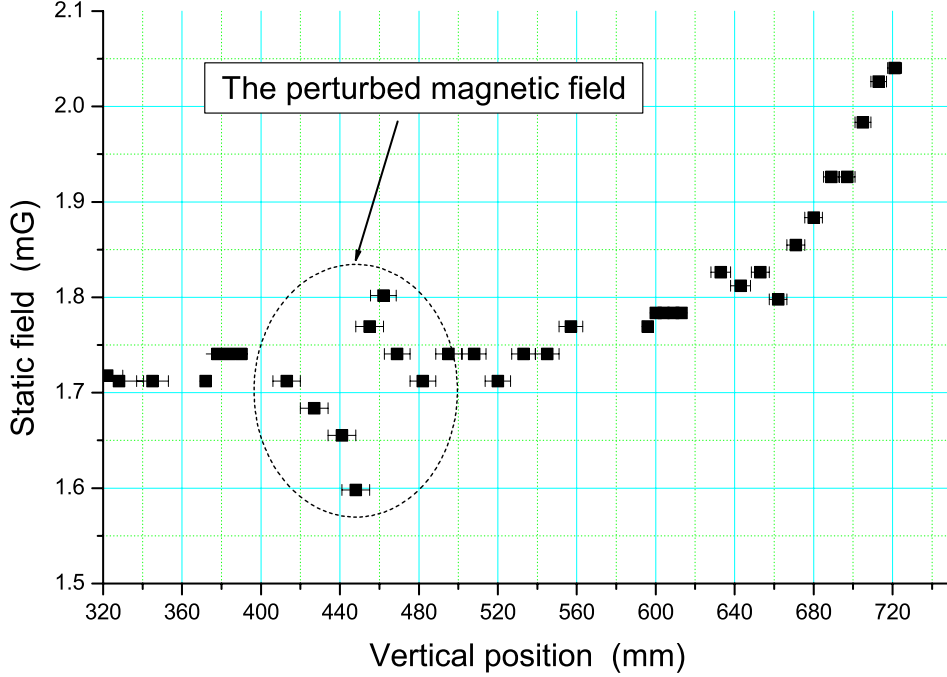


Figure 4.5: *Map of the static magnetic field.*

cavity had been tested before being installed, but this zone was not accessible to the magnetic probe. We measured the static magnetic field map inside the fountain. For that purpose, we disposed an antenna at the top of the FO1 fountain to excite the transition $F = 4, m_F = 1 \leftrightarrow F = 3, m_F = 1$ by short microwave pulses. Figure 4.5 shows the measured C field map. The magnitude of the magnetic perturbation is about 0.2 mG over a distance of 5 mm. This defect induced Majorana transitions which produce a large clock frequency shift. Due to this shift we could not apply the three-zone configuration to measure the microwave field phase effect. A two interaction zones operation was then chosen.

Interrogation using two interaction zones

We can use two launching velocities to perform the test. We apply the state selection microwave pulse (π Rabi transition) when the atoms are in zone A, above the magnetic perturbation position. The interrogation is performed by the combination of interaction process C and D. This was chosen because of the magnetic inhomogeneities above the Ramsey cavity. The current applied inside the compensation coils to reject the effect of the inclusion produced a distortion of the static magnetic field above the cavity. We operated the

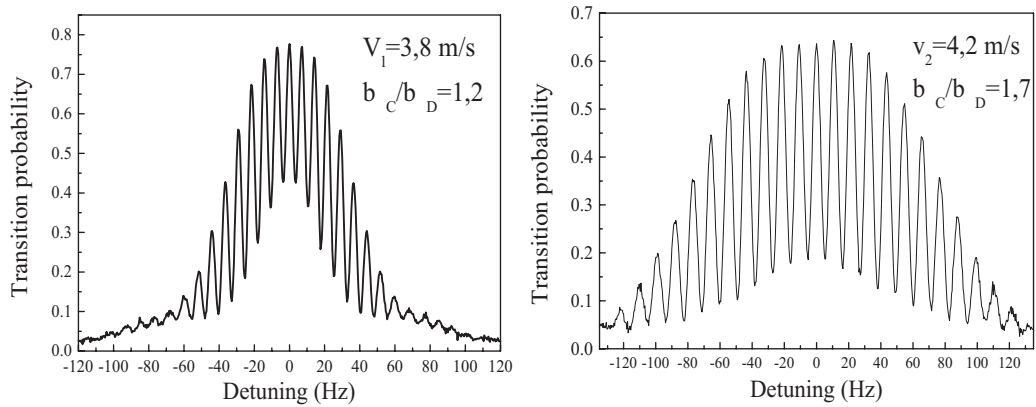


Figure 4.6: *The Ramsey fringes obtained with interaction process C and D for 2 different launching velocities.*

clock with the velocities $v_1 = 3.8$ m/s and $v_2 = 4.2$ m/s. The obtained Ramsey fringes are shown in figure 4.6. We noticed a contrast reduction that is due to the difference of interaction duration between the process C and D, because of the atomic velocity evolution during the parabolic flight.

For this test, it would have been better to apply a differential method alternating v_1 and v_2 . Unfortunately this parameter is not computer controlled in FO1. Thus, we just made a comparison with the H-maser when changing the launching velocity each day. The measurement results are presented in fig. 4.7, where the values are corrected for the main frequency shifts. The quadratic Zeeman frequency shift only depends on the C field inside the cavity, which is homogeneous and identical for the two measurement configurations. The collision shift is estimated at the level of 5×10^{-16} because the atom number and density are much reduced in our measurement¹. The blackbody radiation frequency shift and the red-shift are the same in the two modes of operation. The large error bars are due to the reduced stability $\sim 2 \times 10^{-12} \tau^{-1/2}$, caused by the large resonance width and the small number of detected atoms. The graph shows a dispersion of the points that we attribute to the drift of the maser, especially at the beginning of the measurement (7×10^{-15} per day). Unfortunately, this explanation could not be confirmed with the other fountains, because they were not operational at the time.

The weighted average of the experimental points gives a frequency difference of $(1.8 \pm 16.6) \times 10^{-15}$ between the two launching velocities. This value mainly contains the frequency shift due to the phase difference of the

¹The number of detected atoms is $\sim 10^4$, because of the high launching velocity and the aperture radius of the two cavities.

4.4. TEST OF THE PHARAO RAMSEY CAVITY

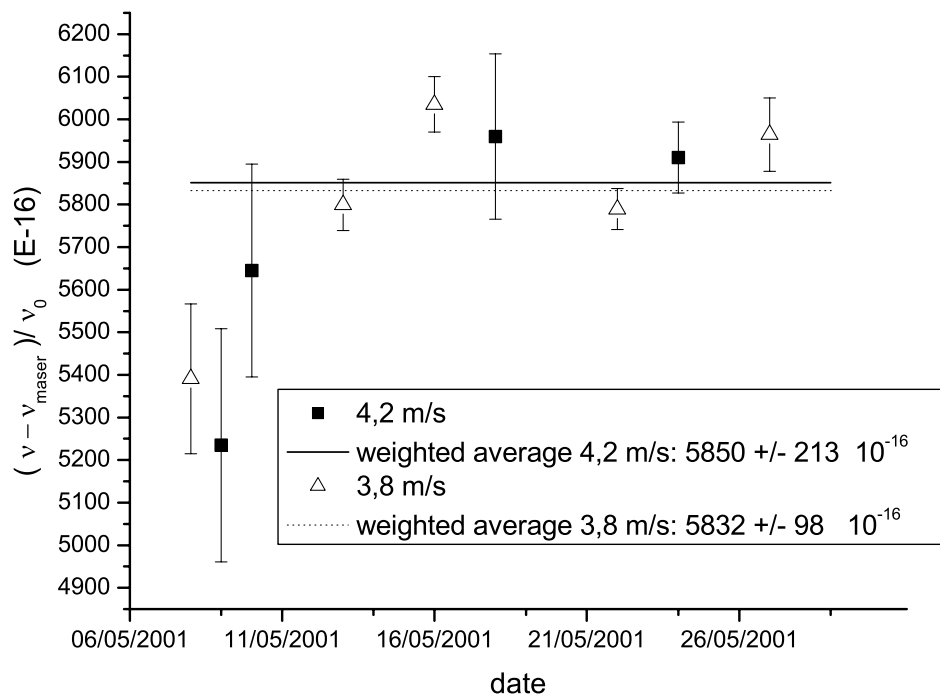


Figure 4.7: *The frequency shift due to the phase difference of the microwave field in the two Ramsey interaction zones compared to the H-maser.*

microwave field inside the two zones. A simulation using the data of IRCOM and assuming again symmetrical phase distributions in the two zones, gives a frequency shift of $6.79 \times 10^{-14}/\text{mrad} + 0.54 \times 10^{-14}$, linear with the phase offset between the two zones [43]. The effect doesn't vanish for zero phase offset because of the atomic velocity difference during the two microwave pulses. With these results, we estimate that the phase difference between the two zones is between -300 and 0 μrad . This preliminary result shows that the geometry of the Ramsey cavity meets the requirement of the PHARAO clock.

A complementary measurement method has been developed to analyze the phase asymmetry of the cavity. It is based on the analysis of the mode structure inside the Ramsey zones, around the dominant mode at 9.2 GHz. This has been simulated by IRCOM. The measurement can be performed in air, with an antenna passing through the cutoff waveguides when scanning the microwave frequency over several gigahertz. Phase asymmetries would exhibit new modes that should not exist if the cavity were perfect. This electronic method is very sensitive to mechanical defects (several micrometres), corresponding to a phase resolution of a few microradians.

Up to now, four new microwave cavities have been constructed. The best one has been selected by electrical measurements. This cavity has been mounted inside the improved FO1 (see chapter 6) to study the phase shift effect before being incorporated into the PHARAO clock. With the measurements and the simulations of IRCOM, we will be able to predict the cavity phase shift of the PHARAO clock operating in space with an uncertainty of few 10^{-17} . In order to improve measurement, we have experimentally studied one main uncertainty source of fountain clocks: the shift due to the blackbody radiation.

Chapter 5

Cs clock frequency shift due to blackbody radiation

5.1 Résumé en français

Le rayonnement du corps noir environnant les atomes de césium lors de leur interrogation dans la fontaine atomique produit une perturbation différentielle des niveaux d'énergie de la transition d'horloge. Cet effet se traduit par un déplacement de la fréquence d'horloge à césium $\delta\nu/\nu = -16.9(4) \times 10^{-15}(T/300)^4$ [94], où T est la température absolue. Ce déplacement est de l'ordre de 1.7×10^{-14} à température ambiante. On montre que dans le cas des horloges à césium, la contribution de la composante magnétique du rayonnement de corps noir est négligeable au niveau de 10^{-16} [55]. Cet effet est très important et doit être estimé à mieux qu'un pourcent pour obtenir une exactitude proche de 10^{-16} . La première vérification directe de cette loi dans une horloge à césium a été effectuée à la PTB sur un jet à sélection magnétique [95]. Cette mesure, en accord avec la théorie, était cependant limitée en résolution (12% à $T=300$ K, soit 2×10^{-15} en fréquence relative), à cause de la stabilité de l'horloge ($3.5 \times 10^{-12}\tau^{-1/2}$). Récemment, le groupe de l'IEN (Istituto Elettrotecnico Nazionale) en Italie a réalisé de nouvelles mesures [96] et Micalizio *et al.* ont fait des études théoriques [97], dont les résultats sont en désaccord de 15% , soit 2×10^{-15} sur la fréquence d'horloge à césium, par rapport aux valeurs couramment utilisées. La largeur de la densité spectrale d'énergie du rayonnement du corps noir est bien inférieure à la différence d'énergie entre l'état fondamental et les états électroniques excités, correspondant aux transitions dipolaires électriques des raies D_1 et D_2 , respectivement à 335 THz et 352 THz. La perturbation produite peut donc être approximée par celle d'un champ électrique lentement variable et de faible amplitude [98]. En tenant compte de l'isotropie de rayonnement,

on trouve que le déplacement de fréquence est proportionnelle à la différence de polarisabilité scalaire entre les deux niveaux hyperfins de l'état fondamental. Il ne dépend alors que de la moyenne du carré du champ électrique $\langle E^2(t) \rangle = (831.9 \text{ V/m})^2 [T(K)/300]^4$ (effet Stark dynamique).

L'effet Stark statique a été beaucoup étudié aussi bien expérimentalement que théoriquement [99, 100, 101, 102]. Au BNM-SYRTE Simon *et al.* ont mesuré dans une fontaine atomique le déplacement de fréquence induit par un champ électrique statique, avec une résolution de 0.2% [103]. La modélisation de cette expérience a permis de déduire l'effet du rayonnement de corps noir en fonction de la température :

$$\Delta\nu_{BBR} = -1.573(3) \times 10^{-4} \left(\frac{T}{300} \right)^4 \text{ (Hz)} \quad (5.1)$$

L'effet du spectre du rayonnement du corps noir peut être obtenu en intégrant chaque composante spectrale. La difficulté du calcul exact provient de la complexité de la somme, tenant compte de tous les états non perturbés. En effectuant quelques approximations développées par Itano [94] et Simon [104], il apparaît un terme en T^6 à l'équation (5.1). l'expression complète de l'effet du rayonnement du corps noir s'écrit donc :

$$\Delta\nu_{BBR} = -1.573(3) \times 10^{-4} \left(\frac{T}{300} \right)^4 \left[1 + \varepsilon \left(\frac{T}{300} \right)^2 \right] \text{ (Hz)}, \quad (5.2)$$

où le terme correctif $\varepsilon = 0.014$. Pour confirmer cette relation et pouvoir obtenir une exactitude dans la gamme des 10^{-16} , nous avons effectué une mesure directe de la dépendance de la fréquence d'horloge avec la température du rayonnement de corps noir. Cette mesure, réalisée sur la fontaine FO1 visait à déterminer la constante K_{Stark} au niveau de 1% et le terme correctif avec une incertitude de 25%. Cette expérience nécessite un chauffage jusqu'à $\sim 500 \text{ K}$ de l'environnement des atomes durant l'interrogation. Comme l'effet est relativement faible et afin de rejeter la dérive long terme du maser à hydrogène utilisé comme référence secondaire ($\sim 1.5 \times 10^{-15}$ /jour), nous avons comparé la fréquence de FO1 à celle de la fontaine rubidium FO2 du laboratoire.

Un dispositif radiatif inséré dans l'enceinte à vide a été spécialement conçu pour cette expérience. Il est composé d'un tube en graphite de 30 cm de long et de 1.6 cm de diamètre (épaisseur de paroi, 12 mm) suspendu 10 cm au dessus de la cavité d'interrogation. Pour une vitesse de lancement typique de 3.43 m/s les atomes passent 75% de leur vol libre à l'intérieur du dispositif. Le chauffage du tube de graphite est réalisé grâce à un fil

résistif en ARCAP de 10 m de long enrollé en double hélice. Le courant de chauffage est sinusoïdal (fréquence 100 kHz) et est appliqué et éteint de façon progressive. Ces deux précautions sont été prises afin de ne pas polariser les blindages magnétiques. Par ailleurs, le courant de chauffage n'est pas appliqué pendant l'interrogation afin de ne pas perturber les atomes par effet Zeeman. Le tube de graphite est entouré de deux blindages thermiques pour éviter tout chauffage excessif de la partie interne de l'enceinte à vide et de la cavité d'interrogation. La température de chauffage est contrôlée à l'aide de 4 thermistances. Elle s'exprime par une température effective au dessus de la cavité $T_{BBR} = (\overline{T^4(t)})^{1/4}$, obtenue par des calculs thermiques avec une exactitude de 0.6% (voir section 5.6).

Le mode opératoire est séquentiel et consiste à alterner des fonctionnements à deux températures, entrecoupé de périodes de thermalisation. La puissance micro-onde est également réajustée automatiquement, afin de tenir compte de l'évolution du désaccord de la cavité évoluant avec le chauffage. La période d'alternance entre chaque phase de mesure est de l'ordre d'une journée, au cours de laquelle la température est stabilisée à mieux que 2°C.

Les mesures ont été effectuées de manière aléatoire en fonction de la température, sur une période totale de plusieurs mois. L'exploitation des données issues de la comparaison avec la fontaine à rubidium FO2(Rb) mène à la relation :

$$\Delta\nu_{BBR} = -1.54(6) \times 10^{-6} \left(\frac{T}{300}\right)^4 \times \left[1 + \varepsilon \left(\frac{T}{300}\right)^2\right], \quad (5.3)$$

où l'incertitude tient compte de l'exactitude des deux fontaines, de leur stabilité et de l'incertitude sur la température effective. Dans cette expression on a pris la valeur théorique $\varepsilon = 0.014$. En effet, la contribution de ce terme n'étant que de 4% à 500 K, la stabilité des horloges lors de l'expérience n'était pas suffisante pour le déterminer. La dispersion des résultats provient des défauts de synchronisation de fonctionnement des deux horloges (~ 1 h), au nombre limité de points de comparaisons et à la gamme en température relativement réduite.

Cette mesure directe de l'effet du rayonnement du corps noir réalisée en comparaison avec la fontaine rubidium est en bon accord avec certains modèles développés sur l'effet Stark statique et dynamique [94, 100, 105], ainsi que sur les mesures les confortant [95, 101, 102, 103]. Notre mesure ne diffère que 2% de la mesure d'effet Stark statique effectuée au laboratoire. Cependant, ces résultats vont à l'encontre de ceux du groupe de l'IEN et d'un modèle développé par Feichtner et ses collègues en 1965 [99]

Néanmoins, l'incertitude que nous estimons sur nos résultats expérimentaux, de 3.9%, constitue une amélioration d'un facteur 3 par rapport aux précédentes mesures [95]. Nous estimons que ces mesures confortent les modèles couramment reconnus, et permettant une évaluation de l'effet du rayonnement du corps noir à température ambiante, avec une incertitude de quelques 10^{-16} .

5.2 Introduction

During their ballistic flight inside the fountain tube the cold atoms interact with a thermal radiation field in equilibrium near room temperature. This blackbody radiation (BBR) shifts the clock frequency. The authors of [94] predicted a fractional frequency shift with respect to the unperturbed Cs atom at $T = 0$ K of $-1.69 \times 10^{-14}(T/300)^4$ with a few percent uncertainty, where T is the thermodynamic temperature. In ref. [94], it is indicated that the main frequency shift is due to the blackbody electric field (through Stark effect). The thermal magnetic field is currently negligible at a level of 10^{-16} .

Up to now, there is only one published direct experimental verification of the BBR shift of atomic ground-state levels [95]. Because of the limit of their clock stability ($3.5 \times 10^{-12}\tau^{-1/2}$), PTB researchers reached a measurement uncertainty of 12% (2×10^{-15} in fractional frequency at $T=300$ K). Recently, a second measurement and a new theoretic calculation have been reported by the IEN (Istituto Elettrotecnico Nazionale) group in Italy [96, 97]. Their result is about 15%, *i.e.*, 2×10^{-15} , away from the currently accepted value.

At BNM-SYRTE, Simon *et al.* have measured the frequency shift induced by a static electric field in a fountain, with tenfold improvement in accuracy over previous results [103].

From these results, a BBR frequency shift has been theoretically deduced. The comparison of a direct measurement with this theoretical value would establish confidence in the Stark shift theories and in the evaluation of the BBR shift at the 10^{-16} level. After introducing the Stark shift theories and the relevant experiments, we will present our direct BBR frequency shift experiment.

5.3 The BBR shift theory

A blackbody heated to a given temperature T emits thermal radiation with a spectrum given by the Planck law¹:

$$\rho(\nu) = \frac{8\pi h\nu^3}{c^3} \frac{1}{e^{h\nu/k_B T} - 1} \quad (5.4)$$

where h is Planck's constant, c is the speed of light, and k_B is Boltzmann's constant. $\rho(\nu)$ is the BBR field energy in J/Hz/m³. The BBR exhibits a very broad spectrum at the room temperature, the full width at half maximum is approximately 30 THz. Figure 5.1 illustrates the behavior of $\rho(\nu)$ as a function of the wavelength for four values of the blackbody temperature. According to Wien's law, $T \lambda_m = b$, where λ_m is the BBR density spectrum peak wavelength, the constant $b = 2.898 \times 10^{-3}$ m·K. So, the peak wavelength is $\lambda_m = 9.66 \mu\text{m}$, $7.25 \mu\text{m}$, and $5.80 \mu\text{m}$ for temperatures $T = 300$, 400 , and 500 K, respectively.

The energy per unit volume of the electric and of the magnetic induction fields of the BBR at frequency ν are equal:

$$\frac{1}{2} [\epsilon_0 \langle E_\nu^2(t) \rangle + \mu_0^{-1} \langle B_\nu^2(t) \rangle] = \rho(\nu) \quad (5.5)$$

where $E_\nu(t)$ and $B_\nu(t)$ are the components of the electric and of the magnetic induction fields in the frequency interval $(\nu, \nu + d\nu)$. The angle brackets represent a time average. An integration over all frequencies (or wavelengths) gives the mean squared values of the fields

$$\langle E^2(t) \rangle = (831.9 \text{ V/m})^2 [T(K)/300]^4 \quad (5.6)$$

$$\langle B^2(t) \rangle = (2.775 \mu\text{T})^2 [T(K)/300]^4 \quad (5.7)$$

The Stefan-Boltzmann law gives the total energy flux Φ in watt emitted from a blackbody surface A at temperature T as:

$$\Phi = A \sigma T^4 \quad (5.8)$$

where $\sigma = 5.67051 \times 10^{-8}$ W/(m² K⁴) is the Stefan-Boltzmann constant.

5.3.1 AC Zeeman frequency shift of Cs clock

The BBR magnetic induction can cause a frequency shift of the $|4, 0\rangle \leftrightarrow |3, 0\rangle$ transition. We summarize the calculation of [55] just to show that this induced frequency shift can be neglected at present.

¹This discovery was the first motivation for the development of quantum theory physics.

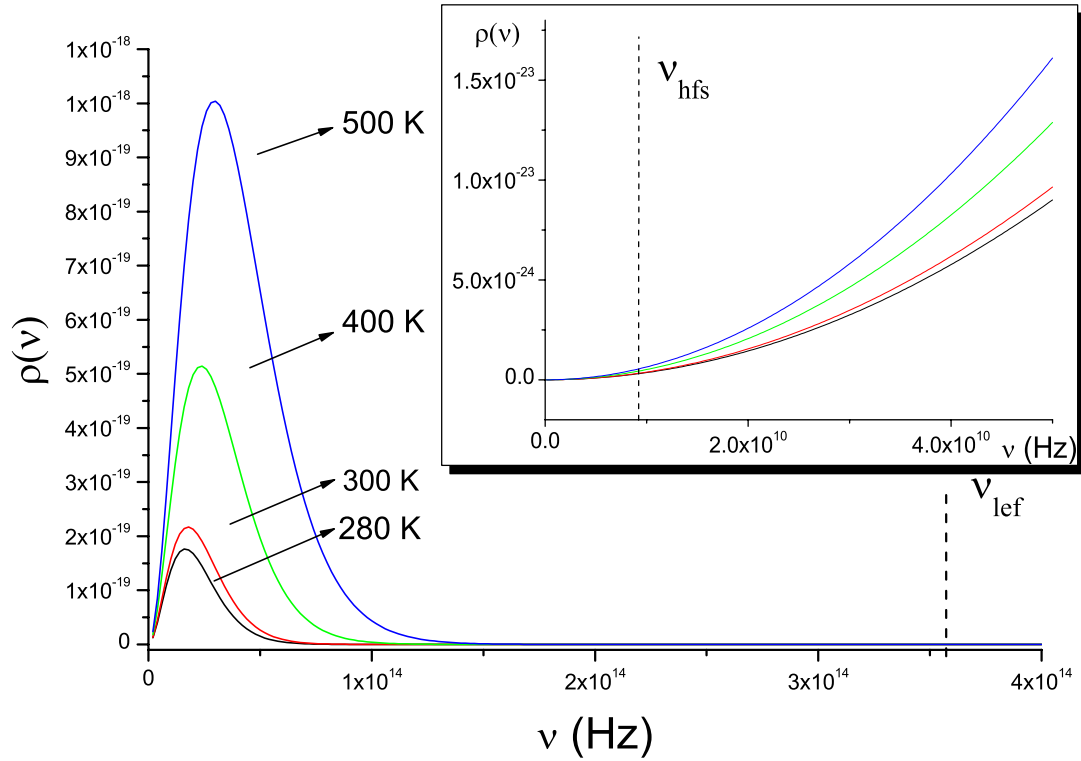


Figure 5.1: Spectral density of blackbody radiation for four temperatures. For Cs, the hyperfine splitting frequency ν_{hfs} in the ground state and the lowest allowed electric dipole transition frequency ν_{lef} are indicated.

The authors of [55] assumed a pure two-level quantum system subjected to a quadratic Zeeman shift by random perturbation. They transposed a simple calculation on AC stark shift for a two-level electric dipole transition coupled by a weak sinusoidal electric field [106] to the AC magnetic perturbation for the Cs clock case. For the clock transition $|4, 0\rangle \leftrightarrow |3, 0\rangle$, the levels involved can only be perturbed to first order by the projection of the random magnetic field induction along the direction of the magnetic C-field. It follows that one third of the isotropic magnetic field induction energy contributes to the AC Zeeman shift. For temperatures ≥ 300 K, one can ignore the calculation in the weak, near-resonant part of the blackbody spectrum (see figure 5.1). Furthermore, the contributions of the high- and low-frequency sides of the clock transition cancel to first order. Thus, we can use the magnetic field contribution for frequencies $\nu \gg \nu_{hfs}$. Finally, the shift is expressed as

$$\begin{aligned} \frac{\Delta\nu_{hfs}}{\nu_{hfs}} &= \frac{(g_j + g_i)^2 \mu_B^2}{3h^2} \int_{\nu \gg \nu_{hfs}}^{\infty} \frac{\frac{1}{2} B_\nu^2}{\nu_{hfs}^2 - \nu^2} d\nu \\ &\simeq -\mu_0 \frac{(g_j + g_i)^2 \mu_B^2}{3h^2} \int_0^{\infty} \frac{\rho(\nu)}{\nu^2} d\nu \\ &= -1.304 \times 10^{-17} (T/300)^2 \end{aligned} \quad (5.9)$$

where B_ν is the amplitude of the magnetic induction component oscillating at frequency ν . In the calculation, $g_j = 2$ and $|g_I/g_j| \ll 1$ have been assumed.

Finally, we conclude that the AC Zeeman shift due to the BBR magnetic field at room temperature is negligible for an accuracy objective of 10^{-16} .

5.3.2 Stark frequency shift of Cs clock

As seen in figure 5.1 the bulk spectral distribution of BBR is much smaller than the separation between the ground state and excited states, such as the lowest allowed electronic dipole lines in Cs, the D_1 line at $\nu_{lef}=335$ THz, and the D_2 line at 352 THz. This means that the electric field of the BBR can be approximated as a weak, slowly varying, non-resonant AC field [98]. Consequently, the rms value of the electric field strength can be an approximation of the BBR.

The hyperfine splitting in the $^2S_{1/2}$ ground of Cs induced by the DC Stark effect has been studied, extensively, both experimentally and theoretically. In the following we outline the principles of the DC Stark and AC Stark theories. Finally, we will arrive at an estimation of the BBR frequency shift in Cs clocks.

DC Stark effect

The classical interpretation can give us a simple, physical image of the quadratic Stark effect: an electric field applied to a one electron atom, such as an alkali metal atom², shifts its energy by

$$\Delta E_{Stark} = - \sum_{i,j} K_{i,j} E_i E_j \quad i, j \in x, y, z \quad (5.10)$$

where $K_{i,j}$ is a 3×3 matrix due to the direction dependence of the induced dipole moment, thus the polarizability is a tensor. If we assume that there is no privileged direction for the unperturbed atom, $K_{i,j}$ should degenerate and thus a scalar. In the case of a Cs clock, the system is symmetric with respect to the C-field direction z . We set $K_{x,x} = K_{y,y} = K_1$, and $K_{z,z} = K_2$. Using formula (5.10), we can express the Stark effect induced by an electronic field \mathbf{E} as shown in figure 5.2 by

$$\begin{aligned} \Delta E_{Stark} &= -(K_1 E_x^2 + K_1 E_y^2 + K_2 E_z^2) \\ &\equiv -E^2 (K_{sca} + K_{ten} \times \frac{3 \cos^2 \phi - 1}{2}) \end{aligned} \quad (5.11)$$

where $K_{sca} = \frac{1}{3}(2K_1 + K_2)$ is a scalar polarizability independent of the field direction, $K_{ten} \times \frac{3 \cos^2 \phi - 1}{2} = \frac{2}{3}(K_2 - K_1) \times \frac{3 \cos^2 \phi - 1}{2}$ is proportional to the polarizability difference between the direction z and x or y . We can easily find that this term vanishes when we average over all directions ($0 \leq \theta \leq 2\pi$; $-\pi/2 \leq \phi \leq +\pi/2$). Taking into account the isotropy of BBR, we can conclude that the contribution to the blackbody shift is only due to the scalar term.

It is more convenient to use the quantum interpretation to evaluate the perturbation, as well as to define the scalar term and the tensor term as mentioned above. An atomic state is perturbed by a uniform, static electric field \mathbf{E} as

$$H^E = \mathbf{E} \cdot \mathbf{P} \quad (5.12)$$

where $\mathbf{P} = - \sum_i e \mathbf{r}_i$ is the electric dipole moment summed over all the electrons, $-e$ is the charge of an electron, and \mathbf{r}_i is its position vector measured from the nucleus as the origin of the coordinate system. If we assume that the eigenfunctions $|0\rangle$ of Hamiltonian in absence of the field \mathbf{E} have a definite

²It possesses a single valence electron orbiting a closed spherically symmetric shell, thus it has no time-averaged electric dipole.

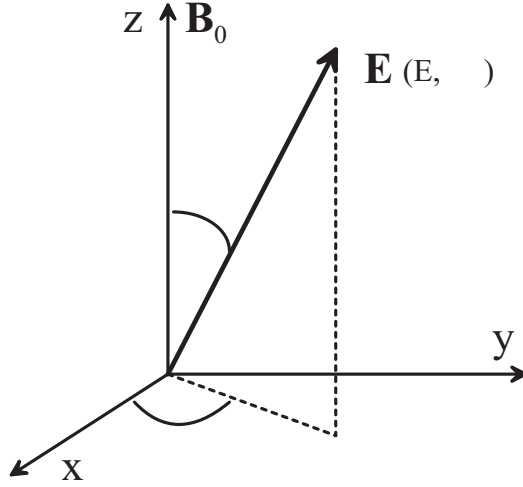


Figure 5.2: The direction of the electric field \mathbf{E} , where \mathbf{B}_0 is the C-field direction.

parity, the first order perturbation term would vanish in the perturbation expansion expression since $\mathbf{E} \cdot \mathbf{P}$ has odd parity. Thus the calculation normally uses the second order approximation. We will see that this is precise enough compared to the experimental uncertainty. The nature of the second order perturbation can be thought as that the atom has no permanent dipole moment, but an induced dipole moment which is then coupled to the external electric field, and then the interaction energy is proportional to the square of the field. According to perturbation theory, the energy change of the state $|0\rangle$ is given by the second-order perturbation as

$$\Delta E(0) = \sum_q \frac{\langle 0|H^E|q\rangle \langle q|H^E|0\rangle}{E(0) - E(q)} \quad (5.13)$$

In order to simplify the expression, we shall use the spherical basis notation where the components of \mathbf{E} are

$$E_{\pm 1}^1 = \mp \frac{\sqrt{2}}{2}(E_x \pm iE_y), \quad E_0^1 = E_z. \quad (5.14)$$

The components of \mathbf{P} are defined similarly. These components form a tensor of rank 1. Thus, H^E can be written as

$$H^E = \mathbf{E} \cdot \mathbf{P} = \sum_i (-1)^i E_{-i}^1 P_i^1, \quad i = -1, 0, +1. \quad (5.15)$$

We can immediately apply the Wigner-Eckart theorem to express the matrix element representing the coupling of two states $|n, L, J, F, m_F\rangle$ and $|n', L', J', F', m'_F\rangle$

by the field in terms of reduced matrix elements (RME)

$$\begin{aligned} \langle n, L, J, F, m_F | P_i^1 | n', L', J', F', m'_F \rangle &= (-1)^{F-m_F} \begin{pmatrix} F & 1 & F' \\ -m_F & i & m'_F \end{pmatrix} \\ &\times \langle n, L, J, F || P^1 || n', L', J', F' \rangle. \end{aligned} \quad (5.16)$$

where the term inside the large parentheses is the 3j coefficient which depends on the direction of the field. The RME is independent of m_F , and involves the radial part of the wave function, thus it represents the property of the Stark effect. After using the formulas 5.13 and 5.15, as in [107], we express the change in energy of the state $|n, L, J, F, m_F\rangle$ as a sum of scalar and tensor terms as

$$\Delta E_{n,L,J,F,m_F} = -\frac{1}{2}E^2 \left[K_S(F) + \left(K_T(F) \times \frac{3m_F^2 - F(F+1)}{F(2F-1)} \right) \times \frac{3\cos^2\phi - 1}{2} \right] \quad (5.17)$$

where

$$\begin{aligned} K_S(F) &= -\frac{2}{6F+3} \sum_{n',L',J',F'} (-1)^{F'-F} \times \frac{|\langle n, L, J, F || P^1 || n', L', J', F' \rangle|^2}{E_F - E'}, \\ K_T(F) &= -4\sqrt{\frac{5}{6}} \frac{(-1)^F \times \sqrt{F(2F-1)}}{\sqrt{(2F+3)(F+1)(2F+1)}} \sum_{n',L',J',F'} \left[\left\{ \begin{matrix} 1 & 1 & 2 \\ F & F & F' \end{matrix} \right\} \frac{|\langle n, L, J, F || P^1 || n', L', J', F' \rangle|^2}{E_F - E'} \right], \end{aligned} \quad (5.18)$$

where the factor in curly brackets is the 6j symbol. The quantum formula (5.17) also expresses the DC Stark shift in terms of the scalar and tensor hyperfine polarizabilities. As mentioned before, the second term is zero when we average over all directions. Thus, only the scalar term in BBR the frequency shift is important.

DC Stark shift of the Cs clock

P. G. H. Sandars has studied the energy levels and the splitting of the Zeeman levels of an alkalis atom in $S_{1/2}$ ground states subjected to a uniform electric field using a non-relativistic single-particle approximation [108]. The contributions of the three hyperfine interactions: the contact, the spin-dipolar and the quadruple, correspond to one scalar polarizability α_{10} and two tensor polarizabilities α_{12} and α_{02} , respectively³. In this way, the simple polarizability-dependent functions $K_S(F)$ and $K_T(F)$ are obtained. Finally, the formula

³The hfs interaction is written as a spherical tensor in the orbital, electron spin and nuclear spin space, hence the appearance of the subscripts.

(5.17) can be expressed in the form

$$\Delta E_{F=I+1, m_F} = -\frac{1}{2}E^2 \left[\alpha + \alpha_{10} + \frac{3m_F^2 - (I + \frac{1}{2})(I + \frac{3}{2})}{I(2I + 1)}(\alpha_{12} + \alpha_{02}) \times \frac{3\cos^2\phi - 1}{2} \right] \quad (5.19)$$

$$\begin{aligned} \Delta E_{F=I-1, m_F} = & -\frac{1}{2}E^2 \left\{ \alpha - \frac{I+1}{I}\alpha_{10} + \frac{3m_F^2 - (I^2 - \frac{1}{4})}{(I-1)(2I-1)} \right. \\ & \times \left[\frac{(2I-1)(I-1)}{I(2I+1)}\alpha_{12} + \frac{(2I+3)(I-1)}{I(2I+1)}\alpha_{02} \right] \times \frac{3\cos^2\phi - 1}{2} \left. \right\} \end{aligned} \quad (5.20)$$

where α is the familiar polarizability in the absence of hfs effects. This does not lead to any differential splitting of the hfs levels. The frequency shift on the clock transition $\Delta\nu_{Stark}$ due to the DC Stark effect is then given by

$$\begin{aligned} h\Delta\nu_{Stark} &= \Delta E_{F=4, m_F=0} - \Delta E_{F=3, m_F=0} \\ &= -\frac{1}{2}E^2 \left(\frac{16}{7}\alpha_{10} - \frac{2}{7}\alpha_{12} \times \frac{3\cos^2\phi - 1}{2} \right) \end{aligned} \quad (5.21)$$

The atomic states involved in Cs clock are the following (see fig. A.1):

$|6S_{1/2}, F=3, m_F=0\rangle : |n=6, L=0, S=1/2, J=1/2, I=7/2, F=3, m_F=0\rangle$; $|6S_{1/2}, F=4, m_F=0\rangle : |n=6, L=0, S=1/2, J=1/2, I=7/2, F=4, m_F=0\rangle$.

According to the properties of the $3j$ coefficient, the condition for the matrix element $\langle n, L, J, F, m_F | P_i^1 | n', L', J', F', m'_F \rangle$ being different from zero is that both $\Delta F = 0, \pm 1$, $F' + F \geq 1$ and $\Delta m_F = 0, \pm 1$. Also according to the selection rule for the electric dipole transition in [109], we can find the atomic states which can perturb the clock transition frequency as follows:

For $|6S_{1/2}, F=3, m_F=0\rangle$: the states $nP_{1/2}$, $F=3,4$, and $m_F=0, \pm 1$; the states $nP_{3/2}$, $F=2,3,4$, and $m_F=0, \pm 1$, where $n \geq 6$.

For $|6S_{1/2}, F=4, m_F=0\rangle$: the states $nP_{1/2}$, $F=3,4$, and $m_F=0, \pm 1$; the states $nP_{3/2}$, $F=3,4,5$, and $m_F=0, \pm 1$, where $n \geq 6$.

S. A. Blundell *et al.* [110] developed a relativistic all-order method to calculate the dipole-matrix elements in Cs. The theoretical and experimental results agree at a level of 0.5%. It is mainly significant for the coupling between the $6P$ and $7P$ states (less than 6 Bohr radii) and decreases with the principal quantum number n . However, the perturbation contribution to the $6S$ state via the $6P$ states ($6P_{1/2}$ and $6P_{3/2}$) is about 185 times bigger than that of the $7P$ state, because the energy separation between $6S_{1/2}$ and $6P_{1/2 \text{ or } 3/2}$ is smaller. The differential perturbations to the ground state of Cs by the state $n=7, 8$, and 9 can be also found in the calculated polarizability

(ratio 64.73:0.301:0.041) [99]. Therefore, usually only the couples $6S - 6P_{1/2}$ and $6S - 6P_{3/2}$ are taken into account as an approximation. This directly yields the polarizability $\alpha_{12}/h = -4.13 \times 10^{-12} \text{ Hz}/(\text{V}/\text{m})^2$ and a ratio of $\alpha_{12}/\alpha_{02} = 578$, when using the experimental values cited in [111].

Using the experimental results of each polarizability, the ratio is about $\alpha_{10} : \alpha_{12} : \alpha_{02} \simeq 10^4 : 5 \times 10^2 : 1$ (see [104]). A measurement of the differential Stark shift induced on the transition $6^2S_{1/2}(F = 4, m_F = -3) \leftrightarrow (F = 4, m_F = -4)$ gave $\alpha_{12}/h = (-3.66 \pm 22) \times 10^{-12} \text{ Hz}/(\text{V}/\text{m})^2$ [112]⁴, and a recent measurement using an all-optical Ramsey resonance technique reported $\alpha_{12}/h = (-3.34 \pm 25) \times 10^{-12} \text{ Hz}/(\text{V}/\text{m})^2$ [113] when we neglect the quadrupole interaction.

In the following, we list several theoretical calculations and experimental data on the clock transition which is related to α_{10} . The applied electric field is parallel to the magnetic field, *i.e.*, $\phi = 0$ and $\Delta\nu_{Stark} = K'E^2 = -\frac{1}{h}(\frac{8}{7}\alpha_{10} - \frac{2}{7}\alpha_{12})E^2$.

$K' = -1.9(2) \times 10^{-10} \text{ Hz}/(\text{V}/\text{m})^2$ theory by J. D. Feichtner *et al.* [99]

$K' = -2.2302 \times 10^{-10} \text{ Hz}/(\text{V}/\text{m})^2$ theory by T. Lee *et al.* [100]

$K' = -2.29(3) \times 10^{-10} \text{ Hz}/(\text{V}/\text{m})^2$ experiment by J. R. Zacharias *et al.* [101]

$K' = -2.25(5) \times 10^{-10} \text{ Hz}/(\text{V}/\text{m})^2$ experiment by J. R. Mowat [102]

The most accurate experimental value [103] performed in FO1 has given:

$$\begin{aligned} \Delta\nu_{Stark} &= -\frac{1}{2}E^2 \left(\frac{16}{7} \frac{\alpha_{10}}{h} + \frac{1}{7} \frac{\alpha_{12}}{h} \right) \\ &= -2.271(4) \times 10^{-10} E^2 \end{aligned} \quad (5.22)$$

where $\phi = \pi/2$ is set by the experimental apparatus. Using the experimental values of α_{12} , we can get $\frac{8}{7h}\alpha_{10} = 2.273(4) \times 10^{-10} \text{ Hz}/(\text{V}/\text{m})^2$. Assuming that the AC Stark frequency shift due to BBR is determined by the rms value of the electric field strength, a theoretical evaluation of the BBR frequency shift on the clock transition at temperature T gives

$$\Delta\nu_{BBR} = -\frac{8}{7} \frac{\alpha_{10}}{h} \langle E^2 \rangle = -1.573(3) \times 10^{-4} \left(\frac{T}{300} \right)^4 \text{ (Hz)} \quad (5.23)$$

Using Mowat's (DC Stark) experimental results [102], Itano deduced that the frequency shift in Cs clock operating at room temperature (300 K) is $1.55(4) \times 10^{-4} \text{ Hz}$ [94].

Frequency shift of Cs clock: effect of the BBR spectrum

The effect of the BBR spectrum can be obtained by integrating each single frequency component $\vec{E}_\nu \cos(2\pi\nu t) \cdot \vec{\epsilon}$ along the direction $\vec{\epsilon}$ at frequency

⁴The reported rate $\Delta\nu/E^2$ is multiplied by 8/3 to infer the polarizabilities.

ν , which is assumed no correlated with others. The total BBR shift of the clock transition due to a the perturbing state $|x\rangle$ can be calculated using second-order perturbation theory [98]:

$$\Delta\nu_{BBR} = \frac{e^2}{2h} \sum_{x \neq 4 \text{ or } 3} \int_0^\infty \left[|\langle 4 | \vec{\epsilon} \cdot \vec{r} | x \rangle|^2 \left(\frac{1}{E_4 - E_x - h\nu} + \frac{1}{E_4 - E_x + h\nu} \right) - |\langle 3 | \vec{\epsilon} \cdot \vec{r} | x \rangle|^2 \left(\frac{1}{E_3 - E_x - h\nu} + \frac{1}{E_3 - E_x + h\nu} \right) \right] \frac{E_\nu^2}{2} d\nu, \quad (5.24)$$

where x represents the complete quantum numbers of an atomic state $|n'P'_{J'}, F'\rangle$, state $|6S_{1/2}, F = 4\rangle$ ($|6S_{1/2}, F = 3\rangle$) is denoted as $|4\rangle$ ($|3\rangle$).

It is possible to separate the expression (5.24) into two terms: scalar and tensor. As previously mentioned, only the scalar polarizabilities contribute to the BBR frequency shift, which is thus independent of the spin and magnetic moment of the nucleus. We can calculate $\Delta\nu_{BBR}$ by exploiting the DC Stark theory result in equation (5.17), but only the scalar term $K_s(F)$ is involved. To simplify the expression, we write

$$\langle 6S_{1/2}, F | P^1 | n'P'_{J'}, F' \rangle = e \sqrt{\frac{2F+1}{3}} \langle 6S_{1/2}, F | r | n'P'_{J'}, F' \rangle \quad (5.25)$$

In this way, the frequency shift of Cs clock $\Delta\nu_{BBR}$ due to the blackbody radiation can be expressed by

$$\Delta\nu_{BBR} = \frac{1}{9} \frac{e^2}{2h} \sum_{x \neq 4 \text{ or } 3} \int_0^\infty \left[|\langle 4 | r | x \rangle|^2 \left(\frac{1}{E_4 - E_x - h\nu} + \frac{1}{E_4 - E_x + h\nu} \right) - |\langle 3 | r | x \rangle|^2 \left(\frac{1}{E_3 - E_x - h\nu} + \frac{1}{E_3 - E_x + h\nu} \right) \right] \frac{E_\nu^2}{2} d\nu. \quad (5.26)$$

The problem of an exact calculation of the quantitative frequency shifts is very difficult and involves evaluating spectral sums over the complete set of unperturbed states. An approximation method has been developed by Itano [94] and Simon [104]. After using the experimental and theoretical data, we can derive a corrective term which accounts for the BBR spectrum with respect to the DC Stark shift of the Cs clock transition. We summarize their approximations and results. The calculation follows four assumptions:

1. The corrected energies ε_3 and ε_4 due to the hyperfine interaction are very small compared to the term $E_x - E_{6S} \pm h\nu$, so we can apply the formula

$$\frac{1}{E_x - E_4 \pm h\nu} \simeq \frac{1}{E_x - E_{6S} \pm h\nu} + \frac{\varepsilon_4}{(E_x - E_{6S} \pm h\nu)^2}. \quad (5.27)$$

2. A wave function decomposition of $|4\rangle = |6S\rangle + |\varepsilon_4\rangle$ is used according to the first-order hyperfine perturbation, and a second-order approximation $|\langle\varepsilon_4|r|6P\rangle|^2 \simeq 0$ is adopted. The treatment of state $|3\rangle$ is similar.

3. The lowest allowed electric dipole transition frequency ν_{lf} is much higher than the bulk spectral distribution of BBR at ambient temperature, thus a *slowly varying perturbation* is taken into account [98]. A second-order approximation in term $h\nu/(E_{6P} - E_{6S})$ is applied.

4. The previous analysis shows that the coupling $6S - 6P$ contributes to 96% of the ground state perturbation [110]. The $6P$ state is used to calculate the first fine structure resonance line. Thus, the summation calculation of $\sum_x h\nu/(E_x - E_{6S})$ is simplified to $h\nu/(E_{6P} - E_{6S})$.

Finally, the frequency shift due to the BBR can be expressed in the form

$$\Delta\nu_{BBR} = (K_1 + K_2) \frac{E_\nu^2}{2} \left[1 + \frac{3K_1 + K_2}{K_1 + K_2} \left(\frac{h\nu}{E_{6P} - E_{6S}} \right)^2 \right]. \quad (5.28)$$

where

$$K_1 = -\frac{2e^2}{9h} \sum_x \frac{\langle 6S|r|x\rangle \langle x|r|\varepsilon_4\rangle - \langle 6S|r|x\rangle \langle x|r|\varepsilon_3\rangle}{E_x - E_{6S}}, \quad (5.29)$$

$$K_2 = -\frac{2e^2}{9h} \sum_x \left(\frac{|\langle 6S|r|x\rangle|^2}{E_x - E_{6S}} \times \frac{E_4 - E_3}{E_x - E_{6S}} \right).$$

K_1 and K_2 come from the contributions of the perturbed wave functions and from the hyperfine splittings of the levels, respectively. Comparing to the DC stark shift formula (5.23), we can immediately find $(K_1 + K_2) = -\frac{8}{7} \frac{\alpha_{10}}{h}$, the scalar polarizability. One can get the value $\frac{3K_1+K_2}{K_1+K_2}$ of 2.33 in [99] and of 2.295 in [100]. An integration over the BBR spectrum gives the frequency shift of the Cs clock due to the BBR Stark effect at temperature T

$$\Delta\nu_{BBR} = K_{Stark} \left(\frac{T}{300} \right)^4 \left[1 + \varepsilon \left(\frac{T}{300} \right)^2 \right]. \quad (5.30)$$

The effect of the frequency distribution of the blackbody electric field increases the frequency shift relative to the value for a DC electric field of the same rms value by a factor of $\varepsilon \left(\frac{T}{300} \right)^2 = 0.014 \left(\frac{T}{300} \right)^2$ when we take the energy of center of gravity of $|6P_j\rangle$ as $E_{6P} - E_{6S} = 2.277 \times 10^{-19}$ J.

We would like perform an uncertainty analysis of the estimation of ε . The simplification of using only the $6P$ state to replace all the states $|x\rangle$ produces an error of about 4%. The theoretical evaluation of the term $\frac{3K_1+K_2}{K_1+K_2}$ has an uncertainty less than 10% according to [99]. We can conclude that the relative

uncertainty of the correction factor ε is about 10%. When a caesium clock is operating at 300K, this uncertainty is 2.6×10^{-17} .

Using the DC Stark experiment result in [103] (the most accurate), one has $K_{Stark} = -1.573(3) \times 10^{-4}$ Hz. Bauch and Schröder found it as $1.53(18) \times 10^{-4}$ Hz using two Cs atomic beam clocks in PTB [95].

Recently, V. G. Pal'chikov *et al.* have theoretically estimated the BBR shift in Cs clocks, including a calculation for the higher-order field contributions (hyperpolarizabilities) [105]. The frequency shift is given by

$$\begin{aligned} \Delta\nu_{BBR} = & -1.58 \times 10^{-4} \left(\frac{T}{300}\right)^4 \\ & \times \left[1 + 0.014 \left(\frac{T}{300}\right)^2 - 3.18 \times 10^{-5} \left(\frac{T}{300}\right)^2 \right]. \end{aligned} \quad (5.31)$$

These theoretical results with an uncertainty⁵ of less than 5% are in agreement with the theory-experiment results in formula (5.30). All the previously reported results (theory and experiment) are in a good agreement but in strong disagreement with the most recent theoretical value ($K_{Stark} = 1.37(6) \times 10^{-4}$ Hz) reported by IEN [97]. In the following sections, we will present a direct BBR frequency shift measurement which verifies these results.

5.4 The experimental setup

In order to check the previous predictions of formula (5.30) at a level of 1% and try to experimentally determine ε , we decided to measure directly the BBR frequency shift in FO1 fountain. In normal operation FO1 can provide a frequency measurement resolution of $\sigma_y = 1 \times 10^{-15}$ in 4 hours. When we want determinate term K_{Stark} at a level of 1%, the the blackbody temperature should be heated to ~ 500 K. At this temperature, it seems possible to measure ε with a 25% uncertainty. In order to reach this measurement accuracy, we also have to determine the temperature⁶ at a level of 0.25%. Even at this high temperature (500 K), the clock shift is only $\sim 10^{-13}$. Furthermore, changing the blackbody temperature from 300 K to 500 K and stabilize it at a given temperature takes a long time. At high temperatures, one measurement with the expected resolution will be extended to 1 or 2 days. Thus, to perform a precise BBR shift measurement, we need a very stable long-term frequency reference.

⁵Private communication.

⁶According equation (5.30), $dK_{Stark}/K_{Stark} \simeq d\Delta\nu_{BBR}/\nu_{BBR} - 4 dT/T$.

5.4.1 Experimental setup

The blackbody experiment should avoid excessive heating of the cavity and must be designed so that we are able to determinate the thermal field experienced by the atoms along their path inside the clock.

The scheme of the experimental set-up is shown in figure 5.3. The BBR radiator is a 30 cm high graphite tube with an aperture of 1.6 cm in diameter. It is suspended 10 cm above the cavity. Typically, it occupies about 75% of the total ballistic flight of atoms above the cavity.

In order to heat the graphite tube, a 10 m long entwined wire pair (to reduce magnetic field radiation) in ARCAP (non-magnetic material) is wound around the tube and electrically isolated by a fiberglass braid. The heating current frequency is 100 kHz and the supplied electrical power is 10.6 W. In order to avoid a possible polarization of the magnetic shield, the amplitude of the heating current is slowly turned off/on within a few miliseconds.

Two thermal shields surrounding the graphite tube prevent excessive heating of the cavity and the vacuum chamber (see fig. 2.1). The first shield, with a square section, is made of 4 sheets and 2 caps (see figure 5.4.1 (b)). These 6 aluminum pieces are highly polished. This shield is fixed to the graphite tube by 8 ceramic pins ($\phi \times l = 6 \times 6$ mm) as shown in figure 5.3. The second shield is an aluminum (AU4G) tube whose inner face is polished as well. In order to reduce the cavity heating, the bottom of this cylinder tube is closed by a cap. The graphite tube and the first shield inside the aluminium tube are suspended by 4 glass rods at each end to reduce thermal conduction. The second shield is thermally connected to the water cooled top of the vacuum tube. As a result, when the graphite tube is heated to about 500 K, the cavity temperature increases by less than 6 K (as measured by its resonance frequency). To avoid thermally induced electrical currents, all the conductive pieces in contact are in aluminium. The thermal properties of these materials are given in table 5.1.

As shown in figure 5.3, the temperature of the graphite radiator and of the second thermal shields are directly measured with a 0.5 K uncertainty by 4 thermistors (Pt100) connected to an ohm-meter by silver wires. In order to reduce heat losses through the thermistor wires, the temperature of the first shield is not measured.

5.4.2 Characteristics

Here, we list some characteristics of our experiment which will be useful for a thermal calculation.

A perfect blackbody surface absorbs all incident radiation. To realize of such a blackbody in the laboratory we use a hollow cavity. The radiation

5.4. THE EXPERIMENTAL SETUP

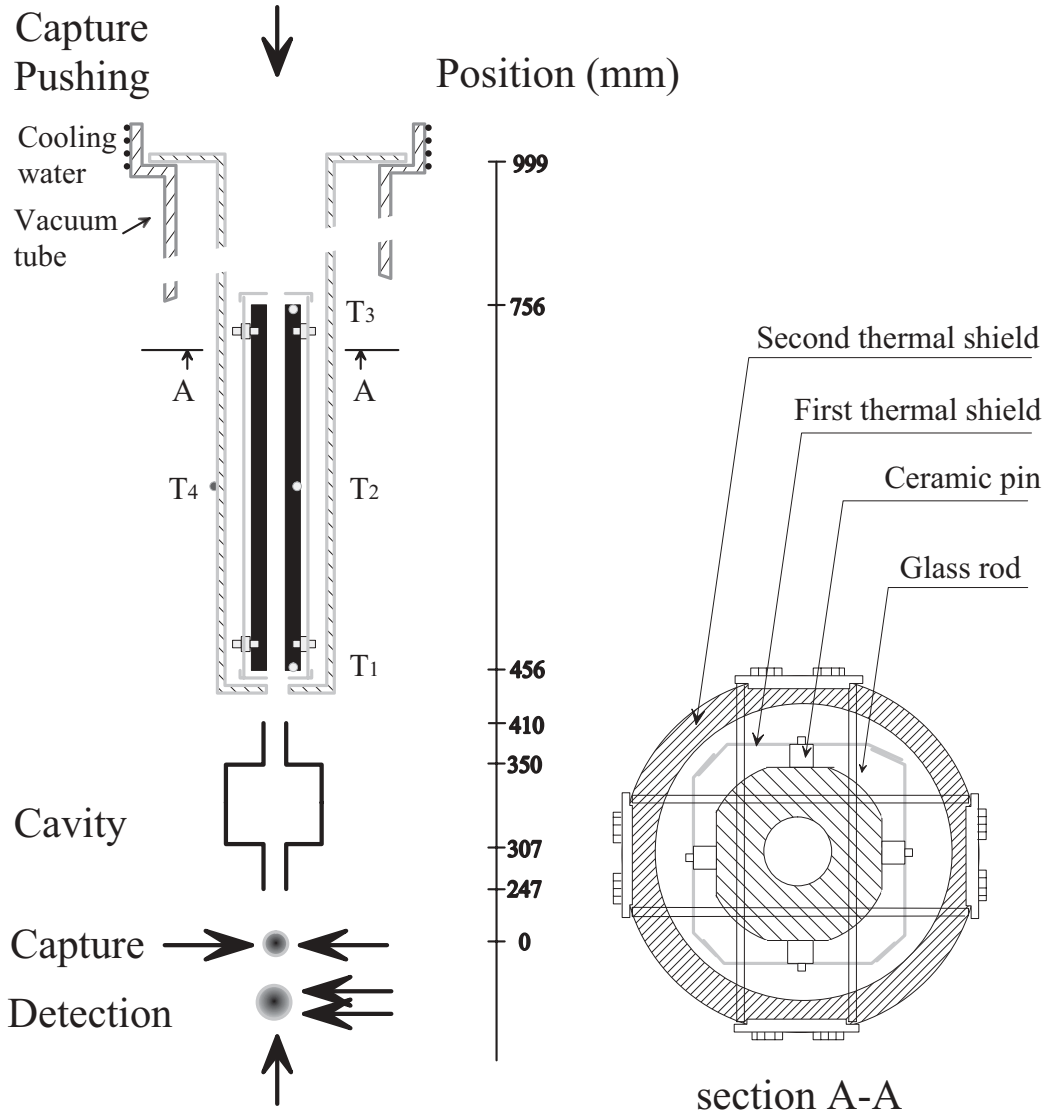


Figure 5.3: Sketch of the BBR frequency shift measurement setup in FO1. T_1 to T_4 indicate the positions of the thermistors inlaid in the graphite tube and the second thermal shield.

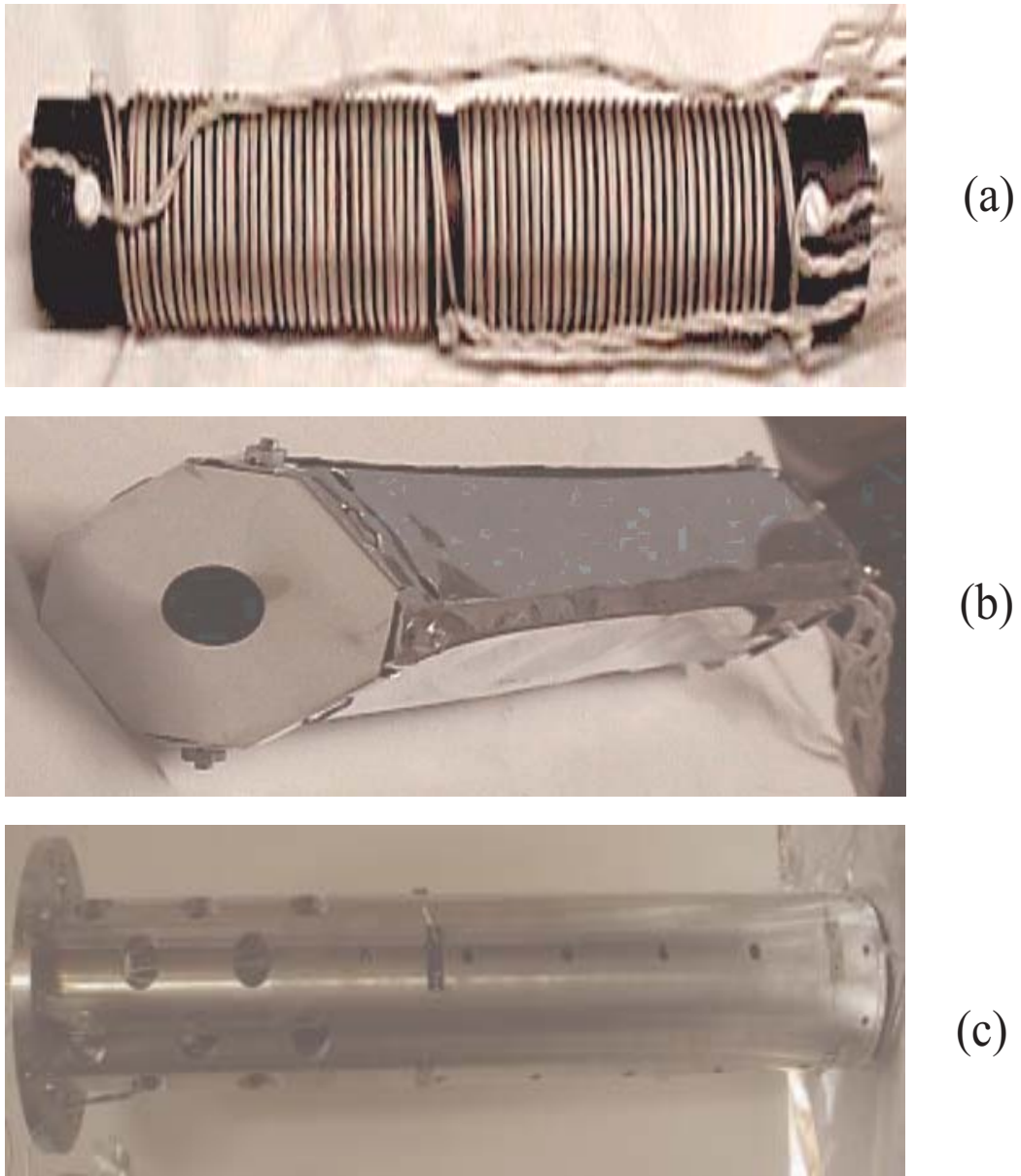


Figure 5.4: *BBR shift measurement setup. (a) The graphite tube with the heating wire and the thermistors. (b) The graphite tube enclosed by the first thermal shield. (c) The cylindrical tube, the second thermal shield.*

5.4. THE EXPERIMENTAL SETUP

Table 5.1: *Thermal conductivity and emissivity values for the materials in our experimental temperature range 300-500 K.*

Material	Conductivity (W/(m k))	Emissivity
Graphite	90	0.70
Polished aluminium	237	0.09
AU4G aluminium	237	0.09, 0.18 (unpolished)
Copper	390	0.15
Ceramic	1.1	0.90
Glass	0.9	0.90
Silver	406	0.02
Fiberglass	0.04	0.75
Steel	50	0.80

field produced in a uniformly heated cavity, regardless of the cavity surface properties, is uniform and equal to the emissive power of an ideal blackbody at the temperature of the walls. If a very small hole is made in the wall of the cavity, the escaping radiation from it would appear to be that from a blackbody.

The surface of the graphite tube has an emissivity of $\epsilon = 0.70 - 0.80$ corresponding to a temperature 0-3600 °C. Both the high conductivity of graphite and the two thermal shields allow a high temperature homogeneity of the graphite tube. The measured temperature difference between $T1$, $T2$, and $T3$ is less than 0.5 K in the temperature range of 300 - 500 K. The surface of the two holes is 2.6% of the total inner surface of the graphite tube. A thermal calculation indicates that only 1.1% of a heat flux entering a hole escapes through the holes mainly due to the non-unitary emissivity of the graphite surface. In a thermal steady state, the radiation flowing from the shields and entering into the graphite tube is about 1.1% compared with the emissive power of the inner surface of the graphite tube. To guarantee as perfect a BBR field as possible, we choose the launch velocity to ensure that the atoms apogee is approximately at the middle part of the graphite tube where they spend more time. The heat escaping from the holes is the same as for a blackbody.

The radiation field inside the copper cavity, even inside the cutoff guide, can be treated as a BBR field⁷. The temperature of the cavity is deduced

⁷The cut-off frequency of the cavity or the cutoff guide is less than 1×10^{10} Hz, being too small comparing to the transition 6S-6P.

from a measurement of the cavity resonance frequency. The plane of the aperture of the cutoff (surface occupation is less than 2×10^{-4}) is considered to be a blackbody surface.

The FO1 copper vacuum tube structure ($\phi = 150$ mm, $l = 700$ mm) is a closed cavity since all the holes are closed by glass windows. These external apertures account only for 0.2% of the total surface. Furthermore, the windows are made of BK7 glass which is extremely dark in the far-infrared where the BBR spectrum reaches its maximum. The estimated energy loss [104] is less than 0.1%.

As illustrated in fig. 5.3, the temperature in the space between the graphite tube and the cavity (a distance of 4.6 cm) is not measured directly. The launch velocity of the cold atoms in normal operation is 3.4 m/s. Thus, during about 11% of the flight time $2\tau + T$, the temperature is not well known. We shall calculate it using heat transfer theory.

In order to calculate the thermal radiation seen by the atoms, we have to determine the temperature of each surface of the thermal radiator. All the surfaces will be taken as diffuse emitters and reflectors (gray surfaces), for which the monochromatic emissivity is independent of wavelength and the total emissive power is calculated as $\epsilon\sigma T^4$. When Kirchoff's law is applied, the absorptivity α is equal to the emissivity, *i.e.*, $\alpha = \epsilon$. Furthermore, the configuration factor or shape factor for diffuse radiation is a purely geometrical property of the two surfaces involved. We have calculated all the shape factors among the 14 surfaces involved by using integral and algebra method. The graphite tube temperature T_B and the second shield temperature T_D are measured by the thermistors. To get the first shield temperature T_S , we divide the thermal surfaces into two complete enclosures: The bigger one is formed by the outside surfaces of the first shield and the inner surfaces of the second shield. The smaller one is enclosed by the outer surfaces of the graphite tube and the inner surfaces of the first shield. The planes of the 6 holes involved are black surfaces with emissive power $E_b = 0$ and $\alpha = \epsilon = 1$. Since the temperature of the entire thermal radiator is stable within 2 K during the frequency measurements. It is reasonable to assume a thermal steady state. This leads to a thermal equilibrium of the first shield, *i.e.*, $q_i = -q'_i$, the net heat flow from the inner and outer surfaces of one or several given sheet pieces. The parameter q_i is given by

$$q_i = A_i \sum_{j=1}^{14} (\delta_{ij} - F_{i-j}) J_j, \quad (5.32)$$

where A_i is the area of the i th surface and F_{i-j} is the configuration or shape factor which determines the fraction of energy leaving the i th surface which

5.4. THE EXPERIMENTAL SETUP

directly strikes the j th surface. J_j is the radiosity used to indicate all radiation (emission + reflection) leaving the j th surface [114], per unit time and unit area. J_i is obtained by

$$J_i = \epsilon_i \sigma T_i^4 + (1 - \alpha_i) \frac{1}{A_i} \sum_{j=1}^{14} F_{j-i} A_j J_j, \quad (5.33)$$

where α_i is the absorptivity of the i th surface, and T_i is its temperature.

To simplify the calculation of the temperature T_S of the first shield, we neglect the small emissivity difference between the surfaces of the ceramic pins and the first shield. Finally, we obtain a temperature relation in the following form:

$$10041.36 T_S^4 = 5596.48 T_B^4 + 4670.57 T_D^4. \quad (5.34)$$

Table 5.2: *Several tests to verify the thermal calculations. q_s , q_h , q_{rod} , q_{wire} refer respectively to the net heat flow away from the outer surface of the first thermal shield, from the two planes of the holes in the first shield, from the transferred heat by the 8 glass rods and by the 6 wires of the 3 thermistors in the graphite tube. $q_{in.}$ represents the injected power. The error term presents the relative difference between the calculated power consumption ($q_s + q_h + q_{stick} + q_{wire}$) and the actual injected power $q_{in.}$.*

Test	T_B (K)	T_D (K)	T_S (K)	q_s (W)	q_h (W)	q_{rod} (W)	q_{wire} (W)	$q_{in.}$ (W)	error (%)
1	368.15	303.15	345.00	1.49	0.19	0.09	0.07	1.90	3
2	396.15	307.50	365.70	2.33	0.30	0.11	0.09	2.95	4
3	429.15	311.65	390.66	3.62	0.47	0.22	0.12	4.73	6

We have performed several tests which all verify these thermal calculations. Table 5.2 shows an example for three temperature. We measured the injected power as well as the temperature of graphite tube and the second shield. We calculated with formula (5.34) the temperature of the first thermal shield. Then we calculated the total heat flow away from the complete enclosure composed by the first shield and the two planes of the holes. When we neglect the energy losses due to the heating wire leads and the radiation of the ceramic parts, the total power consumption can be obtained by summing the net heat flow away from the outer surface of the first shield and from the two planes of the holes in the first shield, the transferred heat by the 8 glass rods and by the 6 wires of the 3 thermistors in the graphite tube. As shown

in the last column, the maximum difference between the calculated power consumption and the actual injected power is 6%. The differences arise from the error in the emissivity and the shape factor (mainly due to the thermal device dimensions). These tests verify the temperature determination of the first shield with an uncertainty of less than 1.5%.

5.5 Measurement sequence

In order to avoid a small AC Zeeman shift induced by the heating current, the measurement operation is sequential. The three following phases are repeated:

Heating: The graphite tube is heated when we do not measure the clock frequency.

Thermalization and microwave power optimization: The heating current is slowly turned off in several milliseconds. We await the homogenization of the graphite tube for several second. The temperature of the graphite tube exponentially drops by about 3 K during this phase. The microwave power is automatically optimized to search for the maximum transition probability ($b\tau = \pi/2$) at the end of this phase. The microwave power uncertainty is less than 0.25 dB with respect to the optimal value.

Measurement: The fountain works in normal operation, the frequency difference $\Delta\nu_{mea}$ between the $F = 3, m_F = 0$ to $F = 4, m_F = 0$ transition and the H-maser is recorded. During this phase, the decrease of the graphite tube temperature is less than 2 K.

As the heating current is constant, we can vary the BBR radiator temperature by changing the sequence. For example, when we choose the following sequence (300, 50, and 60 cycles respectively corresponding to the three phases above), the graphite tube is stabilized at 193 °C, and its maximum fluctuation is 1.5 °C over 33 hours, while the cavity temperature is kept at 35 °C. The frequency measurement resolution reaches 1.5×10^{-15} after about 1.5 days of operation.

5.6 Effective temperature calculation

The strength of the thermal radiation field varies spatially along the atomic trajectory inside the fountain tube as $T^4(h)$, where h is the distance above the capture center. Thus, the launched atoms experience a time dependent temperature, and an application of the atomic sensitivity function $g(t)$ is necessary to estimate the BBR frequency shift in the fountain. We use formula (B.29) in appendix B and experimental parameters to calculate the $g(t)$. As

a time origin, we chose the moment when the atoms first experience a microwave interaction. $\delta\nu_{BBR}(t)$ is the atomic frequency shift induced by the BBR field at a time t . When the microwave power is optimized at $b\tau = \pi/2$, the measured frequency shift $\Delta\nu_{mea}$ due to BBR in FO1 can be given by

$$\begin{aligned}\Delta\nu_{mea} &= \frac{\int_0^{T+2\tau} \delta\nu_{BBR}(t) g(t) dt}{\int_0^{T+2\tau} g(t) dt} \\ &= \frac{0.44500\overline{\delta\nu_{BBR}(T)}}{2 \times 0.01136 + 0.44500} + \frac{2 \times 0.01136 \times \overline{\delta\nu_{BBR}(\tau)}}{2 \times 0.01136 + 0.44500}\end{aligned}\quad (5.35)$$

where $\overline{\delta\nu_{BBR}(\tau)}$ and $\overline{\delta\nu_{BBR}(T)}$ are respectively the time-averaged frequency shifts inside and above the cavity. We are interested in the temperature-dependent frequency shift above the cavity. Therefore we solve the above formula for $\overline{\delta\nu_{BBR}(T)}$ and obtain

$$\overline{\delta\nu_{BBR}(T)} = (1 + \gamma)\Delta\nu_{mea} - \overline{\delta\nu_{BBR}(\tau)} \quad (5.36)$$

where $\gamma = 0.051$ depending on the geometry of the interrogation and on the microwave power. The value of $\gamma = 0.048$ is given in [55] one can obtain. The difference arises come from the author's assumption of a rectangle field amplitude profile rather than the actual sinusoidal one inside the cavity⁸.

When the graphite tube is heated from 303 K to 500 K the cavity temperature T_C rises only from 303 K to 309 K. According to formula (5.30), the temperatures 303, 309, and 500 K correspond to a BBR frequency shift of 163, 177 and 1211 μHz respectively. This means that the second term of the right-hand side of equation (5.36) always contributes less than 5% to the measured frequency shift, and much less when we increase the graphite tube temperature.

The formula (5.35) involves the time averages of T^4 and T^6 which we now calculate. The radiation incident upon atoms is the result of radiosity J_i from all the surfaces seen by atoms. The term $T^4(h)$ at height h is given by

$$T^4(h) = \sum_{i=1}^{14} \frac{J_i}{\sigma} \cdot \frac{d\Omega_i(h)}{4\pi}. \quad (5.37)$$

where $d\Omega_i(h)$ is the solid angle subtended by the i th surface at the height h of the atoms.

⁸ $\gamma \simeq 2\tan(\frac{1}{2}b\tau)/[bT + 4\tan(\frac{1}{2}b\tau)]$, where b is the Rabi angular frequency which is proportional to the intensity of the excitation microwave field inside the cavity.

From the thermal equilibrium of the first shield, we have also obtained the radiosities of the involved surfaces. Having these data at a given temperature in hand, we are able to calculate the time averaged values of the temperature terms $T^4(t)$ and $T^6(t)$. According to the experimental set-up, we divide the atomic trajectory above the cavity into 5 regions with the following approximations:

a. Inside the cavity cut-off. The radiation field is treated as a BBR at the temperature of the cavity wall.

b. Between the cavity cut-off and the horizontal inner surface of the second thermal shield, the atomic flight time is about 8% with respect to T . The atoms experience a BBR at the average temperature of the cavity and the second shield (the difference is less than 3 K), and in addition the radiosity of the hole of the second shield and a BBR from the hole of the cavity cutoff.

c. Between the first and second shields (a trajectory length 6 mm), the radiosity of the hole of the second shield is inferred from a BBR at the average temperature of the cavity and the second shield.

d. Between the first shield and the graphite tube, the radiation from the hole of the graphite tube is assumed as BBR at the temperature of the graphite.

e. Inside the graphite tube, the atoms spend more than 75% of their flight time T above the cavity. Atoms experience a BBR from the inner surface of graphite tube and two small radiosities from the two planes of its holes.

We sub-divide the length of each region into very fine steps dh ($50\mu\text{m}$). Within each step dh , the solid angle under which the atoms experience the involved surfaces is taken to be constant. Thus, the radiation field intensity is regarded as uniform over one step dh . We accumulate the on-axis strength, which is proportional to T^4 as mentioned in formula (5.37). In each fine step, we also assume the terms $T(h)$ are uniform. We transform the parameter h into time t using the launch velocity. Finally, we can calculate the time averaged values of the terms $\overline{T^4(t)}$, $\overline{T^6(t)}$ and $\overline{T(t)}$ over the atomic ballistic flight above the cavity.

It should be noted that there will be an error when one simply replaces the term $\overline{T^4(t)}$ by powering the time averaged temperature $\overline{T(t)}$, *i.e.*, $\overline{T^4(t)} \neq (\overline{T(t)})^4$ as seen in figure 5.5. The temperature term $T_{BBR} = (\overline{T^4(t)})^{\frac{1}{4}}$, the so-called effective temperature, will be used in formula (5.30). Replacing $\overline{T^6(t)}$ by $(\overline{T^4(t)})^{3/2}$ induces an error of $< 4\%$ in the T^6 term in equation (5.30). Since ε is small ($\simeq 0.014$), its influence is negligible compared to the experimental resolution.

Our evaluation of the uncertainty of the effective temperature T_{BBR} is mainly based on the knowledge of $T(h)$, on the relative position of the thermal pieces (the atomic launch velocity can be determined at a level of 10^{-4} in a

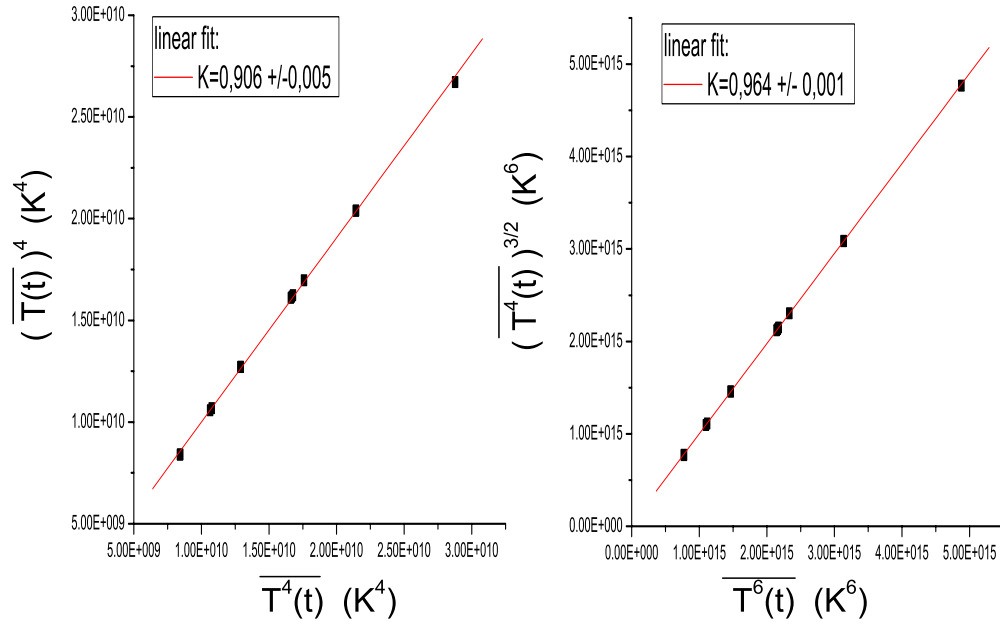


Figure 5.5: *Non-uniform temperature along the atomic trajectory. The first figure represents the fourth power of the time-averaged temperature $(\overline{T(t)})^4$ as a function of the time average of the fourth power of the temperature $\overline{T^4(t)}$. The second shows the relation between $(\overline{T^4(t)})^{3/2}$ and $\overline{T^6(t)}$, their difference is less than 5%.*

fountain) and on the temperature fluctuation during the measurement phase.

As mentioned above, the atoms spend 8% of the flight time in the region **b** without a directly measured temperature value. The maximum error is 3 K, and the corresponding uncertainty in the determination of the effective temperature is less than 0.08%.

The error in the emissivity and the shape factor induces an uncertainty of less than 1.5% on T_S calculation as shown in table 5.2. When we attribute this error to the T_{BBR} determination during in the **c** and **d** regions (total flight time occupation of 3.7% with respect to T), this can induce an error in the determination of the effective temperature T_{BBR} determination of less than 0.6%.

As motioned above, the radiation power inside the graphite tube may be 1.1% less than that of a true BBR field which gives rise to an error in the determination of T_{BBR} in range of 0 – 0.3%.

The error on the relative vertical positions of each piece is less than 2 mm. If the graphite tube is at 500 K, a calculation shows that the maximum induced error is 0.17% of T_{BBR} .

A MOT at 1 μ K is used in FO1 during the measurement. The vertical velocity distribution ($\sigma \simeq 1$ cm/s) can induce an error in the measurement of T_{BBR} determination. The calculated T_{BBR} for the most speedy/slow atom differs 0.5% from that for the atom in center of the atom cloud. The measured frequency is an averaged result for all the detected atoms, thus the effect of the vertical velocity distribution will cancel thanks to symmetry. We attribute an uncertainty of 0.2% due to this effect.

Following the temperature thermalization, the measurement phase continues for about 100 s. According to the time constant of temperature dropping at the graphite tube (measured time constant of 5 h), the calculated temperature fluctuation is less than 0.5% during the measurement phase (including the uncertainty of the thermistors Pt100). It agrees with the maximum measured temperature fluctuation of 2 K. This is the dominant contribution to the uncertainty.

Finally, a quadratic summation of the above-mentioned uncertainty terms shows that T_{BBR} can be obtained with an uncertainty of 0.6%.

5.7 Experimental results

The measurement of the BBR shift took several months. In order to eliminate the H-maser drift (about 1.5×10^{-15} /day), the H-maser frequency is compared to the Rb fountain frequency. Furthermore, we performed the measurement in a random temperature order. Figure 5.6 represents the frequencies $\overline{\delta\nu_{BBR}(T)}$ corrected for the systematic frequency shifts as a function

of T_{BBR} . $\overline{\delta\nu_{BBR}(\tau)}$ is estimated by the parameter K_{Stark} of [103] in formula (5.30). The value of $\gamma = 0.051$ in formula (5.36) depends on the ratio of τ/T and also on the microwave power. The calculation of $g(t)$ in formula (5.36) assumes that the microwave power is optimum ($b\tau = \pi/2$). The “thermalization and microwave power optimization” operation ensures a microwave power of $b\tau = \pi/2$ within ± 0.25 dB with respect to the optimal power. This leads to an accuracy on the value of the factor γ of 0.5% [104]. Thus, we can estimate the time averaged frequency shift $\overline{\delta\nu_{BBR}(T)}$ above the cavity due to the BBR with an accuracy at a level of 10^{-3} arising from the uncertainty of γ . We can neglect its influence on the determination of K_{Stark} compared with the measuremental resolution.

There are other temperature dependent effects which shift the frequency of the fountain FO1. We perform an estimation as follows:

The maximum change of the cavity temperature is 5 K, thus the cavity pulling shift is about 8.0×10^{-7} Hz, hence negligible. The cavity detuning from the conventional temperature condition requires an increase of 6 dB microwave power⁹ in order to maintain the optimum level for the Ramsey spectroscopy ($b\tau = \pi/2$). This may result in an undesirable frequency shift due to the presence of possible microwave leakage in the apparatus. We never detected any frequency difference with a resolution of 1.5×10^{-15} between two continuously applied microwave level: $\pi/2$ and $5\pi/2$ (difference 14 dB). As described in the section 2.9.2, even a microwave field inside the cavity with a power of 90 dB more than the normal operation when the atoms are outside the cavity during their flight, no clock frequency shift is observed with a resolution of 1.5×10^{-15} . Finally, we can neglect the frequency shift due to the microwave leakage compared to the experimental resolution.

Thanks to the cooling water, the maximum temperature change of the vacuum tube of the fountain FO1 (see figure 5.3) is less than 5 K when we vary the temperature from 300K to 500K. We never found a temperature dependent C-field at our measurement resolution. The possible temperature dependent frequency shift is due to the outgassing of the graphite, especially, hydrogen. One key point to eliminate this effect is the outgassing process. Before installing the BBR radiator inside FO1, the pieces of the radiator were outgassed at 700 K inside a vacuum chamber at 10^{-9} Torr for one week. During the installation procedure the pieces were protected by nitrogen gas. The pressure change of the background gas is less than 5×10^{-10} Torr in the fountain when the blackbody is heated up to 500 K. The varying background gas pressure effects the cold atoms density (through ejecting the cold atom out of the flying atoms ball) and induces a collision frequency shift. A simple calculation shows that the resulting uncertainty due to the collisions between

⁹During our measurement, the cavity is pulsed fed.

the thermal atoms and the cold atoms is less than 5×10^{-16} . To estimate the influence order of the background gas, we assume it as caesium atoms. The lifetime¹⁰ of atoms in the atom ball is $\tau \sim 1$ s at a pressure 6×10^{-9} Torr. The averaged fractional difference of the atom number/density¹¹ above the cavity is less than 2% when the pressure was varied between 5×10^{-10} Torr ($\tau \sim 12$ s) and 1×10^{-9} Torr ($\tau \sim 6$ s). The maximum cold collisional shift during the measurement is 312 μHz . Thus, the cold collisional shift above cavity due to change of the ground gas pressure is less than 6 μHz .

As all the above temperature dependent frequency shifts are in the range of the FO1 accuracy, and as the measurement process is long, we safely assume that both fountain frequency fluctuations are within their evaluated accuracy of 2×10^{-15} . The direct measurement resolution of each data point is about 2.5×10^{-15} due to the combined frequency stabilities of both fountains.

The temperature fluctuation of the atoms environment is less than 2 K, thus a maximum $\overline{\delta\nu_{BBR}(T)}$ fluctuations are less than $4.2 \times (T_{BBR}/300)^3 \mu\text{Hz}$. The uncertainty of the T_{BBR} calculation induces a similar influence.

Table 5.3: *Uncertainties of the measured frequency shift $\overline{\delta\nu_{BBR}(T)}$ as a function of the effective BBR temperature T_{BBR} .*

Temperature (K)	FO1 accuracy (μHz)	FO2(Rb) accuracy (μHz)	Measurement resolution (μHz)	2 K temperature fluctuation (μHz)	Temperature calculation (μHz)	Total (μHz)
301.7	18	18	21	5	4	34
360.9	18	18	25	8	9	38
432.6	18	18	28	14	18	44

The resolution of each data point is the quadratic sum of the uncertainties motioned above. It is dominated by the stability and the exactitude of the two fountains. An example of the uncertainty analysis of the $\overline{\delta\nu_{BBR}(T)}$ determination is shown in the in table 5.3. When we use the theoretical value 0.014 [94] for ε , a polynomial fit yields the factor $K_{Stark} = -154(6) \times 10^{-6}$ Hz. Simultaneously, a second fit without the T^6 term gives $K_{Stark} = -159(6) \times 10^{-6}$ Hz. The difference of the two obtained K_{Stark} values lies within the statistical uncertainty (see figure 5.6).

¹⁰In reference [50], the experimental value of the cross section $\sigma \sim 2 \times 10^{-13}$ cm².

¹¹The atom cloud expansion depends only on the atom temperature. The time evolution of the atom number is proportional to $\exp(-t/\tau)$.

5.7. EXPERIMENTAL RESULTS

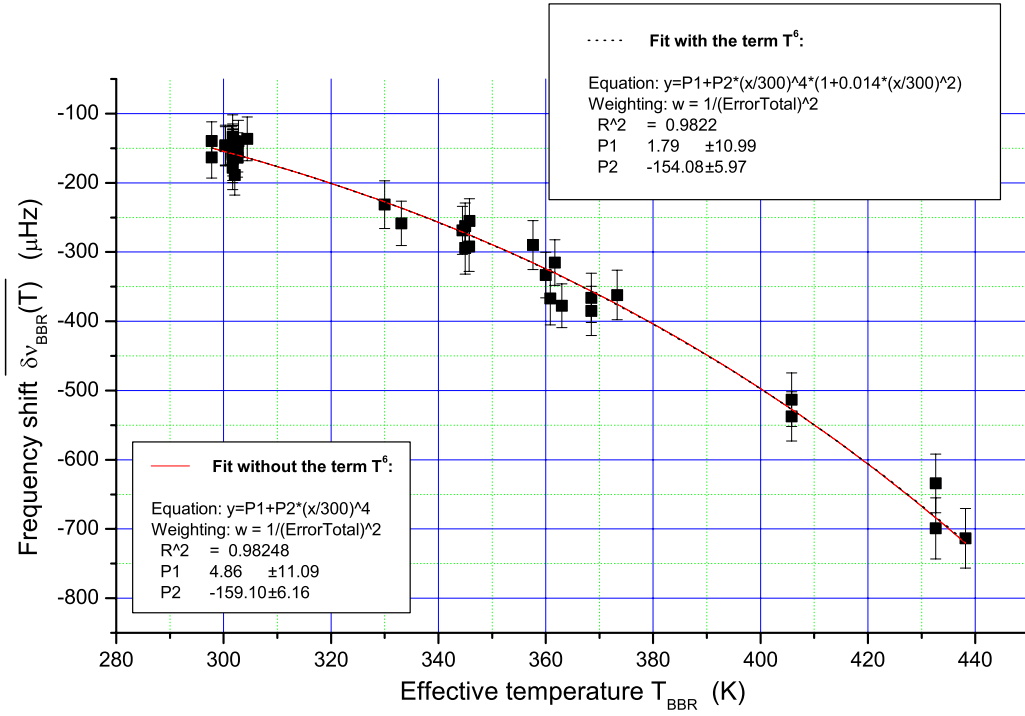


Figure 5.6: The time-averaged frequency shift above the interrogation cavity $\overline{\delta\nu_{BBR}(T)}$ as a function of the effective temperature T_{BBR} . The two lines are polynomial fit weighted with the measurement uncertainty. When we use the theoretical value 0.014 [94] for ϵ , a polynomial fit (dot line) yields the factor $K_{Stark} = -154(6) \times 10^{-6} \text{ Hz}$. A second fit (solid line) without the T^6 term gives $K_{Stark} = -159(6) \times 10^{-6} \text{ Hz}$.

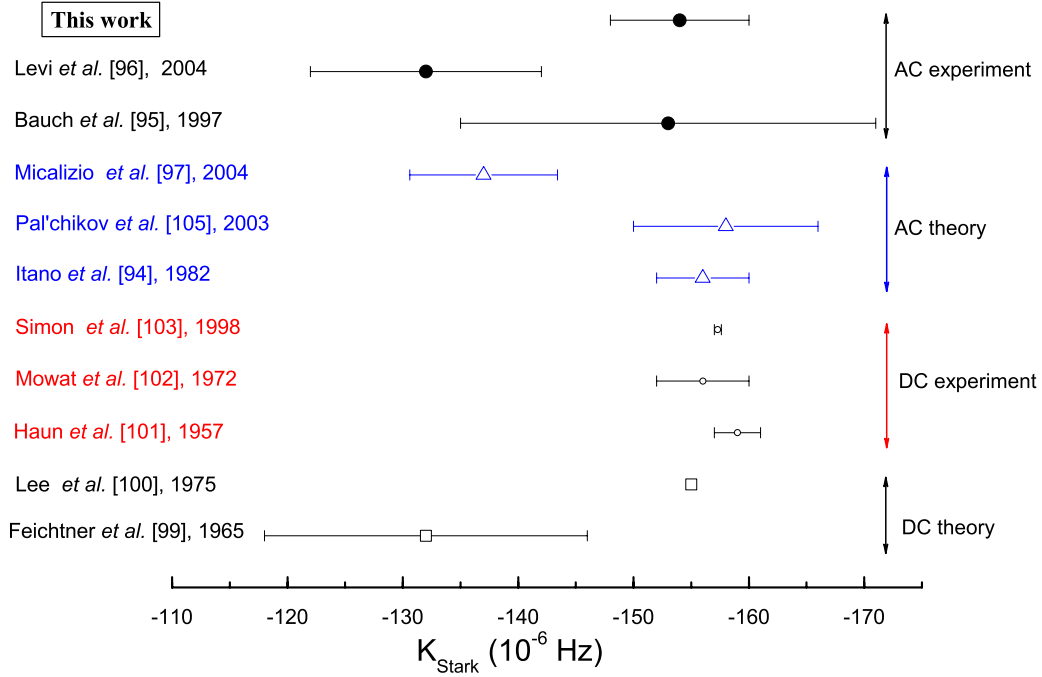


Figure 5.7: *Experimental and theoretical values for K_{Stark} .*

5.8 Conclusion

We have performed a preliminary measurement of the BBR frequency shift from 300 K to 450 K. It is a direct measurement in an atomic fountain. We observed the dependence of the clock transition frequency on temperature. The experimental result of the blackbody radiation shift of the ^{133}Cs hyperfine transition gave $K_{Stark} = -154(6) \times 10^{-6}$ Hz. This value is in good agreement with the ones predicted from AC Stark theories, DC Stark and the BBR shift experiments as shown in figure 5.7. The agreement between the results of the most accurate DC Stark measurement [103] and our direct BBR experiment is $(2 \pm 4)\%$. However, they differ significantly ($\sim 15\%$) from only one experimental result obtained by the IEN group [96] using only two temperature points separated by 30°C in a Cs fountain and from the theoretical results of Feichtner *et al.* [99] in 1965 and of Micalizio *et al.* [97] in 2004. The two models are nearly the same, except the experimental data used in the calculation.

The fractional K_{Stark} uncertainty of our experiment is 3.9%, a 3-fold improvement over a previous measurement [95]. This experimental accuracy can lead to an uncertainty of about 6×10^{-16} for the evaluation of the fre-

quency shift due to BBR near room temperature in a Cs frequency standard.

One calculation shows that the difference between the measured points and the DC Stark law using the value of K_{Stark} obtained by Simon is 4% at the temperature of 440 K. This order of magnitude corresponds to the theoretical prediction of the contribution of the terms in T^6 (there is no T^6 in the DC Stark effect).

Nevertheless, the dispersion of our measurement is still too large to allow for a determination of the ε term in equation (5.30). This dispersion is probably due to the imperfect frequency comparisons between FO1 and Rb fountains. The operation of the two fountains is synchronized to within one hour. We took the average value of the two nearby frequencies to act as the reference when the Rb fountain value was missing. Another reason is that the temperature range is not large enough. The frequency shift contribution of the coefficient ε is less than 4% even at a temperature of 500 K. The limited number of data points is also a reason.

Finally, to improve uncertainty on the effect of the blackbody radiation at a level of 10^{-17} , we should measure the T^6 term. This measurement requires to improve the stability and the accuracy of the fountain, and also improve the frequency comparison between the fountains.

CHAPTER 5. CS CLOCK FREQUENCY SHIFT DUE TO
BLACKBODY RADIATION

Chapter 6

The improved FO1

6.1 Résumé en français

Ce chapitre présente une description détaillée des améliorations de FO1, incluant la source d'atomes, la zone de capture, la zone de sélection, la zone de détection, le système optique, les synthèses de signaux micro-onde et le système de contrôle. Les modifications ont amélioré la fiabilité de la fontaine et ses performances.

Nombre d'atomes capturés Une nouvelle configuration des faisceaux lasers de refroidissement est employée dans la version améliorée de FO1. Dans l'installation actuelle, la direction de l'axe vertical du tube de la fontaine est déterminée par le vecteur de coordonnée (1.1.1) dans le système de coordonnées des trois directions orthogonales de propagation des faisceaux de refroidissement (par rapport à (0.0.1) dans la première version de FO1). En conséquence, la taille des faisceaux de capture n'est plus limitée par l'ouverture de la cavité micro-onde et le système optique est simplifié. De plus, un jet ralenti de césium est employé comme source d'atome au lieu d'une vapeur atomique. Ces deux modifications permettent le chargement d'un plus grand nombre d'atomes dans la mélasse optique avec une basse densité atomique. En plus de ces avantages, puisqu'il n'y a aucun faisceau laser traversant la zone d'interrogation, la nouvelle configuration réduit au maximum le risque de déplacement lumineux parasite.

Bruit technique Le rapport signal à bruit sur la mesure de probabilité de transition a été amélioré en augmentant l'efficacité de collection de la fluorescence du système de détection d'un facteur 3, en contrôlant la puissance des faisceaux de détection, en réduisant la vapeur de Césium dans la zone de détection et en déplaçant la région de détection au-dessus de la zone de

capture. L'utilisation d'un faisceau atomique ralenti et la réduction de la période du vol des atomes après la phase d'interrogation conduisent à une amélioration du rapport durée de fonctionnement sur durée du cycle de la fontaine.

Décalage de fréquence dû aux collisions La méthode de passage adiabatique pour la sélection d'état atomique prépare les échantillons successifs d'atome dans un rapport bien défini en densité atomique et en nombre d'atomes. Ceci permet de mesurer les décalages de fréquence dus aux collisions et déplacement dû à la cavité [59] au niveau de 10^{-16} .

Fuites micro-onde La nouvelle chaîne de synthèse micro-onde réduit au minimum la puissance micro-onde à la fréquence de résonance atomique, réduisant de ce fait le décalage de fréquence induit par les fuites micro-onde. La symétrie de la trajectoire atomique entre la cavité de sélection et la zone de détection par rapport à l'apogée, réduit également le décalage dû aux fuites micro-onde.

Typiquement, le nombre d'atomes capturés en mélasse est de 4×10^8 en 400 ms. L'amélioration par rapport à la première version de FO1 est d'environ un ordre de grandeur. L'application de la méthode du passage adiabatique permet de préparer deux échantillons d'atome dans un rapport de densité de 0.5042(1). Après un jour d'intégration ce rapport est connu à mieux que 10^{-3} la fois en densité atomique et en nombre d'atome. La stabilité de fréquence de l'horloge FO1 en utilisant un oscillateur cryogénique en saphir comme oscillateur local est $2.8 \times 10^{-14} \tau^{-1/2}$. C'est une amélioration d'un facteur 4 par rapport à la première version de FO1 utilisant un quartz de BVA. Les décalages de fréquence dépendants du nombre d'atome sont $-111(3) \mu\text{Hz}$ quand 2×10^6 atomes sont détectés. Le déplacement de fréquence mesuré dû aux collisions entre atomes froids est $\sim -6 \times 10^{-11} \text{ Hz/atome}$, soit environ cinq fois plus petit que dans la première version de FO1 en fonctionnement en MOT-mélasse optique. L'évaluation de l'exactitude est en cours. L'exactitude attendue est de quelques 10^{-16} .

Ces résultats montrent que FO1, après améliorations est l'une des meilleures fontaines atomiques au monde [115, 116, 117, 118].

6.2 Introduction

The first version of FO1 was built 10 years ago. We recently modified the set-up to improve both the reliability of the fountain and its performance.

The schematic of the new FO1 is shown in figure 6.1. We can find the modifications by looking the schematic of the FO1 shown in figure 2.1.

Number of captured atoms A new configuration of the cooling beams is used in the improved version of FO1. In the present setup, the fountain axis is along the direction (1,1,1) with respect to the three orthogonal propagation directions of the cooling beams. Therefore, the size of the capture beams is no longer limited by the aperture of the microwave cavity and the optical system is simplified. In addition, a decelerated caesium beam is used as atom source instead of an atomic vapor. These two modifications allow us to load a larger numbers of the atoms in the optical molasses. Besides this, since there is no laser beam passing through the interrogation zone, the new configuration minimizes possible light shifts.

Technical noise The signal-to-noise ratio on the transition probability measurement has been improved by increasing the collection efficiency of the detection system, by controlling the power of the detection beams, by reducing the Cs vapor pressure in the detection zone and by moving the detection region above the capture zone. The use of a decelerated atomic beam to load the molasses and the reduction of the time of flight of atoms after the interrogation phase has led to an improvement of the fountain duty cycle.

Collisional frequency shift The method of state selection by adiabatic passage allows us to prepare successive atom samples with a well-defined ratio both in atom density and atom number. This allows us to measure at the 10^{-3} level the frequency shifts due to cold collisions and cavity pulling [59].

Microwave leakages A new microwave synthesis chain reduces the generated microwave power at the atomic resonance frequency, thereby reducing the frequency shift induced by microwave leakage.

In this chapter, we describe the main modifications on the fountain set-up and show the performance of the improved version of FO1.

6.3 The optical system

In the following sections, we describe the atom manipulation procedure and the laser sources of the improved fountain.

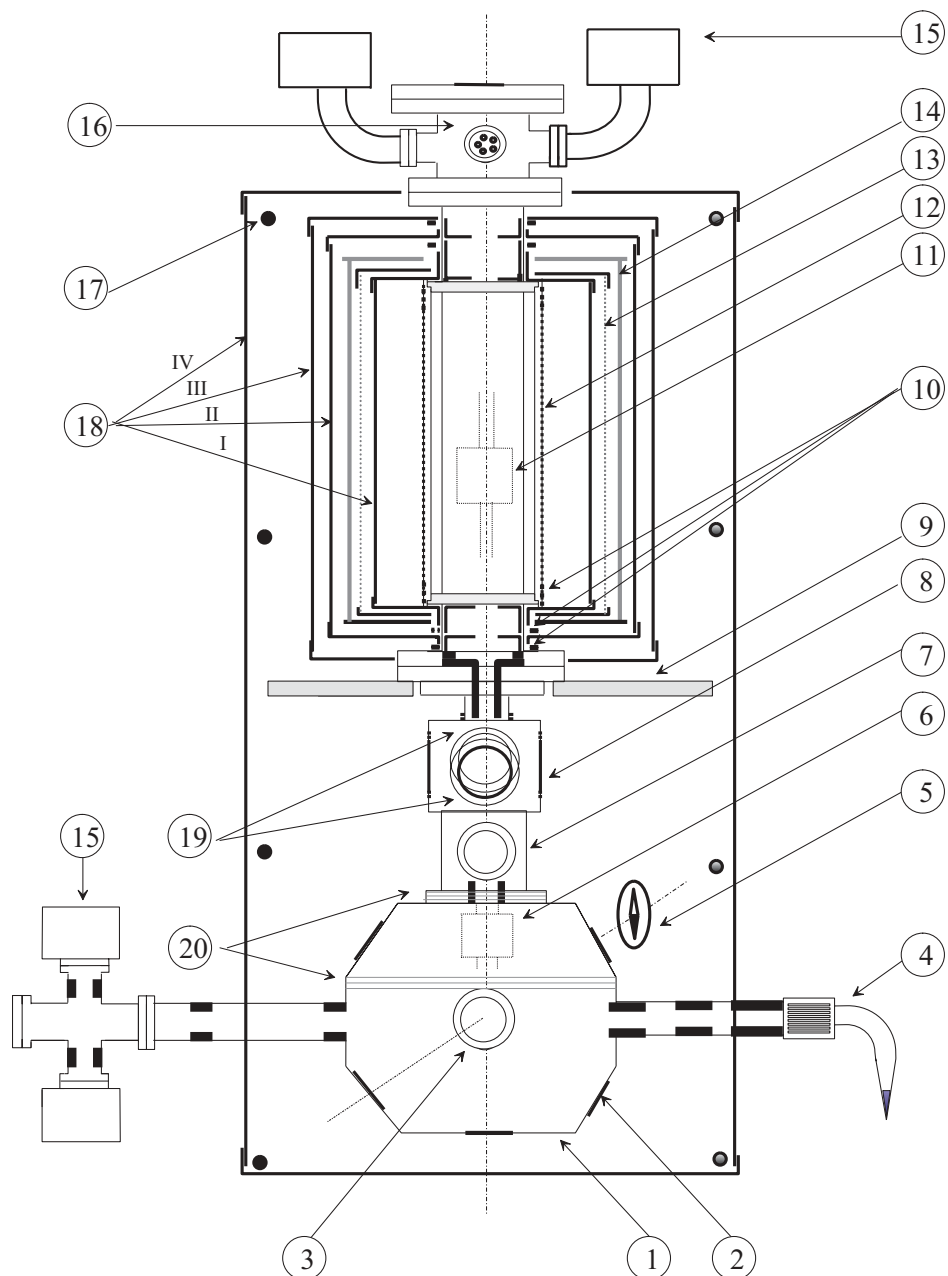


Figure 6.1: *Schematic of the improved FO1. (1) Capture chamber, (2) Capture beams' windows, (3) CCD camera window, (4) Thermal caesium oven, (5) Magnetic field probe, (6) Selection cavity, (7) Push beam windows, (8) Detection beam window, (9) Adjustable table, (10) C-field compensation coils, (11) interrogation cavity, (12) C-field coil, (13) heater coil, (14) Thermal isolator, (15) Ion pumps, (16) Microwave feed-through connector, (17) Compensation coils, (18) Magnetic shields, (19) Fluorescence collection windows, (20) Coils for adiabatic passage.*

6.3.1 Cold atom manipulation

Fig. 6.2 shows the atom manipulation time sequence. The main differences with the old version (see section 2.3) are:

Capture phase : The six cooling laser beams have an intensity of about 5 mW/cm^2 and a detuning of -3Γ from the resonance of $\nu_{45'}$. Atoms are loaded in an optical molasses from a chirp cooled atomic beam (see section 6.5). The chirped laser is switched off 5 ms before the end of the capture phase.

Launch : We launch the cold atoms by changing the detuning of the upward and downward triplets. Their frequencies are red shifted by $-2\Gamma + \Delta\nu_L$ and $-2\Gamma - \Delta\nu_L$ with respect to the transition $F = 4 \rightarrow F' = 5$. The launch velocity depends the frequency detuning $\Delta\nu_L$ and is given by

$$v_L = \sqrt{3} \times \lambda_l \times \Delta\nu_L. \quad (6.1)$$

For Cs, $v_L/\Delta\nu_L = 1.48 \text{ m/s} \cdot \text{MHz}^{-1}$. The frequency detuning between capture and launching is performed with a ramp of $\sim 1 \text{ ms}$ duration (see section 6.3.3).

Selection We combine a microwave cavity and a horizontal push beam (to replacing an antenna and a vertical push beam) to perform the atomic state selection. In the cavity, atoms in the state $F = 4, m_F = 0$ are transferred to $F = 3, m_F = 0$ by adiabatic passage (see section 6.6). Atoms remaining in the $F = 4$ state are pushed away by a transverse laser beam. The laser intensity is about 1 mW/cm^2 .

To efficiently perform this time sequence, we have designed a new optical bench and an improved control system.

6.3.2 The optical bench

The design of the optical bench is shown in fig. 6.4. It consists of a compact, $75 \times 120 \text{ cm}$ optical table. The laser light is produced by 7 laser diodes. The height of all the laser beams is 35 mm above the optical table. We use 9 single-mode polarization maintaining optical fibers to guide the laser beams from this optical bench to the fountain set-up.

Fig. 6.3 shows a schematic diagram of the optical system . One master laser diode locked at the frequency $\nu_{45'}$ by saturation spectroscopy provides two beams to injection lock two slave lasers for the upward and the downward beam triplets, respectively. Five AOMs are used to control the laser power or frequency corresponding to capture, launching, and post-cooling phases. Repumping beams are superimposed on two of the three beams of the downwards pointing triplet.

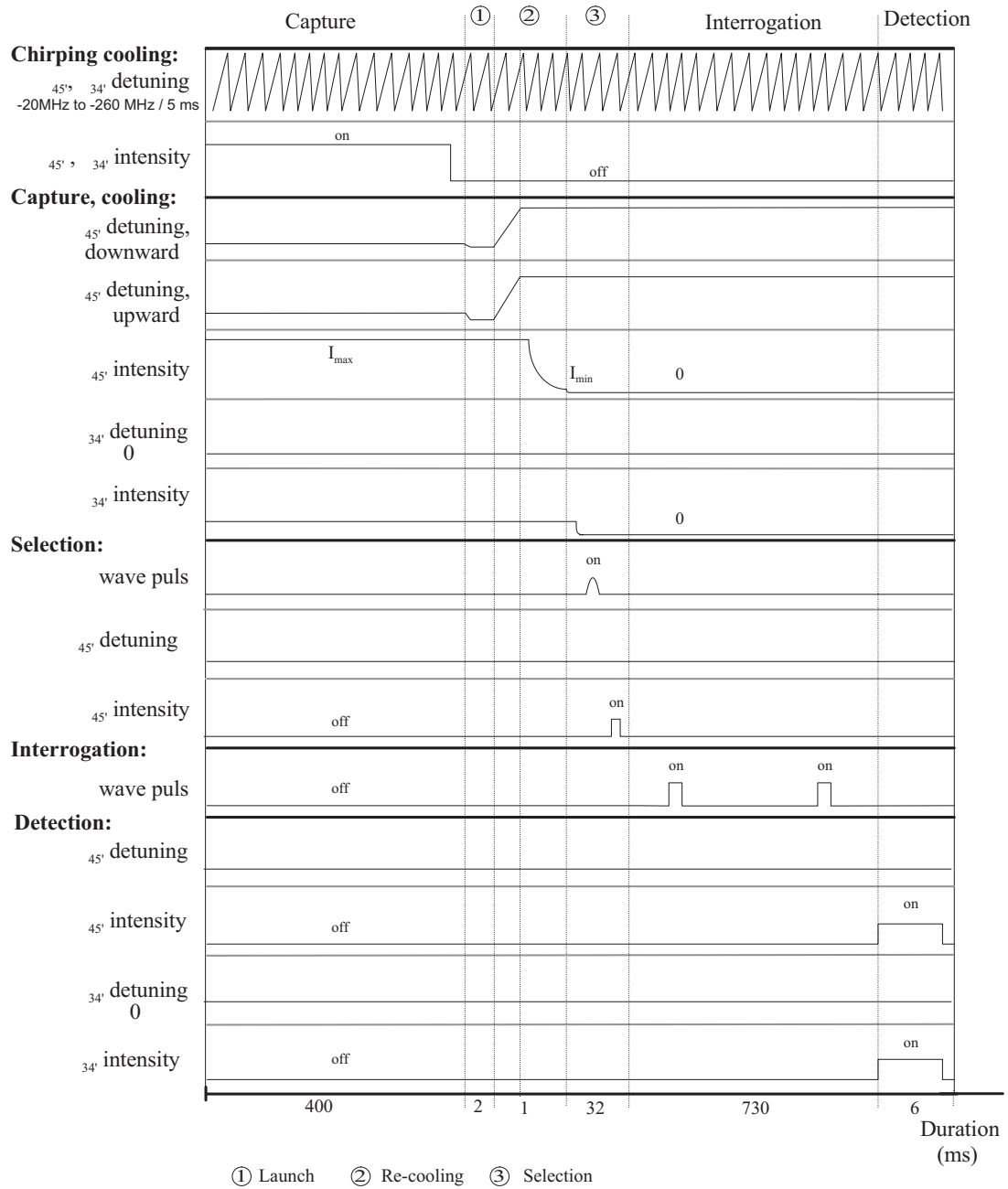


Figure 6.2: The atom manipulation time sequence (not on the scale). As an example, one time configuration is shown as the duration.

6.3. THE OPTICAL SYSTEM

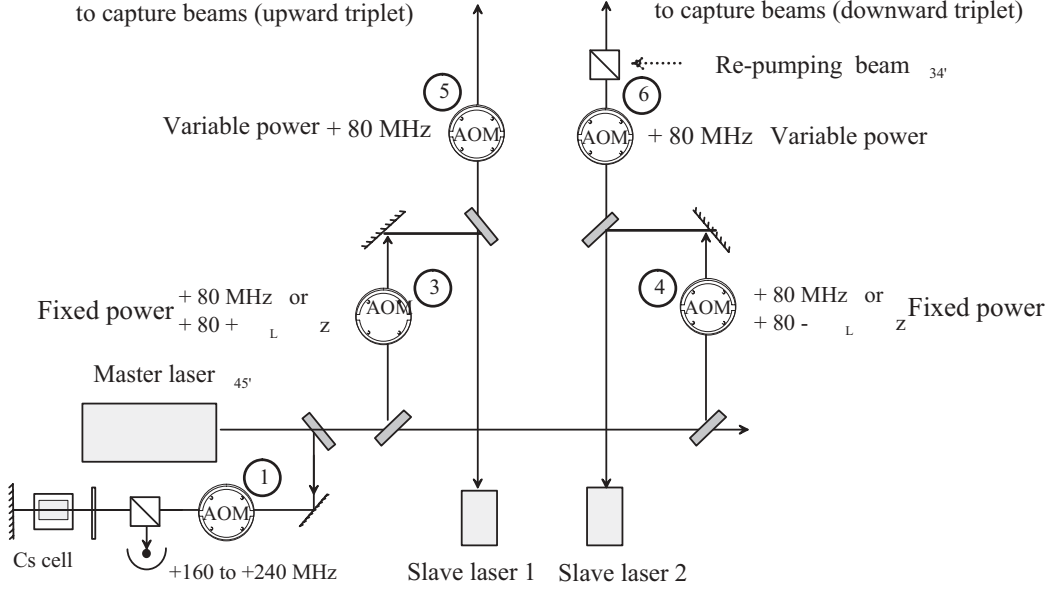


Figure 6.3: *Schematic of the capture laser beams.*

With regard to figure 6.4, the master laser (ML) is a semiconductor laser diode (SDL5422-H1 model) mounted in an 8 cm long extended cavity containing a grating of 1200 lines/mm. One part (1) of its output beam is frequency shifted of $\Delta\nu$ when passing through AOM1 and then directed to a Cs cell. The laser is then frequency stabilized at $\Delta\nu$ (160 MHz to 240 MHz) below the $F = 4 \rightarrow F' = 5$ transition by the saturated absorption technique. This laser provides a 10 mW beam (2) with a linewidth of 100 kHz. This red shifted beam is separated in two parts (3) and (4). After being +80 MHz or +80 MHz $\pm \Delta\nu_L$ (detuning $\pm \Delta\nu_L$ is required by atom launching) frequency shifted by AOM3 or AOM4, each of them (~ 0.3 mW) respectively injection locks the slave lasers SL1 and SL2. In the frequency range of operation of the AOM's, the sensitivity of the saturated absorption set-up and of the slave laser injection is small enough so that we did not need to double pass the beams through the AOM's. The slave lasers are also SDL5422-H1, which provide a maximum output power of 150 mW. Their output beams (5) and (6) are frequency shifted +80 MHz by AOM5 and AOM6. Their power are regulated by these AOM as well. Then, each beam is divided in three beams and coupled into optical fibers. The output of each fiber is collimated to a beam waist radius of 13 mm at $1/e^2$. A maximum intensity of about 7 mW/cm² is obtained at the center of the beam. Two mechanical shutters are placed after AOM 5 and 6 to ensure perfect extinction of the capture beams during microwave interrogation.

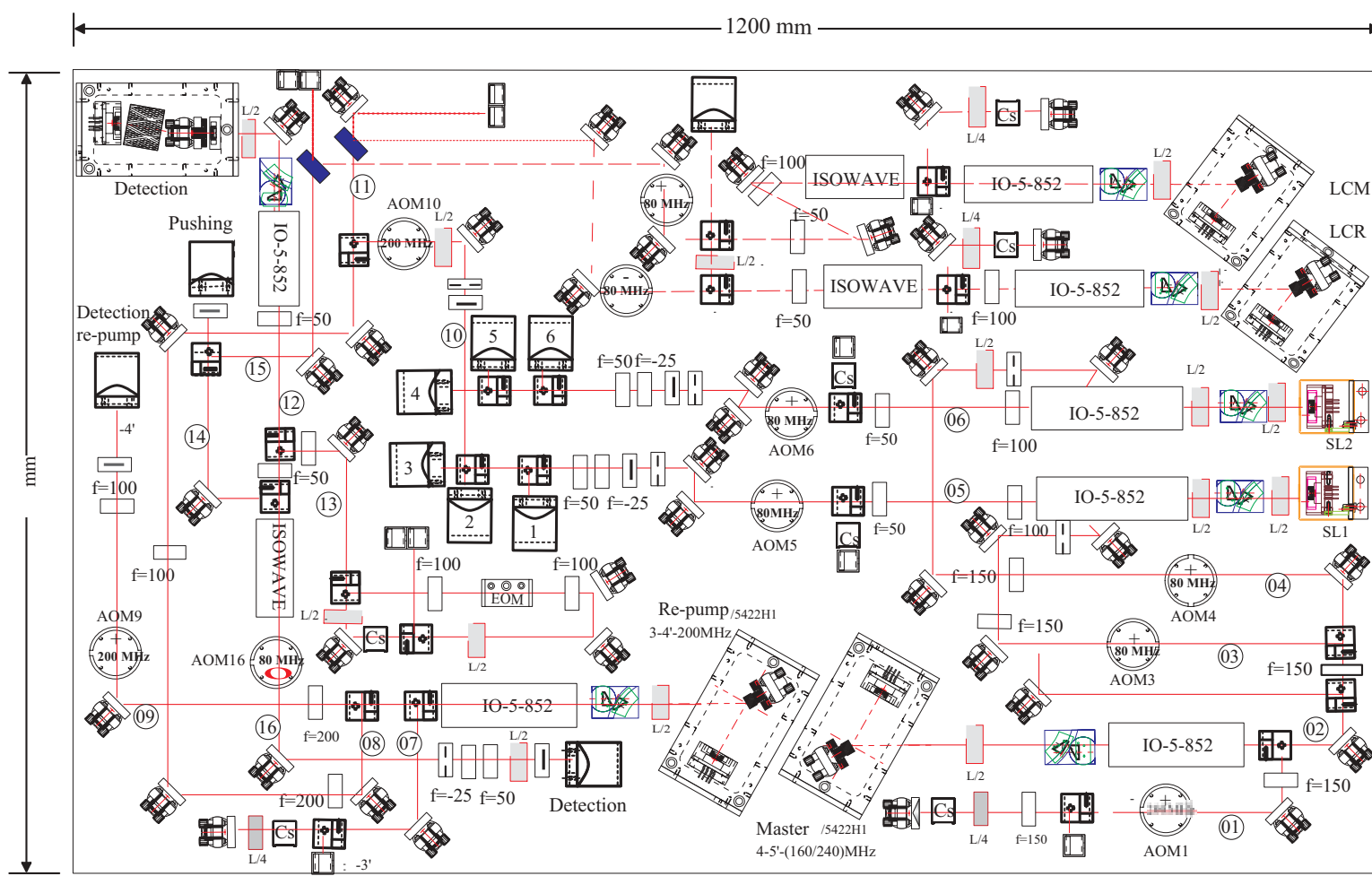


Figure 6.4: Optical bench of the improved F01. The chirp laser system is included here.

The repump laser is similar to the master laser. A small part (7) of the laser power is used for frequency stabilization to the $F = 3 \rightarrow F' = 3$ transition by using the saturated absorption technique. The output beam (8) is divided into two beams ((10) and (11)). Beam (10) is frequency shifted by +200 MHz by AOM10. This detuning corresponds to the $F' = 3 \rightarrow F' = 4$ transition frequency. It is then superimposed to two of the capture beams. A shutter, which we put after the AOM10, is used to block the repumper completely.

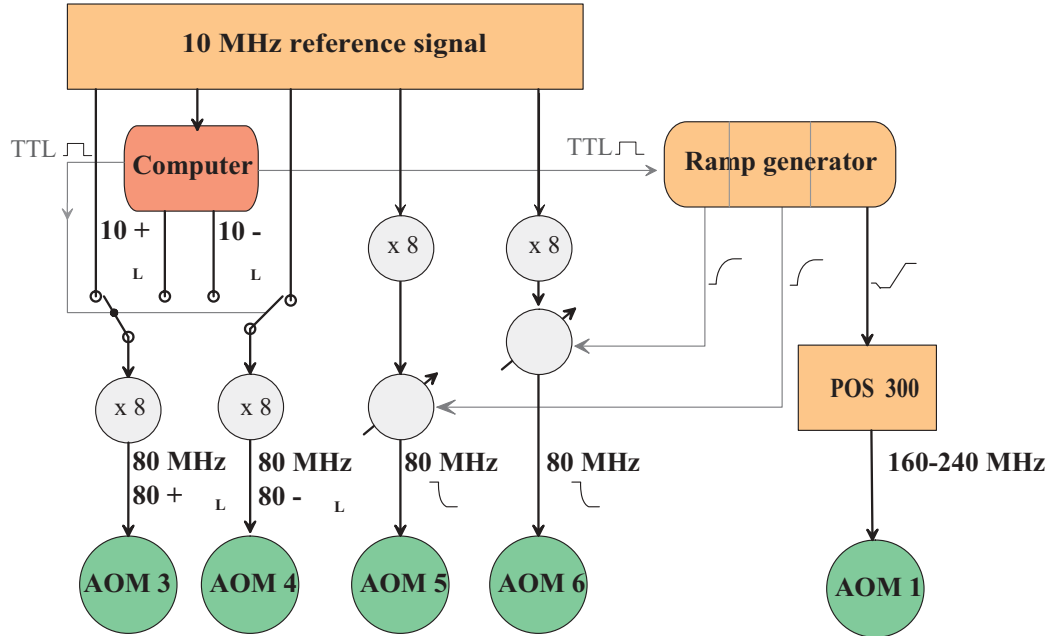
The beam (11) is used as a frequency reference for the beat-note signal to lock the repump chirp laser LCR as described in the section 6.5.2

The output beam (9) of the repump laser is also frequency shifted by +200 MHz by AOM9 to repump the atoms for the detection of the $F = 3$ state. A fiber is used to guide it to a small optical bench (about 30×30 cm) located near the detection zone. A shutter is also used to switch off this repump beam.

The detection laser is a new type of extended cavity laser. Its structure and frequency stabilization system will be detailed in section 6.3.4. The detection laser has three functions: it provides the selection pushing beam (14) and the detection beam (16) on the $F = 4 \rightarrow F' = 5$ transition, and a frequency reference (beam (15)) to frequency lock the chirp master laser LCM. One output beam (13) is used to stabilize the detection laser frequency. The beam (16) passes successively through a second optical isolator (ISOWAVE) and AOM16. The second isolator is used to prevent optical feedback from the fiber head of the detection beam. AOM16 used on the diffraction order 0 actively stabilizes the detection beam power.

6.3.3 Control of the light beam parameters

We explain here how this optical synthesis satisfies the requirement of the atom manipulation in each phase. The scheme for frequency and RF power control of the AOM's is shown un figure 6.5. An AT-TIO-10 board installed inside the computer is programmed to produce TTL signals corresponding to each phase of the atom manipulation. These TTL signals synchronize three electronic ramp generators. One is used to control the AOM1's frequency, via a POS 300 voltage controlled oscillator. The two others, acting on two RF attenuators, are used to control the RF input power of AOM5 and AOM6, respectively. The RF inputs for AOM3, AOM4, AOM5 and AOM6 are generated by 4 VCOs at 80 MHz, which are phase locked to the same 10 MHz external reference signal. During the launch and post cooling phases, the reference of AOM3 and AOM4 is shifted by $\pm\Delta\nu_L/8$ by frequency generator boards (DAQArb 5411) located inside the computer. These boards are also

Figure 6.5: *AOMs control system.*

locked to the 10 MHz reference.

6.3.4 Extended cavity semiconductor laser using a Fabry-Perot etalon

The detection laser is an extended cavity laser diode (ECL) with an intra-cavity etalon as a wavelength selector. The set-up is shown in photo 6.6. The etalon has a thickness of $50\ \mu\text{m}$ corresponding to a free spectral range of 2 THz, and a finesse of 30. Its peak transmission exceeds 95%. The output beam of the laser diode (1) is collimated by an aspherical lens (2) with a focal length of 4.5 mm, and a numerical aperture of 0.55. The solid etalon¹ (3) is glued onto a mirror mount. This enables us to finely adjust the incidence angle of the laser beam on the etalon. An aspheric lens (4) with a focal length of 18.4 mm is glued onto the fixed part of the second mirror mount. It is used to focus the beam on a beam splitter (5) with a thickness of 3 mm that closes the extended cavity. The chosen reflectivity is $R = 30\%$. The other side of this plate is AR coated. The plate is glued on a cylindrical piezoelectric ceramic (6) (from SAINT-GOBAIN with an expansion coefficient of 1 nm/volt) which is glued on the movable part of

¹We preferred the solid fused silica etalons to the air-spaced etalons to select the ECL longitudinal mode because they do not present any pressure tuning.

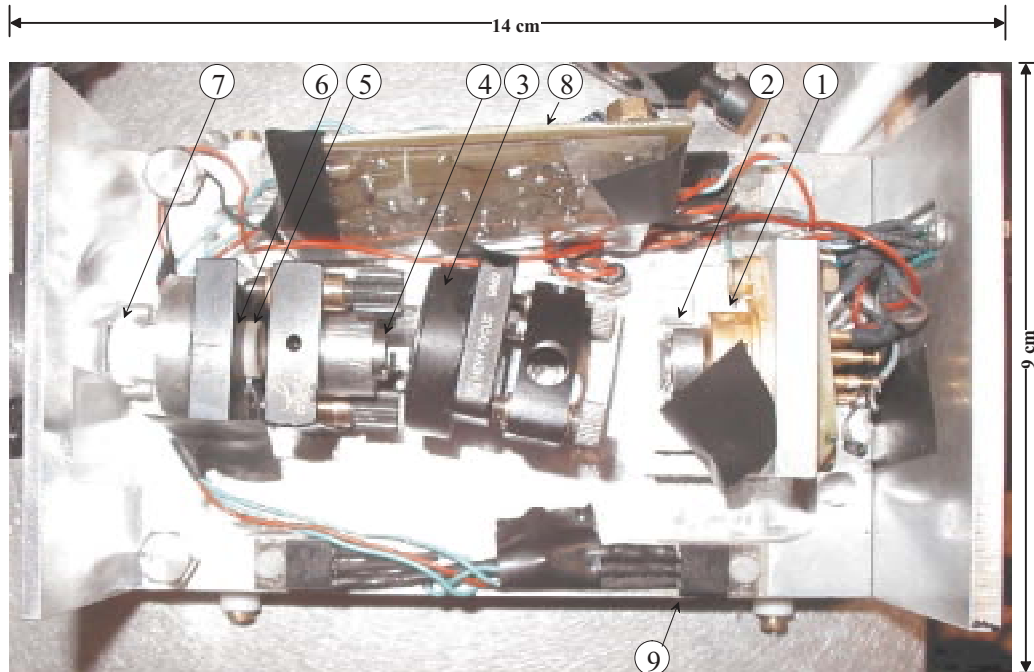


Figure 6.6: *Photograph of the ECL using an intra cavity etalon. (1) Laser diode, (2) Aspherical lens, (3) Solid etalon, (4) Aspherical lens, (5) Beam splitter, (6) Piezoelectric ceramic, (7) Aspherical lens, (8) Temperature controlling card, (9) Silicon transistors.*

the second mirror mount. Another lens (7), with a focal length of 25 mm, is used to collimate the output beam. All mechanical parts are fixed on an aluminum base plate whose position and orientation can be adjusted by three micrometer screws. The setup is enclosed inside a box² with dimensions $14 \times 9 \times 7$ cm. The temperature (~ 3 °C lower than the room temperature) of the box is actively stabilized via 4 silicon transistors (9) controlled by a PI controller (8).

The role of lens (4) is to form a 2D cat's eye for retro-reflection, therefore reducing the sensitivity to possible misalignments. Moreover, this ECL can provide about 30% output power more than that of a standard ECL (using a grating) for the same injection current.

Fig. 6.7 presents the detection laser servo system. A small part of the output beam is split into two beams to perform the saturation spectroscopy. The first one is phase modulated when passing through an electro-optic modulator (EOM) operating at 5 MHz. It is then directed to a caesium cell, enclosed

²Two identical prisms (06GPU001, Melles Griot) are mounted outside the box to correct the laser beam to be near circular.

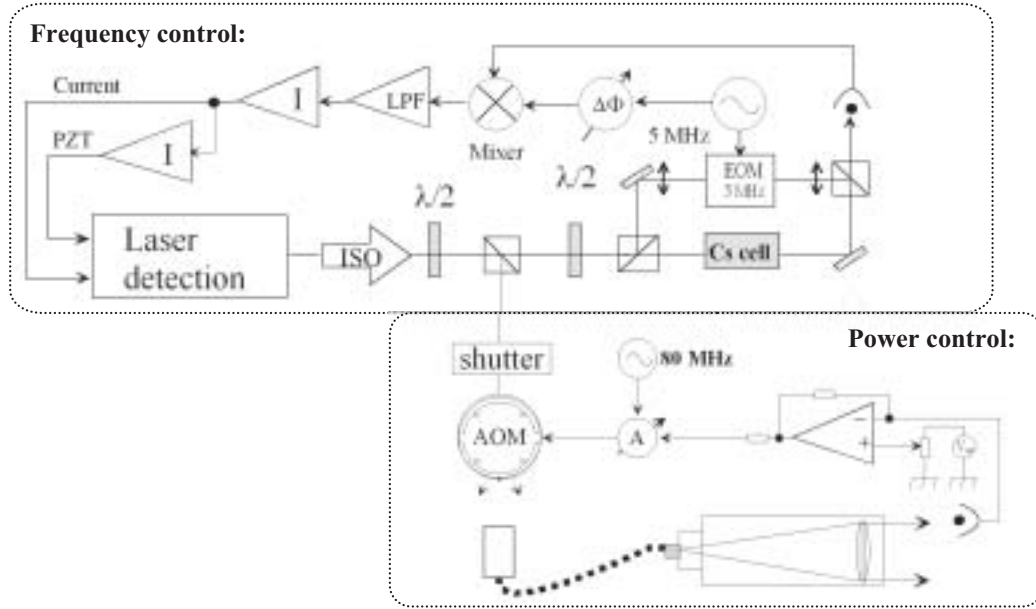


Figure 6.7: Frequency and power servo loops system of the detection laser using an etalon as selective element. LPF=Low pass filter, ISO=Optical isolator.

by a magnetic shield, as saturation beam. The second one, the probe beam, counter-propagates through the cell and illuminates a fast response (cut-off frequency 1.5 GHz) silicon photodiode S5973-01. The saturated absorption converts the phase modulation of the saturation beam to amplitude modulation of the probe beam. We apply a 5 MHz signal of 10 dBm power to the EOM. The saturation spectroscopy signal is mixed with part (0 dBm) of the RF signal itself which is phase shifted by a home-made phase shifter in order to compensate for the phase difference introduced by the setup. The output of the mixer (Mini-Circuits TUF1) provides the error signal used to control the laser current and PZT supply. We set the bandwidth to about 100 Hz for the PZT loop to compensate the slow variation of the cavity length, and to about 100 kHz for the current loop to reduce acoustic-optic noise. The spectral density of the error signal of the locked detection laser is shown in fig. 6.8. According to section 2.9.1, the influence of the laser frequency noise on the fountain frequency stability is negligible ($< 10^{-16} \cdot \sqrt{\frac{T_c}{\tau}}$).

The transmission of the optical fiber fluctuates due to the environmental condition (temperature, mechanical stress, ...), a second servo system is used to control laser power (see fig. 6.7). This is done by driving the RF power of an AOM (AOM16 in fig. 6.4). The zero order output beam is coupled into the fiber and expanded to a parallel beam with 28 mm diameter by the

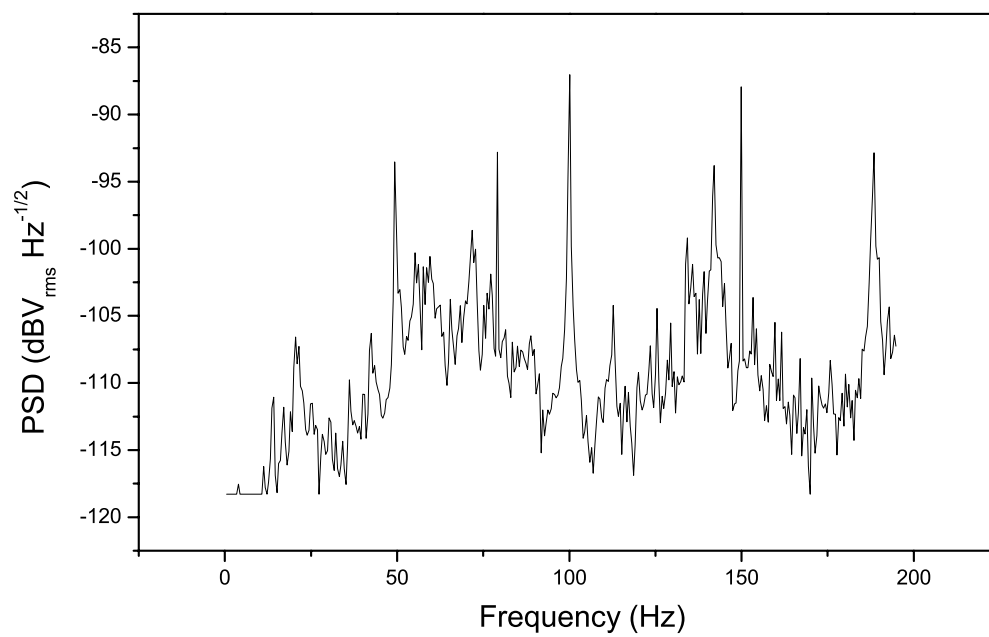


Figure 6.8: *Error signal of the detection laser. The conversion factor $k = 1.325$ MHz/v.*

collimator of the detection system. A small fraction of the output of the collimator irradiates a photodiode used to monitor the beam power. The spectral density of the power fluctuations is $S_{\delta I/I} \sim 10^{-9}/f$ [4]. According to section 2.9.1, the influence of laser intensity noise on fountain frequency stability is negligible ($< 10^{-15} \cdot \sqrt{\frac{T_c}{\tau}}$).

6.4 The capture zone

In the previous version of FO1 atoms were loaded in a MOT in a 4 horizontal and 2 vertical laser beam configuration. This method produces more atoms than an optical molasses, but at the cost of a higher atom densities which in turns increases the collisional frequency shift. In the new arrangement, the beam size is no longer limited by the size of the interrogation cavity cut-off guide ($\phi 10$ mm). We can use larger laser beams to compensate for the reduction of the loading efficiency in pure optical molasses.

The cold atoms are loaded in the intersection of 6 laser beams with orthogonal polarization (lin \perp lin configuration). The three pairs of counterpropagating laser beams have orthogonal directions. In the coordinate system defined by the beams the fountain vertical axis is along the direction (1, 1, 1) (the previous vector was (0.0.1)). The 6 laser beams are guided from the optical bench by fibers whose polarization extinction ratio is better than 20 dB. Since the fiber output is close to the loading zone, it is important to use non-magnetic ferrules. The ferrules are screwed into collimators as show in fig. 6.10. We put a polarizing cube to avoid optical feedback from counter-propagating beams. The reflected beam is used to monitor and stabilize the output power (~ 7 mW). Each collimator provides a Gaussian beam with a diameter of 27 mm. The collimator is screwed onto the surface of the capture chamber. The mechanical angular tolerances of the chamber surfaces is of $\sim 10^{-3}$ rad, and the collimators are pre-aligned within 10^{-3} radian.

The glass windows of the capture zone are made from BK7 glass and have a diameter of 46 mm, and a thickness of 6 mm. They induce a wavefront distortion less than $\lambda/10$. An antireflection coating ensures a transmission ratio larger than 99.8%.

Four windows in the equatorial plate allow one to measure the fluorescence signal of the captured atoms and the atomic cloud size.

The new geometry has many advantages: the use of optical fibers and pre-aligned collimators improves the stability of the loading process. Precise control of only 2 instead of 3 frequencies is necessary to launch the atoms. Larger cooling beams can be used for the molasses. The absence of the vertical beams travelling along the interrogation zone much reduces the possible

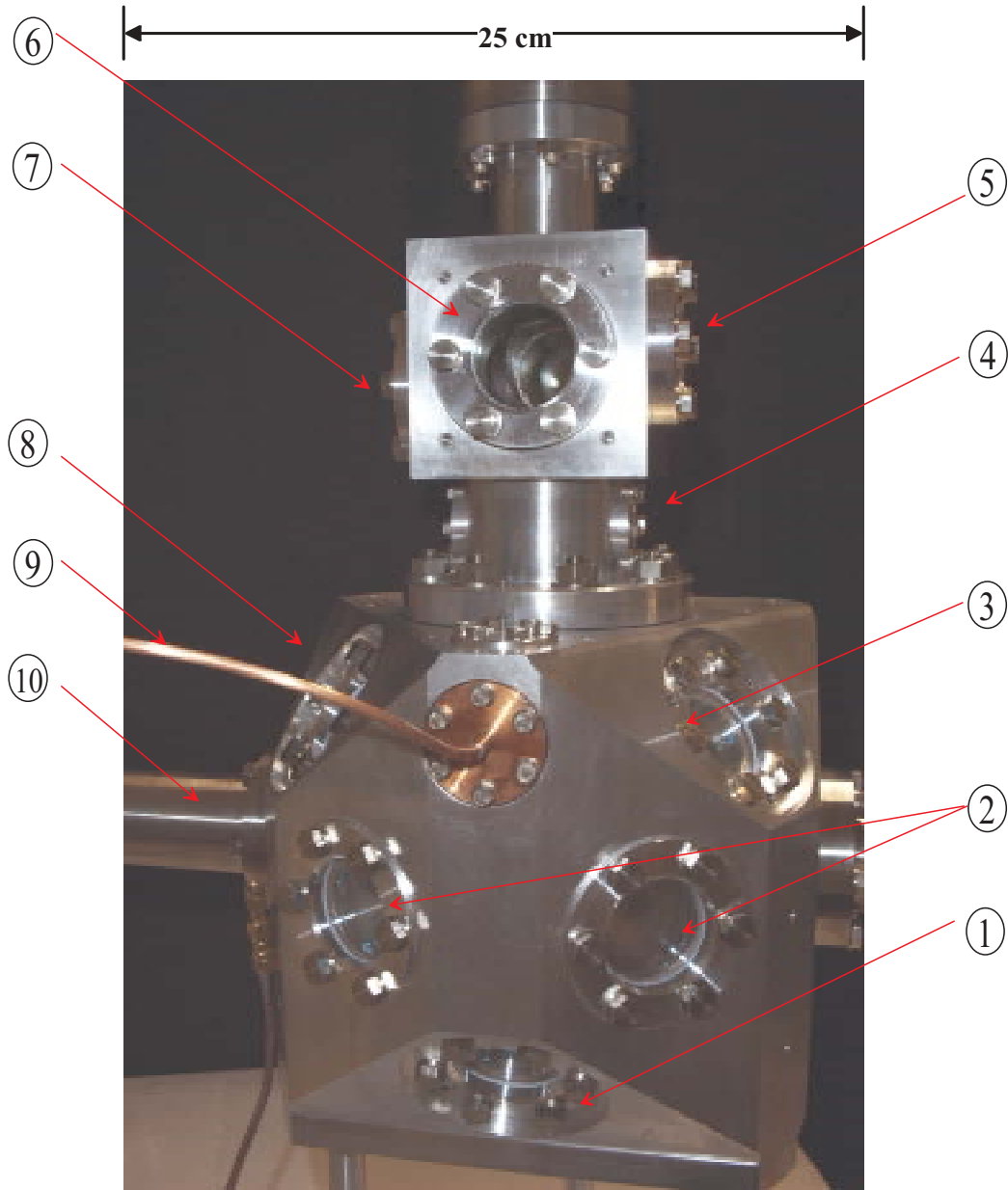


Figure 6.9: Photograph of the capture chamber, the selection zone and the detection zone. Windows (1), (3) and (8) are used for 3 of the 6 molasses beams. Windows (2) are used to measure the number of cold atoms in the molasses and the size of the atomic sample. Window (4) is used for the push beam. From windows (5) and (7) the fluorescence light of atoms induced by the detection beams is collected. The detection beams cross windows (6). (9) is the co-axial cable supplying the microwave for the selection cavity. The tube (10) is along the propagation direction of the decelerated atomic beam.

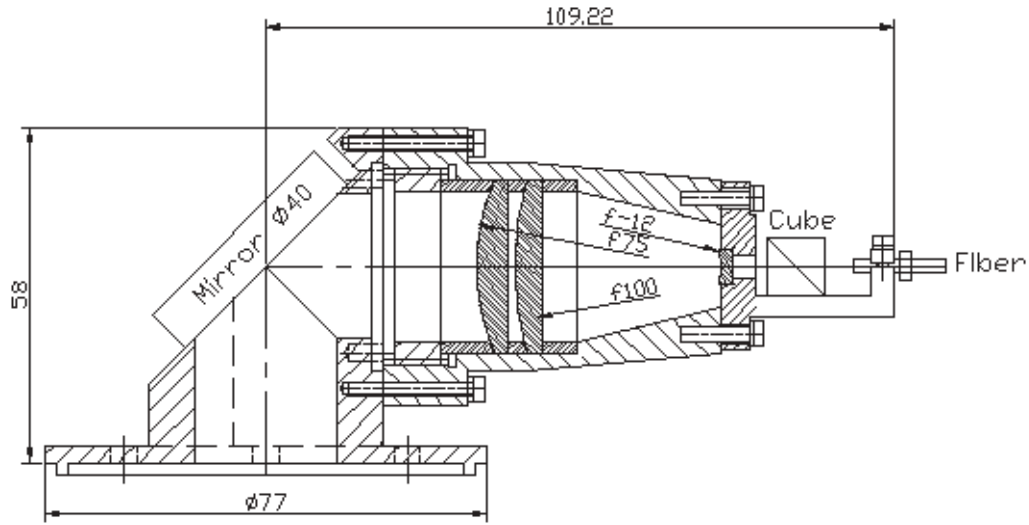


Figure 6.10: *Optical collimator for the capture zone. The design is imposed by the limited space around the capture zone. The fiber end is a non-magnetic ferrule.*

light shift due to stray light in the interaction region.

6.5 Deceleration of the caesium beam

6.5.1 Characteristics of the thermal beam

Figure 6.11 shows a schematic of the atomic source. Several grams of caesium, filled in glass cells are placed in the copper tube (1). Once ultra high vacuum is achieved, the cells are broken with a plyer. The reservoir is heated to ~ 90 °C, corresponding to a Cs vapor pressure of $\sim 5 \times 10^{-2}$ Pa. This pressure corresponds to an atomic density $n = 8 \times 10^{12}$ cm $^{-3}$. The pressure difference between the oven and the loading chamber produces an effusive jet which is collimated by an array of about $N_t = 420$ capillaries (2) of “Monel 400”³, with inner radius $a = 100$ μ m, thickness 50 μ m, and length $L = 8$ mm. The effective output section is about 18 mm 2 . In order to prevent the atoms from collimator sticking to the inside wall, the collimator temperature is kept about 20 °C higher than that of the copper tube. Graphite tubes (3) placed along the propagation direction of the atomic beam absorb the slightly diverging atoms reducing the background Cs vapor. The thermal beam travels over a distance of 50 cm and enters the capture zone (4). A

³Monel is an alloy of copper and nickel

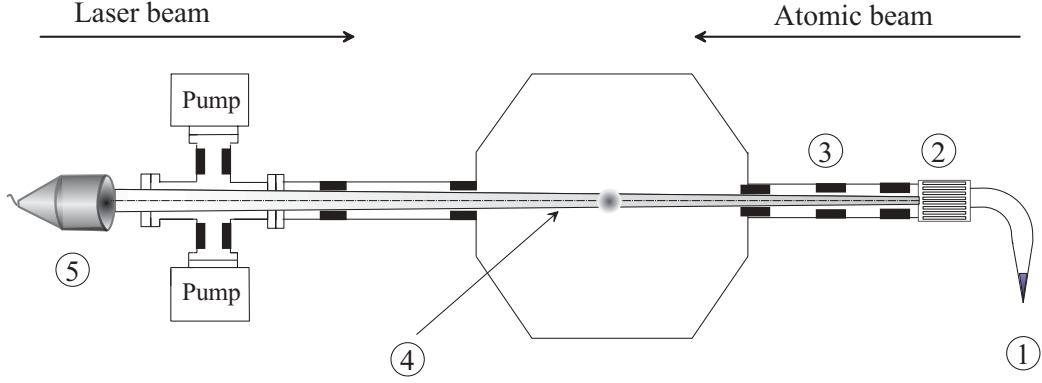


Figure 6.11: *Schematic diagram of the decelerated caesium beam source. (1) Copper tube, (2) Collimator capillaries, (3) Graphite tubes, (4) Capture zone, (5) Laser beam collimator.*

counter-propagating laser beam (5) is superimposed to the beam to reduce by chirp cooling the longitudinal velocity of Cs atoms.

The velocity distribution of the atoms ejected from the capillaries is given by [31]

$$P_B(v) = \frac{2}{\alpha^4} v^3 \exp(-v^2/\alpha^2). \quad (6.2)$$

The average velocity is given by

$$\bar{v} = \frac{3\sqrt{\pi}}{4} \alpha, \quad (6.3)$$

with

$$\alpha = \left(\frac{2k_B T}{m}\right)^{1/2}. \quad (6.4)$$

At the temperature $T = 366$ K, the characteristic velocity (the most probable velocity in a atomic gas) is $\alpha = 214$ m/s and the average velocity is $\bar{v} = 284$ m/s. In the capture zone the vacuum is about 10^{-9} Torr, therefore we can neglect atomic beam diffusion by the background gas. In the capture zone, the atomic beam flux F_B and the divergence angle $\theta_{1/2}$ at half maximum are given by [4]

$$F_B \simeq 1.6 \frac{1}{\frac{4L}{a}(1 + \frac{3L}{8a})} \times n \times \frac{2}{\sqrt{\pi}} \alpha \times N_t \pi a^2 \quad (6.5)$$

$$\theta_{1/2} \simeq 1.7 \frac{a}{L} = 21 \text{ mrad}. \quad (6.6)$$

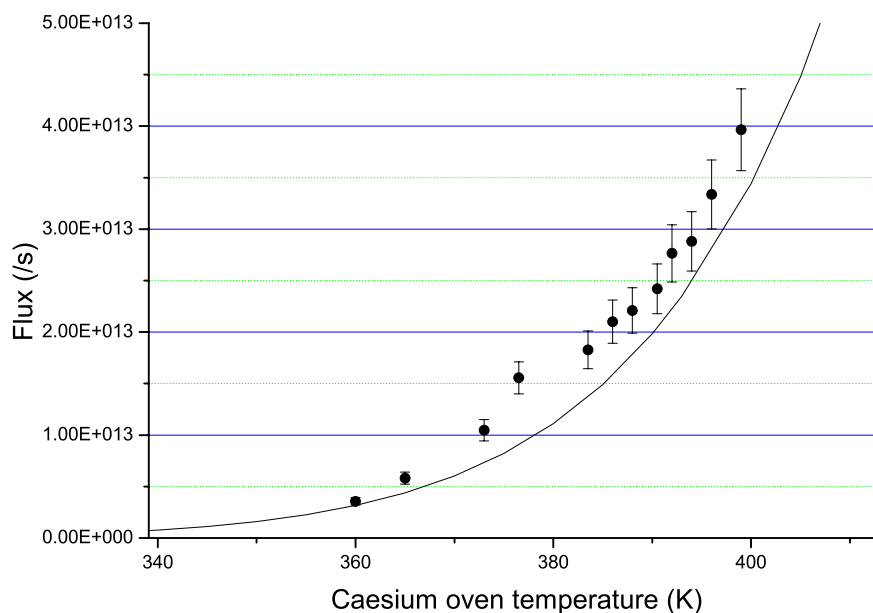


Figure 6.12: *Measurements of the atomic beam flux as a function of Cs oven temperature. The solid line is obtained from equation (6.5).*

Figure 6.12 shows measurements of the atomic beam flux F_B as a function of Cs oven temperature together with the expected flux given by equation (6.5). The flux is measured by detecting the absorption of a laser beam with a diameter of $\phi = 27$ mm and an intensity of 0.2 mW/cm². It is frequency stabilized on the transition $F = 4 \rightarrow F' = 5$. The laser beam illuminates the center of the loading region and is orthogonal to the atomic beam. It is focused on a calibrated photodiode. If ΔN is the number of atoms in the beam deduced from the absorption signal, the atomic beam flux is $F_B = \Delta N / \delta t$, where $\delta t \simeq \phi \times \langle 1/v \rangle$ is the averaged transit time of the atoms through the probe beam, and $\langle 1/v \rangle$ the average inverse velocity.

6.5.2 Deceleration of the atomic beam

We decelerate the thermal atomic beam by using the radiation pressure effects on atoms induced by a counter-propagating laser beam. The compensation of the Doppler shift during the atom deceleration can be done by modifying either the laser frequency ω_l or the atomic resonance frequency ω_a . The most commonly used methods are the chirp cooling technique and the Zeeman-slower. In the first case, the laser frequency is chirped so as to

follow the Doppler effect variation during deceleration. In the second case, frequency tuning is achieved with a spatially varying Zeeman effect induced by an inhomogeneous static magnetic field. Since the strong magnetic fields necessary for Zeeman-slower can perturb the fountain operation, we use chirp cooling technique.

6.5.3 The chirp laser system

The scattering rate γ of photons from the laser field is given by [40]

$$\gamma = \frac{\Gamma}{2} \frac{I/I_s}{1 + I/I_s + [2(\Delta\omega + \Delta\omega_D)/\Gamma]^2} \quad (6.7)$$

where $\Delta\omega = \omega_l - \omega_a$ is the detuning between the atomic resonance and the laser, I_s is the saturation intensity, and $\Delta\omega_D = -\vec{k} \cdot \vec{v}$ is the Doppler shift (positive for our case). The net force on the atoms is therefore

$$\vec{F} = \hbar \vec{k} \gamma. \quad (6.8)$$

Our deceleration beam has a power of 10 mW, has a diameter of 26 mm at the vacuum chamber input window, and is focused onto the output of the Cs oven. 1 mW of repump light is superimposed on the slowing beam with the same geometrical and chirp characteristics. We adjust the parameters of the frequency chirp so as to optimize the measured capture rate of the optical molasses. Optimum is found for a deceleration duration of 5 ms, and an initial (resp. final) frequency detuning of -260 MHz (resp. -23 MHz). The corresponding deceleration is $4 \times 10^4 \text{ m/s}^2$.

Fig. 6.13 shows servo system used for the chirping laser. A ramp generator produces an adjustable signal which acts on the laser diode current sweeping its frequency (about 100 MHz/mA).

The scheme of the chirped lasers is shown in fig. 6.14. We employ two laser diodes SDL5422 mounted in a grating tuned extended cavities. The cavity length has been limited to 2.5 cm so as to maximize the continuous frequency tuning of the laser via the diode current ($\sim 100 \text{ MHz/mA}$). Both lasers are frequency locked to reference lasers (beams (15) and (11) of figure 6.4) with the scheme shown in figure 6.13. AOMs shift the frequency of the two beat notes by 80 MHz. The beat-note signal is divided by 512, and sent to a frequency-to-voltage converter. The output is compared to a ramp which gives the error signal of the servo loop. The ramp is also fed forward to the diode currents so as to limit the excursion of the error signals. The behavior of the chirped lasers is monitored by saturated absorption spectroscopy (see fig. 6.15). The servo system is fast enough to improve the linearity of the frequency chirp. It increases the number of slowed atoms by a factor of 2.

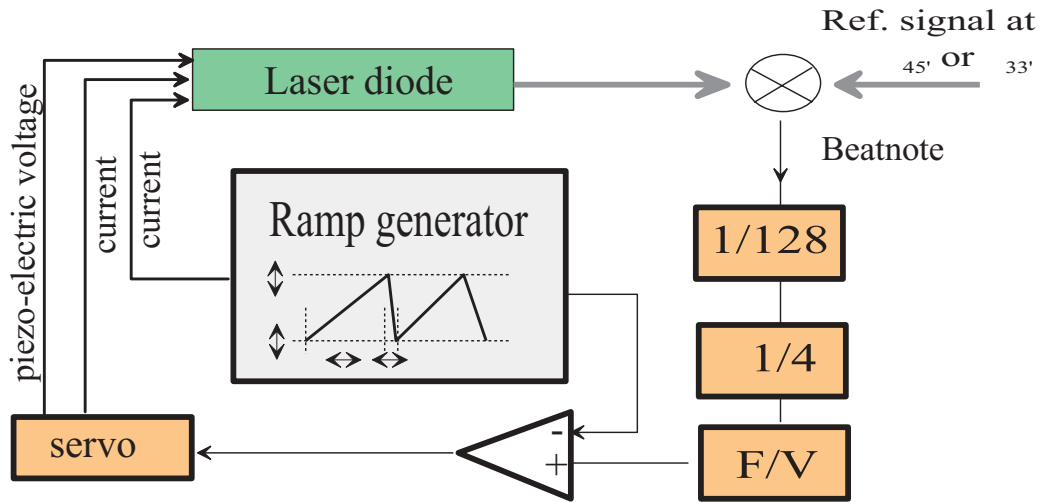


Figure 6.13: Schematic of the chirp servo system.

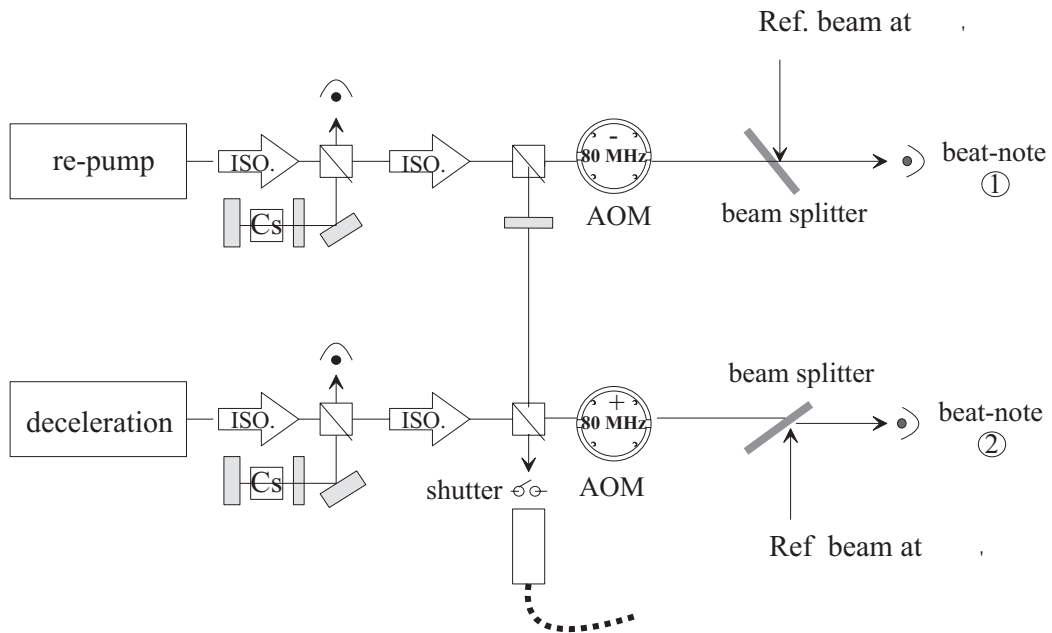


Figure 6.14: Schematic of the chirp lasers sources.

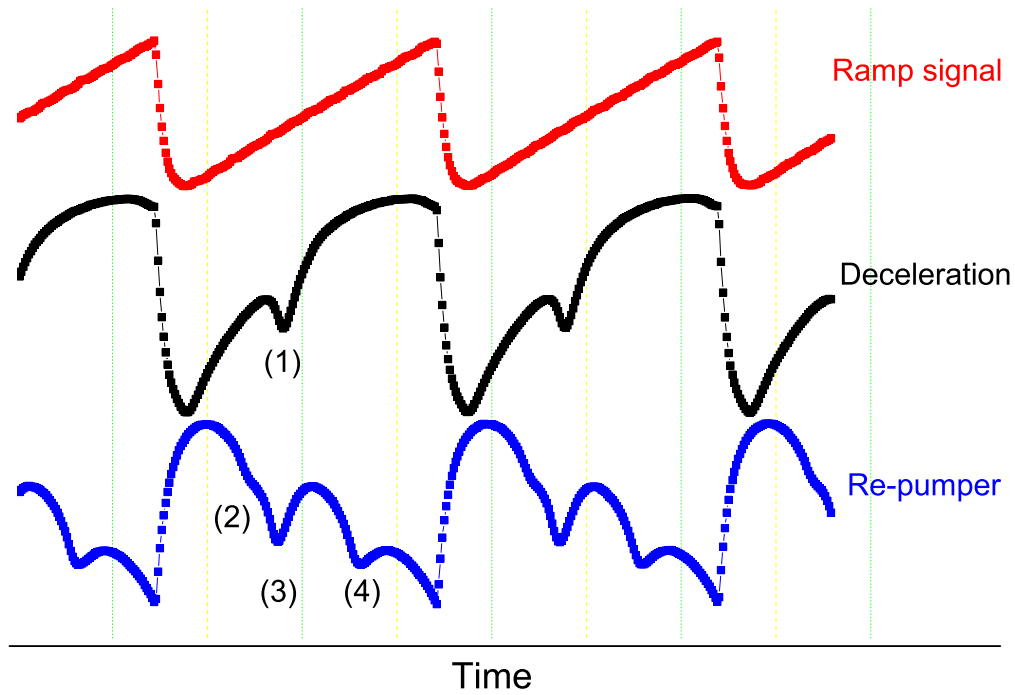


Figure 6.15: Saturated absorption spectroscopy signal of the chirp lasers. (1) represents the crossover signal between the transitions $F = 4 \rightarrow F' = 4$ and $F = 4 \rightarrow F' = 5$. (2), (3) and (4) are the transition $F = 3 \rightarrow F' = 3$, the crossover between transitions $F = 3 \rightarrow F' = 2$ and $F = 3 \rightarrow F' = 4$, and the crossover between transitions $F = 3 \rightarrow F' = 3$ and $F = 3 \rightarrow F' = 4$, respectively.

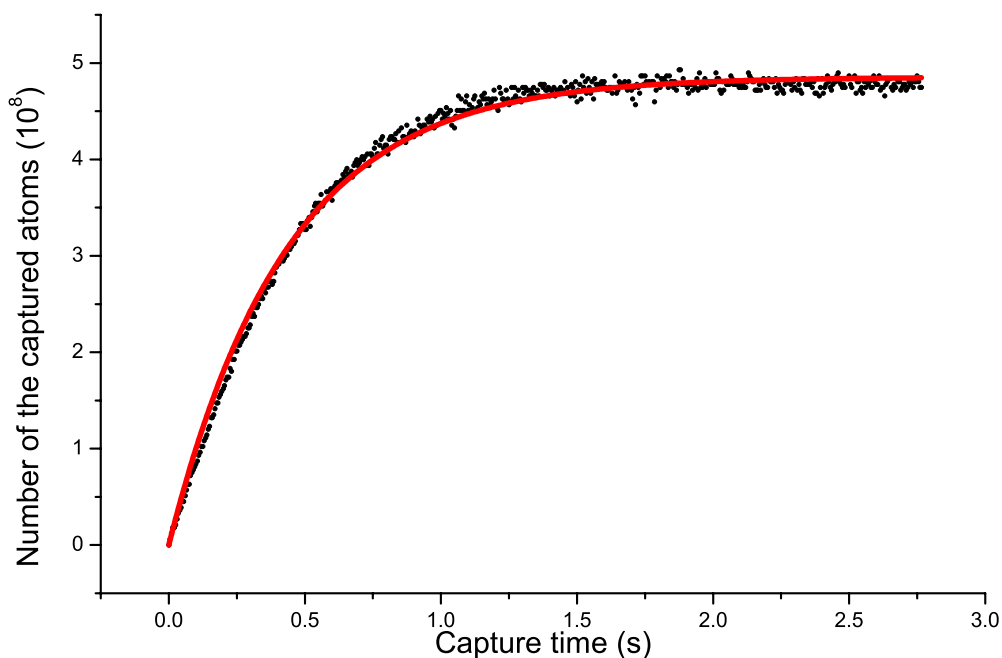


Figure 6.16: *The optical molasses loading curve. Experimental data (points) is fitted by using the model function (line) $N(t) = N_0(1 - e^{-t/\tau})$.*

6.5.4 Atom capture results

Fig. 6.16 shows a typical loading curve of the optical molasses. The captured atom number is proportional to the fluorescence signal. The loading time constant is $\tau \sim 420$ ms. The estimated steady state atom number is $\sim 7.5 \times 10^8$. The improvement as compared to the old setup of FO1 is about one order of magnitude.

6.6 State selection system

The state selection system has been modified so as to implement the adiabatic passage method [115]. Atoms in $F = 4, m_F = 0$ are first transferred to $F = 3, m_F = 0$ by adiabatic passage with an RF pulse inside a microwave cavity. Depending on the pulse characteristics, one can transfer either all the atoms or exactly one half of them. Atoms remaining in $F = 4$ are then blasted away by a pushing laser beam.

6.6.1 Selection cavity

The selection cavity is mechanically carved into the upper part of the vacuum chamber containing the capture zone (see figure 6.9). The selection cavity has the dimensions as the interrogation cavity. Its Q however is smaller ($Q = 5500$) in order to minimize the effect of thermal fluctuations. We feed the cavity with a circular antenna formed by the core of a coaxial cable soldered on its shield. The antenna is placed at half height of the cylinder inner surface. Its axis is parallel to the cavity axis. In order to keep an ultra-high vacuum, we solder the co-axial cable into a copper feed-through with “Castolin” and “Eutectic” at a temperature of 220°C. The same procedure has been used for the interrogation cavity (see section 2.5.2). The TM_{111} mode is eliminated by a ring filter that cuts the current lines of the mode and shifts its resonance frequency. With this setup, the mode TM_{111} was not measurable at our level of resolution.

6.6.2 Adiabatic passage

In a Cs fountain, the collisional frequency shift represents the largest and most difficult systematic error. It can be expressed by the formula $\delta\nu_{coll} = K_{coll} n_{eff}$, where K_{coll} is a constant that depends on the collisional parameters, and n_{eff} is the effective density: the time-averaged atomic density, weighted by the sensitivity function, averaged over the atomic trajectories [119]. It depends largely on parameters, such as the molasses temperature, the initial size of the molasses, the initial atom number, the launch velocity, the microwave power inside the Ramsey cavity, the sensitivity function $g(t)$, the fountain geometry, the geometry of the detection zone and the detection beam parameters.

Usually, the collisional frequency shift is measured by alternating cycles with high atom density (HD) and low atom density (LD) of the atom sample. Then, a linear extrapolation to zero density gives the corrected clock frequency. Unfortunately, n_{eff} can not directly be measured, only the number of detected atoms. Therefore the method is useful only if n_{eff} is proportional to the detected atoms N_{at} . In this case, the collisional frequency shift is $\Delta\nu = K'_{coll} N_{det}$. Up to now, two ways have been used to change the atom density: varying the capture phase parameter (loading time and capture laser beam intensity) or changing the selection microwave power. Both techniques modify not only atomic number but also affect the position and velocity distribution. Consequently the K' coefficients differs from the HD and LD case. A numerical simulation shows that these two methods lead in the best case to a 10-20% error in the determination of the collisional shift [115].

Improvement can be made however by using the method of adiabatic passage (AP) during selection. Here the number of atoms in the sample can be changed without affecting the velocity and position distributions. In addition, this method is insensitive to fluctuations of experimental parameters such as the size and temperature of the atomic sample, and the power coupled into the selection cavity.

Adiabatic transfer of the atomic population Adiabatic transfer has its origins in nuclear magnetic resonance, where it was used to achieve population inversion of spin systems [120, 121]. Loy [122] first observed the population inversion in the optical regime.

A clear physical interpretation of the atom-photon interaction is offered by the dressed-atom approach [123]. The eigenenergies of the manifold E_n for a two level atom coupled by light field are

$$\begin{aligned} E_{+,n} &= (n+1)\hbar\omega - \frac{\hbar\delta}{2} + \frac{\hbar\Omega}{2} \\ E_{-,n} &= (n+1)\hbar\omega - \frac{\hbar\delta}{2} - \frac{\hbar\Omega}{2} \end{aligned} \quad (6.9)$$

where $\Omega = \sqrt{b^2 + \delta^2}$ and $b = \frac{\mu_B B}{\hbar}$ is the Rabi frequency, and δ is the frequency detuning of the light field with respect to the atomic resonance. The dressed states

$$\begin{aligned} |\psi_+, n\rangle &= \sin\theta |3, n+1\rangle + \cos\theta |4, n\rangle \\ |\psi_-, n\rangle &= \cos\theta |3, n+1\rangle - \sin\theta |4, n\rangle \end{aligned} \quad (6.10)$$

are a linear superposition of the two uncoupled levels $|3, n+1\rangle$ and $|4, n\rangle$, where $|F, n\rangle$ is the wave function corresponding to n photons in the field and an atom in the $|F, m_F = 0\rangle$ state. The mixing angle θ is defined by

$$\tan(2\theta) = -b/\delta. \quad (6.11)$$

Both θ with $0 < \theta < \pi/2$ and the eigenenergies are functions of the detuning δ . In fig. 6.17, the ‘‘anti-crossing’’ of the states $|\psi_+, n\rangle$ and $|\psi_-, n\rangle$ induced by the strong coupling at $\delta = 0$ ($\theta = \pi/4$) becomes apparent. Equation (6.10) indicates that on resonance the states $|\psi_+, n\rangle$ and $|\psi_-, n\rangle$ are a superposition of the uncoupled levels with equal weight. For weak coupling ($\theta = 0, \pi/2$), the perturbed states are only slightly different from the unperturbed levels. When δ is swept across the resonance, as long as the adiabaticity condition is fulfilled, $|\psi_-, n\rangle$ evolves from $|3, n+1\rangle$ to $|4, n\rangle$ and vice versa for $|\psi_+, n\rangle$.

The adiabaticity criterion is satisfied when the time variation of the projection of state $|\psi_-, n\rangle$ on the $|\psi_+, n\rangle$ state is sufficiently small. Messiah

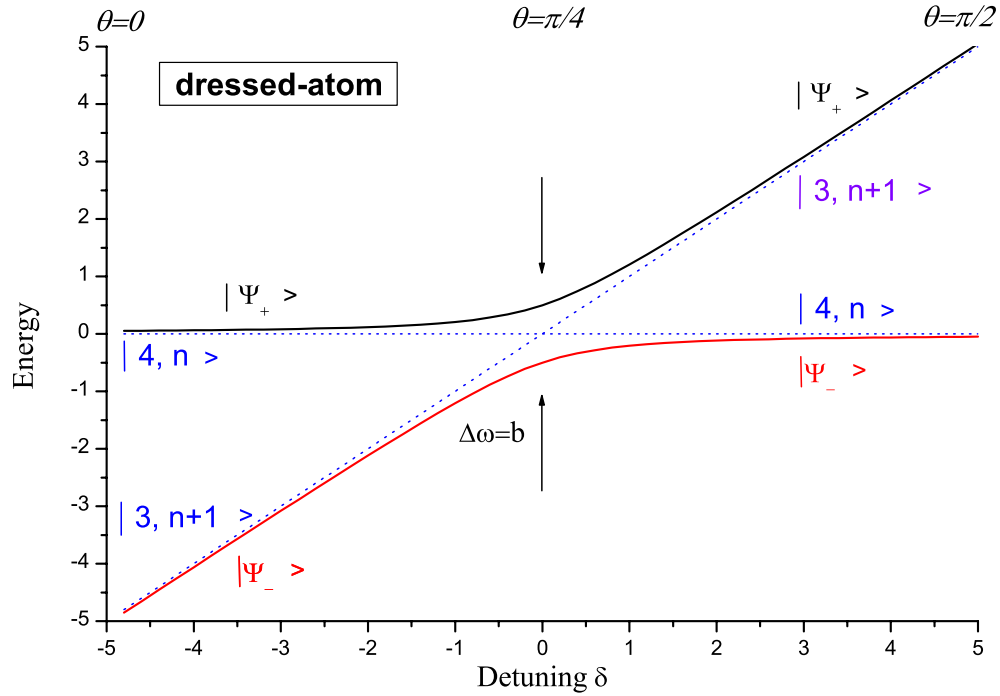


Figure 6.17: Variation of the energies $E_{+,n}$ and $E_{-,n}$ with respect to detuning δ . The eigenenergy of $|4, n\rangle$ is chosen to be zero. The solid lines reflecting $E_{+,n}$ and $E_{-,n}$ repel each other, an “anti-crossing” appears on resonance ($\delta = 0$). These curves are the branches of hyperbolae whose asymptotes are the unperturbed levels $|4, n\rangle$ and $|3, n + 1\rangle$.

has established the adiabaticity condition in a more general context of quantum mechanics [124]. It can be expressed as

$$\left| \langle \psi_+ | \frac{d}{dt} | \psi_- \rangle \right| \ll \frac{\Delta E}{\hbar}, \quad (6.12)$$

where ΔE is the value of the energy difference between the states. This condition is most stringent at the resonance, where it reduces to

$$\left| \frac{\partial \delta}{\partial t} \right| \ll b^2(t). \quad (6.13)$$

In order to fulfill this condition, we choose the detuning from resonance, δ according to

$$\dot{\delta}(t) \propto b^2(t). \quad (6.14)$$

In order to get an excitation spectrum with a single peak and no side lobe that could produce unwanted off-resonant excitations (this effect decreases the the desired transfer efficiency of 100% at the end of the chirp), we prefer a Blackman pulse (BP) for amplitude $b(t)$ [125]. The Blackman pulse is defined by

$$b(t) = b_0 \left[0.42 - 0.5 \cos\left(\frac{2\pi t}{\tau}\right) + 0.08 \cos\left(\frac{4\pi t}{\tau}\right) \right] \quad (6.15)$$

for $0 \leq t \leq \tau$, where τ is the pulse duration (see figure 6.18). This pulse has a small power spectral density far from the central excitation frequency. The experimental results in [126] indicate that the Blackman pulse (BP) reduces unwanted excitations by at least 3 orders of magnitude outside the central lobe.

To fulfill the adiabaticity condition and to optimize our experimental conditions, we vary the frequency shape by a small parameter ε :

$$\begin{aligned} \delta(t) &= \varepsilon \int b^2(t) dt \\ &= \delta_0 + \Delta\delta \left[\frac{t}{\tau} + \frac{1}{2\pi} \frac{1}{9138} \left(-13800 \sin \frac{2\pi t}{\tau} + 2883 \sin \frac{4\pi t}{\tau} - 400 \sin \frac{6\pi t}{\tau} + 24 \sin \frac{8\pi t}{\tau} \right) \right], \end{aligned} \quad (6.16)$$

where ε is chosen in order to fulfill the condition (6.13) and $\Delta\delta = 0.3046 \varepsilon b_0^2 \tau$. The frequency chirping is fast at high Rabi frequencies and slow at small ones. This shape ensures that the adiabaticity condition (6.14) is satisfied for all atoms passing through the selection cavity.

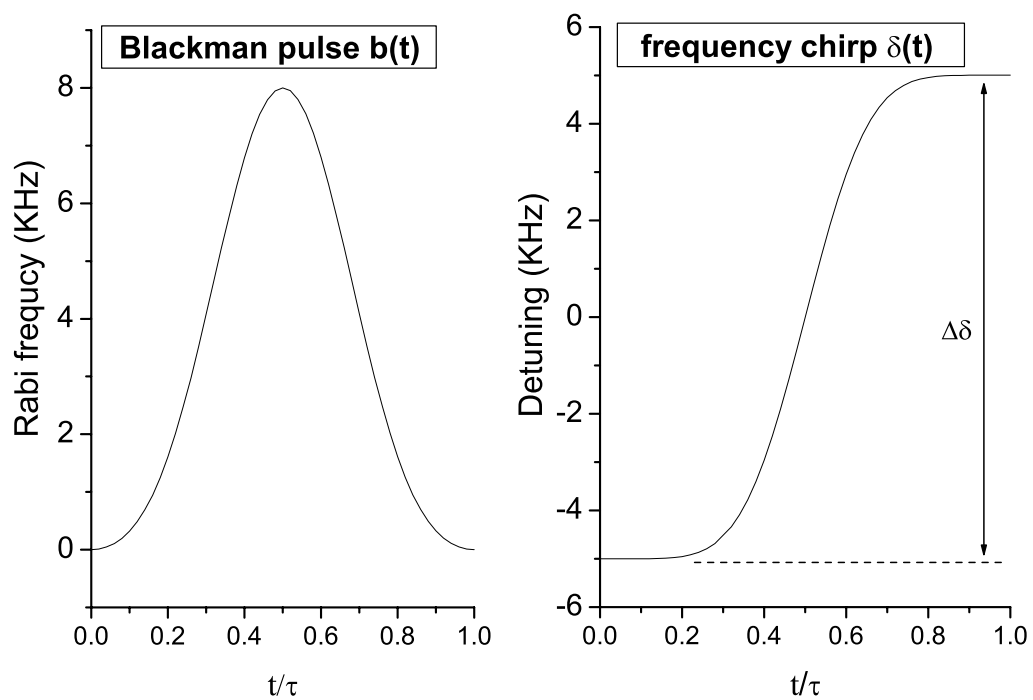


Figure 6.18: *Blackman pulse and the associated detuning which satisfies the adiabaticity condition. The resonance frequency shift induced by the static magnetic field is not considered here.*

The method of adiabatic passage allows us to transfer atoms from the $|3, n+1\rangle$ level to the $|4, n\rangle$ level with almost 100% efficiency. Besides this, it has another striking property: by stopping AP at the resonance (half Blackman pulse (HBP)) using an attenuator, the atoms are left in a superposition of the unperturbed levels $|3, n+1\rangle$ and $|4, n\rangle$ with equal amplitudes independent of the Rabi frequency (see figure 6.19). This allows us to prepare two atomic samples, where both the ratio of the effective densities and the ratio of the atom numbers are exactly 1/2. This is ideal for performing collisional frequency shift measurements.

A numerical simulation was performed by solving the time-dependent Schrödinger equation for a two level atom in a TE_{011} mode inside the microwave selection cavity. The spatial distribution of the cold atom cloud, as well as its trajectory were taken into account. This work was performed to determine the optimum parameters realizing an efficient transfer with small sensitivity to fluctuations.

Table 6.1: *The optimized parameters for BP and HBP in the improved FO1. The calculation uses the following parameters: Field mode TE_{011} ; Selection cavity length 43 mm; Initial atom velocity 4 m/s, Initial atomic cloud having a Gaussian spatial distribution with $\sigma_0 = 3.5$ mm.*

Term	BP	HBP	Unit
Maximum Rabi frequency b_0	8	8	kHz
Maximum detuning of the frequency chirp δ_0	5	5	kHz
Duration τ ; $(\tau/2)$	4	4	ms
The position at which atoms experience the maximum Rabi frequency with respect to the cavity center ⁴ $\Delta z(\tau)$; $\Delta z(\tau/2)$	± 5	0	mm
Final frequency detuning $\delta(\tau)$; $\delta(\tau/2)$	+5	0	KHz

The optimized parameters for our fountain (the parameters are shown in figure A.2) are listed in table 6.1. The simulation shows that the transition probabilities deviate from 100% and 50% by less than 10^{-3} . The HBP duration is equal to that of BP with an advantage of the same fountain cycle.

The only critical parameter of the the AP method is the accuracy of the final frequency detuning of the HBP. The simulation indicates that the sensitivity of transfer efficiency to the final detuning is $6.23 \cdot 10^{-5}/\text{Hz}$ with our optimized parameters (see fig. 6.19).

Experiments After launch, the cold atoms are almost equally distributed among the 9 levels $F = 4, m_F = -4 \dots m_F = 4$ (can see figure 2.12). In order

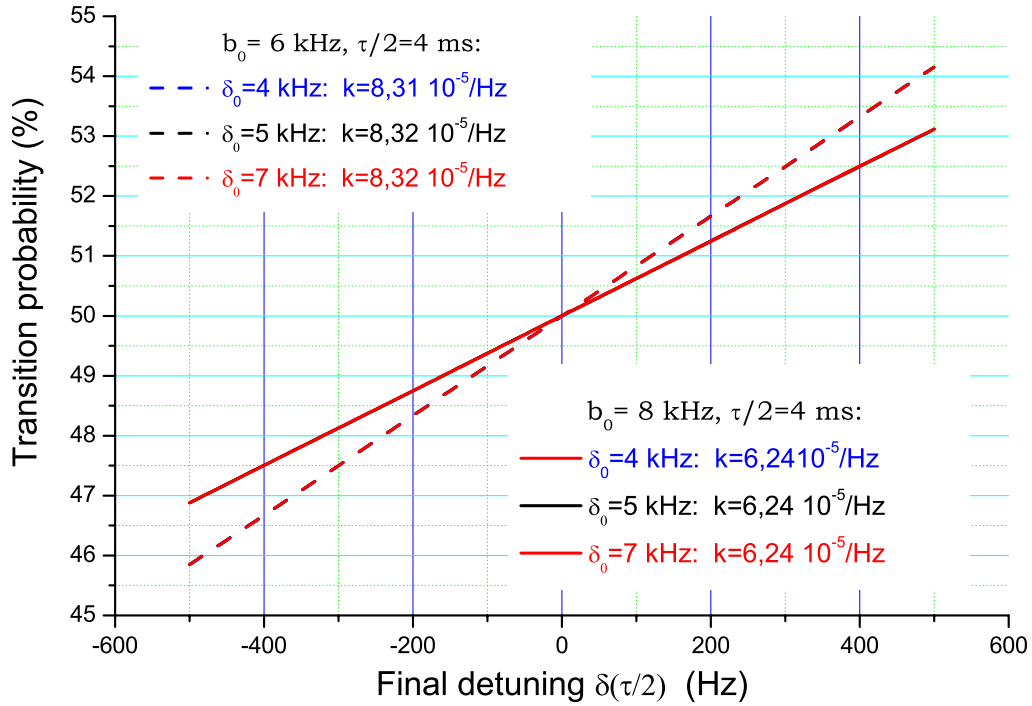


Figure 6.19: Sensitivity of the transition probability for HBP ($\tau/2 = 4$ ms) as a function of the final detuning between the TE_{011} mode and the atomic resonance. The calculation was done for an atom launched along the cavity axis. The slope depends on the maximum Rabi frequency b_0 , but the transition probability of HBP is independent of b_0 .

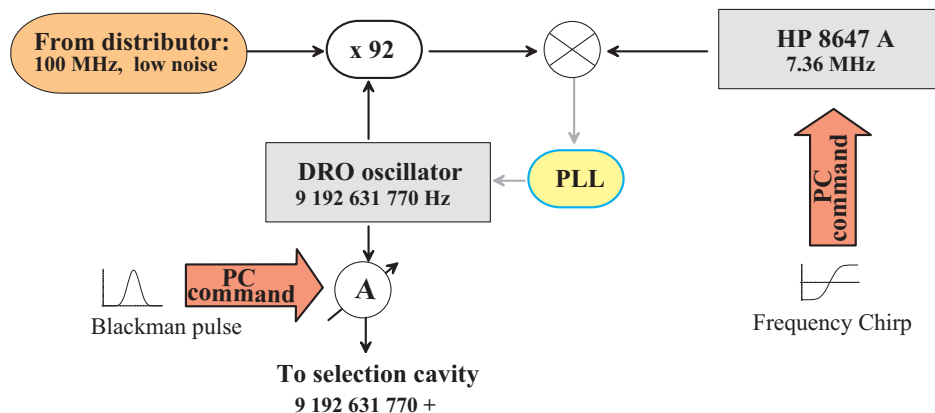


Figure 6.20: *The microwave chain used to drive the adiabatic passage in the selection cavity.*

to separate these Zeeman levels and provide a quantization axis, a uniform static magnetic field B_0 is applied. As the frequency chirp ranges between -5 kHz and $+5$ kHz, a magnetic field of $B_0 = 280$ mG is applied during all of the AP phase is sufficient to shift the adjacent transitions by more than 196 kHz from the $0 - 0$ transition. A calculation shows that in this case the excitation of $m_F \neq 0$ is below 0.25%. The magnetic field also induces a quadratic Zeeman shift on the transition $0 - 0$ of 33.5 Hz which is taken into account for the central frequency during AP. This magnetic field pulse is produced by two coils shown in fig. 6.1 coils (20).

Fig. 6.20 presents the microwave chain used to perform the adiabatic passage. The Blackman pulse is obtained by applying an adequate voltage sequence (500 steps) to a voltage-controlled microwave attenuator with a dynamic range of 60 dB. The frequency chirp is realized using a function generator HP8647A (Hewlett-Packard).

We alternated the Blackman and half-Blackman pulses every 50 fountain cycles to perform a differential measurement. In figure 6.21, the Allan variance of the ratio $\sigma_R(N_{cycle})$ of the number of the atoms detected in $|F = 4, m_F = 0\rangle$ is plotted, where N_{cycle} is the number of the fountain cycles. The stability of R reaches 4×10^{-4} after about four hours of integration. This reflects the insensitivity of the AP to the fluctuations of the experimental parameters. The mean value of the ratio is $R = 0.5042(4)$, whereas it was expected to be better than $0.500(1)$. We attribute this deviation ($< 1\%$) to the uncertainty in the final frequency of the HBP sweep. In the present setup, the frequency sweep is generated by an voltage controlled oscillator inside the HP 8647A, whose specified accuracy is limited to 50 Hz for a frequency sweep from -5 to $+5$ kHz. The numerical simulation shown

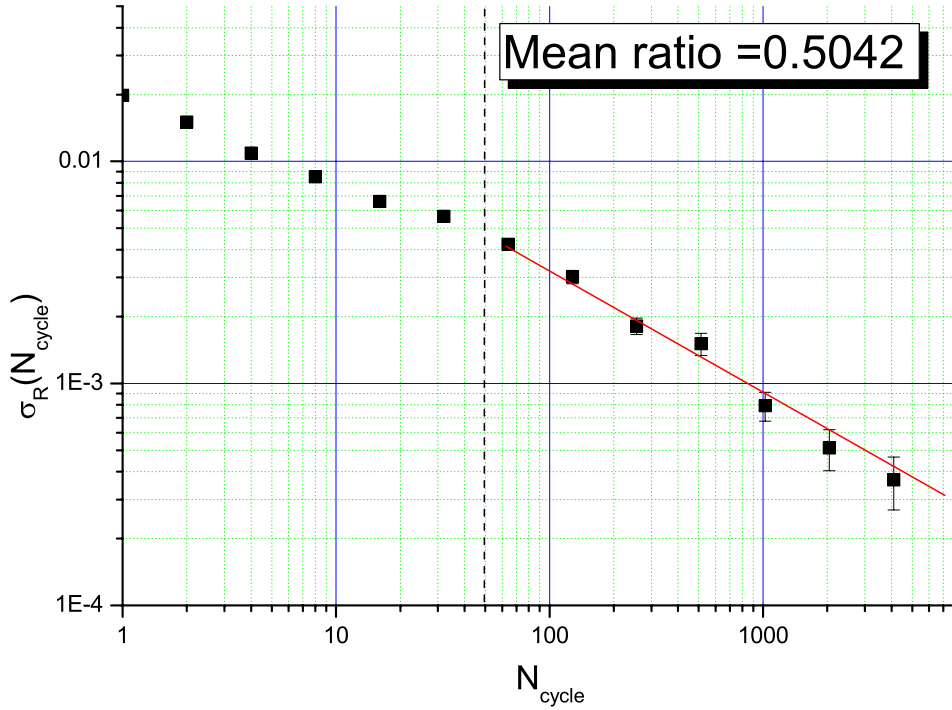


Figure 6.21: Allan standard deviation of the ratio R of the number of the atoms detected in $|F = 4, m_F = 0\rangle$ between for the half-Blackman and Blackman pulses, as a function of the number N_{cycle} of fountain cycles. The solid line indicates a dependance $\propto N_{\text{cycle}}^{-1/2}$.

in figure 6.19 demonstrates a linear deviation in the transition probability of 6.24×10^{-5} /Hz. This can explain a deviation of the ratio R by about 3×10^{-3} . Finally, the ratio R is estimated to be at least accurate at the 1% level. This uncertainty could be improved by using a dedicated DDS (Direct Digital Synthesizer).

In summary, the application of the adiabatic passage method in the improved FO1 can provide two atom samples with a ratio of 50% to better than 1% both in atom density and atom number. This allows us to directly determine the collisional frequency shift (proportional to n_{eff}) and the cavity pulling frequency shift (proportional to the number of atoms passing through the interrogation cavity) as linear with the number of the atoms detected with a resolution better than 1%.

6.7 The detection system

In the new set-up, as shown in fig. 6.9, the detection zone ((5), (6) and (7)), is located closely above the push beam (4). This change has several advantages: (a) After state selection, the launched atoms fly over an almost symmetric path from the push beam to the detection beam. This symmetry significantly reduces the clock frequency shift due to possible microwave leakage. (b) The flight time is shorter. Thus the duty cycle of the fountain is increased and atom loss is reduced leading to an improvement of the clock frequency stability. In addition, the fluorescence collection efficiency has been increased by a factor of 4 and the power of the detection beams is actively controlled (see fig. 6.7). These also help to improve the frequency stability.

The three laser beams used in the detection system set-up have a cross section of 7×13 mm. Fig. 6.22 shows the detection beam profile. The two beams detecting the atoms in the state $|F = 4\rangle$ are vertically separated by a distance of 15 mm. The intensity of each beam is 0.87 mW/cm² giving a saturation parameter of $S_0 = 0.8$. The intensity difference between the two beams is less than 5 %. The detuning of the detection beams from the $F = 4 \rightarrow F' = 5$ transition is adjusted between 0 and $-\Gamma/2$ to maximize the fluorescence signal and to avoid heating of the detected atoms. The repump beam has an intensity of 10 μ W/cm² and is used to pump atoms from the state $|F = 3, m_F = 0\rangle$ to the state $|F = 4\rangle$ which can then be detected on the cycling transition. All these three beams are circularly polarized to maximize the fluorescence signal and avoid the atoms from falling into the $|F = 3$ state. A retroreflecting mirror orthogonal is used to realize a standing wave. The inner surface of the detection and push zone is painted by colloidal graphite NEXTELL-811-21 in order to diminish residual stray light and Cs vapor.

The fluorescence light is collected by an optical system and focused onto

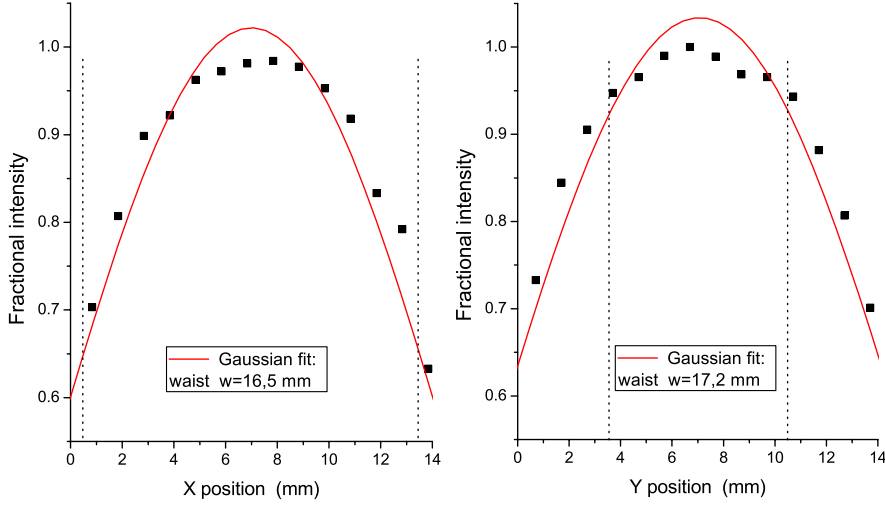


Figure 6.22: *Intensity profiles of the detection beams. The dashed lines the size of diaphragms on the detection beam.*

a 10×10 mm silicon photodiode (Hamamatsu S1337-1010BR) as shown in figure 6.23. The sensitivity of the photodiode is $S_{photo} = 0.55$ A/W. The collection optics and the photodiode are arranged inside a large tube painted by colloidal graphite. The collection angle is $\Omega_{coll} = 0.36$ rad, corresponding to a collection efficiency $\eta_{coll} \simeq 2.87\%$. The magnification of the collection system is 0.7 and its depth of field is 42.5 mm. We convert the current signal into a voltage with a low noise transimpedance amplifier (OPA637, Burr-Brown) with $R = 10^8 \Omega$. According to the formula (6.7), the spontaneous emission rate for one atom is 4.77×10^6 photon/s for a detuning of $\Gamma/2$. This corresponds to a signal of 1.76×10^{-6} Volt/atom. Assuming a launch velocity of 4 m/s, the vertical velocity of the falling atom at the detection zone is 3.52 m/s. There, the interaction time of the atoms with the detection beam is 2.0 ms, corresponding to a contribution to the time of flight signal of 3.52×10^{-9} V \cdot s/atom.

The detection noise mainly originates from the photodiode and the transimpedance amplifier. In order to reduce this noise, the photodiode is placed close to the electronics. We pay much attention to the ground connection. After the installation on the fountain set-up, we analyze the dark response of the photodiode and its electronics with an FFT analyzer (FR760, Stanford Research System), The results are shown in fig. 6.24. The averaged fluctua-

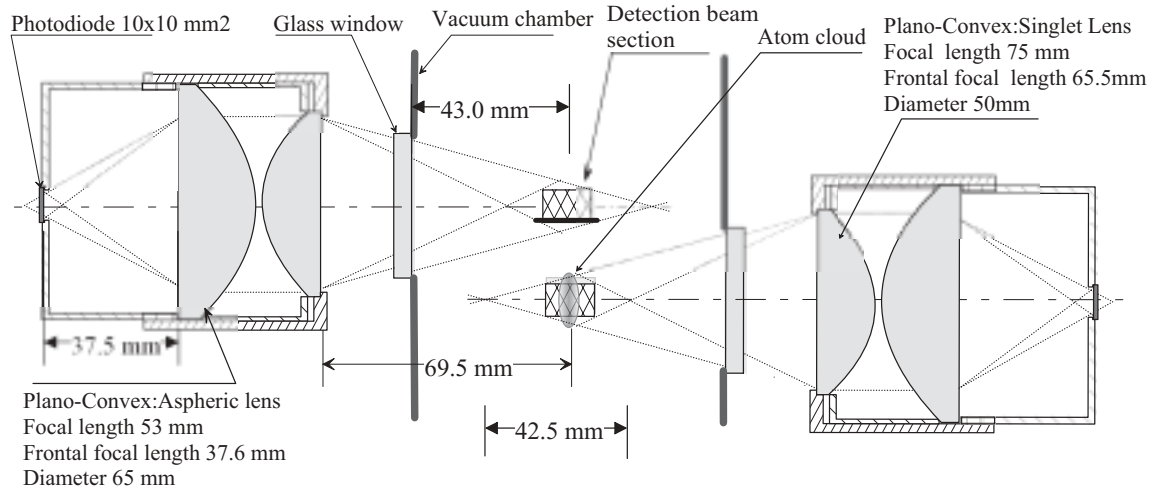


Figure 6.23: *Fluorescence collection system.*

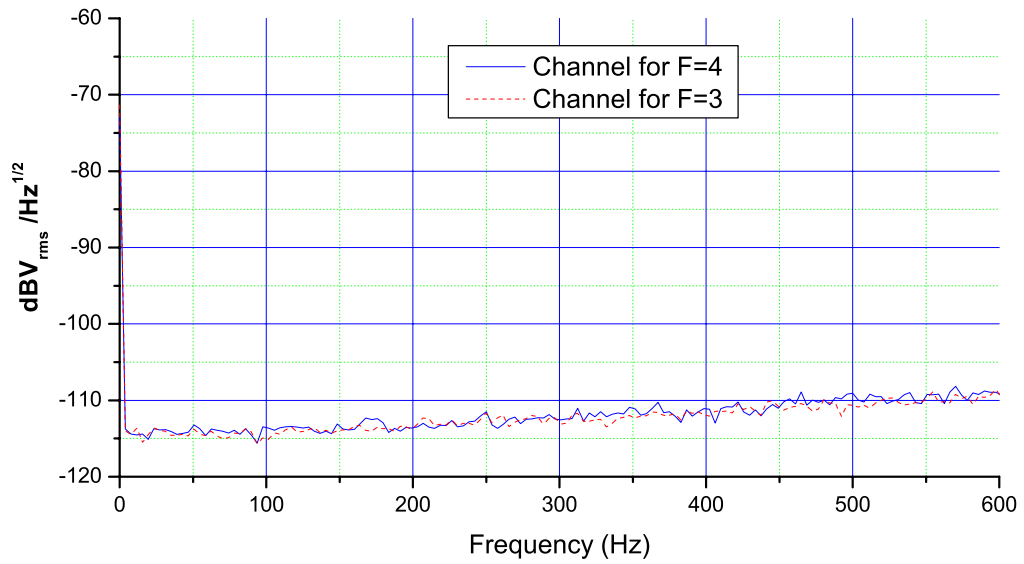


Figure 6.24: *Noise spectral density of the detection electronic system. It is measured with neither the detection laser beams nor caesium atoms.*

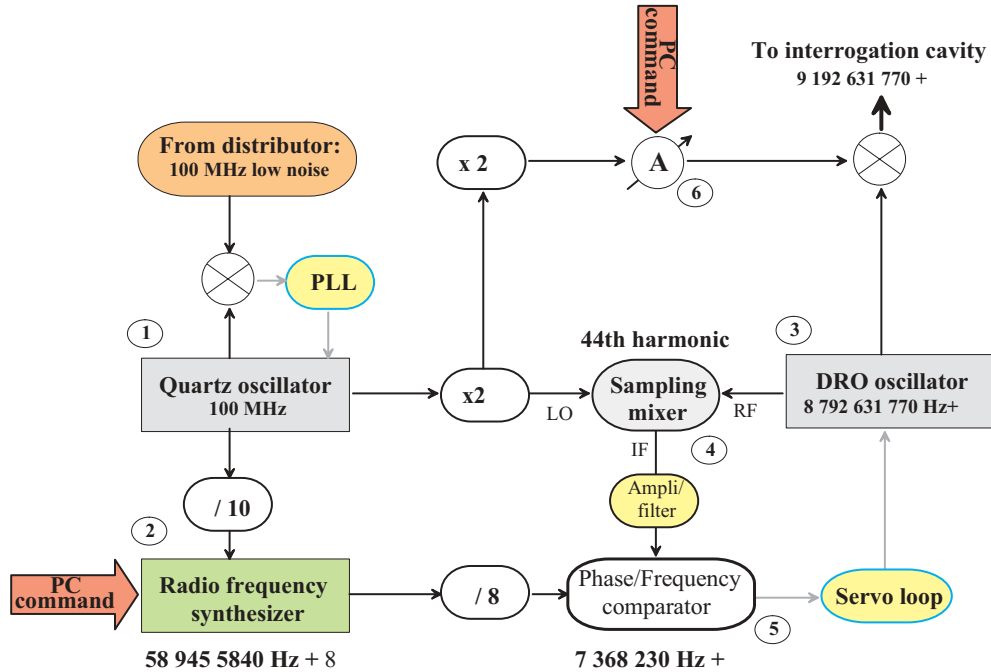


Figure 6.25: Block diagram of the microwave synthesis chain used for the improved FO1.

tion spectrum of the output signal is $1.78 \times 10^{-6} \text{ V}/\sqrt{\text{Hz}}$, it agrees well with the the value $1.6 \times 10^{-6} \text{ V}/\sqrt{\text{Hz}}$ deduced from the specifications. This noise is mainly dominated by the thermal noise ($1.3 \times 10^{-6} \text{ V}/\sqrt{\text{Hz}}$) of the resistance $R = 10^8 \Omega$. The NEP of the photodiode is $8.2 \times 10^{-15} \text{ A}/\sqrt{\text{Hz}}$. For the amplifier OPA637, the input voltage noise at $f=10 \text{ Hz}$ and the input bias current noise at 100 Hz are $2.0 \times 10^{-8} \text{ V}/\sqrt{\text{Hz}}$ and $2.5 \times 10^{-7} \text{ V}/\sqrt{\text{Hz}}$, respectively. The calculated variance⁵ of the integrated TOF signal is $\sigma_{STOF} = 4.86 \times 10^{-7} \text{ V} \cdot \text{s}$, corresponding to 138 detected atoms⁶.

6.8 Interrogation microwave synthesis chain

In order to reduce the phase noise of the interrogation microwave signal and to minimize the microwave field leakages at the atomic resonance from the frequency synthesis chain, a new microwave synthesis chain has been built.

The principle of the frequency synthesis chain is presented in fig. 6.25. A quartz oscillator (1) at 100 MHz is phase locked to the 100 MHz reference

⁵Experimental parameters in filter function 2.25 are $t_m = 60 \text{ ms}$ and $t_b = 20 \text{ ms}$, respectively.

⁶It decreases with a smaller detuning.

signal (see figure 2.26) with a bandwidth of 500 Hz. Then we phase lock a dielectric resonator oscillator (DRO) (3) to this quartz oscillator through a sampling mixer (Watkins-Johnson, W-J6300) (4): The frequency of the quartz oscillator is doubled and injected into the local oscillator (LO) input port of the sampling mixer. This device mixes the 44th harmonic of the 200 MHz signal with the hyper frequency of 8.792 GHz generated by the DRO. The output beatnote at 7.36 MHz is low-pass filtered and combined in a phase/frequency comparator (5) with the frequency divided (factor 8) output of the low phase noise synthesizer (HP 3325B)(2), which is synchronized to the 100 MHz quartz signal. The output of the comparator is fed to a servo system which controls the frequency of DRO. Furthermore the 100 MHz quartz signal is frequency multiplied by 4 and its level is adjusted (via a programmable attenuator (6)). It is summed to the 8.792GHz signal to obtain the Cs clock transition frequency. The microwave synthesis chain is closed by a magnetic field shielding box itself contained in a bigger aluminium box which is temperature controlled within ± 0.1 °C.

A computer controls the power and frequency of the interrogation microwave. Power is controlled through the attenuator with a resolution of 0.1 dB. The frequency control is achieved by acting on the synthesizer. The frequency resolution is 125 μ Hz.

Fig. 6.26 shows the power spectral density of the microwave synthesis chain at 9.2 GHz. The measurement is obtained by beating two similar chains using the same 100 MHz reference signal. Between 0.01 Hz and 10 kHz, a fit gives the spectral density of the phase noise as

$$S_y(f) = h_{+2}f^{+2} + h_{+1}f^{+1} + h_0f^0 + h_{-1}f^{-1} \quad (6.17)$$

where

$$\begin{aligned} h_{+2} &= 4.3 \times 10^{-31} \text{ Hz}^{-3} \\ h_{+1} &= 2.3 \times 10^{-28} \text{ Hz}^{-2} \\ h_0 &= -1.1 \times 10^{-28} \text{ Hz}^{-1} \\ h_{-1} &= 1.8 \times 10^{-29}. \end{aligned}$$

The noise induced by this chain is negligible if compared to the BVA quartz oscillator noise, but it is about 15 dB above the noise of a cryogenic sapphire oscillator (CSO) [127]. The microwave signal probing the atomic transition is synthesized from the CSO weakly phase-locked to a hydrogen maser from 2003. The frequency stability of the CSO is $\sim 10^{-15}$ up to 800 s, whereas the long-term stability is given by the H-maser.

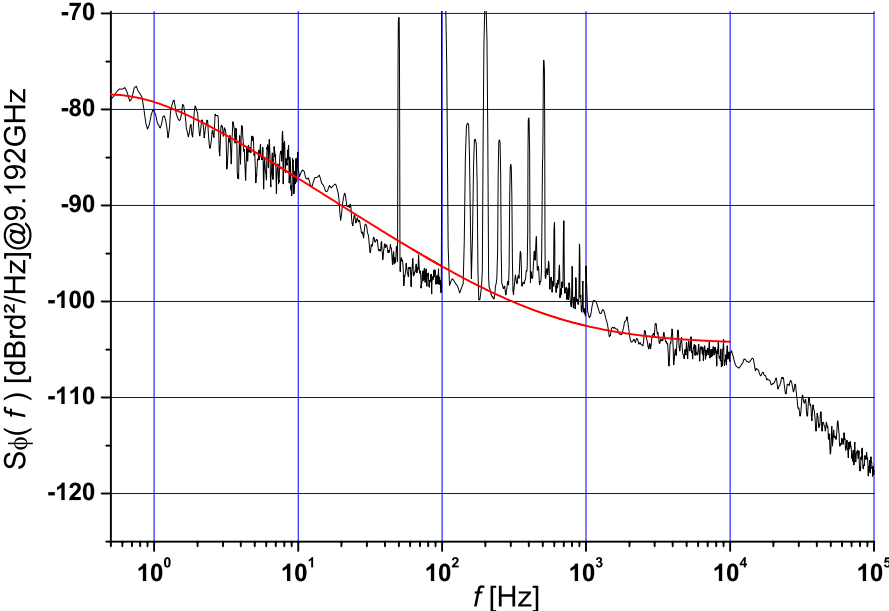


Figure 6.26: *Phase noise of the frequency synthesis chain at 9.192 GHz. The measurement is realized by a comparison between two similar chains using the same reference source at 100 MHz. The parasite peaks between 50 Hz and 1000 Hz arise from the measurement system.*

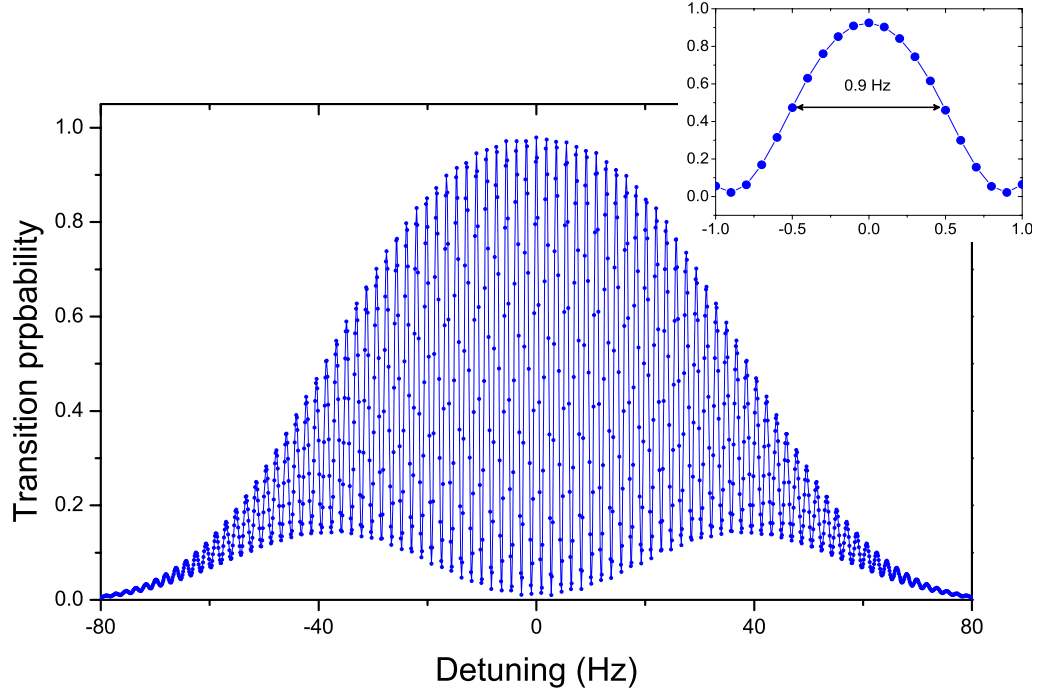


Figure 6.27: Ramsey fringes obtained in the improved FO1. The inset shows an enlargement of the central fringe which has a line-width of 0.9 Hz at half maximum of the transition probability, corresponding to a atom quality factor of $Q_{at} \simeq 1 \times 10^{10}$.

6.9 Recent results of the improved FO1

6.9.1 Frequency stability

Figure 6.27 shows Ramsey fringes obtained in the improved FO1. The corresponding experimental parameters are presented in appendix A.4. The central fringe shown in the inset has a line-width of 0.9 Hz at half maximum of the transition probability, corresponding to a atom quality factor of $Q_{at} \simeq 1 \times 10^{10}$.

When we operate the fountain at a cycle time of 1.3 seconds, the number of the detected atoms is about 4×10^6 per cycle. This number corresponds to a quantum projection noise (QPN) on the transition probability of $\sigma_{\delta P} = 2.5 \times 10^{-4}$. In order to estimate the technical noise without the influences of the noise of the interrogation oscillator, we set the frequency of the interrogation signal at the atomic resonance ($\delta\nu = 0$) and its power as $b\tau = \pi/4$, thus the transition probability is $P = 1/2$. A measurement gives the transition

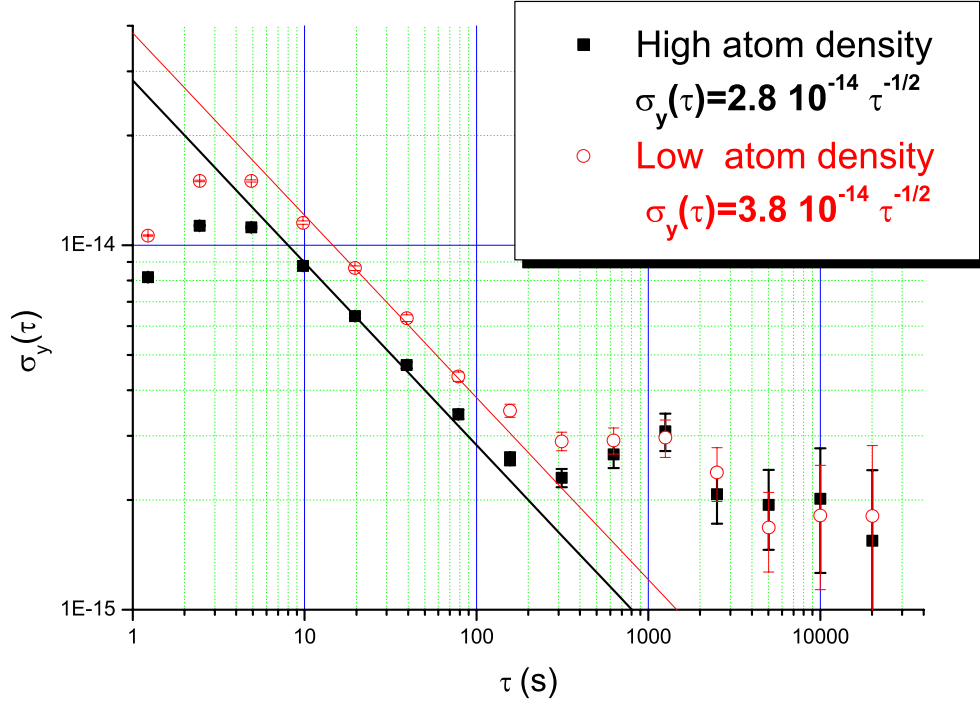


Figure 6.28: The frequency stability of the improved FO1 vs cryogenic sapphire oscillator phased locked to a H-maser for high atom density (about 4×10^6 detected atoms) and low atom density. The stability ratio is 1.35 close to the expected value of $\sqrt{2}$.

probability fluctuations $\sigma_{\delta P} \simeq 2.6 \times 10^{-4}$. In comparison with the QPN, we find the technical noise $\sim 7 \times 10^{-5}$, really negligible. When the frequency of the interrogation signal is detuned by an amount equal to the width of the atomic resonance ($\delta\nu = \delta\nu_{\text{Ramsey}}/2$) and the power is adjusted so that $b\tau = \pi/2$, the measured transition probability fluctuations are $\sigma_{\delta P} \simeq 4 \times 10^{-4}$, *i.e.*, a signal-to-noise ratio of 2500. An improvement by a factor of about 4 (compared to the first version of FO1) has been obtained. We can thus estimate the influence of the phase noise of the interrogation signal, it corresponds to $\sigma_{\delta P} \simeq 3 \times 10^{-4}$. We attribute it to the 150 m transmission cable of the 100 MHz frequency reference signal. When a cryogenic sapphire oscillator (CSO) is used as the local oscillator, the phase noise at 9.192... GHz is negligible at present. For the frequency synthesizer, a numerical calculation using the microwave phase noise ($h_{-1} \sim 1.8 \times 10^{-29}$) and formula (2.37) ($d \sim 0.45$) gives the Dick noise $\sigma_{\delta P} \simeq 4.6 \times 10^{-5}$ (corresponding a QPN limit when $N_{\text{det}} \sim 1 \times 10^8$). Finally, the expected frequency stability is $\sim 3 \times 10^{-14} \tau^{-1/2}$.

The cryogenic sapphire oscillator phase locked to a H-maser with a time constant of the order of 1000 s acts as the reference oscillator [4]. During an integration time of 10 s to 200 s, as shown in figure 6.28, the obtained frequency stability is $2.8 \times 10^{-14} \tau^{-1/2}$. This marks an improvement by a factor of 4 for FO1 over the stability obtained previously using a BVA quartz oscillator (Oscilloquartz). With this performance, the improved FO1 is one of the best primary frequency standards in the world today. For an integration time longer than 300 s, we see the slow frequency fluctuations of the CSO due to its operation conditions. Limited by the frequency fluctuations of the H-maser, we can only achieve a frequency stability of about 1×10^{-15} in one day of integration. A frequency comparison using three synchronized fountains at SYRTE, which will soon be carried out, can reject this noise.

6.9.2 Frequency accuracy

Collisional frequency shift and cavity pulling frequency shift Both collisional frequency shift and cavity pulling frequency shift are atom number dependent effects.

The application of the adiabatic passage method provides two cold atom samples with a ratio $R = 0.5$ both in the atom number and in the effective atom density n_{eff} . After about four hours of integration the stability of R reaches 4×10^{-4} (see figure 6.21). It is negligible compared to the systematic uncertainty of 1%.

This enables us to measure the shift of collision $\delta\nu_{coll}$ and the cavity pulling shift $\Delta\nu_{cp}$ at the same time. The measurement can be carried without any absolute calibration, nor numerical simulation.

$$\begin{aligned} \delta\nu_{coll} + \Delta\nu_{cp} &= K_{coll} n_{eff} + K_{cp} N_{at} \\ &\equiv K N_{det} \end{aligned} \quad (6.18)$$

where N_{at} is the averaged number of atoms crossing twice the interrogation cavity, K_{cp} and K are the cavity pulling frequency shift factor and the total frequency shift factor, respectively. The measured clock frequencies ν^H and ν^L at high and low atom density, can be expressed as

$$\begin{cases} \nu^H = \nu'_0 + K N_{det}^H \\ \nu^L = \nu'_0 + K N_{det}^L \end{cases} \quad (6.19)$$

where ν'_0 is the corrected frequency. It is easy to obtain the frequency correction for high density configuration

$$K N_{det}^H = (\nu^H - \nu^L) \frac{1}{1 - R}. \quad (6.20)$$

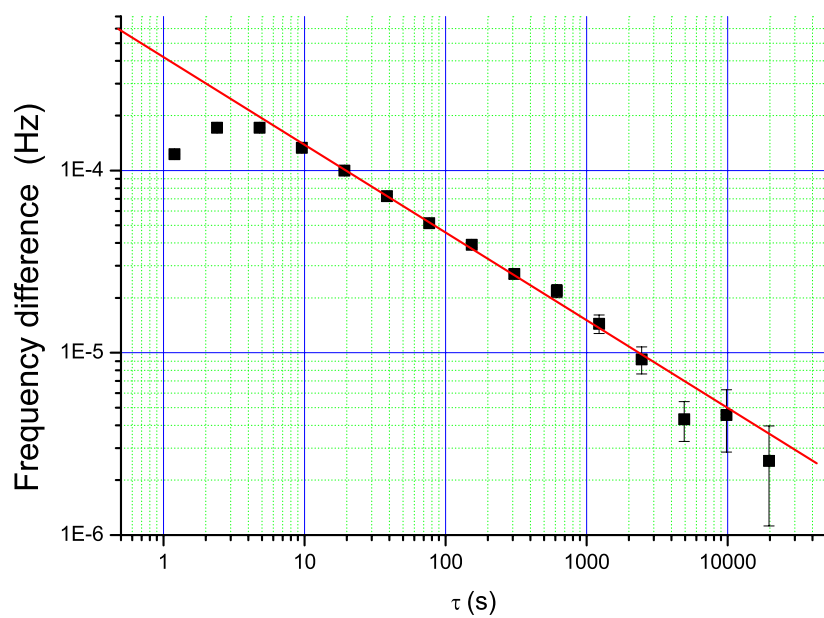


Figure 6.29: Allan standard deviation of frequency difference between the high and the low atom density configurations. It varies as $\tau^{-1/2}$

Experimentally, alternating sequences of measurements with high and low atomic densities (HD and LD) for each 50 cycles allows us to measure the atom number dependent shifts in real time. This procedure efficiently rejects slow frequency fluctuations and drifts of the local oscillator. In one day of integration the frequency difference ($\nu^H - \nu^L$) is measured with a resolution of $\sim 2 \mu\text{Hz}$ (see figure 6.29). With $\sim 4 \times 10^6$ detected atoms in the HD configuration, the measured mean frequency difference is $-109(2) \mu\text{Hz}$. This corresponds to the atom number dependent frequency shifts of $-218(4)(2) \mu\text{Hz}$ for the HD case. The error bars in parentheses reflect the statistical and systematic uncertainties, respectively. Over a long period, such as one month, this statistical uncertainty of the differential frequency measurement can be negligible. Thus a resolution of 1% can be obtained. We could also improve it by using a dedicated DDS in the microwave chain for the state selection.

Due to the imperfections of the selection (mainly from the push beam which de-pumps atoms from the $|4, m_F\rangle$ states to the $|3, m_F\rangle$ states), atoms in $|F = 3, m_F \neq 0\rangle$ populate the atomic cloud to 0.6%. Under the regular clock condition, the contribution of the collisional shift of $m_F \neq 0$ atoms is at most 1/3 of that of atoms in the clock states [128]. Hence, the uncompensated collisional shift of the $m_F \neq 0$ atoms is taken into account in the uncertainty of the collisional shift.

The measured collisional frequency shift factor is $K \sim -6 \times 10^{-11} \text{ Hz/atom}$, about one fifth of that in the first version of FO1 with MOT-optical molasses. This shows the advantage of the operation with optical molasses.

Frequency accuracy The accuracy evaluation of the improved FO1 is not yet completely finished. As we can determine the atom number dependent shifts at a level of 1%, the predicted frequency accuracy of the improved fountain FO1 is a few times 10^{-16} .

Chapter 7

Conclusion

7.1 Conclusions en français

La dernière exactitude de FO1 évaluée en 2002 avant modification de horloge, était de 1×10^{-15} , pour un fonctionnement avec une mélasse optique, ce qui constituait le meilleur résultat obtenu avec ce dispositif.

Les fontaines atomiques sont également des instruments utilisés pour des tests de physique fondamentale et pour des mesures extrêmement précises. Disposant au laboratoire de trois fontaines fonctionnant au césium ou au rubidium, nous avons pu effectuer les études expérimentales suivantes:

- afin de vérifier le principe d'équivalence d'Einstein, nous avons comparé les énergies hyperfines du ^{133}Cs et du ^{87}Rb pendant 5 années consécutives. Ces mesures constituent le test de laboratoire le plus contraignant sur une éventuelle dérive de la quantité $(\mu_{\text{Rb}}/\mu_{\text{Cs}})\alpha^{-0.44}$ à $(-0.2 \pm 7.0) \times 10^{-16}\text{yr}^{-1}$, soit une amélioration d'un facteur 5 par rapport à nos tests précédents en utilisant des fontaines atomiques et d'un facteur 100 par rapport la fréquence comparaison entre l'ion mercure et hydrogène [3].

- L'horloge spatiale PHARAO pourra tirer profit de l'environnement à gravitation réduite. Son exactitude attendue est de 1×10^{-16} (une exactitude de 7×10^{-16} pour FO2(Rb) [115]). La cavité de Ramsey développée pour l'horloge PHARAO est une cavité en anneau avec deux zones d'interaction micro-onde. Un résultat expérimental préliminaire a indiqué que la différence de phase du champ micro-onde entre les deux zones $\Delta\varphi$ est comprise entre 0 et $300 \mu\text{rad}$ et prouve ainsi que la géométrie de la cavité est adéquatée.

- grâce à la longue durée d'interaction, au fonctionnement pulsé et à la stabilité de fréquence très élevée, nous avons pu mesurer directement le déplacement de fréquence hyperfine dû à l'effet du rayonnement thermique avec une incertitude relative de 3.9%, une amélioration d'un facteur 3 par rapport aux mesures précédentes. La variation de ce déplacement de

fréquence en fonction de la température est donnée par l'expression $\Delta\nu(T) = 154(6) \times 10^{-6} \left(\frac{T}{300}\right)^4 \left[1 + \varepsilon \left(\frac{T}{300}\right)^2\right]$ Hz avec $\varepsilon = 0.014$, qui est en bon accord avec certains modèles développés sur l'effet Stark statique et dynamique [94, 100, 105], ainsi que sur les mesures les confortant [95, 101, 102, 103]. Notre mesure ne diffère que 2% de la mesure d'effet Stark statique effectuée au laboratoire. Cette valeur expérimentale nous conduit à une incertitude de quelques 10^{-16} pour l'évaluation due cet effet à température ambiante. Ces résultats vont à l'encontre de ceux du groupe de l'IEN [96, 97] et d'un modèle développé par Feichtner en 1965 [99].

Un grand nombre d'atomes détectés pour un fonctionnement avec un piège magnéto-optique améliore la stabilité. Cependant, il amplifié le déplacement de fréquence dû à l'effet des collisions entre atomes froids dans la fontaine de césium, ce qui constitue l'une des principales limitations de l'exactitude de l'horloge FO1. Dans l'horloge FO1 améliorée, la mise en oeuvre d'un dispositif de mélasse optique pure, chargée par un jet d'atomes ralentis par laser permet de refroidir un grand nombre d'atomes (4×10^8 en 400 ms) mais avec une densité 5 fois plus faible qu'avec un MOT. En outre, l'application de la méthode du passage adiabatique nous permet d'évaluer le déplacement de fréquence du aux collisions entre atomes froids et à l'effet d'entraînement de fréquence par la cavité au niveau de 10^{-16} . Afin de réduire le déplacement possible de fréquence induit par les fuites micro-onde, nous avons déplacé la zone de détection au-dessus de la zone de capture et avons développé une nouvelle chaîne micro-onde, de manière à ce que la puissance à la fréquence de résonance atomique soit ce que l'on exige pour l'alimentation de la cavité et pas plus. Le nouveau faisceau laser de détection, qui est asservi en fréquence en utilisant une modulation de phase et dont la puissance est aussi contrôlée, est bénéfique à la stabilité de l'horloge. Par ailleurs, la nouvelle disposition des faisceaux laser de capture simplifie le système électro-optique de manipulation des atomes froids. Cette simplification constitue une nette amélioration pour une utilisation continue de la fontaine FO1.

Les résultats préliminaires de l'horloge FO1 améliorée montrent qu'elle est l'une des meilleures fontaines au monde [115, 116, 117, 118]:

Le rapport du signal à bruit est amélioré d'un facteur 4. La stabilité à court terme en utilisant un résonateur à saphir cryogénique comme oscillateur local est $2.8 \times 10^{-14} \tau^{-1/2}$.

L'exactitude évaluée est en cours d'évaluation. Quelques 10^{-16} sont attendus.

Perspectives L'utilisation d'un piège magnéto-optique à deux dimensions comme source d'atomes peut aboutir à une amélioration du nombre d'atomes froids et à une importante réduction du temps de chargement, ainsi qu'à un net progrès dans la stabilité. Ces modifications seront être apportées prochainement.

Afin de bénéficier des hautes performances de l'horloge FO1 améliorée et des autres fontaines au BNM-SYRTE, nous pourrons éliminer l'influence du maser à hydrogène en synchronisant les trois fontaines à une minute près. Une résolution de mesure de quelques unités de 10^{-16} sur un temps intégration d'un jour est réalisable. Enfin, en effectuant une mesure plus précise du déplacement de fréquence dû à l'effet du rayonnement thermique, on pourra déterminer la valeur du terme ε plutôt s'appuyer sur une prévision théorique. En prolongeant la durée de mesure du rapport ν_{Cs}/ν_{Rb} , en améliorant l'exactitude des fontaines et en ajoutant des horloges optiques à la comparaison, on pourrait améliorer d'un ordre de grandeur le test sur la stabilité de α .

7.2 Conclusions and outlook in English

Conclusions The most recent evaluated accuracy of FO1 when operating with optical molasses was 1×10^{-15} in 2002, it was the lowest one compared to any previous reports.

Atomic fountains are also extremely precise and stable instruments for fundamental physics experimental studies and technical measurements. Taking advantage of the three fountains operating with caesium or rubidium, we have carried out several experimental studies as following:

- To test the Einstein Equivalence Principle, we have compared ^{133}Cs and ^{87}Rb hyperfine energies for 5 years using Cs and Rb fountains. We have set a stringent upper limit to a possible fractional variation of the quantity $(g_{\text{Rb}}/g_{\text{Cs}})\alpha^{-0.44}$ at $(-0.2 \pm 7.0) \times 10^{-16} \text{yr}^{-1}$, where g_{Rb} and g_{Cs} are respectively the nuclear g-factors of rubidium and caesium. The uncertainty is about 5 times smaller than our previous laboratory test and a 100-fold improvement over the $\text{Hg}^+\text{-H}$ hyperfine energy comparison.

- The cold atom space clock PHARAO will take advantage of the reduced gravity environment in space. Its projected accuracy is 1×10^{-16} . The Ramsey cavity developed for the PHARAO clock is a ring cavity with two microwave-atom interaction zones. A preliminary experimental result indicated that the offset phase between them is inside a range of 0 to 300 μrad and thus showed that the geometry of the cavity meets the requirement of the PHARAO clock.

- By making use of the long interaction, the pulsed operation and the high frequency stability, we have directly measured the AC hyperfine Stark shift in the fountain FO1 with a fractional uncertainty of 3.9%, which is 3 times better than previous measurements. The observed temperature dependent frequency shift of the Cs clock is $\Delta\nu(T) = 154(6) \times 10^{-6} \left(\frac{T}{300}\right)^4 \left[1 + \varepsilon \left(\frac{T}{300}\right)^2\right]$, with the theoretical value $\varepsilon = 0.014$. This result is in good agreement with Stark theories and Stark experiments with exception of the reports [96, 97] by the IEN group (15% difference). Our experimental results can lead us to an uncertainty of a few 10^{-16} for the evaluation of frequency shift due to BBR near room temperature in a caesium frequency standard.

A large number of the detected atoms when using a MOT improves the stability, however, it induces a large cold atom collisional frequency shift in caesium fountains, which was the main performance limitation in the first FO1. With the new cold atom source design, the size of the capture laser beams is no longer limited by the aperture of the interrogation cavity. A pure optical molasses loaded with a decelerated caesium beam can keep a large number of the loading atoms but with a small atomic density. Furthermore, the application of the adiabatic passage method allows us to evaluate the atom number dependent shifts (cold atoms collision and cavity pulling effects) at a level of 10^{-3} . In order to reduce a possible frequency shift induced by microwave leakage, we have moved the detection zone above the capture zone and developed a new microwave synthesis chain, in which the output power around atomic resonance frequency is just the desired quantity. The new detection laser beam, which is frequency locked using an external phase modulation and power controlled, is beneficial to the clock stability.

The preliminary results show that the improved FO1 is one of the best fountains in the world [115, 116, 117, 118]: the stability when using a cryogenic sapphire oscillator as the local oscillator is $2.8 \times 10^{-14} \tau^{-1/2}$. The frequency accuracy is currently under evaluation. As the atom number dependent frequency shifts are determined at the level of 1%, the expected frequency accuracy of the improved FO1 should be a few time 10^{-16} .

Perspectives Very soon, to load the optical molasses, the laser slowed atom beam will be replaced by a 2D MOT (loading rate 10^{10} atoms/s in place of 10^9 atoms/s with our present setup). This will allow a large reduction of the molasses loading time, resulting in an improvement of the frequency stability.

A new microwave synthesizer locked on the cryogenic oscillator with a lower phase noise than present one will lead to a frequency stability better than 2×10^{-14} at 1 s.

To take the advantages of the high performance of the improved FO1 and others fountains in SYRTE, we will eliminate the influence of the H-maser by synchronizing the three fountains to within one minute. A measurement resolution of 10^{-16} in one day of integration would then be feasible. A more precise measurement of the BBR shift will allow us to determine the value of the ε term rather than having to rely on a theoretical prediction.

Finally, a future frequency comparison between improved Rb and Cs fountains and a strontium optical frequency standard using femtosecond laser techniques at BNM-SYRTE will lead to a more sensitive test of α stability.

Appendix A

A.1 Abbreviations

ACES	Atomic Clock Ensemble in Space
AOM	Acousto-Optic Modulator
BBR	BlackBody Radiation
BIPM	Bureau International des Poids et Mesures
BNM-LPTF	Bureau National de Métrologie-Laboratoire Primaire du Temps et des Fréquences (Composante de l'actuel BNM-SYRTE depuis 2001)
BNM-SYRTE	Bureau National de Métrologie-SYstèmes de Référence Temps Espace
BP	Blackman Pulse
BVA	Boitier à vieillissement amélioré
CCIR	Comité Consultatif International des Radiocommunications
CENS	Centre National d'Etudes Spatiales, France
CIPM	Comité International des Poids et Mesures
CSO	Cryogenic Sapphire Oscillator
DDS	Direct Digital Synthesizer
DRO	Dielectric Resonator Oscillator
EAL	Echelle Atomique Libre
ECL	Extended Cavity Laser
EEP	Einstein's Equivalence Principle
ESA	European Space Agency
ET	Ephemeris Time
FO1	La première FOtaine de l'Obsevatoire de Paris, également le premier étalon de fréquence en fontaine à césium dans le monde
FO2	La deuxième FOntaine de l'Obsevatoire de Paris, qui peut fonctionner alternativement avec du rubidium et du césium
FOM	FOntaine Mobile de l'Obsevatoire de Paris
GALILEO	European global navigation satellite system, called Galileo
GLONASS	GLObal NAvigation Satellite System
GPS	Global Positioning System

HBP	Half Blackman Pulse
IEN	Istituto Elettrotecnico Nazionale, Italy
IRCOM	Institut de Recherche en Communications et Micro-onde, France
ISS	International Space Station
LCM	Laser of the Chirp Master
LCR	Laser of the Chirp Repumper
LKB	Laboratoire Kastler-Brossel, France
MJD	Modified Julian Day
MOT	Magnet-Optical Trap
MWL	Micro-Wave Link
NEP	Noise Equivalent Power
NIST	National Institute of Standards and Technology, USA
OFHC	Oxygen Free High Conductivity
PHARAO	Projet d'Horloge Atomique par Refroidissement d'Atomes en Orbite
PLL	Phase Lock Loop
PTB	Physikalisch-Technische Bundesanstalt, Germany
QPN	Quantum Projection Noise
RF	Radio Frequency
SHM	Space active Hydrogen Maser
SI	Système International d'Unités
TAI	Temps Atomique International
TOF	Time Of Flight
UT	Universal Time
VCO	Voltage Controlled Oscillator
VLBI	Very Long Baseline Interferometry

A.2 Physical constants

Constant	symbol	value (CODATA 1998)
Bohr magneton	μ_B	$9,27\,400\,899(37)\,10^{-24}\,\text{J}\cdot\text{T}^{-1}$
Speed of light in vacuum	c	$299\,792\,458\,\text{m}\cdot\text{s}^{-1}$
Magnetic permeability of the vacuum	μ_0	$4\pi\,10^{-7}\,\text{N}\cdot\text{A}^{-2}$
Electrical permeability of the vacuum	ϵ_0	$8,854\,187\,817\dots\,10^{-12}\,\text{F}\cdot\text{m}^{-1}$
Planck constant	h	$6,62\,606\,876(52)\,10^{-34}\,\text{J}\cdot\text{s}$
Boltzmann constant	k_B	$1,38\,650\,3(24)\,10^{-23}\,\text{J}\cdot\text{K}^{-1}$
Elementary charge	e	$1,602\,176\,462(63)\,10^{-19}\,\text{C}$
Fine-structure constant	α	$7,297\,352\,533(27)\,10^{-3}$
Stefan-Boltzmann constant	σ	$5,670\,400(40)\times 10^{-8}\,\text{W}/(\text{m}^2\,\text{K}^4)$

A.3 The atom ^{133}Cs

quantity	value ([40, 129])
Atomic number	$Z=55$
Atomic mass	$m= 2,206\ 946\ 50(17)\times 10^{-25}$ kg
Valence electron	$6S^1$
Melting point	$28,44$ °C
Vapor pressure at 25 °C	$1,3 \times 10^{-3}$ Torr
Relative nature abundance($^{133}\text{C}_s$)	100%
Nuclear lifetime	(stable)
Nuclear spin	$I = 7/2$
Nuclear Landé factor	$g_I = -4,013\ 10^{-4}$
Electronic Landé factor ($6^2S_{1/2}$)	$g_J=2,002\ 540\ 32$ (20)
Hyperfine transition frequency	$9\ 192\ 631\ 770$ Hz (exact)
Wavelength of the D_1 line (vacuum)	$\lambda_{D1} = 894,36$ nm
Wavelength of the D_2 line (vacuum)	$\lambda_{D2} = 852,347\ 275\ 82(27)$ nm
Wave number of the D_2 line (vacuum, $2\pi/\nu_{D2}$)	$k = 7,0235 \times 10^{-6}$ m $^{-1}$
Frequency of the D_2 line	$\nu_{D2} = 351,725\ 718\ 50(11)$ THz
Upper state lifetime of the $6^2P_{3/2}$ state	$\tau = 30,473(39)$ ns
Linewidth of the D_2 line ($1/\tau$)	$\Gamma = 2\pi \times 5,2152$ MHz
Saturation intensity of the D_2 line ($\pi\hbar c/3\lambda^3\tau$)	$I_S = 1,09$ mW.cm $^{-2}$
Cross section for D_2 absorption	$\sigma_{ge} = 346,9\ 10^{-15}$ m 2
Maximum acceleration by saturation of D_2 line	$a_{max} = 5,7\ 10^4$ m/s $^{-2}$
Catering power under saturation of D_2 line	$3,88$ pW
Recoil velocity from a D_2 photon ($\hbar k/m$)	$v_r = 3,52$ mm.s $^{-1}$
Recoil temperature ($\hbar^2 k^2/mk_B$)	$T_r = 0,198$ μK
Laser cooling capture velocity ($1/\tau k$)	$v_c = 4,42$ m.s $^{-1}$
Doppler temperature ($\hbar\Gamma/2K_B$)	$T_D = 124$ μK
Doppler velocity 1D ($\sqrt{\hbar\Gamma/2m}$)	$v_D = 8.82$ cm.s $^{-1}$

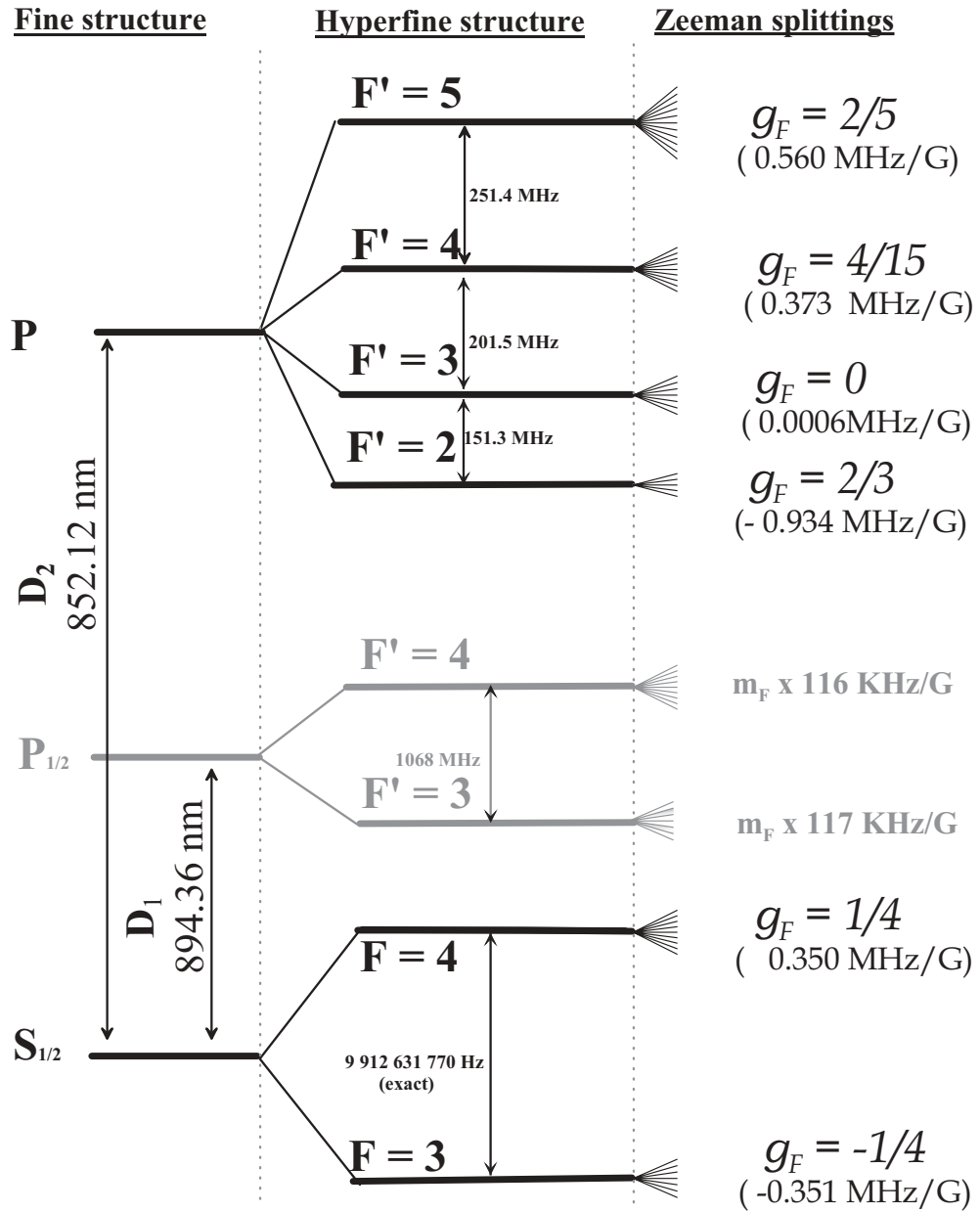


Figure A.1: Level scheme of the ground and first excited states ($6^2P_{1/2}$ and $6^2P_{3/2}$) of the ^{133}Cs atom.

A.4 Parameters of the improved FO1

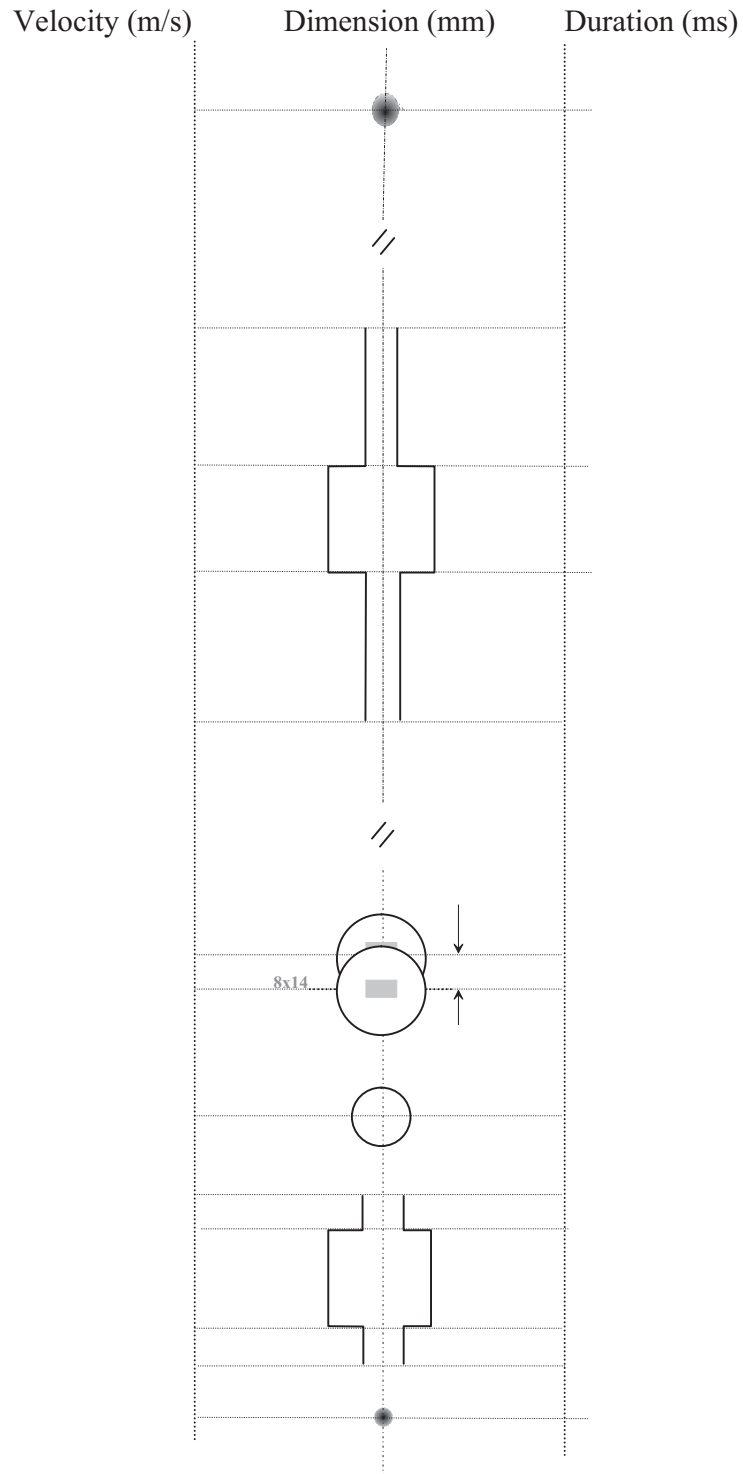


Figure A.2: *Parameters of improved FO1. The durations indicated correspond to a launch velocity of 4 m/s.*

Appendix B

B.1 Ramsey microwave interrogation

The two levels of interest in a Cs clock are the $F = 4, m_F = 0$ and $F = 3, m_F = 0$ hyperfine levels of the ground state. We denote them $|4\rangle$ and $|3\rangle$, respectively. We consider the following 2×2 matrix of a two-level system:

$$\rho = \begin{pmatrix} \rho_{3,3} & \rho_{3,4} \\ \rho_{4,3} & \rho_{4,4} \end{pmatrix} \quad (\text{B.1})$$

The Hamiltonian H describes the hyperfine interaction between the states $|4\rangle$ and $|3\rangle$, we note respectively E_4 and E_3 as their eigenvalues. The value $\frac{1}{2}(E_4 + E_3)$ is chosen as the origin for energy. The unperturbed Hamiltonian H_0 can be written as

$$H_0 = \frac{\hbar}{2} \begin{pmatrix} \omega_{at} & 0 \\ 0 & -\omega_{at} \end{pmatrix} \quad (\text{B.2})$$

where \hbar is Planck's constant divided by 2π and $\omega_{at} = 2\pi\nu_{at}$, is the hyperfine transition angular frequency in the presence of the weak static magnetic field.

We assume that the microwave magnetic induction $B_z(t)$, parallel to the direction z is a sinusoidal function of time, with an angular frequency ω and a constant amplitude B :

$$B_z(t) = \frac{B}{2}(e^{i(\omega t + \phi)} + e^{-i(\omega t + \phi)}). \quad (\text{B.3})$$

The phase ϕ is introduced to allow a possible phase difference between the two microwave fields of the two interaction regions, or account for a possible residual travelling wave. Assuming the $\omega \sim \omega_{at}$, we can use the two-level system density matrix for the caesium ground state. Including the interaction of the atom with the microwave field. If the lifetime of the state

$|4\rangle$ is much longer than the interaction time and the other relaxation effects such as atom-atom collisions are negligible, the whole Hamiltonian can be written as

$$H = \frac{\hbar}{2} \begin{pmatrix} \omega_{at}/2 & be^{-i(\omega t + \phi)} \\ be^{i(\omega t + \phi)} & -\omega_{at}/2 \end{pmatrix} + cc \quad (\text{B.4})$$

with

$$b = \frac{1}{2}\mu_B(g_j + g_I)/\hbar \simeq \mu_B B/\hbar \quad (\text{B.5})$$

where “cc” means complex conjugate. μ_B is the Bohr magneton, and b is the Rabi angular frequency of the atoms. The Landé factor for the nucleus g_I is about 1000 times smaller than that for the electron, $g_j = 2.002540$. We take $(g_j + g_I) \simeq 2$ with a precision which is sufficient for our present purpose. The evolution of ρ can be written using the analogue of Liouville’s theorem derived from the Schrödinger equation as:

$$\frac{d\rho}{dt} = \frac{1}{i\hbar}[H, \rho] \quad (\text{B.6})$$

replacing as follows:

$$\begin{cases} \rho_{4,3} = \frac{1}{2}(a_1(t) + ia_2(t))e^{-i\omega t} \\ \rho_{3,4} = \rho_{4,3}^* \\ \rho_{4,4} - \rho_{3,3} = a_3(t) \end{cases} \quad (\text{B.7})$$

were $a_1(t), a_2(t), a_3(t)$ are real quantities, representing the population after an interaction time t , and $a_1(0), a_2(0), a_3(0)$ are their initial values. When the amplitude and the phase of the microwave field phase are constant, and using the rotating-wave approximation (RWA)¹, we can get an exact analytic expression of the evolution of the atomic states. The system can also be solved via the Laplace transform method with the expression in matrix form [55]:

$$a(t) = R(b_1, b_2, \Omega_0, t)a(0) \quad (\text{B.8})$$

¹The interrogation microwave field inside the cavity has a linear polarization which can be decomposed in two rotating wave components. When the microwave frequency is $\omega \simeq \omega_{at}$, only one component can interact with the atom. The other negligible component produces only a Bloch-Siegert shift at the level of 10^{-18} because the interaction time $\tau \simeq 20$ ms is much longer than the period of the microwave 1/9.2 GHz.

A calculation of the transition probability without RWA is given in [130]

with

$$R(b_1, b_2, \Omega_0, t) = \begin{pmatrix} \cos(\Omega t) & -\frac{\Omega_0}{\Omega} \sin(\Omega t) & -\frac{b_1 \Omega_0}{\Omega^2} (1 - \cos(\Omega t)) \\ +\frac{b_1^2}{\Omega^2} (1 - \cos(\Omega t)) & +\frac{b_1 b_2}{\Omega^2} (1 - \cos(\Omega t)) & -\frac{b_2}{\Omega} \sin(\Omega t) \\ \frac{\Omega_0}{\Omega} \sin(\Omega t) & \cos(\Omega t) & \frac{b_1}{\Omega} \sin(\Omega t) \\ +\frac{b_1 b_2}{\Omega^2} (1 - \cos(\Omega t)) & +\frac{b_2^2}{\Omega^2} (1 - \cos(\Omega t)) & -\frac{b_2 \Omega_0}{\Omega^2} (1 - \cos(\Omega t)) \\ -\frac{b_1 \Omega_0}{\Omega^2} (1 - \cos(\Omega t)) & -\frac{b_1}{\Omega} \sin(\Omega t) & 1 - \frac{b^2}{\Omega^2} (1 - \cos(\Omega t)) \\ +\frac{b_2}{\Omega} \sin(\Omega t) & -\frac{b_2 \Omega_0}{\Omega^2} (1 - \cos(\Omega t)) & \end{pmatrix} \quad (\text{B.9})$$

where

$$\begin{cases} b_1 = b \cos \phi \\ b_2 = -b \sin \phi \\ \Omega_0 = \omega - \omega_{at} \\ \Omega^2 = b^2 + \Omega_0^2 \end{cases} \quad (\text{B.10})$$

After the interaction time t , the transition probability $P(t)$ between the two levels is related to the fractional population difference $a_3(t)$

$$P(t) = \frac{1}{2} \left(1 - \frac{a_3(t)}{a_3(0)} \right) \quad (\text{B.11})$$

and

$$\rho_{4,4}(t) = \rho_{4,4}(0)(1 - P(t)) + \rho_{3,3}(0)p(t) \quad (\text{B.12})$$

(A) The Rabi probability

In the Rabi magnetic resonance method [131], in which a single interaction pulse is applied, the atoms are introduced in the field region without coherence between $|4\rangle$ and $|3\rangle$ levels. In this case, $a_1(0) = a_2(0) = 0$, the transition probability $P(\tau)$ after an interaction time τ is obtained by using the proper elements of the equations (B.8) and (B.9):

$$P_{Rabi}(\tau) = \frac{b^2}{2\Omega^2} (1 - \cos \Omega \tau) \quad (\text{B.13})$$

The probability reaches the largest value, equal to unity, when the condition

$$b\tau = \pi \tag{B.14}$$

and $\Omega_0 = 0$ are satisfied. The full width at half maximum (FWHM) in frequency space, $\Delta\nu_{Rabi}$ is given by

$$\Delta\nu_{Rabi} = 0.799/\tau \tag{B.15}$$

(B) The Ramsey probability

In Cs clocks, we use the Ramsey resonance method [31]. The microwave field is applied in two identical interaction regions separated by a microwave-free drift space. We assume that the static magnetic field is the same for the three regions. The transition angular frequency ω_{at} is then constant over the whole atom trajectory. We set the interaction duration and drift time as τ and T , respectively. The caesium atoms enter the first interaction region without any coherence ($a_1(0) = a_2(0) = 0$), but a perfect population difference has created through state selection (see § 6.6). Either $a_3(0) = 1$ or $a_3(0) = -1$ for all atoms being in state $|3\rangle$ or in state $|4\rangle$.

We assume that the amplitude of the microwave field in the two interaction regions is the same. The quantum state of the atom at the output of the second interaction region is described by $a(\tau, T, \tau)$

$$\begin{pmatrix} a_1(\tau, T, \tau) \\ a_2(\tau, T, \tau) \\ a_3(\tau, T, \tau) \end{pmatrix} = R(b_1, b_2, \Omega_0, \tau)R(0, 0, \Omega_0, T)R(b_1, b_2, \Omega_0, \tau) \begin{pmatrix} 0 \\ 0 \\ a_3(0) \end{pmatrix} \tag{B.16}$$

We set $\phi = 0$ for the first interaction and we call ϕ , the phase lead of the microwave field in the second one. From the equations (B.8) and (B.9), we find the Ramsey probability $P_{Ramsey}(\tau, T, \tau)$ as

$$P_{Ramsey}(\tau, T, \tau) = \frac{4b^2}{\Omega^2} \sin^2\left(\frac{\Omega\tau}{2}\right) \left[\cos\left(\frac{\Omega\tau}{2}\right) \cos\left(\frac{\Omega_0 T + \phi}{2}\right) - \frac{\Omega_0}{\Omega} \sin\left(\frac{\Omega\tau}{2}\right) \sin\left(\frac{\Omega_0 T + \phi}{2}\right) \right]^2 \tag{B.17}$$

The value of $P_{Ramsey}(\tau, T, \tau)$ reaches a maximum for $\Omega_0 = 0$ and $\phi = 0$. Its value depends on the quantity b . If the condition

$$b\tau = \frac{\pi}{2} + n\pi. \tag{B.18}$$

B.2. SERVO ON THE ATOMIC RESONANCE IN RAMSEY INTERROGATION MODE

is satisfied, where n is an integer, the transition probability reaches unity (see figure1.2). For $\phi = \pi$, it is minimized. For $\Omega_0 \neq 0$, the motion of the atoms in the drift space, produce an interference effect. The appearance shown in figure1.2 is called Ramsey pattern. The central fringe is used as the atomic reference to control the quartz frequency in an atomic frequency standard. Its fullwidth at half maximum $\Delta\nu_{Ramsey}$ is given by

$$\Delta\nu_{Ramsey} \simeq \frac{1}{2T} \quad (B.19)$$

If $\Omega_0 \ll b$, we can get a simple expression of $P_{Ramsey}(\tau, T, \tau)$ as

$$P_{Ramsey}(\tau, T, \tau) \approx \frac{1}{2} \sin^2(b\tau) \left[1 + \cos\left(\pi \frac{\nu - \nu_{at}}{\Delta\nu_{Ramsey}} + \phi\right) \right] \quad (B.20)$$

B.2 Servo on the atomic resonance in Ramsey interrogation mode

The interrogating field is square frequency modulated around the clock transition at the frequency $1/2T_c$ with a modulation depth ν_m , in order to generate the servo error signal required to measure or lock the interrogation oscillator frequency with respect to atomic resonance. The average result gives the atomic resonance $\nu_{at} = \nu_0 + \delta\nu_F$. $\delta\nu_F \ll \nu_m$ is the frequency shift due to all the systemic perturbations. We are going express it as a function of the measured transition probability. The frequency servo system is to balance the difference of the two successive measurements of the transition probability

$$P(\nu_0 + \delta\nu_F + \nu_m) = P(\nu_0 + \delta\nu_F - \nu_m) \quad (B.21)$$

At the first order approximation, we have:

$$\begin{aligned} P(\nu_0 + \delta\nu_F \pm \nu_m) &= P^{(0)}(\nu_0 \pm \nu_m) + \delta P_{\pm} \\ &\approx P^{(0)}(\nu_0 \pm \nu_m) + \delta\nu_F \left. \frac{\partial P^{(0)}}{\partial \nu} \right|_{\nu=\nu_0 \pm \nu_m} \end{aligned} \quad (B.22)$$

where $P^{(0)}(\nu)$ is the transition probability without any perturbation. It is an even function of the detuning with respect to the atomic resonance. δP_{\pm} contains the probability changes due to the perturbations at $\nu_0 \pm \nu_m$. The modulation depth is adjusted to the detuning at half maximum of the atomic resonance, *i.e.*, $\nu_m = \Delta\nu_{Ramsey}/2$.

According the formula (B.20), the slope is given by $\left. \frac{\partial P^{(0)}}{\partial \nu} \right|_{\nu=\nu_0 \pm \nu_m} = \mp \frac{\pi}{2\Delta\nu_{\text{Ramsey}}}$.
 Finally, we can get the frequency shift:

$$\delta\nu_F = \frac{\Delta\nu_{\text{Ramsey}}}{\pi} \left(\delta P_+ - \delta P_- \right) = \frac{\delta P_+ - \delta P_-}{2\pi T} \quad (\text{B.23})$$

which is given in relative value as:

$$\frac{\delta\nu_F}{\nu_0} = \frac{\delta P_+ - \delta P_-}{\pi Q_{at}} \quad (\text{B.24})$$

B.3 The atomic sensitivity function in fountain

The atomic sensitivity function is used to express the atomic response to a perturbation during the microwave-atom interaction process. It was first introduced by G. J. Dick to explain the stability degradation of the periodic operating clock due to the arising of the local oscillator phase noise [41, 46]. This function is as well useful to explain some frequency shifts and to calculate some perturbations on clock frequency.

The sensitivity function $g(t)$ in Ramsey interaction is defined as

$$\delta P = \frac{1}{2} \int_{T+2\tau} g(t) \delta\omega(t) dt, \quad (\text{B.25})$$

where $\delta\omega(t) = \omega_{at} - \omega(t)$, represents the fluctuation of the frequency difference between the interrogation field and the atomic resonance. $g(t)$ is a perturbation function that express the sensitivity of the transition probability response δP to a perturbation $\delta\omega(t)$.

The sensitivity function can be obtained as the response of an infinitesimal phase step $\Delta\phi(t) = \Delta\phi H(t - t')$ at time t in the interrogation signal, which is equivalent to the dirac ϕ disturbance $\Delta\omega(t) = \frac{\Delta\phi}{2\pi} \delta(t - t')$. Practically as in reference [132], $g(t)$ can be also expressed in the following form:

$$g(t) = 2 \lim_{\Delta\phi \rightarrow 0} \frac{\delta P(t, \Delta\phi)}{\Delta\phi} \quad (\text{B.26})$$

The physical meaning of $g(t)$ is the response of the atomic system to a phase step of the interrogation oscillator, or the impulse response with respect to a frequency change occurring at time t .

B.3. THE ATOMIC SENSITIVITY FUNCTION IN FOUNTAIN

For the frequency servo loop in clock, we can also get the slope at half-height of Ramsey resonance central fringe expressed by the sensitivity function $g(t)$:

$$\frac{d}{d\omega}P(\nu_0 \pm \omega_m) = \frac{1}{2} \int_{2\tau+T} g_{\pm}(t) dt \equiv \mp \frac{1}{2} T_{eff} \quad (\text{B.27})$$

where T_{eff} defines the effective Ramsey interrogation time, which normalizes the sensitivity function, and $g_{\pm}(t)$ are the sensitivity function $g(t)$ respectively for the positif or negative detuning of the modulating frequency ω_m . One can show $g(t)$ is odd with respect to the frequency detuning, *i.e.*, $g_+(t) = -g_-(t)$. According to formula (B.23), for a independent perturbation in frequency difference $\delta\nu(t)$ between the interrogation field and the atomic resonance, the fountain clock frequency shift can be expressed as:

$$\delta\nu = \frac{\int_{2\tau+T} g_+(t) \delta\nu(t) dt}{T_{eff}} \quad (\text{B.28})$$

The electric-magnetic field mode is TE_{011} in our fountain as presented before. The amplitude of the magnetic field seen by atoms (along the axis of the cavity) is not constant, but varies as a sinuous function (see formula (2.6) and fig. 2.6). For our symmetrical interrogation, we can easily get the sensitivity function $g(t)$ using a geometric picture of the fictitious spin rotation [4], $g(t) = \sin(\theta(t))$ for one interrogation zone at half height of the atomic resonant fringe, where $\theta(t) = \int_0^t b(t) dt$ is the impulsion accumulated by an atom when crossing the cavity. $g(t)$ is obtained when $\Omega_0 = -\Delta\nu_{Ramsey}/2$:

$$g(t) = \begin{cases} \sin(\theta_2(\tau))\sin(\theta_1(t)) & 0 \leq t < \tau, \\ \sin(\theta_2(\tau))\sin(\theta_1(\tau)) & \tau \leq t < T + \tau, \\ \sin(\theta_2(2\tau + T - t))\sin(\theta_1(\tau)) & \tau + T \leq t < T + 2\tau, \\ 0 & t < 0 \text{ or } t > T_c. \end{cases} \quad (\text{B.29})$$

where $\theta_1(t)$ and $\theta_2(t)$ are defined as

$$\begin{cases} \theta_1(t) = \int_0^t b(t) dt \\ \theta_2(t) = \int_t^{2\tau+T} b(t) dt \end{cases} \quad (\text{B.30})$$

A numerical simulation for a fountain operation has been carried out. To take in account that the microwave amplitude is not constant, we divide each atom trajectory into 0.2 mm long elementary intervals in which the

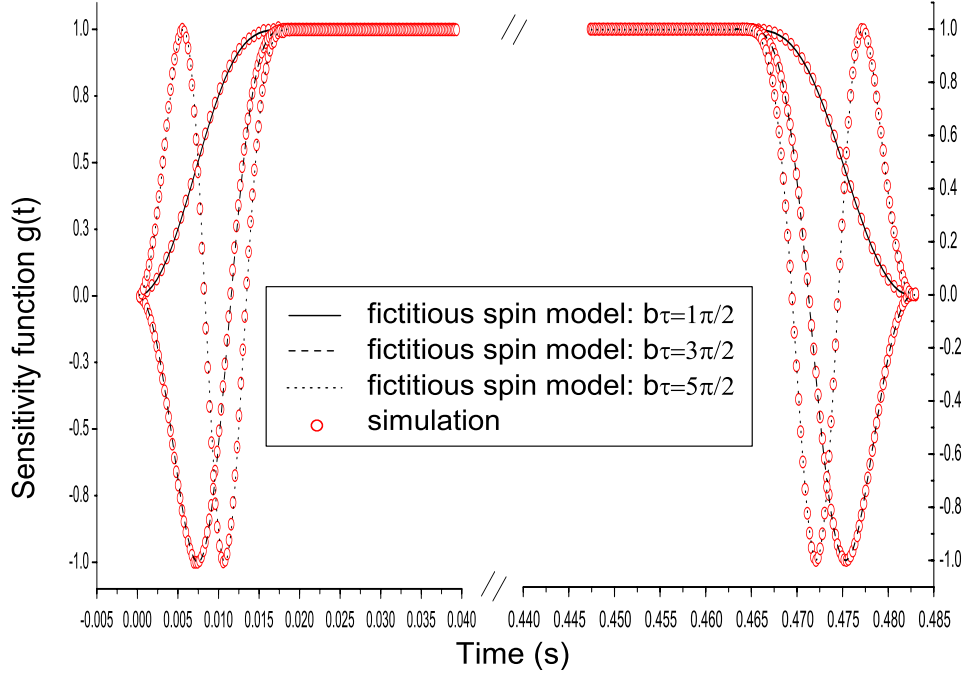


Figure B.1: Atomic sensitivity function $g(t)$ at half maximum of the Ramsey resonance ($\Omega_0 = -\Delta\nu_{\text{Ramsey}}$) when atomic trajectory is along the cavity axis. The calculations have been performed by using the fictitious spin model (eq. B.29) and $g(t)$ definition (eq. B.26) in FO1, where $\tau = 19$ ms, $T = 445$ ms and $b\tau = \pi/2$.

microwave amplitude is assumed to be constant. After having solved the Schrödinger equation, we obtain $g(t)$ by directly using its definition (B.26). The results of the fictitious rotation spin model (B.29) and the numerical simulation are both shown in fig. B.1. We find a very good agreement between them (difference $< 1\%$ for microwave pulses $\pi/2$, $3\pi/2$ and $5\pi/2$).

However, because of the velocity distribution and spatial distribution of the cold atoms inside the molasses, each atom has a different trajectory. The inhomogeneous field inside the TE_{011} cavity implies that each atom sees a different microwave field. As a consequence, each atom has a individual function $g_i(t)$. The frequency shift $\delta\nu$ of a perturbation results from the average value over all the detected atoms trajectories:

$$\frac{\delta\nu}{\nu_0} = \left\langle \frac{1}{\pi Q_{at}} \int g(t) \delta\omega(t) dt \right\rangle_i, \quad (\text{B.31})$$

where the re-defined atom Q factor is $Q_{at} = 2\nu_{at}T_{eff}$.

B.4 Conversion of the frequency stability analysis between frequency and time domains

Table B.1 lists the correspondence between the various noise components and the Allan variance of the normalized frequency ν_0 . The phase spectral density is $S_\phi(f) = (\frac{\nu_0}{f})^2 S_y(f)$.

Table B.1: *The noise expression correspondence in the two domains when $2\pi f_h \tau \gg 1$, where f_h is the cut-off frequency of an assumed single-pole low-pass filter. The values of the constants h_α depend on the source considered.*

Noise	$S_y(f)$	$\sigma_y^2(\tau)$	$K(\alpha)$
White phase	$h_2 f^2$	$\frac{3h_2 f_h}{4\pi^2} \tau^{-2}$	0.99
Flicker phase	$h_1 f$	$\frac{h_1 [1.04 + 3 \ln(2\pi f_h \tau)]}{4\pi^2} \tau^{-2}$	0.99
White frequency	h_0	$\frac{1}{2} h_0 \tau^{-1}$	0.87
Flicker frequency	$h_{-1} f^{-1}$	$2h_{-1} \ln 2$	0.77
Random walk frequency	$h_{-2} f^{-2}$	$\frac{2}{3} \pi^2 h_{-2} \tau$	0.75

Bibliography

- [1] *Résolution 1 CR 103*. 13^e conférence générale des poids et mesures, 1967.
- [2] N. F. Ramsey. The method of successive oscillatory fields *Phys. Today*. **33(7)**, 25 (1980).
- [3] J. D. Prestage, R. L. Tjoelker, and L. Maleki. Atomic clocks and variations of the fine structure constant *Phys. Rev. Lett.* **74**, 3511 (1995).
- [4] S. Bize. *Tests fondamentaux à l'aide d'horloges à atomes froids de rubidium et de césium*. PhD thesis of the Université Paris VI, 2001.
- [5] H. Marion, F. Pereira Dos Santos, M. Abgrall, S. Zhang, Y. Sortais, S. Bize, I. Maksimovic, D. Calonico, J. Grünert, C. Mandache, P. Lemonde, G. Santarelli, Ph. Laurent, A. Clairon, and C. Salomon. A search for the variation of fundamental constants using atomic fountains *Phys. Rev. Lett.* **90**, 150801–4 (2003).
- [6] K. Gibble, S. Chang and R. Legere. Direct observation of *s*-wave atomic collisions *Phys. Rev. Lett.* **75**, 2666 (1995).
- [7] E. Simon, Ph. Laurent, C. Mandache, and A. Clairon. Experimental measurement of the shift of caesium hyperfine splittings due to a static electric field. In *Proceedings of the 11th European Frequency and Time Forum*, Neuchâtel, Switzerland, 4-7 March 1997. FSRM.
- [8] P. Wolf. Proposed satellite test of special relativity *Phys. Rev. A.* **51**, 5016 (1995).
- [9] Ph. Laurent, M. Abgrall, A. Clairon, P. Lemonde, G. Santarelli, P. Urich, N. Dimarcq, L. G. Bernier, G. Busca, A. Jornod, P. Thomann, E. Simain, P. Wolf, F. Gonzalez, Ph. Guillemot, S. Leon, F. Nouel, Ch. Sirmain, S. Feltham, and C. Salomon. Cold atom clocks in space:

- PHARAO and ACES. In P. Gill, editor, *Proceedings of the 6th Symposium on Frequency Standards and Metrology*, page 241, St Andrews, Scotland, 9-14 September 2001. World Scientific.
- [10] C. Salomon and A. Clairon. Pharao: A cold atom clock in space, proposal in reponse to: ESA SP1201. volume missing in (1997).
- [11] D. S. Weiss, B. C. Young, and S. Chu. Precision measurement of the photon recoil of an atom using atomic interferometry *Phys. Rev. Lett.* **70**, 2706 (1993).
- [12] R. Battesti, P. Cladé, S. Guellati-Khélifa, C. Schwob, B. Grémaud, F. Nez, L. Julien, and F. Biraben. Acceleration of ultracold atoms:towards a measurement of $h/M_{87\text{Rb}}$ *J. Opt. B.:Quantum and Semiclass. Opt.* **5**, S178 (2003).
- [13] P. Berman (Ed.). *Atom Interferometry*. Academic, San Diego, 1997.
- [14] N. F. Ramsey. A molecular beam resonance method with separated oscillating field *Phys. Rev.* **78**, 695 (1950).
- [15] L. Essen and J. V. L Parry. The caesium resonator as a standard of frequency and time *Phil. Trans. R. Soc. London Ser.A.* **250**, 45–69 (1957).
- [16] J. R. Zacharias. *unpublished (1953) as described in [17, 31]*.
- [17] N. F. Ramsey. History of atomic clocks *Journal of Research NBS.* **88**, 301 (1983).
- [18] C. Cohen-Tannoudji, S. Chu, and W. D. Phillips. Nobel lectures *Rev. Mod. Phys.* **70**, 685–741 (1998).
- [19] T. W. Hänsch and A. L. Schawlow. Cooling of gases by laser radiation *Opt. Comm.* **13**, 68 (1975).
- [20] D. Wineland and H. Dehmelt. Proposed $10^{14} \delta\nu < \nu$ laser fluorescence spectroscopy on ti^+ mono-ion oscillator iii *Bull. Am. Phys. Soc.* **20**, 637 (1975).
- [21] W. D. Phillips and H. J. Metcalf. Laser deceleration of an atomic beamt *Phys. Rev. Lett.* **48**, 596 (1982).
- [22] S. Chu, L. Hollberg, J. E. Bjorkholm, A. Cable, and A. Ashkin. Three-dimensional viscous confinement and cooling of atoms by resonance radiation pressure *Phys. Rev. Lett.* **55**, 48 (1985).

- [23] P. D. Lett, R. N. Watts, Ch. I. Westbrook, W. D. Phillips, P. L. Gould, and H. J. Metcalf. Observation of atoms laser cooled below the doppler limit *Phys. Rev. Lett.* **61**, 169 (1988).
- [24] J. Dalibard and C. Cohen-Tannoudji. Laser cooling below the doppler limit by polarization gradients: simple theoretical models *J. Opt. Soc. Am.* **B6**, 2023–2045 (1989).
- [25] P. Ungar, D. Weiss, E. Riis, and S. Chu. Optical molasses and multi-level atoms: theory *J. Opt. Soc. Am.* **B6**, 2058–2071 (1989).
- [26] M. A. Kasevich, E. Riis, S. Chu, and R. G. DeVoe. Rf spectroscopy in an atomic fountain *Phys. Rev. Lett.* **63**, 612 (1989).
- [27] A. Clairon, C. Salomon, S. Guellati, and W. D. Phillips. Ramsey resonance in a zacharias fountain *Europhys. Lett.* **16**, 165–170 (1991).
- [28] A. Bauch and T. Heindorff. The primary caesium atomic clocks of the ptb. In A. De Marchi, editor, *Proceedings of the 4th Symposium on Frequency Standards and Metrology*, page 370, Ancona, Italy, 5-9 September 1988. Springer.
- [29] A. Clairon, Ph. Laurent, G. Santarelli, S. Ghezali, S. N. Lea, and M. Bahoura. A caesium fountain frequency standard: preliminary results *IEEE Trans. Instrum. Meas.* **44**, 128–131 (1995).
- [30] A. Clairon, S. Ghezali, Ph. Laurent, M. Bahoura, S. N. Lea, E. Simon, K. Sczymaniec, and S. Weyers. Preliminary accuracy evaluation of a caesium fountain frequency standard. In J. C. Bergquist, editor, *Proceedings of the 5th Symposium on Frequency Standard and Metrology*, pages 49–59, Massachusetts, USA, 15-19 October 1995. World Scientific.
- [31] N. F. Ramsey. *Molecular Beams*. Oxford University Press, 1956.
- [32] D. W. Allan. Statistics of atomic frequency standard *Proc. IEEE.* **54**, 221–231 (1966).
- [33] A. Kastler. Some suggestions concerning the production and the detection by optical means of inequalities in the population levels of spatial quantization in atoms: application to the stern and gerlach magnetic resonance experiments *J. Phys. Radium.* **11**, 255–265 (1950).
- [34] M. Arditi and J. L. Picqué. A caesium beam clock using laser optical pumping. preliminary tests *J. Phys. Lett.* **41**, 379–381 (1980).

-
- [35] A. Makdissi and E. de Clercq. Evaluation of the accuracy of the optically pumped caesium beam primary frequency standard of the BNM – LPTF *Metrologia*. **38**, 409–425 (2001).
- [36] J. Dalibard, C. Salomon, A. Aspect, E. Arimondo, R. Kaiser, V. Vansteenkiste, and C. Cohen-Tannoudji. In J. C. Gay S. Hariche and G. Grynberg, editors, *Proceedings of the 11th International Conference on Atomic Physics*, Paris, France, 4-8 July 1988. World Scientific.
- [37] C. Cohen-Tannoudji and W. D. Phillips. New mechanisms for laser cooling *Physics Today*. **43**, 33–40 (1990).
- [38] B. Sheehy, S-Q. Shang, P. van der Straten, S. Hatamian and H. J. Metcalf . Magnetic-field-induced laser cooling below the doppler limit *Phys. Rev. Lett.* **64**, 858 (1990).
- [39] C. Salomon, J. Dalibard, W. D. Phillips, A. Clairon, and S. Guellati. Laser cooling of caesium atoms below 3 μk *Europhys. Lett.* **12**, 683 (1990).
- [40] H. J. Metcalf and P. van der Straten. *Laser cooling and trapping*. Springer, 1999.
- [41] G. J. Dick. Local oscillator induced instabilities in trapped ion frequency standards. In *Proc. 19th Precise Time and Time Interval (PTTI) Applications and Planning Meeting*, pages 133–147, Redondo Beach, USA, 1-3 December 1987.
- [42] E. Tiesinga, B. J. Verhaar, H. T. C. Stoof, and D. van Bragt. Spin-exchange frequency shift in a caesium atomic fountain *Phys. Rev. A*. **45**, R2671 (1992).
- [43] M. Abgrall. *Evaluation des performances de la fontaine atomique PHARAO, Participation à l'étude de l'horloge spatiale PHARAO*. PhD thesis of the Université Paris VI, 2003.
- [44] S. Ghezali, Ph. Laurent, S. Lea, and A. Clairon. An experimental study of the spin exchange frequency shift in a laser cooled caesium fountain *Europhys. Lett.* **36**, 25 (1996).
- [45] G. Dudle, G. Mileti, A. Jolivet, E. Fretel, P. Berthoud, and P. Thomann. An alternative cold caesium frequency standard : the continuous fountain *IEEE Trans. on Ultr., Ferr. and Freq. Contr.* **47**, 438–442 (2000).

- [46] C. A. Greenhall. Derivation of the long term degradation of a pulsed atomic frequency standard from a control-loop model *IEEE Trans. on Ultr. Ferr. Freq. Contr.* **45**, 895 (1998).
- [47] C. Audoin, G. Santarelli, A. Makdissi, and A. Clairon. Properties of an oscillator slaved to a periodically interrogated atomic resonator *IEEE Trans. on Ultr. Ferr. and Freq. Contr.* **45**, 877 (1998).
- [48] W. M. Itano, J. C. Bergquist, J. J. Bollinger, J. M. Gilligan, D. J. Heinzen, F. L. Moore, M. G. Raizen, and D. J. Wineland. Quantum projection noise: Population fluctuations in two-level systems *Phys. Rev. A.* **47**, 3554 (1993).
- [49] S. Bize, Y. Sortais, P. Lemonde, S. Zhang, Ph. Laurent, G. Santarelli, C. Salomon, and A. Clairon. Interrogation oscillator noise rejection in the comparison of atomic fountains *IEEE Trans. on Ultr. Ferr. and Freq. Contr.* **47**, 1253–55 (2001).
- [50] C. Monroe, W. Swann, H. Robinson, and C. Wieman. Very cold trapped atoms in a vapor cell *Phys. Rev. Lett.* **65**, 1571–74 (1990).
- [51] Y. Sortais. *Construction d'une fontaine double à atomes froids de ^{87}Rb et ^{133}Cs ; Etude des effets dépendant du nombre d'atomes dans une fontaine.* PhD thesis of the Université Paris VI, 2001.
- [52] D. Kajfez and P. Guillon. *Dielectric resonators.* Artech House, Inc., 1986.
- [53] S. Ghezali. *Première évaluation de l'exactitude d'une fontaine d'atomes froids de césium à 2×10^{-15} et perspectives.* PhD thesis of the Université Paris VI, 1997.
- [54] A. Khurshed, G. Vecchi, and A. De Marchi. Spatial variations of field polarization and phase in microwave cavities: application to the caesium fountain cavity *IEEE Trans. on Ultr. Ferr. Freq. Contr.* **43**, 201–210 (1996).
- [55] J. Vanier and C. Audoin. *The quantum physics of atomic frequency standards.* Adam Hilger, Bristol, 1989.
- [56] J. S. Bendat and A. G. Piersol. *Random data: analysis and measurement procedures.* John Wiley & Sons, Inc., New York, 1971.
- [57] G. Santarelli. *Contribution à la réalisation d'une fontaine atomique.* PhD thesis of the Université Paris VI, 1996.

-
- [58] P. Wolf, S. Bize, A. Clairon, A. Landragin, Ph. Laurent, P. Lemonde, and Ch. J. Bordé. Recoil effects in microwave atomic frequency standards: an update. In P. Gill, editor, *Proceedings of the 6th Symposium on Frequency Standards and Metrology*, page 593, St Andrews, Scotland, 9-14 September 2001. World Scientific.
- [59] S. Bize, Y. Sortais, C. Mandache, A. Clairon, and C. Salomon. Cavity frequency pulling in cold atom fountains *IEEE Trans. Instrum. Meas.* **50**, 503–506 (2001).
- [60] B. Bousset, G. Théobald, P. Cézé, and E. de Clercq. Frequency shifts in caesium beam clocks induced by microwave leakages *IEEE Trans. on Ultr. Ferr. Freq. Contr.* **45**, 728–738 (1998).
- [61] G. Vecchi and A. De Marchi. Spatial phase variation in a TE₀₁₁ microwave cavity for use in a caesium fountain primary frequency standard *IEEE Trans. Instrum. Meas.* **42**, 434 (1993).
- [62] R. Schröder, U. Hübner, and D. Greibsch. Design and realization of the microwave cavity in the PTB caesium atomic fountain clock CSF1 *IEEE Trans. on Ultrason. Ferr. Freq. Contr.* **49**, 383–392 (2002).
- [63] P. Lemonde. *Pharao : Etude d'une horloge spatiale utilisant des atomes refroidis par laser; réalisation d'un prototype*. PhD thesis of the Université Paris VI, 1997.
- [64] P. Lemonde, Ph. Laurent, G. Santarelli, M. Abgrall, Y. Sortais, S. Bize, C. Nicolas, S. Zhang, G. Schehr, A. Clairon, and C. Salomon. Cold atom clocks on earth and in space. In A. N. Luiten, editor, *Frequency measurements and controls*, pages 131–152. Springer Verlag, 2001.
- [65] P. A. M. Dirac. The cosmological constants *Nature*. **139**, 323 (1937).
- [66] W. J. Marciano. Time variation of the fundamental “constants” and kaluza-klein theories *Phys. Rev. Lett.* **52**, 489 (1984).
- [67] J. D. Barrow. Observational limits on the time evolution of extra spatial dimensions *Phys. Rev. D.* **35**, 1805 (1987).
- [68] Y. Fujii. Possible link between the changing fine-structure constant and the accelerating universe via scalar-tensor theory *Int. J. Mod. Phys.* **D11**, 1137 (2002).

- [69] J. K. Webb, M. T. Murphy, V. V. Flambaum, and S. J. Curran. Does the fine structure constant vary? a third quasar absorption sample consistent with varying α *Astrophysics and Space Science*. **283**, 565 (2003).
- [70] R. Srianand, H. Chand, P. Petitjean, and B. Aracil. Limits on the time variation of the electromagnetic fine-structure constant in the low energy limit from absorption lines in the spectra of distant quasars *Phys. Rev. Lett.* **92**, 121302 (2004).
- [71] K. S. Thorne, D. L. Lee, and A. P. Lightman. Foundations for a theory of gravitation theories *Phys. Rev. D*. **7**, 3563 (1973).
- [72] S. M. Carroll. Quintessence and the rest of the world *Phys. Rev. Lett.* **81**, 3067 (1998).
- [73] T. Damour and F. Dyson. The oklo bound of the time variation of the fine structure constant revisited *A. Nucl. Phys.* **B480**, 37 (1996).
- [74] K. A. Olive, M. Pospelov, Yong-Zhong Qian, A. Coc, M. Cassé, and E. Vangioni-Flam. Constraints on the variations of the fundamental couplings *Phys.Rev. D*. **66**, 045022 (2002).
- [75] A. Songaila and L. Cowie. Fine-structure variable? *Nature*. **398**, 667 (1999).
- [76] S. G. Karshenboim. Some possibilities for laboratory searches for variations of fundamental constants *Canadian Journal of Physics*. **78**, 639–768 (2000).
- [77] A more precise calculation in [84] gives $d \ln(f_{rel})/d(\ln \alpha) = 0.83$ for ^{133}Cs , which differs by 10% from the casimir formula.
- [78] X. Calmet and H. Fritzsche. The cosmological evolution of the nucleon mass and the electroweak coupling constants *Eur. Phys. J. C*. **24**, 639 (2002).
- [79] S. Bize, S. A. Diddams, U. Tanaka, C. E. Tanner, W. H. Oskay, R. E. Drullinger, T. E. Parker, T. P. Heavner, S. R. Jefferts, L. Hollberg, W. M. Itano, and J. C. Bergquist. Testing the stability of fundamental constants with the $^{199}\text{Hg}^+$ single-ion optical clock *Phys. Rev. Lett.* **90**, 150802 (2003).

-
- [80] M. Niering, R. Holzwarth, J. Reichert, P. Pokasov, Th. Udem, M. Weitz, and T. W. Hänsch, P. Lemonde, G. Santarelli, M. Abgrall, Ph. Laurent, C. Salomon, and A. Clairon. Measurement of the hydrogen $1s - 2s$ transition frequency by phase coherent comparison with a microwave caesium fountain clock *Phys. Rev. Lett.* **84**, 5496–5499 (2000).
- [81] Th. Udem, S. A. Diddams, K. R. Vogel, C. W. Oates, E. A. Curtis, W. D. Lee, W. M. Itano, R. E. Drullinger, J. C. Bergquist, and L. Hollberg. Absolute frequency measurements of the Hg^+ and Ca optical clock transitions with a femtosecond laser *Phys. Rev. Lett.* **86**, 4996 (2001).
- [82] J. P. Turneaure, C. M. Will, B. F. Farrell, E. M. Mattison, and R. F. C. Vessot. Test of the principle of equivalence by a null gravitational red-shift experiment *Phys. Rev. D.* **27**, 1705 (1983).
- [83] A. Godone, C. Novero, P. Tavella, and K. Rahimullah. New experimental limits to the time variations of $g_p(m_e/m_p)$ and α *Phys. Rev. Lett.* **71**, 2364 (1993).
- [84] V. A. Dzuba, V. V. Flambaum, and J. K. Webb. Calculation of the relativistic effects in many-electron atom and space-time variation of the fundamental constants *Phys. Rev. A.* **59**, 230 (1999).
- [85] S. Bize, Y. Sortais, M. Abgrall, S. Zhang, D. Calonico, C. Mandache, P. Lemonde, Ph. Laurent, G. Santarelli, C. Salomon, and A. Clairon. Cs and Rb fountains: recent results. In P. Gill, editor, *Proceedings of the 6th Symposium on Frequency Standards and Metrology*, pages 53–63, St Andrews, Scotland, 9-14 September 2001. World Scientific.
- [86] S. Bize, Y. Sortais, M. S. Santos, C. Mandache, A. Clairon, and C. Salomon. High-accuracy measurement of the ^{87}Rb ground-state hyperfine splitting in an atomic fountain *Europhys. Lett.* **45**, 558 (1999).
- [87] Y. Sortais, S. Bize, M. Abgrall, S. Zhang, C. Nicolas, C. Mandache, P. Lemonde, Ph. Laurent, G. Santarelli, N. Dimarcq, O. Petit, A. Clairon, A. Mann, A. Luiten, S. Chang, and C. Salomon. Cold atoms clocks *Physica. Scripta.* **T**, 50–57 (2001).
- [88] N. A. Demidov, E. M. Ezhov, B. A. Uljanov, A. Bauch, and B. Fischer. Investigations of the frequency instability of CH1 – 75 hydrogen masers. In J. J. Hunt, editor, *Proc. of 6th European Frequency and Time Forum*, page 409, Noordwijk, Netherlands, 17-19 March 1992. ESA Publications Division.

- [89] L. A. Breahiron. A comparative study of clock rate and drift estimation. In *Proceedings of the 25th Precise Time Interval (PTTI) Application and Planning Meeting*, page 401, Narina Del Rey, USA, 29 November-2 December 1993. NASA. Goddard Space Flight Center.
- [90] C. Salomon, N. Dimarcq, M. Abgrall, A. Clairon, Ph. Laurent, P. Lemonde, G. Santarelli, P. Urich, L.G. Bernier, G. Busca, A. Jornod, P. Thomann, E. Samain, P. Wolf, F. Gonzalez, Ph. Guillemot, S. Léon, F. Nouel, Ch. Sirmain, and S. Feltham. Cold atoms in space and atomic clocks : ACES. In *C. R. Acad. Sci.*, pages 1313–1330, Paris, 2001.
- [91] A. Bauch and S. Weyers. New experimental limit on the validity of local position invariance *Phys. Rev. D.* **65**, 081101 (2002).
- [92] C. Salomon and C. Veillet. Aces: Atomic clock ensemble in space. In *First Symposium on the Utilisation of the International Space Station*, volume SP-385, page p295. ESA Special Publication, 1997.
- [93] R. F. C. Vessot, M. W. Levine, E. M. Mattison, E. L. Blomberg, T. E. Hoffman, G. U. Nystrom, B. F. Farrel, R. Decher, P. B. Eby, C. R. Baugher, J. W. Watts, D. L. Teuber, and F. D. Wills. Tests of relativistic gravitation with a space-borne hydrogen maser *Phys. Rev. Lett.* **45**, 2081 (1980).
- [94] W. M. Itano, L. L. Lewis, and D. J. Wineland. Shift of $^2S_{1/2}$ hyperfine splittings due to blackbody radiation *Phys. Rev. A.* **25**, 1233 (1982).
- [95] A. Bauch and R. Schröder. Experimental verification of the shift of the caesium hyperfine transition frequency due to blackbody radiation *Phys. Rev. Lett.* **78**, 622 (1997).
- [96] F. Levi, D. Calonico, L. Lorini, S. Micalizio, and A. Godone. Measurement of the blackbody radiation shift of the ^{133}Cs hyperfine transition in an atomic fountain. In <http://arxiv.org/abs/physics/0310051>, 2004.
- [97] S. Micalizio, A. Godone, D. Calonico, F. Levi, and L. Lorini. Blackbody radiation shift of the ^{133}Cs hyperfine transition frequency *Phys. Rev. A.* **69**, 053401 (2004).
- [98] J. W. Farley and W. H. Wing. Accurate calculation of dynamic stark shifts and depopulation rates of rydberg energy levels induced by blackbody radiation. Hydrogen, helium, and alkali-metal atoms *Phys. Rev. A.* **23**, 2397 (1981).

-
- [99] J. D. Feichtner, M. E. Hoover, and M. Mizushima. Stark effect of the hyperfine structure of caesium-133 *Phys. Rev.* **137**, A702 (1965).
- [100] T. Lee, T. P. Das, and R. M. Sternheimer. Perturbation theory for the stark effect in the hyperfine structure of alkali-metal atoms *Phys. Rev. A.* **11**, 1784 (1975).
- [101] R. D. Haun, Jr. and J. R. Zacharias. Stark effect on caesium-133 hyperfine structure *Phys. Rev.* **107**, 107 (1957).
- [102] J. R. Mowat. Stark effect in alkali-metal ground-state hyperfine structure *Phys. Rev. A.* **5**, 1059 (1972).
- [103] E. Simon, Ph. Laurent, and A. Clairon. Measurement of the stark shift of the cs hyperfine splitting in an atomic fountain *Phys. Rev. A.* **57**, 436 (1998).
- [104] E. Simon. *Vers une stabilité et une exactitude de 10^{-16} pour les horloges atomiques : le rayonnement du corps noir, la détection optique.* PhD thesis of the Université Paris VI, 1997.
- [105] V G Pal'chikov, Yu S Domnin, and A V Novoselov. Black-body radiation effects and light shifts in atomic frequency standards *J. Opt. B: Quantum and Semiclass. Opt.* **5**, s131–s135 (2003).
- [106] C. H. Townes and A. L. Schawlow. *Microwave spectroscopy.* McGraw-Hill, New York, 1955.
- [107] J. R. P. Angel and P. G. H. Sandars. The hyperfine structure stark effect *Proc. Roy. Soc. A.* **305**, 125–138 (1968).
- [108] P. G. H. Sandars. Differential polarizability in the ground state of the hydrogen atom *Proc. Phy. Soc.* **92**, 857 (1967).
- [109] C. Cohen-Tannoudji, B. Diu, and F. Laloë. *Quantum Mechanics*, volume 2. Hermann, 1973.
- [110] S. A. Blundell, W. R. Johnson, and J. Sapirstein. Relativistic all-order calculations of energies and matrix elements in caesium *Phys. Rev. A.* **43**, 3407 (1991).
- [111] J. P. Carrico, A. Adler, M. R. Baker, S. Legowski, E. Lipworth, P. G. H. Sandars, T. S. Stein, and M. C. Weisskopf. Atomic-beam resonance measurement of the differential polarizability between zeeman substates in the ground state of the caesium atom *Phys. Rev.* **170**, 64 (1968).

- [112] H. Gould, E. Lipworth, and M. C. Weisskopf. Quadratic stark shift between zeeman substates in Cs^{133} , Rb^{87} , Rb^{85} , K^{39} , and Na^{23} *Phys. Rev.* **188**, 24 (1969).
- [113] C. Ospelkaus, U. Rasbach, and A. Weis. Measurement of the forbidden tensor polarizability of cs using an all-optical ramsey resonance technique *Phys. Rev. A.* **67**, 011402 (2003).
- [114] A. J. Chapman. *Heat transfer*. Macmillan, New York, 1984.
- [115] F. Pereira Dos Santos, H. Marion, M. Abgrall, S. Zhang, Y. Sortais, S. Bize, I. Maksimovic, D. Calonico, J. Grünert, C. Mandache, P. Lemonde, G. Santarelli, Ph. Laurent, A. Clairon, and C. Salomon. ^{87}Rb and ^{133}Cs laser cooled clocks: testing the stability of fundamental constants. In J. R. Vig, editor, *Proceedings of the joint meeting of 17th European Frequency and Time Forum and the IEEE International Frequency Control Symposium*, Tampa, USA, 4-8 May 2003.
- [116] S. Weyers, U. Hübner, R. Schöder, C. Tamm, and A. Bauch. Uncertainty evaluation of the atomic caesium fountain CSF1 of the PTB *Metrologia.* **38**, 343–352 (2001).
- [117] T. E. Parker T. P. Heavner D. M. Meekhof C. Nelson F. Levi G. Costanzo A. De Marchi R. Drullinger L. Hollberg W. D. Lee S. R. Jefferts, J. Shirley and F. L. Walls. Accuracy evaluation of NIST – F1 *Metrologia.* **138**, 321–336 (2002).
- [118] F. Levi, L. Lorini, D. Calonico, and A. Godone P. Systematic shift uncertainty evaluation of IENCSF1 primary frequency standard *IEEE Trans on Instr. and Meas.* **52**, 267 (2002).
- [119] Y. Sortais, S. Bize, C. Nicolas, A. Clairon, C. Salomon, and C. Williams. Cold collision frequency shifts in a ^{87}Rb atomic fountain *Phys. Rev. Lett.* **85**, 3117 (2000).
- [120] F. Bloch. Nuclear induction *Phys. Rev.* **70**, 460 (1946).
- [121] A. Abragam. *Principles of nuclear magnetism*. Clarendon Press. Oxford, 1961.
- [122] Michael M. T. Loy. Observation of population inversion by optical adiabatic rapid passage *Phys. Rev. Lett.* **32**, 814 (1974).
- [123] C. Cohen-Tannoudji and S. Haroche. Dressed-atom description of resonance fluorescence and absorption spectra of a multi-level atom in an intense laser beam *J. Physique.* **30**, 153 (1969).

- [124] A. Messiah. *Mécanique Quantique*, volume 2. Dunod, Paris, 1999.
- [125] R. B. Blackman and J. W. Tukey. *The measurement of power spectra from the point of view of communications engineering*. Dover, New York, 1958.
- [126] M. A. Kasevich and S. Chu. Laser cooling below a photon recoil with 3-level atoms *Phys. Rev. Lett.* **69**, 1741–1744 (1992).
- [127] A. N. Luiten, A. Mann, M. Costa, and D. Blair. Power stabilized cryogenic sapphire oscillator *IEEE Trans. Instrum. Meas.* **44**, 132–135 (1995).
- [128] H. Marion, S. Bize, L. Cacciapuoti, D. Chambon, F. Pereira Dos Santos, G. Santarelli, P. Wolf, A. Clairon, A. Luiten, M. Tobar, S. Kokkellmans, and C. Salomon. First observation of Feshbach resonances at very low magnetic field in a ^{133}Cs fountain. In *Proceedings of the 18th European Frequency and Time Forum*, Guildford UK, 5-7 April 2004. (in press).
- [129] D.A. Steck. Cesium d line data. In <http://steck.us/alkalidata/>, 1998.
- [130] J. H. Shirley. Solution of the schrödinger equation with a hamiltonian periodic in time *Phys. Rev.* **138**, B979 (1965).
- [131] I. I. Rabi, J. R. Zacharias, S. Millman, and P. Kusch . A new method of measuring nuclear magnetic moment *Phys. Rev.* **53**, 318 (1938).
- [132] G. Santarelli, C. Audoin, A. Makdissi, Ph. Laurent, G. J. Dick, and A. Clairon. Frequency stability degradation of an oscillator slaved to a periodically interrogated atomic resonator *IEEE Trans. on Ultr. Ferr. Freq. Contr.* **45**, 887–894 (1998).

Résumé FO1, du laboratoire BNM-SYRTE, a été la première fontaine à Cs fonctionnant comme un étalon primaire de fréquence dans le monde. La dernière évaluation d'exactitude en 2002 était de 1×10^{-15} avec une mélasse optique. Travaillant comme instrument, FO1 a contribué à la physique fondamentale et à des mesures extrêmement précises:

- la comparaison de la fréquence entre les fontaines à Cs et à Rb pendant un intervalle de 5 ans a fixé une limite supérieure à la variation possible de la constante de structure fine $|\Delta\alpha/\alpha| < 2 \times 10^{-15} \text{yr}^{-1}$. L'évaluation est environ 5 fois meilleur que celle obtenue précédemment au laboratoire.

- l'exactitude attendu pour l'horloge spatiale PHARAO est de 1×10^{-16} . Nous avons confirmé les performances de la cavité Ramsey en examinant la différence de phase entre les deux zones d'interaction dans la fontaine FO1.

- le déplacement de fréquence mesuré dans l'horloge à Cs dû au rayonnement du corps noir en fonction de la température T a donné: $\Delta\nu(T) = 154(6) \times 10^{-6} (T/300)^4 [1 + \varepsilon(T/300)^2]$ Hz avec la valeur théorique $\varepsilon = 0,014$. Ce résultat représente une amélioration d'un facteur 3 par rapport à la mesure précédente par le group PTB.

Diverses améliorations ont été apportées à FO1. La nouvelle version de FO1 fonctionne directement en mélasse optique en utilisant un jet de césium ralenti comme source atomique. L'application de la méthode du passage adiabatique pour la sélection du niveau $F=3$, $m_F=0$ nous permet d'évaluer le déplacement de fréquence dû aux collisions entre atomes froids et à l'effet d'entraînement de fréquence par la cavité au niveau de 10^{-16} . Les résultats récemment obtenus avec l'horloge FO1 améliorée montrent qu'elle est l'une des meilleures fontaines au monde: la stabilité de fréquence en utilisant l'oscillateur cryogénique en saphir est maintenant de $2,8 \times 10^{-14} \tau^{-1/2}$. L'exactitude est en cours d'évaluation. Quelques 10^{-16} sont attendus.

Mots clés Fontaine atomique, horloge spatiale, métrologie temps-fréquence, collisions entre atomes froids, rayonnement du corps noir, constante de structure fine

Abstract FO1 was the first caesium fountain primary frequency standard in the world. The most recent evaluation in 2002 before improvement reached an accuracy of 1×10^{-15} when operated with optical molasses. Working as an extremely precise and stable instrument, FO1 has contributed to fundamental physics and technical measurements:

- Frequency comparison between Cs and Rb fountains over an interval of 5 years sets an upper limit for a possible variation of the fine structure constant as $|\Delta\alpha/\alpha| < 2 \times 10^{-15} \text{yr}^{-1}$. The resolution is about 5 times better than the previous test in our laboratory.

- The projected accuracy of the space clock PHARAO is 1×10^{-16} . We confirmed its Ramsey cavity performance by testing the phase difference between the two interaction zones in FO1.

- The measured temperature T dependent frequency shift of the Cs clock induced by the blackbody radiation field is given as $\Delta\nu(T) = 154(6) \times 10^{-6} (T/300)^4 [1 + \varepsilon(T/300)^2]$ Hz with the theoretical value $\varepsilon = 0,014$. The obtained accuracy represents a 3 times improvement over the previous measurement by the PTB group.

Some improvements have been carried out on FO1. The new FO1 version works directly with optical molasses loaded by a laser slowed atomic beam. The application of the adiabatic passage method to perform the state selection allows us to determine the atom number dependent frequency shifts due to the cold collision and cavity pulling effects at a level of 10^{-16} . Recently, the obtained frequency stability is $2,8 \times 10^{-14} \tau^{-1/2}$ for about 4×10^6 detected atoms. The accuracy is currently under evaluation, the expected value is a few times 10^{-16} .

Key words Atomic fountain clock, space clock, time and frequency metrology, cold collisions, black-body radiation, fine structure constant

摘要 FO1是世界上第一台铯原子喷泉基准钟。2002年评定的准确度为 1×10^{-15} 。除作为时间频率基准，它对基础物理和超精度测量做出了贡献：

5年的铷喷泉钟和铯喷泉钟的频率比对，限定了精细结构常数的相对变化 $|\Delta\alpha/\alpha| < 2 \times 10^{-15}/\text{年}$ 。该测量精度优于先前实验室测量5倍。

欧洲空间原子钟集合计划 ACES 中的空间站冷原子钟 PHARAO 的设计准确度为 1×10^{-16} 。利用 FO1 的测量确定了该钟 Ramsey 腔的两作用区相位差满足要求。

由于交流Stark效应，黑体辐射频移是限制原子喷泉钟准确度的一项最主要因素。在 FO1中实现的 ^{133}Cs 基态超精细跃迁黑体辐射频移测量比其它报导的的精度高3倍。

对FO1已作了许多改进。新的 FO1利用光学粘团直接装载激光冷却了的原子束。绝热过程技术的应用使我们可以在 10^{-16} 量级测定与原子数有关的频移：冷原子碰撞频移和腔牵引频移。初步结果证明改进了的FO1仍居世界领先地位。对于 4×10^6 个检测原子，我们获得了 $2.8 \times 10^{-14} \tau^{-1/2}$ 稳定度，其预测准确度在 10^{-16} 量级。

关键词 原子喷泉钟，空间原子钟，时间频率计量，冷原子碰撞，黑体辐射频移，精细结构常数